

Modeling and Simulation  
of the Static and Dynamic Magnetic Properties  
of Nanostructured Magnetic Multilayer Systems

Dissertation

"Doctor rerum naturalium" (Dr. rer. nat.)

submitted to the  
Faculty of Physics  
of the Bielefeld University

by Irina Stockem, M.Sc.

born on January the 18th, 1986 in Wesel

Reviewers:

Prof. Dr. Günter Reiss

Prof. Dr. Christian Schröder

Gedruckt auf alterungsbeständigem Papier gemäß ISO 9706.

# Declaration of Authorship

I hereby confirm that I wrote this thesis by myself and used none but the indicated resources.

Wesel, May 2016

(Irina Stockem)



# Contents

<b>1</b>	<b>Introduction</b>	<b>1</b>
<b>2</b>	<b>Fundamentals</b>	<b>7</b>
2.1	Quantum mechanical description of the Heisenberg model . . . . .	7
2.2	From a quantum mechanical model to a classical description . . . . .	8
2.3	Energy terms of the extended classical Heisenberg Hamiltonian . . . . .	10
2.3.1	Exchange interaction . . . . .	10
2.3.2	Zeeman term . . . . .	10
2.3.3	Uniaxial anisotropy . . . . .	11
2.3.4	Magnetic dipole-dipole interactions . . . . .	11
<b>3</b>	<b>Calculation Methods</b>	<b>15</b>
3.1	Magnetic states of spin systems with low complexity . . . . .	17
3.1.1	Stoner-Wohlfarth model . . . . .	17
3.1.2	Classical spin dimer . . . . .	21
3.2	Atomistic spin dynamics . . . . .	24
3.2.1	Landau-Lifshitz equation . . . . .	24
3.2.2	Monte Carlo approach . . . . .	27
3.3	Micromagnetics . . . . .	28
3.4	Macrospin approach . . . . .	30
<b>4</b>	<b>Hysteresis Modeling</b>	<b>33</b>
4.1	Fundamentals of magnetic hysteresis . . . . .	33
4.2	Serial calculation of hysteresis curves . . . . .	39
4.2.1	Solving the Landau-Lifshitz equation of motion . . . . .	39
4.2.2	Applying a modified Monte Carlo scheme . . . . .	40
4.2.3	Application: Magnetization curve of a thin CoFe layer . . . . .	42

4.3	Parallel calculation of hysteresis curves . . . . .	45
4.3.1	Division into independent parts . . . . .	45
4.3.2	Calculation of the magnetization within the intervals . .	48
4.3.3	Hybrid scheme for dipole-dipole interactions . . . . .	49
4.3.4	Temperature . . . . .	50
4.3.5	Limitations of the method . . . . .	51
4.4	Concluding words on hysteresis modeling . . . . .	52
<b>5</b>	<b>Exchange Bias: Theory and Modeling</b>	<b>55</b>
5.1	Discovery of the exchange bias effect . . . . .	56
5.2	Exchange bias models . . . . .	62
5.2.1	Meiklejohn-Bean model . . . . .	62
5.2.2	One dimensional chain model . . . . .	68
5.2.3	Other important exchange bias models . . . . .	72
5.3	Classification of exchange bias applications . . . . .	84
5.3.1	Conventional exchange bias systems . . . . .	84
5.3.2	Switchable exchange bias systems . . . . .	85
5.3.3	Exchange spring magnets . . . . .	89
5.3.4	Systems showing mixed magnetic characteristics . . . . .	91
<b>6</b>	<b>Exchange Bias: NiFe/IrMn</b>	<b>93</b>
6.1	NiFe/IrMn: AFM TAMR at an exchange spring system . . . . .	93
6.2	Crystal structures and material parameters of NiFe/IrMn . . . . .	96
6.2.1	Material data of NiFe . . . . .	99
6.2.2	Material data of IrMn <sub>3</sub> . . . . .	100
6.3	Ground state configurations of NiFe, IrMn and NiFe/IrMn . . .	100
6.3.1	Ground states of NiFe . . . . .	101
6.3.2	Ground states of IrMn <sub>3</sub> . . . . .	101
6.3.3	Ground states of the NiFe/IrMn stack . . . . .	104
6.4	Applied simulation methods . . . . .	105
6.5	<i>3Mn3C</i> magnetization curves with an ideal interface structure .	107
6.6	Including interfacial defects . . . . .	109
6.6.1	Asymmetric coupling . . . . .	109
6.6.2	Replacement of one Mn spin . . . . .	111

6.7	Towards qualitative and quantitative comparable magnetization curves . . . . .	114
6.7.1	Influence of the exchange coupling constant . . . . .	114
6.7.2	Influence of the NiFe layer thickness . . . . .	115
6.7.3	Influence of the lateral dimensioning . . . . .	116
6.7.4	Influence of the sweep rate . . . . .	119
6.8	Switching by high magnetic fields at finite temperatures . . . . .	120
6.8.1	Applying a high magnetic field pulse . . . . .	121
6.8.2	Applying a magnetic field ramp . . . . .	122
6.9	Atomistic spin dynamics of NiFe/IrMn at finite temperatures . . . . .	123
6.9.1	Temperature dependence of the 1.5 nm IrMn sample . . . . .	125
6.9.2	Temperature dependence of the 3 nm IrMn sample . . . . .	127
6.10	Comparison with experimental properties and conclusion . . . . .	129
<b>7</b>	<b>Exchange Bias: Pt/Co/Cr<sub>2</sub>O<sub>3</sub>/Pt</b>	<b>133</b>
7.1	Characteristics of the multilayer Pt/Co/Cr <sub>2</sub> O <sub>3</sub> /Pt stack . . . . .	133
7.2	Simulation method and periodic boundary conditions . . . . .	140
7.3	Material properties and material parameters of Pt/Co/Cr <sub>2</sub> O <sub>3</sub> . . . . .	141
7.3.1	Perpendicular magnetized Co . . . . .	141
7.3.2	Antiferromagnetic Cr <sub>2</sub> O <sub>3</sub> . . . . .	146
7.3.3	Structure of the interface . . . . .	153
7.4	Weak coupling between interfacial Co and Cr spins . . . . .	155
7.5	Strong coupling between interfacial Co and Cr spins . . . . .	156
7.5.1	Creation of an interfacial domain wall . . . . .	157
7.5.2	Properties of an interfacial domain wall . . . . .	158
7.5.3	Shift of the hysteresis loop . . . . .	162
7.5.4	Origin of the second unidirectional anisotropy . . . . .	165
7.6	Explained and non-explained effects . . . . .	167
7.6.1	Switching of the exchange bias . . . . .	168
7.6.2	Temperature dependence . . . . .	169
7.7	Open-ended questions and outlook . . . . .	170
<b>8</b>	<b>Summary and Outlook</b>	<b>171</b>





# List of Figures

2.1	Discrete levels of spin eigenvalues . . . . .	9
2.2	Exchange interaction . . . . .	10
2.3	Energy term of the uniaxial anisotropy . . . . .	12
2.4	Dipole-dipole interaction . . . . .	12
3.1	Stoner-Wohlfarth particle . . . . .	18
3.2	Energy curves and hysteresis of Stoner-Wohlfarth particle . . . .	21
3.3	Spin dimer . . . . .	22
3.4	Energy curves and hysteresis of spin dimer . . . . .	23
3.5	Spin motion due to an effective field . . . . .	25
3.6	Standard problem no. 3 . . . . .	32
4.1	Schematic representation of a hysteresis curve . . . . .	34
4.2	Representation of an energy barrier . . . . .	35
4.3	Relaxation time against temperature . . . . .	37
4.4	Relaxation time against magnetic field . . . . .	38
4.5	Functions of the magnetic field . . . . .	40
4.6	Restriction of spin rotations . . . . .	41
4.7	Exchnage interaction constants of CoFe . . . . .	43
4.8	Hysteresis loops of CoFe . . . . .	44
4.9	Division into branches . . . . .	46
4.10	Energy curves of a switchable exchange bias model . . . . .	47
4.11	Evolution of the magnetization at a critical field . . . . .	49
4.12	Quasi-static hysteresis loop calculation . . . . .	50
4.13	Parallel calculation including dipole-dipole interactions . . . . .	51
4.14	Temperature averaging . . . . .	52
5.1	Spin valve and the related hysteresis curve . . . . .	56

5.2	Magnetization loop and torque magnetometer . . . . .	57
5.3	Schematic torque curves . . . . .	58
5.4	Measured torque curves . . . . .	59
5.5	Exchange bias stack of the Meiklejohn-Bean model . . . . .	63
5.6	Hysteresis loop of the Meiklejohn-Bean model . . . . .	64
5.7	Magnetization curves of MB model . . . . .	65
5.8	Exchange bias fields and coercive fields . . . . .	66
5.9	One dimensional chain model . . . . .	69
5.10	Energy curves of the $N + 1$ chain model. . . . .	71
5.11	Schematic representation of the Mauri model . . . . .	72
5.12	Characteristic magnetization curves of the Mauri model . . . . .	74
5.13	Domain wall movement related to the random field model . . . . .	75
5.14	Compensated and uncompensated interfaces . . . . .	76
5.15	Interfacial roughness . . . . .	77
5.16	Tetragonal structure within Koon's model . . . . .	78
5.17	Spin orientation within Koon's model . . . . .	79
5.18	Energy curves of Koon's model . . . . .	80
5.19	Initial and final spin-flop states . . . . .	81
5.20	Representation of the domain state model . . . . .	83
5.21	Switchable exchange bias . . . . .	87
5.22	Spin flip and spin flop states . . . . .	88
5.23	Reversible and irreversible demagnetization curves . . . . .	90
5.24	Exchnage spring model . . . . .	91
6.1	Experimental results of NiFe/IrMn/MgO/Pt . . . . .	95
6.2	Workflow of the investigation of NiFe/IrMn/MgO/Pt . . . . .	97
6.3	NiFe and IrMn units cells . . . . .	98
6.4	Exchange interaction constants of NiFe . . . . .	99
6.5	Material parameters of IrMn . . . . .	100
6.6	NiFe Ground state . . . . .	101
6.7	Evolution of the energy during a Monte Carlo simulation . . . . .	102
6.8	IrMn <sub>3</sub> ground states . . . . .	103
6.9	NiFe/IrMn ground states on the surface of a unit sphere . . . . .	104
6.10	Eight degenerated ground states of the NiFe/IrMn . . . . .	106
6.11	Calculation setup . . . . .	107

6.12	Magnetization curves of the $3Mn3C$ model . . . . .	108
6.13	Representation of the $3Mn2C$ model . . . . .	110
6.14	Magnetization curves of the $3Mn2C$ model . . . . .	110
6.15	Magnetization curves of the Mn atoms . . . . .	111
6.16	Interfacial Mn spins of the $3Mn2C$ and the $2Mn2C$ model . . .	112
6.17	Magnetization curves of the $3Mn2C$ and the $2Mn2C$ model . . .	113
6.18	Magnetization curves of the antiferromagnetic layers within the $3Mn2C$ and the $2Mn2C$ model . . . . .	113
6.19	Variation of the interfacial exchange constant . . . . .	114
6.20	Variation of the NiFe layer thickness . . . . .	116
6.21	NiFe replaced by a macrospin . . . . .	117
6.22	Representation of the interfacial magnetic atoms . . . . .	117
6.23	Periodic boundary conditions applied at the $2Mn2C$ model . . .	118
6.24	Influence of the lateral dimensioning . . . . .	119
6.25	Influence of the sweep rate . . . . .	120
6.26	Resistance switched by a high magnetic field pulse . . . . .	121
6.27	Final states after applying a rectangular field pulse . . . . .	122
6.28	Final states after applying a field ramp . . . . .	123
6.29	Temperature dependence of NiFe/IrMn . . . . .	124
6.30	Temperature dependence of the $2Mn2C$ model ( $h_{AFM} = 1.5$ nm)	126
6.31	Temperature dependence of the $2Mn2C$ model ( $h_{AFM} = 3.0$ nm)	128
7.1	Representation of the Pt/Co/Cr <sub>2</sub> O <sub>3</sub> /Pt stack . . . . .	134
7.2	Vertical and horizontal shift of the hysteresis loops . . . . .	135
7.3	Element specific hysteresis loops . . . . .	136
7.4	Hysteresis loops after field cooling . . . . .	137
7.5	Magnetoelectric switching . . . . .	138
7.6	Layer thickness and temperature dependence . . . . .	139
7.7	Thickness dependence of perpendicular magnetic anisotropy . .	142
7.8	Magnetization curve of Co layer . . . . .	143
7.9	Pt spin magnetic moment . . . . .	144
7.10	Hysteresis loops of Pt/Co/Cr . . . . .	145
7.11	Cr <sub>2</sub> O <sub>3</sub> hexagonal unit cell . . . . .	147
7.12	Projection of the unit cell . . . . .	147
7.13	Spin states of Cr <sub>2</sub> O <sub>3</sub> at different magnetic fields . . . . .	148

7.14	Illustration of periodic boundary conditions. . . . .	150
7.15	Magnetization curve at increasing external fields . . . . .	151
7.16	Spin flop fields against the number of spins . . . . .	153
7.17	Top view of interfacial layers . . . . .	154
7.18	Spin structure of $\text{Cr}_2\text{O}_3$ with a stepped (0001) surface . . . . .	155
7.19	Extension of the projection of $\text{Co}/\text{Cr}_2\text{O}_3$ . . . . .	156
7.20	Magnetization curves with a weak exchange interaction . . . . .	157
7.21	Strong interfacial exchange coupling . . . . .	158
7.22	Magnetization curves of the $\text{Cr}_2\text{O}_3$ layer . . . . .	159
7.23	Domain wall of different angles . . . . .	160
7.24	Shift of the Cr atoms . . . . .	161
7.25	Domain wall motion and ferrimagnetic $\text{Cr}_2\text{O}_3$ magnetization . .	161
7.26	$\text{Co}/\text{Cr}_2\text{O}_3$ magnetization curves with different anisotropy axes .	163
7.27	$\text{Co}/\text{Cr}_2\text{O}_3$ magnetization curves with second interfacial interaction	164
7.28	$\text{Co}/\text{Cr}_2\text{O}_3$ magnetization curves with additional spin . . . . .	164
7.29	Magnetic Skyrmion states . . . . .	165
7.30	Co layer with Dzyaloshinskii-Moriya interaction . . . . .	166
7.31	Switchable behavior of exchange bias stack . . . . .	169

# List of Tables

5.1	Exchnage bias categories . . . . .	85
7.1	Exchange interaction constants of $\text{Cr}_2\text{O}_3$ . . . . .	147



# Publications

- M. Pohlitz, I. Stockem, F. Porrati, M. Huth, C. Schröder, J. Müller, “Experimental and Theoretical Investigation of the Magnetization Dynamics of an Artificial Square Spin Ice Cluster,” *Journal of Applied Physics*, submitted, 2016.
- I. Stockem, C. Schröder, G. Reiss, “Atomistic Spin Dynamics Simulations of the Exchange Spring System IrMn/NiFe,” *Joint MMM-Intermag 2016*, January 11-15, 2016, poster presentation, San Diego, USA.
- I. Stockem, C. Schröder, “A Fast Method for Calculating Magnetic Hysteresis Loops,” *IEEE Transactions on Magnetics*, vol. 51, 2015.
- I. Stockem, C. Schröder, “A Fast Method for Calculating Magnetic Hysteresis loops,” *Intermag 2015*, May 11-15, 2015, poster presentation, Beijing, China.
- I. Stockem, C. Schröder, G. Reiss, “Atomistic Spin Dynamics and Effective Models of AFM/FM Multilayer Systems,” *International Conference on Magnetism*, July 5-10, 2015, oral presentation, Barcelona, Spain.
- I. Stockem, S. Muschack and C. Schröder, “Effective Models for Exchange Bias Systems based on Atomistic Spin Dynamics Simulations,” *DPG Spring Meeting 2015*, March 15-20, 2015, oral presentation, Berlin, Germany.
- I. Stockem, C. Schröder, G. Reiss, “Finite Temperature Atomistic Spin Dynamics Simulations for Nanostructured CoFe Multilayer Systems,” *10th International Workshop on Magnetism and Superconductivity at the Nanoscale*, June 30 - July 4, 2014 poster presentation, Coma-Ruga, Spain.





# Constants & Symbols

## Constants<sup>1</sup>

speed of light in vacuum	$c_0 = 2.99792458 \cdot 10^8 \text{ ms}^{-1}$
vacuum permeability	$\mu_0 = 4\pi \cdot 10^{-7} \text{ VsA}^{-1}\text{m}^{-1}$
vacuum permittivity	$\epsilon_0 = 8.8541878 \cdot 10^{-12} \text{ AsV}^{-1}\text{m}^{-1}$
Bohr magneton	$\mu_B = 9.2740089937 \cdot 10^{-24} \text{ JT}^{-1}$
Boltzmann constant	$k_B = 1.380650324 \cdot 10^{-23} \text{ JK}^{-1}$
reduced Planck constant	$\hbar = 1.05457159682 \cdot 10^{-34} \text{ Js}$
fundamental charge	$e = 1.60217646263 \cdot 10^{-19} \text{ C}$
electron rest mass	$m_e = 9.1093818872 \cdot 10^{-31} \text{ kg}$
electron g-factor <sup>2</sup>	$g = -2.00231930436182$

## Symbols

$\mathcal{H}$	: Hamiltonian, discrete form	
$\mathcal{E}$	: Hamiltonian, continuous form	
$\vec{S}$	: spin vector, spin operator	
$s$	: spin quantum number	
$m_z$	: spin projection quantum number	
$\vec{B}$	: magnetic B-field	$[B] = \text{T} = \text{Vsm}^{-2}$
$\vec{H}$	: magnetic H-field	$[H] = \text{Am}^{-1}$
$E$	: energy	$[E] = \text{J} = 6.242 \cdot 10^{18} \text{ eV}$

---

<sup>1</sup>From [1].

<sup>2</sup>From NIST, <http://physics.nist.gov/cuu/Constants/index.html>, retrieved May 21th, 2016.

$\vec{T}$	: torque	$[T] = \text{Nm} = \text{J}$
$J$	: exchange interaction constant	$[J] = \text{J} = 6.242 \cdot 10^{18} \text{eV}$
$\mu$	: effective magnetic moment	$[\mu] = \mu_{\text{B}}$
$D$	: uniaxial anisotropy constant	$[D] = \text{J} = 6.242 \cdot 10^{18} \text{eV}$
$A$	: exchange stiffness	$[A] = \text{S} = \text{Jm}^{-1} = 6.242 \cdot 10^{18} \text{eVm}^{-1}$
$\vec{M}$	: magnetization	$[M] = \text{Am}^{-1}$
$K$	: anisotropy constant	$[K] = \text{Jm}^{-3} = 6.242 \cdot 10^{18} \text{eVm}^{-3}$
$T$	: temperature	$[T] = \text{K}$
$t$	: time	$[t] = \text{s}$
$\tau$	: relaxation time	$[\tau] = \text{s}$
$\lambda, \alpha$	: damping parameter	
$a, c$	: lattice constant	$[a] = [c] = \text{m}$
$V$	: volume	$[r] = \text{m}^3$
$r$	: radius	$[r] = \text{m}$
$h$	: height	$[h] = \text{m}$
$L, t, \xi$	: length	$[L] = [t] = [\xi] = \text{m}$
$N_x, N_y, N_z$	demagnetization factors	
$R_c$	: cone size	
$\alpha, \beta, \theta, \phi$	: angles	
$\vec{r}_{i,j}$	: distance vector	$[r] = \text{m}$
$l_{\text{ex}}$	: intrinsic length	$[l_{\text{ex}}] = \text{m}$
$R_s$	: sweep rate	$[R_s] = \text{Ts}^{-1}$

# Chapter 1

## Introduction

Magnetism and some of its fascinating phenomena are known for more than 2500 years. Thales von Milet observed the magnetism of lodestone around 600 years B.C. The lodestone was used as compasses, first in China, later in Europe [2]. Although early applications are rarely known, the magnetic effects have been studied throughout history. After first explanations of the earth magnetic field, the relation between magnetism and electricity has been described within Maxwell's equations [3, 4]. Finally, the origin of all discovered effects could only be understood by the introduction of quantum mechanics and the consideration of the electron spin at the beginning of the 20th century. At that time, Weiss proposed the creation of ferromagnetic domains by a mean field, whose microscopic origin has been explained by Heisenberg within his famous Heisenberg model [5, 6]. Until now, the Heisenberg model builds the fundamental concept to investigate magnetism theoretically.

With the investigation of smaller magnetic structures up to single domains, the application of magnets is extended from motors and generators to tiny data storage devices. The growing number of applications has attracted by high research activities in this area. Especially at thin magnetic layers further effects have been found during the last decades. One famous example is the giant magneto resistance (GMR) discovered by Grünberg and Fert in 1988 [7]. A GMR device consists of at least two thin ferromagnetic layers separated by a non-magnetic material. The electrical resistance depends on the magnetization alignment of the ferromagnetic layers. While an antiparallel alignment

leads to a high resistance, a parallel alignment of the magnetization leads to a low resistance. As their resistance can be easily changed by rotating the magnetization of one layer with an external magnetic field, GMR devices are used for example as sensors or as read heads in memory devices.

A similar effect is the tunneling magnetoresistance (TMR), at which a thin insulating structure is sandwiched by two ferromagnetic layers. In case of TMR the probability of electrons to tunnel through the barrier depends on the magnetization alignment of both ferromagnetic layers to each other [8]. Therefore the resistive signal is a response to the magnetic field.

Besides the development of industrial applications, the theoretical understanding of effects related to magnetic thin films has been pushed forward. Simulation methods have been introduced and further developed to study and understand the new discovered effects. In the mid of the 20th century the investigation of domains and especially domain walls lead to micromagnetics [9]. In this approach the magnetization was modeled as a continuous quantity that enables the calculation of magnetic structures in the micrometer range. As the dimensions of industrial devices have been shrunk, the investigations based on a continuous approach became insufficient. Nowadays, the effects of interest are influenced by single atoms within the material or interactions of the atoms at the interface of different materials. To study effects, occurring from interface roughness or defects at thin layers, simulation methods are required that model the structure atomistically. The atomistic structure would be naturally considered within a quantum mechanical approach. But the computational effort of a pure quantum mechanical calculation is much too high for magnetic structures in the nanometer range. Classical spin dynamics methods, as discussed in this thesis, fill the gap between micromagnetic approaches and quantum mechanical calculations.

Within this thesis different multilayer stacks have been investigated by atomistic spin dynamics approaches [10] based on a classical form of the Heisenberg Hamiltonian. As a consequence to that the relation between the quantum mechanical Heisenberg model and its classical counterpart is explained in the

second chapter. The calculation methods themselves are introduced in the subsequent chapters 3 and 4.

The emphasis of the thesis is on exchange bias stacks, which are part of magnetic storage devices. The exchange bias effect has been discovered by Meiklejohn and Bean in 1958. But up to now there is no model, which explains all related effects at different materials and structures. Instead, several specific models have been developed during the last decades. A short overview of the most important models is given in section 5.2.3.

To investigate the magnetic properties of complex multilayer systems, the concept of several models have to be partially used, combined or extended. For the exchange bias systems examined within this thesis, the procedure described below has been used.

- Evaluation of provided experimental data.
- Determination of the material parameters including crystal structures.
- Selection or development of suitable basic models to determine ground states of each single layer.
- Consideration of possible interface scenarios.
- Development of the parametrized new specific model.
- Calculation of the magnetization curve of single and combined layers.
- Parameter deviation analysis to find the most sensitive parameters.
- Adaption of the model.
- Validation against experimental outcomes.

As a basic computing environment a spin dynamic software has been used which put emphasis on molecular structures. This environment has been extended to fulfill the requirements of multilayer systems. Multilayer structures require an extended parameter set, e.g., to describe the crystal structure and layer interfaces. Hence the input interfaces have been adapted. Furthermore

the graphical output has been extended to utilize 3D animations. To visualize X3D data<sup>1</sup>, an X3D viewer<sup>2</sup> from the Fraunhofer Institute for Computer Graphics Research has been used.

The magnetic hysteresis is one of the key properties of exchange bias multilayer systems. The determination of field and time dependent magnetic states of a quasi-static hysteresis loop comes along with huge computational efforts. To achieve a fast calculation in a feasible time range, different acceleration techniques have been developed and implemented (sections 3 and 4). In particular different approaches have been developed and implemented to calculate the long range dipole-dipole interactions. This includes a hybrid implementation of openMP and MPI [11, 12].

Subsequently, these methods have been applied to investigate magnetic properties of mainly two exchange bias systems (cf. chapters 6 and 7). Both systems are subject of current research.

The first one under investigation is the NiFe/IrMn/MgO/Pt tunnel junction which exhibits a magnetization dependent resistance [13]. In opposite to conventional TMR devices, an antiferromagnetic layer is next to the tunnel barrier and the change of the magnetoresistive signal is caused by the antiferromagnetic material. The authors of [13] suppose a spring-like rotation within the NiFe/IrMn stack as the origin of this unconventional effect. To verify this supposition, the magnetic behavior of the two layer stack is investigated by spin dynamics calculations of an effective model proposed in chapter 6.

The second one under investigation is the Pt/Co/Cr<sub>2</sub>O<sub>3</sub>/Pt stack. This exchange bias stack is characterized by a perpendicular magnetization and a switchable sign of the hysteresis loop shift [14]. The preferred magnetization direction of an exchange bias system is usually defined during the growth of the structure and by the field annealing process. Afterwards the sign of the exchange bias is a static feature. At Pt/Co/Cr<sub>2</sub>O<sub>3</sub>/Pt, the sign of the shift is changed during operation by applying a high magnetic field [14]. Alterna-

---

<sup>1</sup><http://www.web3d.org/>, retrieved May 19th, 2016

<sup>2</sup><http://www.instantreality.org/>, retrieved May 19th, 2016

tively, the sign is switchable by an electric field pulse combined with a rather low magnetic field [15]. The ability to change the sign of the loop shift during operation establishes a new functionality applied for example as a dual input for spin valves [14]. The switchable shift of the loop along the horizontal axis, is accompanied by a “vertical loop shift” [16]. Usually, such a vertical shift is explained by pinned spins within the antiferromagnetic layer or at the interface of this layer [17]. As this explanation is not appropriate for Pt/Co/Cr<sub>2</sub>O<sub>3</sub>/Pt, the origin of the horizontal shift is still unknown. In chapter 7 different effective models are proposed to unveil the magnetic behavior of the Pt/Co/Cr<sub>2</sub>O<sub>3</sub>/Pt.

A conclusion of the main concepts and the results of the investigations are summarized in chapter 8. Additionally, some questions for future research are being proposed there.





# Chapter 2

## Fundamentals

The magnetic properties of the investigated multilayer structures within this thesis are determined by exploiting an extended classical Heisenberg model. In this chapter the quantum mechanical Heisenberg model and its classical analogon are introduced. In the original work of Heisenberg [6], the Hamiltonian is based on the interactions between next neighboring electron spins and on the interaction of the electron spins with an external magnetic field. To describe the effects occurring at multilayer structures, the classical Heisenberg Hamiltonian is extended by further energy terms as described in the last section of this chapter.

In the following, the term *spin* refers to electron spin.

### 2.1 Quantum mechanical description of the Heisenberg model

Heisenberg proposed in 1928 a quantum mechanical model to explain ferromagnetism [6]. Previously Weiss developed a model that described the generation of magnetic domains within the material due to magnetic fields of the atoms [5, 18]. The microscopic origin of the molecular fields in Weiss's theory was yet unknown. Heisenberg supposed that a quantum mechanical exchange interaction between neighboring spins is the origin of the Weiss fields. He calculated the strength of the exchange interaction  $J$  as the energy difference between a singlet and a triplet state of two electrons within a Heitler-London approxi-

mation [19]. The related Hamiltonian in equation 2.1 describes the interaction between neighboring spins and the interaction of the spins with an external magnetic field.

$$\underline{H} = - \sum_{\langle i,j \rangle} J_{i,j} \vec{\mathcal{S}}_i \cdot \vec{\mathcal{S}}_j - g\mu_B \vec{B} \cdot \sum_{i=1}^N \vec{\mathcal{S}}_i \quad (2.1)$$

The notation is taken from [10], at which the spin operators  $\vec{\mathcal{S}}_i$  and  $\vec{\mathcal{S}}_j$  are given in units of  $\hbar$ . The tilde is used to distinguish between quantum mechanical operators and classical quantities.  $g$  and  $\mu_B$  denote the electron Landé g-factor and the Bohr magneton, respectively. The external magnetic field is given by  $\vec{B}$ . The first sum of equation 2.1 is over all pairs of neighboring atoms. The sign of the exchange constant determines the orientation of the neighboring spins to each other. A positive sign leads to a ferromagnetic ground state, while a negative sign leads to an antiferromagnetic ground state.

## 2.2 From a quantum mechanical model to a classical description

The spin states of magnetic systems are described within the quantum mechanical Heisenberg model. A calculation of the spin states is only possible for a small number of spins. One option to calculate larger systems is the quantum Monte Carlo approach. However, this approach suffers from the so-called *negative sign* problem for frustrated systems [10]. Another approach, used within this thesis, is based on a classical description of the Heisenberg Hamiltonian. Here, the spin operators are replaced by classical vectors of unit length. A conversion of the quantum mechanical to a classical Heisenberg model is presented in this section. However, this is not a mathematically exact transformation, as no direct relation between both descriptions exists.

The  $z$ -component of a spin operator within the quantum mechanical description  $\vec{\mathcal{S}}_{i,z}$  is quantized and exhibits  $(2s + 1)$  eigenvalues  $m_{i,z}$ , where  $s$  is the spin quantum number. These eigenvalues are sketched as quantized vectors in figure 2.1. In a classical approach the spin is proposed as a three dimensional vector, which is continuous in any of the three Cartesian dimensions. The

continuous classical description of a spin and the discrete quantum mechanical description would coincide, if the number of eigenvalues, i.e. the spin quantum  $s$  approaches infinity.

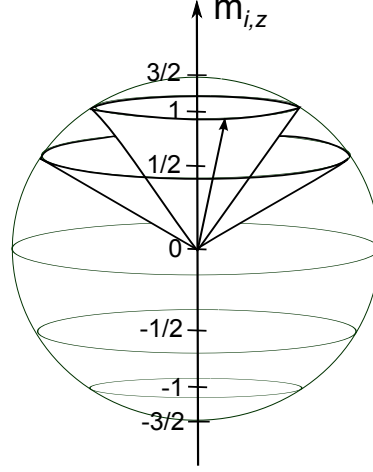


**Figure 2.1:** Schematic representation of discrete levels of spin eigenvalues  $m_{i,z}$ .

To deduce the classical Heisenberg Hamiltonian, the spin operators are first normalized by

$$\vec{\tilde{S}}_i^u = \frac{\vec{S}_i}{\sqrt{s(s+1)}}. \quad (2.2)$$

Assuming  $\vec{S}_i$  and  $\vec{S}_j$  have the same spin quantum numbers  $s$  one can replace these by  $\vec{\tilde{S}}_i^u$  and  $\vec{\tilde{S}}_j^u$  the resulting Hamiltonian becomes

$$\underline{H} = - \sum_{\langle i,j \rangle} J_{i,j} (s(s+1)) \vec{\tilde{S}}_i^u \cdot \vec{\tilde{S}}_j^u - g\mu_B \sqrt{s(s+1)} \vec{B} \cdot \sum_{i=1}^N \vec{\tilde{S}}_i^u. \quad (2.3)$$

Now, it is assumed, that the normalized operators are written as classical vectors of unit length. In this case, the classical Heisenberg Hamiltonian is written as

$$\mathcal{H} = - \sum_{\langle i,j \rangle} J_{i,j}^C \vec{S}_i^u \cdot \vec{S}_j^u - \mu_B^C \vec{B} \cdot \sum_{i=1}^N \vec{S}_i^u. \quad (2.4)$$

The effective moment and the exchange constant in this classical approach are  $J_{i,j}^C = J_{i,j} \cdot (s(s+1))$  and  $\mu_B^C = g\mu_B \sqrt{s(s+1)}$ . Thus, in a classical treatment one has to scale the quantum mechanical exchange constants by the spin

quantum number  $s$ . In the following equations the indices  $u$  and  $C$  will be neglected in the classical description.

Further energy terms are described in the next section.

## 2.3 Energy terms of the extended classical Heisenberg Hamiltonian

Within this thesis four different energy terms are mainly used to determine the spin states of different multilayer structures. The influence of each energy term on the orientation of the spins is described in following.

### 2.3.1 Exchange interaction

The exchange interaction favors a ferro- or antiferromagnetic alignment of the structure as explained in section 2.1. The exchange constant  $J_{i,j}$  in equation 2.5 defines the strength the of the coupling between the neighboring spins  $\vec{S}_i$  and  $\vec{S}_j$ . Figure 2.2 represents the spin alignment due to a ferromagnetic exchange ( $J_{i,j} > 0$ ) and an antiferromagnetic exchange ( $J_{i,j} < 0$ ).

$$\mathcal{H}_{\text{exch}} = - \sum_{\langle i,j \rangle} J_{i,j} \vec{S}_i \cdot \vec{S}_j \quad (2.5)$$



(a) Spin alignment due to a ferromagnetic exchange interaction ( $J_{1,2} > 0$ ).



(b) Spin alignment due to an antiferromagnetic exchange interaction ( $J_{1,2} < 0$ ).

**Figure 2.2:** Exchange interaction between two classical spins.

### 2.3.2 Zeeman term

The Zeeman term describes the interaction of the spins with an external magnetic field  $\vec{B}$ . This term is considered in the quantum mechanical Heisenberg

model as well. Without an magnetic field the spin states corresponding to each eigenvalue  $m_{i,z}$  are degenerated. The magnetic field leads to a splitting of the energies of these states.

In the classical Hamiltonian the corresponding energy term is described by equation 2.6.  $\mu_{\text{eff},i}$  denotes the effective magnetic moment related to each spin  $\vec{S}_i$ . This equation is minimized by a parallel alignment of the spins with the external field.

$$\mathcal{H}_{\text{field}} = -\mu_0 \vec{B} \cdot \sum_{i=1}^N \mu_{\text{eff},i} \vec{S}_i \quad (2.6)$$

### 2.3.3 Uniaxial anisotropy

The exchange term of the classical Heisenberg model is isotropic. In opposite to that, most structures show a preferred magnetization direction even in the absence of an applied magnetic field. The anisotropy is caused by different effects and depends either on the atomic structure or on the shape of the magnetic sample. The uniaxial energy term in equation 2.7 models the magnetocrystalline anisotropy, which is mainly caused by the spin-orbit coupling [20]. It is very common to describe the uniaxial anisotropy by a power series expansion with two terms and two anisotropy constants [18]. Within this thesis only the first term with a single anisotropy constant is taken into account. The unit vector  $\vec{e}_i$  points along the preferred direction of each classical spin.

$$\mathcal{H}_{\text{aniso}} = - \sum_{i=1}^N \left( \vec{S}_i \cdot \vec{e}_i \right)^2 \quad (2.7)$$

Figure 2.3 represents the energy as a function of the an angle  $\theta$  between the easy axis and the magnetization direction of a classical spin.

### 2.3.4 Magnetic dipole-dipole interactions

Besides the spin-orbit coupling, the shape of the sample affects the preferred orientation of the magnetization. The shape anisotropy is caused by magnetic dipole-dipole interactions. Equation 2.8 expresses the long range interactions

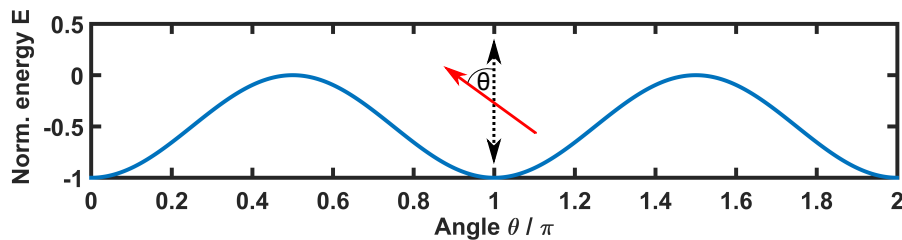
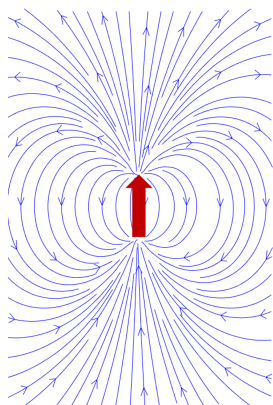


**Figure 2.3:** Energy as a function of the angle  $\theta$ . The dashed line between the ends of the double arrow represents the easy axis of the anisotropy. The red arrow denotes the magnetization direction.

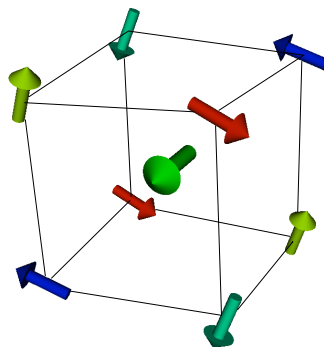
at which the orientation of each spin is influenced by the dipole fields of all other spins within the sample.

$$\mathcal{H}_{\text{dip}} = -\frac{\mu_0}{4\pi} \sum_{i < j} \frac{3 \left( \mu_{\text{eff},i} \vec{S}_i \cdot \vec{e}_{i,j} \right) \left( \mu_{\text{eff},j} \vec{e}_{i,j} \cdot \vec{S}_j \right) - \mu_{\text{eff},i} \mu_{\text{eff},j} \vec{S}_i \cdot \vec{S}_j}{r_{i,j}^3} \quad (2.8)$$

The unit vector  $\vec{e}_{i,j}$  points from the lattice site of spin  $\vec{S}_i$  to the lattice site of spin  $\vec{S}_j$ . The distance between the two lattice sites is denoted by  $r_{i,j}$ . The field lines of a single magnetic dipole are illustrated in figure 2.4a. The alignment of five spins of a CoFe unit cell, which are coupled by dipole-dipole interactions, are shown in figure 2.4b.



(a) Field lines of a single spin.



(b) Five dipolar coupled spins.

**Figure 2.4:** Dipole-dipole interaction.

Furthermore the Dzyaloshinskii-Moriya interaction is supposed to be a possible origin of a spin canting near the interface between Co/Cr<sub>2</sub>O<sub>3</sub> in section 7.2. This energy term is only considered with regard to this stack and a more detailed description is given in the corresponding section.





# Chapter 3

## Calculation Methods

To determine the static and dynamic properties of multilayer systems, many different methods are available. A pure quantum mechanical approach models the exact physical behavior, but the computation is by far much too time consuming. Micromagnetics, at which the magnetization is seen as a continuous property, provides short computational times, but conceals the atomistic structure. This leads to many problems at small structure at which the influence single atoms has to be taken into account. The methods used and further developed in this thesis are based on atomistic calculations. A macrospin approach is an in-between of an atomistic and a micromagnetic approach as several spins are combined into a single macrospin. This reduces the computational time drastically. Furthermore, macrospins can be combined with atomistic structures.

At the end of the previous chapter, the different energy terms of an extended classical Heisenberg Hamiltonian have been introduced. A minimization of these energy terms reveals the local energy states of a magnetic system. For models of low complexity, the magnetic states and field dependent magnetization curves could be obtained by pure analytical methods. For more complex models, the spin states of local energy minima can be determined by numerical calculations. In the first section the energy minima of the Stoner-Wohlfarth model [21] and a spin dimer are discussed. For the development of exchange bias models, a basic understanding of these fundamental models is required. Even if these models are not explicitly used, parts of the ideas have been in-

corporated into other models. On the basis of these fundamental models, basic properties like magnetic hysteresis and spin flop state are introduced. These basic properties can be recognized in most of the chapters within this thesis. Furthermore, a graphical representation of the so-called *energy curves* is explained, which is used in section 5.2.2 of chapter 5 to illustrate the thickness dependent spin reversal of an antiferromagnetic layer within an exchange bias stack.

Time dependent spin evolutions are not considered in the sections 3.1.1 and 3.1.2 treating the Stoner-Wohlfarth model and the spin dimer. The energy minimizing states of the models in these sections reflect only the static solutions of the Heisenberg model. In section 3.2 two methods are introduced to obtain the dynamic behavior of a magnetic system. Within this thesis, spin dynamics calculations are applied to atomistic structures of dimensions in the nanometer range. For larger structures in the micrometer range, the calculations based on atomistic approaches are way too time consuming. The dynamics of the multi-domain structures could be investigated by micromagnetics [9] or by macrospin approaches [22] (sections 3.3 and 3.4). The micromagnetic approach itself is not used in this thesis. Nevertheless, the micromagnetic parameters can be converted into effective parameters for an atomistic or a macrospin approach. This is useful as reliable atomistic data is rarely available. Many parameters can only be obtained indirectly and in a continuous and averaged form.

Moreover results from micromagnetic calculations have been used during software development for the verification of new algorithms. Such a comparison is based on a macrospin approach introduced in the last section of this chapter. A macrospin model is used to model the complete ferromagnetic NiFe layer of the NiFe/IrMn/MgO/Pt, which leads to a huge reduction of the computational times. This model is explained in section 6.7.2 of chapter 6.

## 3.1 Magnetic states of spin systems with low complexity

In order to obtain the magnetic states of a structure at zero temperature, the energy terms within the classical Heisenberg model have to be minimized. This is addressed to two important models discussed within this section.

The first one is the Stoner-Wohlfarth model, which has been proposed by Stoner and Wohlfarth to investigate the magnetic behavior of homogenous magnetized particles in 1948 [21]. Although the Stoner-Wohlfarth model is a model of low complexity, it is often used to explain experimentally determined hysteresis curves [18].

The second one is the classical spin dimer. This model consists of two ferromagnetic or antiferromagnetic coupled spins with uniaxial anisotropies. It is used to demonstrate the effect of a simple energy barrier and to illustrate the graphical representation of energy curves in more detail.

### 3.1.1 Stoner-Wohlfarth model

The Stoner-Wohlfarth model [21] describes the magnetic behavior of ferromagnetic particles. A single Stoner-Wohlfarth particle has an ellipsoidal shape and a uniform magnetization (figure 3.1). In this case, the exchange interactions between the next neighboring spins within one particle lead to a constant energy term of the Hamiltonian. As magnetic states are found by minimizing the energy terms within the Hamiltonian, this energy term is neglected in the Stoner-Wohlfarth model. In the original work of Stoner and Wohlfarth the shape anisotropy of the particle due to the dipole-dipole interactions is considered, whereas a uniaxial anisotropy is not taken into account. However, the resulting Hamiltonian could also be applied to particles with a uniaxial anisotropy [18]. Stoner and Wohlfarth discussed the results of prolate, oblate, and general ellipsoids [21]. Here, only the case of the prolate ellipsoid is presented.

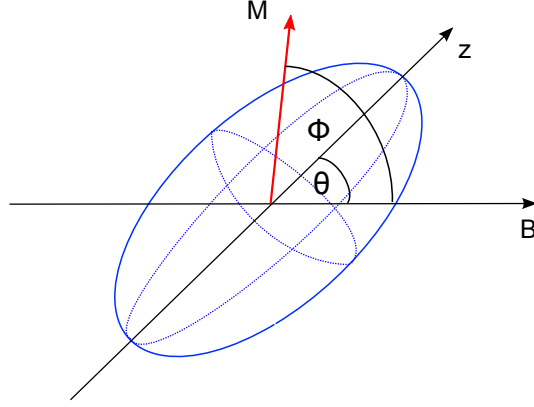


**Figure 3.1:** Schematic representation of the Stoner-Wohlfarth particle as prolate ellipsoid.

In general, the energy of the shape anisotropy can be expressed by the integral over the particle

$$E_D = -\frac{\mu_0}{2} \int \vec{M} \cdot \vec{H}_D dV, \quad (3.1)$$

where  $\vec{M}$  is the magnetization and  $\vec{H}_D$  denotes the demagnetization field resulting from the dipole-dipole interactions of the spins within the particle. In the case of an ellipsoidal particle equation 3.1 becomes

$$E_D = \frac{1}{2}V (N_x M_x^2 + N_y M_y^2 + N_z M_z^2). \quad (3.2)$$

$N_x$ ,  $N_y$  and  $N_z$  are the demagnetization factors and  $V$  is the volume of the ellipsoid. In case of a prolate ellipsoid,  $N_x$  equals  $N_y$ . By using the relation  $M_s = \sqrt{M_x^2 + M_y^2 + M_z^2}$  the shape energy can be expressed as a function of  $M_z$  [18].

$$\begin{aligned} E_D &= \frac{1}{2}V [N_x (M_x^2 + M_y^2) + N_z M_z^2] \\ &= \frac{1}{2}V [(N_z - N_x) M_z^2 + N_z M_s^2] \\ &= -\frac{1}{2}V (N_x - N_z) M_z^2 + \text{const.} \end{aligned} \quad (3.3)$$

$M_s$  is the constant saturation magnetization of the particle. Hence the last part of the second row in equation 3.3 contains only constant values and can be neglected within the calculation of energies.

In case of an uniaxial anisotropy with an anisotropy energy density  $K$  and an easy axis parallel to the  $z$ -axis, the energy term is given by

$$E = KV \sin^2(\phi - \theta). \quad (3.4)$$

Apart from a constant term, equation 3.3 and 3.4 exhibit the same mathematical form. Including the Zeeman term, the Hamiltonian of the system describing a particle of uniform magnetization is given by

$$\mathcal{H} = K_{\text{eff}}V \sin^2(\phi - \theta) - BM_sV \cos(\phi). \quad (3.5)$$

The anisotropy energy density  $K_{\text{eff}}$  is either related to the shape anisotropy or the uniaxial anisotropy or to the superposition of both. The magnetization rotates within the plane defined by the directions of field and the long axis of the ellipsoid. The angles  $\theta$  and  $\phi$  are related to the field axis and to the long axis of the ellipsoid as represented in figure 3.1. The hysteresis loop (cf. section 4.1) can be determined by minimizing equation 3.5 with respect to  $\theta$ . In the case of  $\theta = 0$ , the external field  $\vec{B}$  is parallel to the easy axis of the particle and the coercive fields can be obtained analytically.  $K_{\text{eff}}$  is greater than zero as the anisotropy has an easy axis aligned with the  $z$ -axis.  $M_s$  is greater than zero as well.

$$\begin{aligned} \frac{d\mathcal{H}}{d\phi} &= 2K_{\text{eff}}V \cos(\phi) \sin(\phi) + B_z M_s V \sin(\phi) \stackrel{!}{=} 0 & (3.6) \\ \Rightarrow \phi_0 &= \begin{cases} \arccos\left(-\frac{B_z M_s}{2K_{\text{eff}}}\right) \\ \pm n\pi \end{cases} & (3.7) \end{aligned}$$

The three solutions of equation 3.6 reflect the minima, maxima or inflection points for  $K_{\text{eff}} > 0$ ,  $M_s > 0$  at a corresponding field strength  $B_z$ . To get the energy minimizing spin orientations with respect to the magnetic field  $B_z$ , these three solutions are inserted into the second derivative of the Hamiltonian. Only angles and field ranges, at which equation 3.8 holds, might be valid spin states.

$$\frac{d^2\mathcal{H}}{d\phi^2}\Big|_{\phi_0} = 2VK_{\text{eff}}\cos^2(\phi) - 2VK_{\text{eff}}\sin^2(\phi) + B_zM_sV\cos(\phi)\Big|_{\phi_0} \stackrel{!}{>} 0 \quad (3.8)$$

$$\Rightarrow \phi_0 = \begin{cases} \pi + 2\pi n & \text{if } B_z < \frac{2K_{\text{eff}}}{M_s} \\ 2\pi n & \text{if } B_z > -\frac{2K_{\text{eff}}}{M_s} \\ \arccos\left(-\frac{B_zM_s}{2K_{\text{eff}}}\right) & \text{if } B_z < -\frac{2K_{\text{eff}}}{M_s} \vee B_z > \frac{2K_{\text{eff}}}{M_s} \end{cases}$$

with  $n = 0, 1, 2, \dots$

The last solution of  $\phi$  in equation 3.8 is non-physical, as  $\phi$  becomes complex valued. Thus,  $\phi = 0$  and  $\phi = \pi$  are the only valid spin states for the corresponding field ranges  $B_z < \frac{2K_{\text{eff}}}{M_s}$  and  $B_z > -\frac{2K_{\text{eff}}}{M_s}$ .

The results of the calculation above are visualized using the energy curves in figure 3.2a. The energy curves are a graphical representation of the energy minimizing magnetic states as a function of the applied magnetic field in a certain direction. Here, the energy of the states are plotted against the  $z$ -component of the magnetic field  $B_z$ . The different magnetic states are separated by energy barriers. The evolution of the states and thus, the hysteresis loop can be deduced from the graphical representation in figure 3.2a. At negative magnetic fields, the system is in its global minimum at  $\phi = \pi$ . This state is represented by the red curve. By increasing the external field, the energy of this magnetic state becomes a *local* minimum. The energy barrier between the states prohibits a spin reversal before the coercive field  $B_c = \frac{2K_{\text{eff}}}{M_s}$  is reached. At the coercive field the energy barrier is decreased to zero and the spins reverse their magnetization to reach the *global* minimum. The related hysteresis curves, including the case of  $\theta = 0$ , are illustrated in figure 3.2b.

Although the Stoner-Wohlfarth model is based on many simplifications, it can be used to calculate the shape of experimentally determined hysteresis curves [21, 18]. A large structure consists of many particles, which are arbitrarily orientated. Thus, the angles between each anisotropy axis and the magnetic field are random. The shape of measured hysteresis curves of ferromagnetic materials can be obtained by averaging over all angles  $\theta$ .

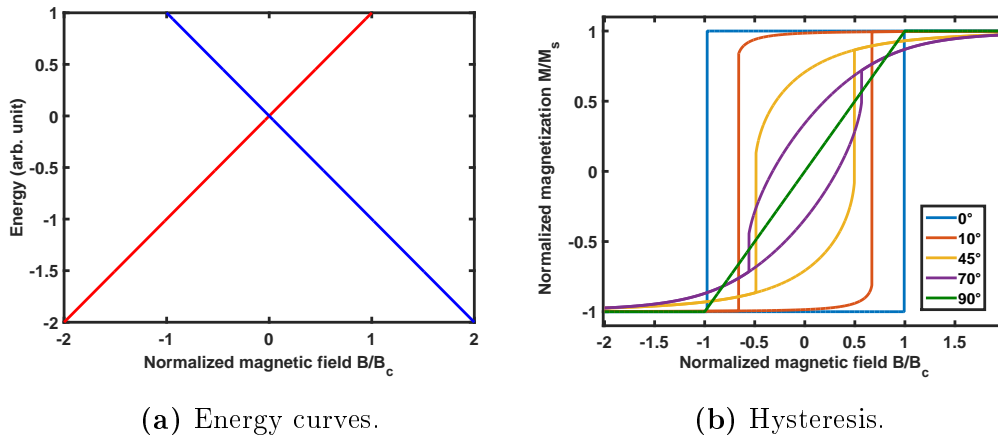


**Figure 3.2:** (a) Energy curves representing local energy minima of the Stoner-Wohlfarth model. (b) Hysteresis curves of the Stoner-Wohlfarth model for different magnetic field angles.

### 3.1.2 Classical spin dimer

The spin dimer consists of two exchange coupled spins. The spins are either antiferromagnetically ( $J < 0$ ) or ferromagnetically ( $J > 0$ ) coupled. Both spins exhibit the same uniaxial anisotropy in the  $z$ -direction with an anisotropy constant  $D_z$  and the same effective magnetic moment  $\mu$ . In the simplest case, the external field  $\vec{B}$  is also applied along the  $z$ -axis.

The rotation of the spins is assumed to be restricted to a plane, so that the corresponding Hamiltonian (equation 3.9) is given by the angles  $\alpha$  and  $\beta$  between the spin vectors and the  $z$ -direction as illustrated in figure 3.3.

$$\mathcal{H} = -J \cos(\beta - \alpha) - D_z(\cos^2(\alpha) + \cos^2(\beta)) - \mu B_z(\cos(\alpha) + \cos(\beta)). \quad (3.9)$$

Figure 3.4 illustrates the energy curves and the hysteresis curves for the ferromagnetic and the antiferromagnetic coupling, which are found by minimizing equation 3.9.

A hysteresis curve represents a history dependent process (cf. section 4). Thus, at least the initial states have to be known to obtain the hysteresis curves in figure 3.4. In both cases it is assumed, that the spins are initially aligned along the direction of a high magnetic field. Each field range of a local minimum has a different color. The related hysteresis branches are illustrated with the same

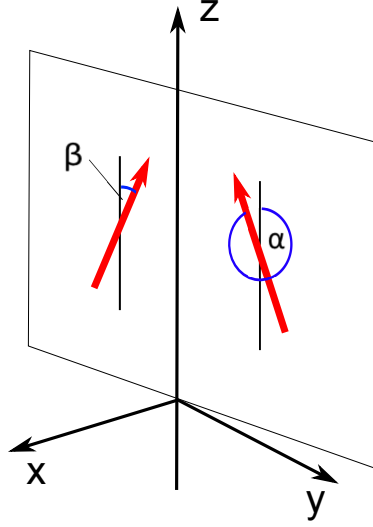


**Figure 3.3:** Spin dimer.

color. The arrows sketch the spin states. A state transition does not occur, as long as the state is a local minimum, i.e. as long as equation 3.10 and equation 3.11 hold for a given field strength  $B_{z,0}$ .

$$\frac{\partial \mathcal{H}}{\partial \alpha} = \frac{\partial \mathcal{H}}{\partial \beta} \Big|_{B_{z,0}} = 0 \quad (3.10)$$

$$\frac{\partial^2 \mathcal{H}}{\partial \alpha^2} \Big|_{B_{z,0}} > 0 \quad \& \quad \frac{\partial^2 \mathcal{H}}{\partial \beta^2} \Big|_{B_{z,0}} > 0 \quad \& \quad \frac{\partial^2 \mathcal{H}}{\partial \alpha \beta} \Big|_{B_{z,0}} > 0 \quad (3.11)$$

In general, a spin reversal cannot occur at the intersection points of the energy curves, because the states are still separated by energy barriers.

In the ferromagnetic case, the hysteresis consists of two branches. The field ranges of the related energy minima are single-sided restricted by the coercive fields, at which a spin reversal into the global minimum state occurs. The green branch in 3.4 (a) is related to the energy of an antiparallel spin state. This spin state cannot be reached from any other spin state. It can only occur as an initial state under the condition, that the uniaxial anisotropy constant  $D_z$  is larger than  $2J$ .



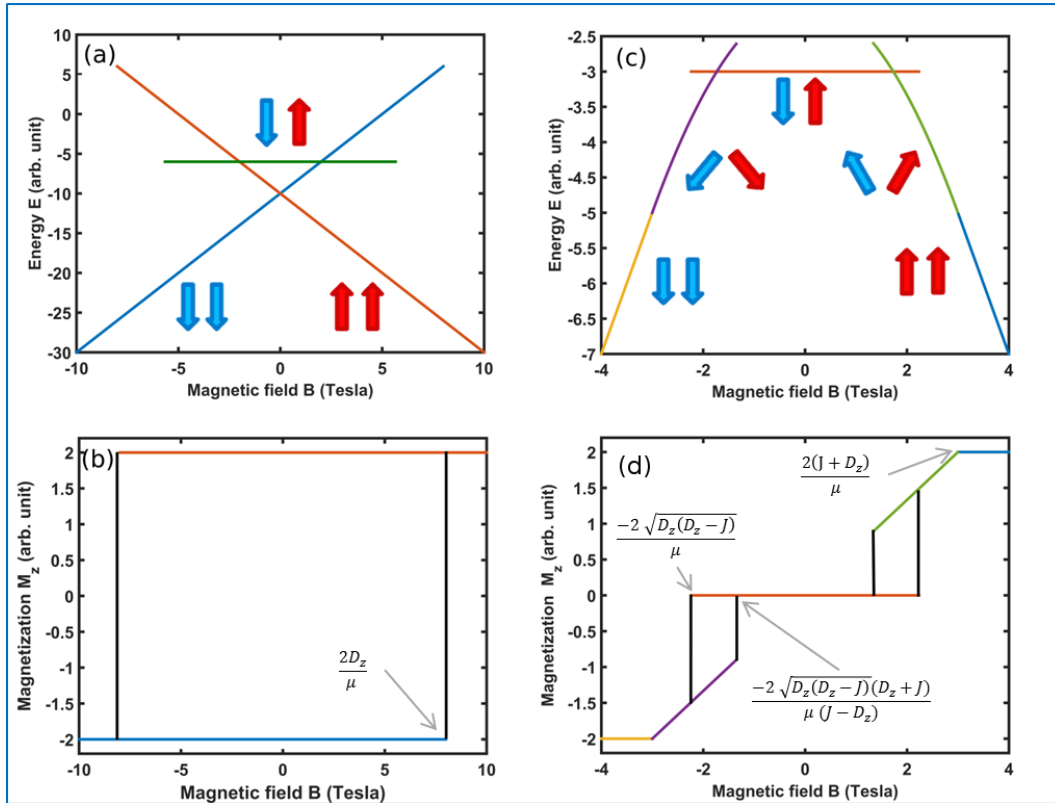


**Figure 3.4:** Energy curves (top) and hysteresis loops (bottom) of a spin dimer. The curves on the left are related to the ferromagnetic dimer, the curves on the right are related to the antiferromagnetic dimer. The spin states are illustrated by blue and red arrows. The branches in both representations are illustrated by the same colors.

In the antiferromagnetic case, the uniaxial anisotropy is set to a much lower value than the exchange constant and thus, the spins are antiparallely aligned close to zero fields. At increasing fields, the spins flop into a state, at which both spins are in the same angle to the easy axis while pointing slightly upwards. This state is called spin flop, which is discussed in section 7.3.2 at  $\text{Cr}_2\text{O}_3$  in more detail. At high fields, both spins align with the external field.

## 3.2 Atomistic spin dynamics

All calculations above, as well as the results of the Stoner-Wohlfarth model and the spin dimer do not include time-dependence, i.e. the dynamic evolution of the spin states. Furthermore, they do not describe any temperature dependence. Two different methods are used within this thesis to calculate the spin dynamics. The first one is based on the Landau-Lifshitz equation, which is a time dependent equation of motion. The second one is a Metropolis Monte Carlo algorithm, which is mainly used to calculate ground states of the exchange bias stacks described in chapters 6 and 7.

### 3.2.1 Landau-Lifshitz equation

The Landau-Lifshitz equation is a classical equation, which describes the motion of spins exposed to an effective field. It consists of two terms, namely the precession and the damping term. The equation of motion for a spin precessing around the effective field  $\vec{H}_{\text{eff}} = \frac{\partial \mathcal{H}}{\partial \vec{S}_j}$  is described by

$$\frac{d\vec{S}_j}{dt} = \frac{\partial \mathcal{H}}{\partial \vec{S}_j} \times \vec{S}_j, \quad (3.12)$$

where  $\vec{S}_j$  denotes the normalized classical spin and  $\mathcal{H}$  is the extended classical Heisenberg Hamiltonian as described in section 2.2. One can deduce this classical equation from the quantum mechanical Heisenberg equation of motion in combination with the Ehrenfest theorem [10, 23].

The precession term conserves the magnitude of each spin and the energy. Landau and Lifshitz added a second term [24], which also conserves the magnitude, but allows dissipation. The term models a damped precession towards

the local effective field. The strength of this damping is described by  $\lambda$ , the phenomenological Landau-Lifshitz damping factor. The complete Landau-Lifshitz equation is given by

$$\frac{d\vec{S}_i}{dt} = \frac{\partial \mathcal{H}}{\partial \vec{S}_i} \times \vec{S}_i + \lambda \left( \frac{\partial \mathcal{H}}{\partial \vec{S}_i} \times \vec{S}_i \right) \times \vec{S}_i. \quad (3.13)$$

The spin motion due to the precession and the damping in equation 3.13 is sketched in figure 3.5.

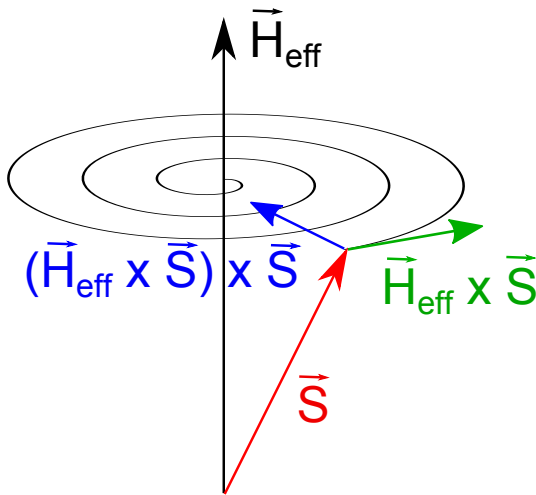


**Figure 3.5:** Illustration of the spin motion in an effective field  $H_{\text{eff}}$  due to the precession term (green) and the damping term (blue) of the Landau-Lifshitz equation.

Until now the influence of the temperature has not been taken into account. A finite temperature leads to thermal fluctuations which have to be considered within the spin equations of motion. To model a heat bath coupling with finite temperatures, fluctuations of the spins are introduced using a Langevin approach [25]. Langevin describes the Brownian motion of a particle in a liquid by Newton's second law of motion. He introduced an additional stochastic force to model the collisions with the much smaller fluctuating particles within the liquid [26]. In this case the equation of motion for a particle at position  $\vec{x}(t)$  reads

$$m \frac{d^2 \vec{x}(t)}{dt^2} = -\zeta \frac{d\vec{x}(t)}{dt} + \vec{F}(t). \quad (3.14)$$

The first part of equation 3.14 is the friction term with the coefficient of friction  $\zeta$ . This term models the velocity dependent deceleration of the particle. The second term is the fluctuating force due to the collisions. The fluctuations are independent of the motion of the particle and assumed to vary in a much shorter time scale than the particle's motion.

The principle of an additive force field can be used to extend the Landau-Lifshitz equation to the so-called stochastic Landau-Lifshitz equation:

$$\frac{d\vec{S}_i}{dt} = \left( \frac{\partial \mathcal{H}}{\partial \vec{S}_i} + \vec{f}_i \right) \times \vec{S}_i + \lambda \left( \frac{\partial \mathcal{H}}{\partial \vec{S}_i} \times \vec{S}_i \right) \times \vec{S}_i \quad (3.15)$$

The duration of the fluctuations and the time interval between the fluctuations are much shorter than the time scale of the spin precession [10]. The following equations express the properties of the fluctuations, i.e. the mean of the random fluctuation fields is zero and the fields are uncorrelated in time.

$$\langle \vec{f}_i \rangle = 0 \quad (3.16)$$

$$\langle f_i^\alpha(t) f_j^\beta(t') \rangle = 2\lambda k_B T \delta_{ij} \delta_{\alpha\beta} \delta(t - t'). \quad (3.17)$$

The stochastic Landau-Lifshitz equation preserves the magnitude of the spins as well.

The spin dynamics is determined by solving the stochastic Landau-Lifshitz equation. The accuracy of the numerical calculation is of the order  $O(h^4 + \epsilon^2 h^2)$ , where  $h$  is the time step length and  $\epsilon = \sqrt{2\lambda T}$  [27]. Therefore, at high temperatures and rather long time steps the magnitude of the spins fluctuates around 1, i.e. is no longer preserved. In these cases, the time step length has to be adjusted in order to keep the magnitude fluctuations within about 1% over the whole simulation time. However, shorter time step lengths suffer from an increase of the computational time.

Within the Landau-Lifshitz approach, thermal averages of physical properties can be determined by either sampling and averaging over many time steps or by averaging over many configurations of system's replicas. In both cases, the system has to be thermalized prior to the sampling process in order to prevent non-physical states in the ensemble resulting from artificial initial states [10].

For simulations at  $T = 0$  one has to avoid the case where all spins are parallelly or antiparallelly aligned to the effective field. In this case, the right hand side of equation 3.13 becomes zero, i.e. the system is frozen in its initial state. To avoid such a scenario it is useful to start from a random initial configuration. Another option is to apply a very low temperature, at which the fluctuations produce an additional torque, but the results are otherwise not biased by the temperature.

### 3.2.2 Monte Carlo approach

The second approach, used to model spin dynamics, is based on a Metropolis Monte Carlo algorithm [28]. Within this scheme, a new spin configuration is found by a random rotation of a single spin. This configuration is either accepted or rejected depending on the energy difference between the previous configuration and the new configuration. The energies are determined from the classical Heisenberg Hamiltonian. Each trial change of a spin is called a Monte Carlo step and a Monte Carlo cycle denotes a trial change of all spins of the structure.

The ensemble spin states of a model with  $N$  spins at finite temperature  $T$  are found by applying the following procedure:

1. The system is prepared in a proper initial state. In most cases, the initial state is a random orientation of all spins.
2. A spin at site  $i$  is selected and its local energy is calculated. This energy is denoted by  $E_{\text{old}}$ .
3. The direction of this spin is rotated to a new position. This new position is either an arbitrary position on the surface of a unit sphere or restricted to a spherical segment centered around the former spin direction (cf. section 4.2.2).
4. The local energy related to the new configuration  $E_{\text{new}}$  is calculated.

5. The old and the new energies are compared. If  $E_{\text{new}} < E_{\text{old}}$ , then the new configuration is accepted. Else, an evenly distributed random number  $r$  between 0 and 1 is chosen. If  $r < \exp(-\frac{E_{\text{new}} - E_{\text{old}}}{k_{\text{B}}T})$ , then the new configuration is accepted. Otherwise this configuration is rejected and the old one is kept.
6. If the new configuration has been accepted,  $E_{\text{old}} = E_{\text{new}}$ .
7. Steps 2 to 5 are repeated.

The spin states have to be sampled to compute thermal averages. This sampling might be done after each Monte Carlo cycle. At the end, the averaging is performed over all samples. The configurations should not be sampled before the system reaches physical states. This is required to prevent non-physical states from initial spin states.

### 3.3 Micromagnetics

Micromagnetics [9] is a classical approach, at which the material parameters are assumed to be continuous. In comparison to atomistic approaches, the atomistic structure is ignored and the method is appropriate for rather large structures in the micrometer range. The term micromagnetics is somehow misleading, but it is understandable in its historical context. Brown, who mainly developed micromagnetics with the aim to study domain walls, has chosen this wording to distinguish his theory from domain theory. In domain theory, the focus is on much larger domains. The small regions of the domain boundaries are neglected in the domain theory [18].

The micromagnetic approach is based on the different energy terms introduced in section 2.3 as well, but these terms are rewritten in a continuous form [23].

$$\mathcal{E}_{\text{exch}} = -A \int_V (\nabla \vec{S})^2 dV \quad (3.18a)$$

$$\mathcal{E}_{\text{aniso}} = -K \int_V (\vec{S} \cdot \vec{e}_u)^2 dV \quad (3.18b)$$

$$\mathcal{E}_{\text{field}} = -M_s \int_V (\vec{B} \cdot \vec{S}) dV \quad (3.18c)$$

$$\mathcal{E}_{\text{dip}} = -\frac{\mu_0}{2} \int_V (\vec{M} \cdot \vec{H}_D) dV \quad (3.18d)$$

Here,  $A$  is the exchange stiffness,  $K$  the micromagnetic uniaxial anisotropy constant associated to an preferred magnetization direction  $\vec{e}_u$ ,  $M_s$  the saturation magnetization and  $\vec{H}_D$  denotes the demagnetization field. The conversion from a discrete form in section 2.3 to the continuous form is based on the assumption, that the next neighboring spins differ only slightly in their direction. Thus, the summations over all spins of the structure within the energy terms in section 2.3 can be replaced by integrals. For the complete derivation we refer to [18, 23].

By comparing both forms of the energy terms, the constants of the micromagnetic approach are derived from their atomistic counterparts by

$$A = \frac{cJ}{2a} \quad (3.19a)$$

$$K = \frac{D}{a^3} \quad (3.19b)$$

$$M_s = \frac{\mu_{\text{eff}}}{a^3}. \quad (3.19c)$$

In the equations above,  $c$  denotes a lattice dependent coefficient which is equal to  $c = 1, 2, 4$  for bcc, fcc, and hcp, respectively [18]. The second constant  $a$  in equations 3.19a-3.19c is the lattice constant of the crystal. The time independent magnetic states of a structure are determined by minimizing all energy terms analytically or by numerical evaluation. The magnetization dynamics, i.e. the time dependent evolution of the magnetization  $\vec{M}$ , is commonly calculated by solving the Landau-Lifshitz-Gilbert equation (equation 3.20) [18]. This equation is very similar to the Landau-Lifshitz equation explained in section 3.2.1. As the Landau-Lifshitz equation fails in case of large damping, Gilbert introduced a different damping term [29]. Here, the Landau-Lifshitz-

Gilbert equation is described in its continuous form as all given parameters in a micromagnetic approach are continuous.

$$\frac{\partial \vec{M}}{\partial t} = -\frac{\gamma}{(1 + \gamma^2 \alpha^2 M_s^2)} \vec{M} \times \vec{H}_{\text{eff}} + \frac{\gamma^2 \alpha}{(1 + \gamma^2 \alpha^2 M_s^2)} \vec{M} \times (\vec{M} \times \vec{H}_{\text{eff}}), \quad (3.20)$$

In this equation  $\alpha$  denotes the phenomenological Gilbert damping coefficient. The Landau-Lifshitz-Gilbert equation and the Landau-Lifshitz equation become identical in the limiting case of low damping in both, the atomistic and the continuous description.

As the micromagnetic approach is based on a continuous description of the material properties, the complete structure can be divided into cells independently of discrete atomic positions. Hence, the Landau-Lifshitz-Gilbert equation can be solved by finite element methods. The grid size for such a calculation is adjustable which permits the calculation of the magnetization and other quantities of rather large structures. However, the application of micromagnetics is more restricted than the application of atomistic approaches. The characteristic length of the determined quantities has to be much larger than the size of a single cell. Besides the restriction of the cell size, the continuous description prohibits the investigation of antiferromagnetic materials without further adaptations [30]. Furthermore, high temperatures cannot be taken into account in the common micromagnetic approaches, as finite temperatures change the saturation magnetization locally. This local change is in contradiction to the assumption of constant saturation magnetization within micromagnetic approaches [31].

### 3.4 Macrospin approach

In a macrospin approach, the magnetic moments of several neighboring spins are combined into a single macrospin. This is only valid by assuming a homogenous magnetization of the neighboring spins within the volume, which is modeled by the macrospin. Thus, the macrospin is represented by a classical spin with a single effective magnetic moment. The effective magnetic moment and the total uniaxial anisotropy are calculated by a summation over



the effective magnetic moments and the anisotropies of the atomistic spins within the volume. The shape anisotropy resulting from dipole-dipole interactions is also considered by the total uniaxial anisotropy. As the macrospin approach is based on a homogenous magnetization within the volume, the exchange interactions of the atomistic spins are neglected. In opposite to that, the interactions between different macrospins might play a crucial role. The exchange constants can be deduced from the exchange stiffness of a continuum approach like the micromagnetic approach described in the previous section. The calculation of the magnetic states is determined by the same methods as introduced for atomistic descriptions in section 3.19a-3.19c. The Stoner-Wohlfarth particle can be seen as an example for a single macrospin. Within a macrospin approach, finite temperature could not be considered without further assumptions. Thermal fluctuations change the alignment of the spins and reduce the saturation magnetization, which is not considered in such an approach [32].

The macrospin approach might be seen as a theory, which is an in-between of the atomistic and micromagnetic approaches. In some cases results from micromagnetic simulations can be determined by a macrospin approach as well. In the following example, the macrospin method is used to calculate the different ground states of a cubic structure, whose results are known from micromagnetic calculations. The example is the standard problem no. 3, which is one of five standard problems to compare the results of different micromagnetic implementations. The standard problems are described on the webpage of the  $\mu$ MAG micromagnetic modeling group at the National Institute of Standards and Technology (NIST)<sup>1</sup>. The third standard problem has been proposed and calculated by Hubert [33].

---

<sup>1</sup><http://www.ctcms.nist.gov/mumag/mumag.org.html>, retrieved May 10th, 2016

A cube of edge length  $L$  exhibits either a magnetic flower or a vortex state. Both are illustrated in figure 3.6. The transition of the vortex to the flower state depends on the edge length and the material parameters. The material parameters are given by the intrinsic length  $l_{ex} = \sqrt{\frac{A}{K_m}}$  and the magneto-static energy density  $K_m = \frac{\mu_0 M_s^2}{2}$ . The uniaxial anisotropy is supposed to be  $K_u = 0.1 K_m$ . From [33] it is known, that the transition should occur at approximately  $L = 8 l_{ex}$ .

To determine the different states using a macrospin approach, the cube is modeled by  $9 \times 9 \times 9$  macrospins on a simple cubic lattice. The material parameters are derived using equations 3.19a-3.19c under the assumption that  $M_s = 1 \cdot 10^6$  A/m. The resulting flower and vortex states in figure 3.6 are related to  $L = 10 l_{ex}$  and  $L = 7 l_{ex}$ . Thus, the expected transition length of approximately  $L = 8 l_{ex}$  could be reproduced by a macrospin model.

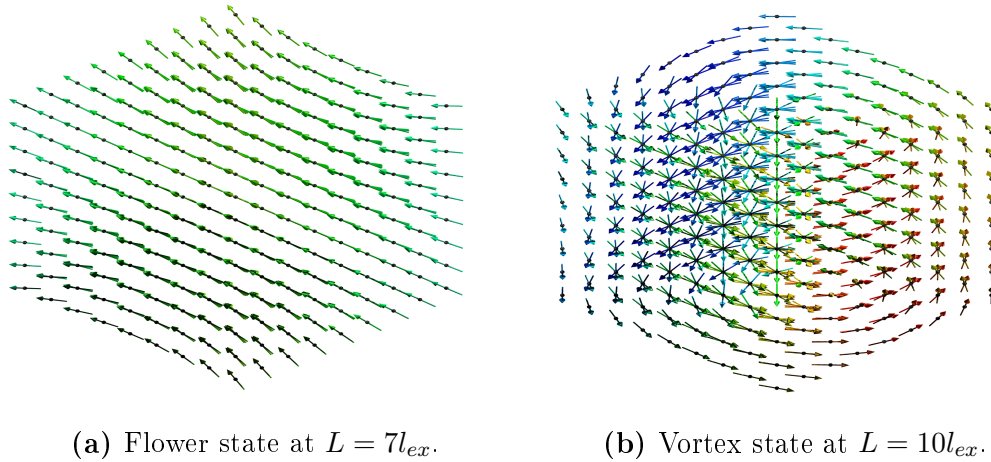


**Figure 3.6:** Flower and vortex state of  $9 \times 9 \times 9$  classical macrospins. The alignment of the spins depend on the edge length  $L$  of the cubic structure.

# Chapter 4

## Hysteresis Modeling

Theoretical models in the area of magnetism are developed to explain and predict the magnetic behavior of materials and systems. During model development, the magnetic properties of the model are considered and compared with experimental findings. One of the major properties is the hysteresis of the magnetic material. It describes the history dependent behavior of the magnetization in response to a magnetic field whose strength is varied in time. In a simulation such a magnetization curve can be directly calculated. In opposite, the magnetization within an experiment is often indirectly obtained, for example by the measurement of a current, voltage, resistance or by reflected and absorbed light waves. Nevertheless, the field dependent curves of these quantities are also used to verify the quality of a model. Rather than a comparison of the magnetization, characteristic values like coercivity or distinct curve shapes are used to compare experimental and theoretical results.

Within the following sections the main terms related to magnetic hysteresis curves are explained and different simulations methods to calculate the field dependent and time dependent curves are introduced.

### 4.1 Fundamentals of magnetic hysteresis

In case that a material exhibits a magnetic hysteresis, its magnetization is neither proportional to the applied field, nor it is a one-valued function of the field [18]. Typical hysteresis curves are plotted in figure 4.1. The blue dotted line represents the virgin magnetization curve after demagnetization

of the sample. The red line represents one of the minor loops, occurring by decreasing the applied field again before reaching the saturation magnetization  $M_s$ . The limiting magnetization curve is sketched by a green solid line. The magnetization at zero field of the limiting curve is denoted by  $M_r$ , which is the remanent magnetization or remanence. The minor hysteresis loops and the limiting curve are bounded by two slopes of either increasing or decreasing magnetization. The coercive fields  $B_1^c$  and  $B_2^c$  indicate the field strength at which the magnetization of the limiting curve becomes zero. Within this thesis the coercivity is calculated by  $B_c = \frac{1}{2}(B_1^c - B_2^c)$ . If the hysteresis loop is symmetric to the vertical axis, this value equals  $B_1^c$ .

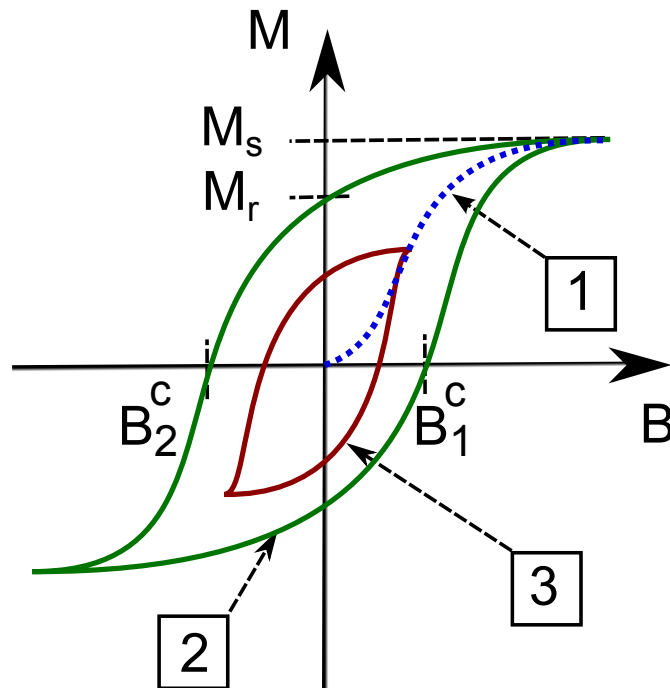


**Figure 4.1:** Schematic representation of a hysteresis curve. The numbers are related to the virgin curve (1), the limiting hysteresis curve (2) and a minor hysteresis curve (3).

On one hand the shape of magnetization curve depends on the former magnetization and thus, on its history and the applied magnetic field. On the other hand, the shape and especially the coercivity depend on the sweep rate of the

external field. The sweep rate determines the time, in which the magnetization of the structure can relax at each field value. Furthermore, the hysteresis loops depend on the temperature.

The relation between temperature, sweep rate and magnetic field is explained on the basis of a simple system with two energy minima, which are separated by an energy barrier of a finite height as illustrated in figure 4.2.

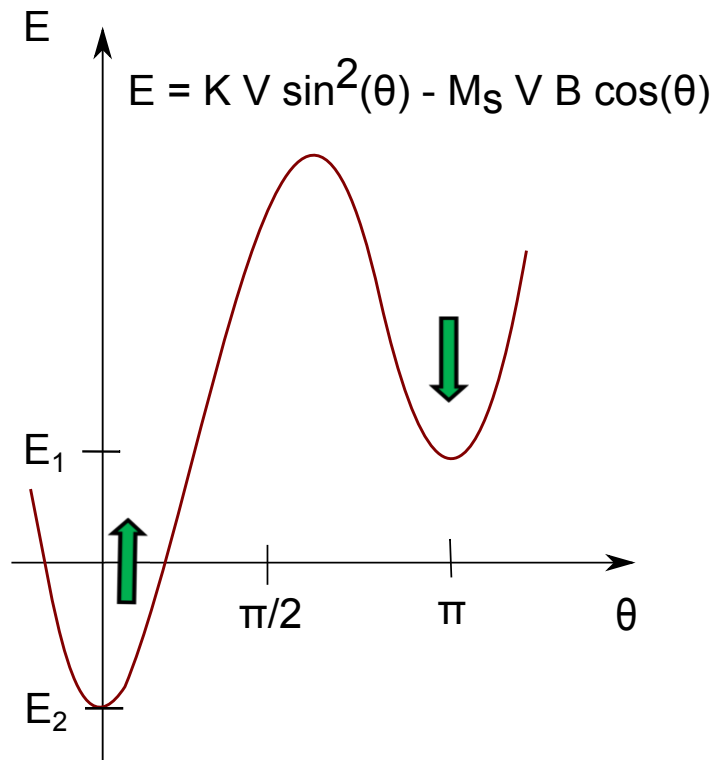


**Figure 4.2:** Representation of an energy barrier between two energy minimizing spin states related to a Stoner-Wohlfarth particle.

The Stoner-Wohlfarth model, introduced in section 3.1.1, describes such a system. First, it is assumed that the temperature is zero. By applying a magnetic field, one of the two minima represents the global minimum, while the other is a local minimum. Initially, the system is in its local minimum, at which the spins are pointing against the positive field direction (cf. figure 4.2). As there is no temperature considered, the structure will reverse its magnetization as soon as the height of the barrier reaches zero due to an increase of the external field. The barrier equates zero at the coercive field  $B_c = 2K/M_s$ .  $K$  and  $M_s$  denote the energy of the anisotropy per unit volume and the saturation mag-

netization, respectively. If the reversal occurs in an infinite small time interval, it does not matter how fast the field is increased or decreased, the hysteresis loop looks the same. The hysteresis loop is said to be rate-independent [34].

If a small temperature is taken into account, the hysteresis loop becomes rate-dependent. A finite temperature can be described by a stochastic process, which leads to a random walk of the spin orientations in time. If the time interval of distinct field strength is long, it is probable, that the system overcomes the energy barrier and reaches its thermal equilibrium. In other words, the finite temperature permits, that a system might overcome its energy barrier, although the external field is lower than the coercive field without temperature.

The time interval, which is necessary to flip from one magnetic state into the other by thermal agitation, is called the relaxation time  $\tau$ . In case of zero field its value is given by the Néel-Arrhenius equation

$$\tau = \tau_0 e^{\frac{KV}{k_B T}}, \quad (4.1)$$

at which  $\tau_0$  denotes a constant of approximately  $10^{-10}$ s [18]. This value depends on the material and the dimensions of the structure. It is often assumed to be constant, but this is only applicable at narrow energy minima and high energy barriers. Brown developed a differential equation based on a random walk, at which  $\tau_0$  can be determined numerically [9]. At Brown's approach  $\tau_0$  is no constant anymore and depends among other parameters on the temperature.

Nevertheless, equation 4.1 is used to explain the rate-depended hysteresis in more detail. In figure 4.3 the relaxation time is plotted against the temperature at zero external fields. The anisotropy constant is  $3.9 \cdot 10^6$  erg/cm<sup>3</sup>, which is the value for hcp-Co [18]. The geometry of the Co particle is a sphere with radius of  $r = 5$  nm. It can be seen from figure 4.3, that the relaxation time reaches high values in the geological range of more than million years, while the relaxations at rather high temperatures shrinks to a few milliseconds (inset of figure 4.3).

Thus, in many experiments, the relaxation time is much higher than the time of the measurement. In this case, the magnetization seems to be stable. For

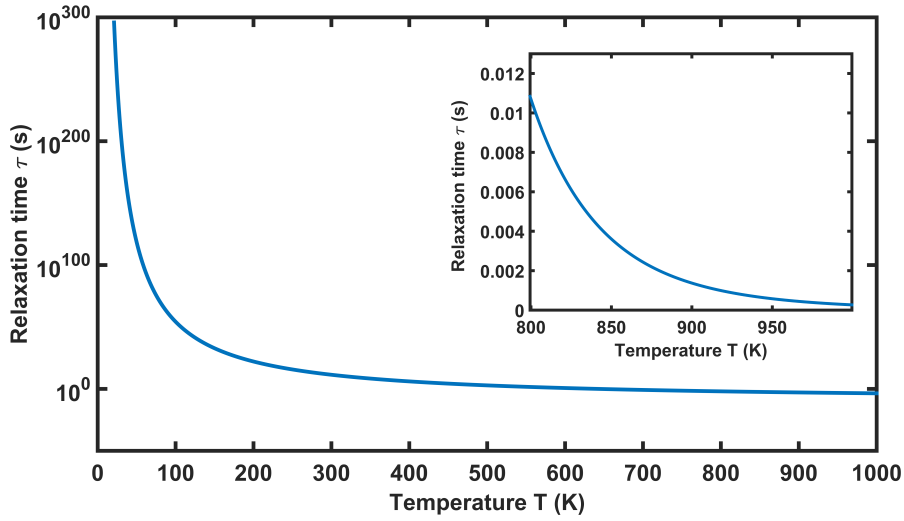


**Figure 4.3:** Representation of the relaxation time against temperature calculated by the Néel-Arrhenius equation.

measurements, larger than the relaxation time, the magnetization is changed during the measurement. Effects like superparamagnetism, at which the magnetization seems to be zero, are observed. This class of magnetism is not further studied within this thesis. Instead of that, the hysteresis loops resulting from experiments at which the relaxation time is much larger than the measurement time, are discussed in detail. The hysteresis loops are measured by applying an external magnetic field, which shrinks the energy barrier and thus forces a state transition. As the height of the energy barrier is decreased by the external field, a finite temperature might lead to a spin reversal before the coercive field  $B_c$  is reached. How much the field strength, which forces the spin reversal, deviates from the coercive field at zero temperature, depends on the time interval the system could spend to relax at a given field value. This is sketched in figure 4.4 by modifying the Néel-Arrhenius equation 4.1 [18]. It is assumed that the system is in its local minimum and the global minimum can be reached by increasing fields. With an external field, equation 4.1 becomes

$$\tau = \tau_0 e^{\frac{KV(1-BM_s/2K)^2}{k_B T}}. \quad (4.2)$$

The Néel-Arrhenius equation and thus also equation 4.2, is only applicable at rather high energy barriers and narrow energy minima, i.e. at low temperatures and negative or low positive fields away from coercivity. Anyhow, figure

4.4 illustrates the decrease of time, until a reversal occurs at a constant magnetic field due to thermal agitation. The curves flatten by increasing higher temperatures. At finite temperatures, the hysteresis curves of measurements at low sweep rates and long time intervals exhibit smaller coercivities than measurements at high sweep rates with short time intervals per field value. These relations have also been measured by Wernsdorfer at a  $\text{Mn}_2\text{Ni}$  single chain magnet [35].

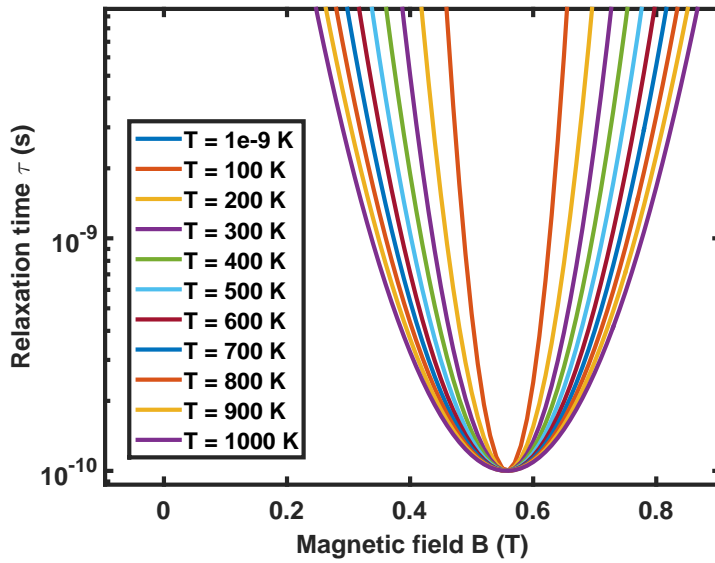


**Figure 4.4:** Relaxation time against magnetic field at different temperatures.

Up to now the motion of spins during the state transition has not been taken into account within these explanations. The resulting hysteresis curves are denoted as static or quasi-static. In ultra-fast measurements and in typical atomistic spin dynamics simulations of larger systems, the determined coercivities might be larger than the theoretical values needed to force a state transition. If the sweep rate is very high, the time spent at each field value is too short to relax into the new minimum. This occurs for example at systems with rather complicated spin reversal mechanisms, like reversals based on domain wall motions [36]. Thus, the so called dynamic hysteresis loops are measured or calculated at high sweep rates. Especially the comparison of measured static hysteresis curves with hysteresis loops resulting from atom-



istic spin dynamics calculations is problematic, because these calculations are very time consuming. A typical time step in the simulation is in the femtosecond range, while a reversal process is in the nanosecond regime [37]. Thus, an atomistic spin dynamics calculation could easily exceed months, while a comparable experimental measurement takes only seconds. This dilemma is further discussed in the next section. A parallel algorithm to speed up the calculations of hysteresis loops is introduced in the section one after.

## 4.2 Serial calculation of hysteresis curves

Two different methods have been introduced in section 3.2 to calculate the spin dynamics of small magnetic structures atomistically. Within the first method, the Landau-Lifshitz equation is solved by a stochastic Runge-Kutta scheme to calculate the field and time depended magnetization. The second method is based on a Monte Carlo algorithm to determine the lowest energy states. Both approaches are applicable to calculate hysteresis loops. In the next section these approaches are abbreviated by SRK and MC, which stands for *Stochastic Runge-Kutta* and *Monte Carlo*, respectively.

### 4.2.1 Solving the Landau-Lifshitz equation of motion

The Landau-Lifshitz equation is solved to calculate the spin state at each time step. The spin state of the previous time step represents the initial spin state of the actual time step. Thus, the necessary history-depended evolution of the spin states is a naturally build-in feature.

The crucial parameters of a hysteresis loop calculation based on the SRK approach are the sweep rate and the phenomenological damping factor. The magnetic field strength can be arbitrarily chosen at each time step  $t$ . Typically, a triangular function  $B(t) = B_0 \cdot [2 \cdot \text{tri}(\frac{t}{t_{\max}} - 1) - 1]$  with an up and down field ramp or a sinusoidal function  $B(t) = -B_0 \cdot \cos(\frac{t}{t_{\max}} 2\pi)$  are used to determine the hysteresis loops of the structure or system.  $B_0$  denotes the field amplitude and  $t_{\max}$  equates the time period of the complete field cycle.

The sweep rate  $R_s = \frac{\Delta B}{\Delta t}$  equals the ratio of the field amplitude and the time interval covering half of a signal period as illustrated in figure 4.5.

The second crucial parameter is the Landau-Lifshitz damping factor  $\lambda$ , which

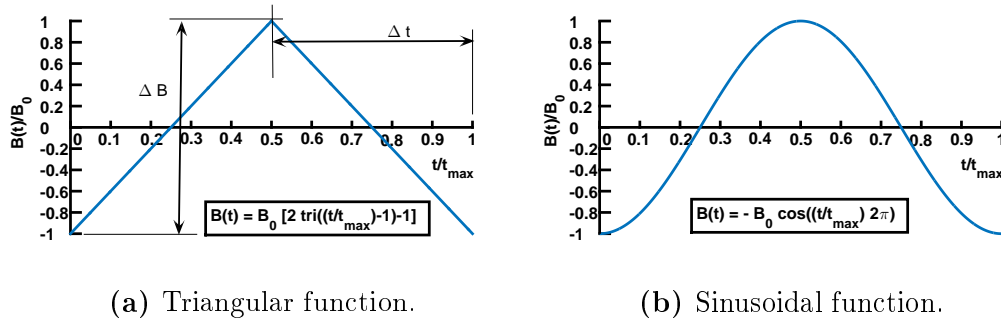


**Figure 4.5:** Different functions of the magnetic field to determine a magnetic hysteresis curve. The sweep rate is calculate as the ratio of  $\Delta B$  and  $\Delta t$ .

is related to the relaxation time of the magnetization introduced in the former section. Different mechanisms, which permit an energy transfer, contribute to the damping. These are for example the spin-orbit coupling and the spin-phonon coupling in an atomistic approach [38, 39]. If the Landau-Lifshitz equation is used to calculate the dynamics of a macrospin model or used within a micromagnetic approach, the damping constant includes also damping due to lattice defects or complex and time-consuming magnetization reversal processes.

By choosing a proper damping constant and sweep rate, the resulting magnetization curves are directly comparable to experimental hysteresis loops. If finite temperatures are taken into account, the magnetization values are determined by thermal averaging.

The influence of the sweep rate on the hysteresis loop is exemplarily illustrated by a thin CoFe layer in section 4.2.3.

## 4.2.2 Applying a modified Monte Carlo scheme

Instead of solving the Landau-Lifshitz equation, a modified MC scheme can be used to determine hysteresis loops. The typical aim of Monte Carlo methods in the area of magnetism is the determination of lowest energy states. As each spin is rotated randomly to a position on the surface of a unit sphere within a MC cycle, possible energy barriers might be exceeded within a small amount of MC steps. A thermal averaging would reveal a superparamagnetic behavior of the structure. To force a hysteretic behavior, the system has to be

confined in one of its local energy minima, until the respective energy barrier is exceeded either by the applied magnetic field or by thermal agitation with a rather high temperature. One option to realize the confinement is to restrict the random change of the spins [40, 41]. In a classical view, the spin is thought as a vector, which can be represented by an arrow pointing to a position on the unit sphere (cf. 2.2). Without any restrictions, the new spin state is related to an arbitrary position on the surface of the unit sphere. If the rotation is confined, the arrow of the new state can only point onto a spherical segment located around the position related to the former state. Figure 4.6 illustrates one of these segments, which can be seen as the convex ground of a cone. The segment is constructed by adding a vector to the initial position. The coordinates of this vector are equally distributed on the surface of a sphere with a radius  $R_c$ . Afterwards, the total vector is normalized. In figure 4.6, the radius of the sphere is  $R_c = 0.5$ .

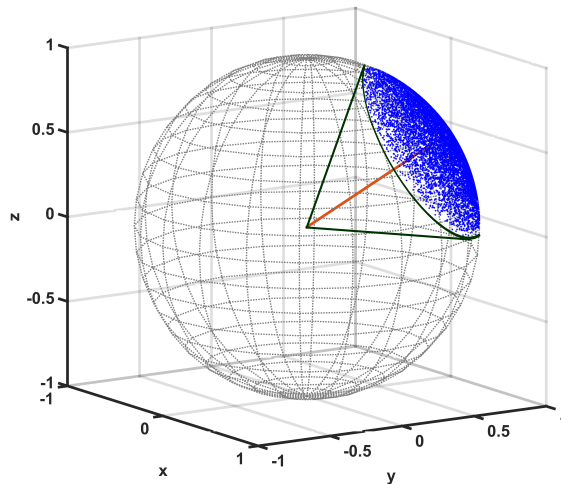


**Figure 4.6:** Restriction of the random rotation of a spin to a spherical segment in a modified MC scheme. The spherical segment is constructed by adding a sphere of radius  $R_c = 0.5$  to the spin vector.

By the restriction of the rotation a kind of pseudo dynamics is implied. A comparison of the spin dynamics within a Landau-Lifshitz-Gilbert approach and the pseudo dynamics of the modified MC scheme leads to a relation between a time interval  $\Delta t$  of the stochastic differential equation and a Monte

Carlo cycle [41]. The relation is given in equation 4.3. It is only valid in the high damping limit.

$$R_c^2 = \frac{20k_B T \alpha \gamma}{(1 + \alpha^2) \mu_s} \Delta t. \quad (4.3)$$

$\alpha$  denotes the Gilbert-damping factor, which is part of the Landau-Lifshitz-Gilbert equation and a phenomenological constant like the Landau-Lifshitz damping factor. The Boltzmann constant  $k_B$  multiplied with the temperature  $T$  represents the thermal energy.  $\mu_s$  is the effective magnetic moment of the spins within the structure and  $\gamma$  denotes the gyromagnetic ratio. This equation is further studied within [42] at classical spin chains. It is shown that the high damping limit in this case is reached for  $\alpha > 4$ . Thus, the relation in equation 4.3 fails for the investigation of the dynamics at structures with a rather low damping.

In the modified Monte Carlo scheme, finite temperatures are considered implicitly (section 3.2.2). A thermal averaging over each magnetization value of a single field value reveals the hysteresis loop as described for the SRK approach.

### 4.2.3 Application: Magnetization curve of a thin CoFe layer

A 1 nm and a 1.2 nm thick CoFe(B) layer are part of a magnetic tunnel junction, which is switchable by a thermal spin-transfer torque (T-STT) [43, 44]. In a T-STT device, the spin state is changed by a spin-polarized current, which is caused by a temperature gradient. The two layers are separated by an ultrathin non-magnetic MgO layer in the Ta/CoFe(B)/MgO/CoFe(B)/Ta stack. The B atoms are thought to diffuse into the neighboring layers during annealing. The remaining CoFe layers exhibit a bcc-structure. Together with the MgO layer and the Ta layers a perpendicular magnetic anisotropy (PMA) is induced at CoFe(B)[45, 46]. The PMA is thought to be an interfacial effect, which is explained in more detail within section 7.3.1. The strength of the perpendicular anisotropy depends on the CoFe(B) layer thickness. Kim *et al.* proposed a calculation of the magnetocrystalline and the shape anisotropy of thin ordered B2 FeCo film at which a transition from in-plane to out-of-plane magnetization is expected at approximately 15 monolayers ( $\approx 2.2$  nm) [47]. The authors of

[47] expect that the change of the lattice constant from the surface to the bulk is responsible for the large perpendicular anisotropy. While the shape anisotropy, which is caused by the long range dipole-dipole interactions, increases with the layer thickness, the sum of the magnetocrystalline anisotropy over all atoms decreases.

To demonstrate the challenges of a hysteresis calculation a model is developed, which is related to an ordered bcc-CoFe layer with a thickness of 1 nm. The effective uniaxial anisotropy of each Co and Fe atom is based on the results from Kim *et al.* In a first instance, the influence of the dipole-dipole interactions is neglected and the uniaxial anisotropy is assumed to be  $175 \mu\text{eV}$  of each atom. The effective magnetic moments ( $\mu_{\text{Fe}} = 2.76 \mu_{\text{B}}$ ,  $\mu_{\text{Co}} = 1.74 \mu_{\text{B}}$ ) and the exchange constants of the first nine neighbor shells are obtained by density functional theory calculations and illustrated in figure 4.7 [48].

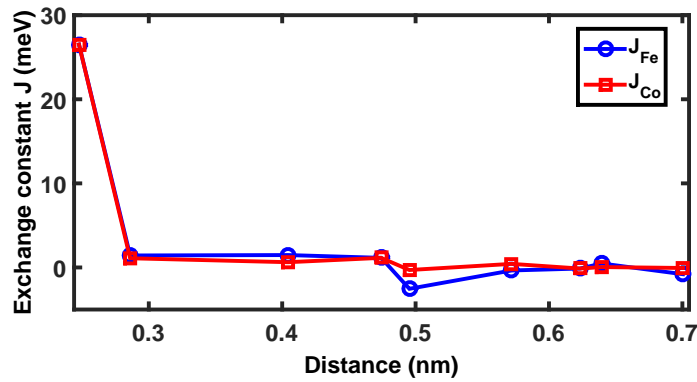
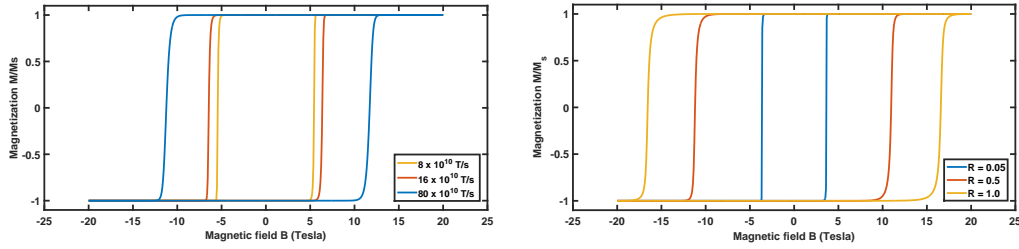


**Figure 4.7:** Exchange interaction between the first nine neighboring atoms of CoFe. From I. Stockem and C. Schröder, IEEE Trans. Mag., 51, 11, 2015. ©2016 IEEE.

The lattice constant is assumed to be 0.286 nm. The rather high first neighbor exchange interactions dominate the behavior and thus, no significant difference of the magnetization curve is observable, if the exchange interactions are restricted to the first neighbor shell.

The hysteresis loops in figure 4.8a and figure 4.8b are obtained by solving the stochastic equation of motion or by applying the modified Monte Carlo scheme, respectively. In the stochastic equation, the sweep rate is varied. In the case of the Monte Carlo scheme the cone size  $R_c$  is changed.



(a) Hysteresis loops at different sweep rates of the magnetic field determined by solving the Landau-Lifshitz equation.

(b) Hysteresis loops determined by a modified Monte Carlo approach with different cone size  $R_c$ .

**Figure 4.8:** Hysteresis loops of CoFe.

The hysteresis loops in figure 4.8a illustrate the sweep rate dependence. The Landau-Lifshitz damping factor is assumed to be  $\lambda = 0.1$ . The high ferromagnetic coupling and the uniaxial anisotropy would cause a spin flop at the coercive fields of approximately 3 T. This would lead to a sudden jump in the magnetization. As the time step length is 0.1 fs, the spins could not reverse within one time step and the dynamic rotation is reflected in the curved shape of the hysteresis loops. The hysteresis loop calculation of a cylindrical sample with a radius of  $r = 2.5$  nm and 1684 magnetic atoms takes 280 minutes on a single processor for the curve with the sweep rate of 80 T ns. The resulting curve illustrates a dynamic behavior, as the expected coercivity is not reached.

At this example, the determination of the hysteresis loops is less time consuming by applying the MC approach. The calculation with  $10^7$  MC steps takes approximately 30 min on a single processor. Although this approach is much faster than solving the equation of motion, its application is in question. The relation described in equation 4.3 is valid only in the high damping limit and does not apply to the calculation of time step sensitive dynamic hysteresis loops with low damping. In opposite to this, the MC method might be a good choice for the calculation of quasi-static hysteresis loops, at which the measurement time is larger than any dynamic spin flip, but much less than the relaxation time at zero field.

In case of the CoFe structure with a uniaxial anisotropy, the hysteresis loop

width decreases by decreasing the cone size  $R_c$  from  $R_c = 1.0$  to  $R_c = 0.05$ . This is in contrast to equation 4.3 and might be caused by the rather high exchange interaction between the next neighboring spins. The Monte Carlo procedure is based on a single spin flip. A rotation of a single spin away from the orientation of the surrounding spins leads probably to an increase of the energy and the rejection of the new configuration is very likely. At small angles the energy reduction due to the Zeeman term might exceed the energy gain from the exchange interaction and thus the state is more likely accepted.

The calculation of a quasi-static hysteresis curve for such a small structure, excluding the long range dipole-dipole interactions, is a feasible task. But as the radius increases, the number of atoms and interactions grows at least quadratically and becomes impractical. The next section provides an approach that reduces the computational time by a parallelization of the hysteresis loop calculation.

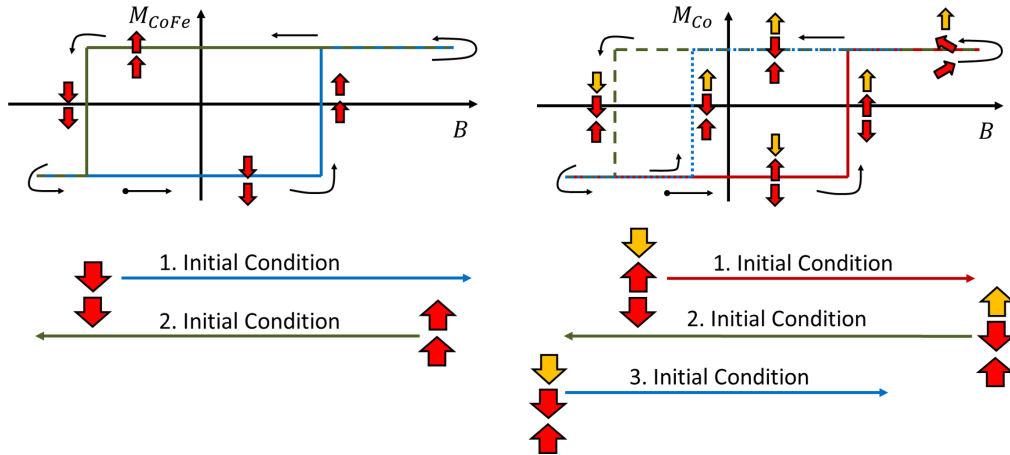
### 4.3 Parallel calculation of hysteresis curves

The subsequent approach [48] is established to calculate quasi-static hysteresis loops efficiently. A magnetization curve, which exhibits a hysteresis loop, represents the history dependent behavior of the magnetization. As the magnetization depends on former magnetic states, the hysteresis loop is measured by increasing or decreasing the magnetic field in a serial manner. But in several cases some former states are known and the magnetization curve can be divided into independent parts, allowing a parallel calculation. In these cases, the parallel calculation leads to an enormous reduction of the computational time.

#### 4.3.1 Division into independent parts

A hysteresis of the field dependent magnetization occurs, when a system is temporary trapped in local minima that are separated by energy barriers. In the simplest case, the system is represented by a single spin with a uniaxial anisotropy. Without temperature, two local minima are separated by one energy barrier. The two states are those at which the spin points either up- or downwards. By applying a large magnetic field parallel to the anisotropy

axis the spin is reversed from one state into the other. If the energies of the local minima are plotted against the magnetic field, the overlapping range represents the width of the hysteresis loop (cf. section 3.1.1). To speed up the hysteresis loop calculation, the complete field cycle is subdivided into branches, at which the magnetization is calculated independently by choosing proper initial conditions.



(a) Hysteresis curve and branches for a structure with a uniaxial anisotropy.

(b) Hysteresis curve and branches for switchable exchange bias systems. From I. Stockem and C. Schröder, *IEEE Trans. Mag.*, 51, 11, 2015. ©2016 IEEE.

**Figure 4.9:** Schematic representation of hysteresis curves (top) and branches with related initial conditions (bottom) used for a parallel calculation.

In this example the hysteresis loop consists of two branches with different initial conditions. In the upper branch the spin is initially pointing upwards and in the lower branch the spin is initially pointing downwards. Figure 4.9a illustrates the branches for the case of a symmetric hysteresis loop. Each branch can be further divided into small intervals until each interval consists of only one field value and a related initial condition. Thus, the history is reflected in the initial conditions and the magnetization at each interval can be calculated in parallel.



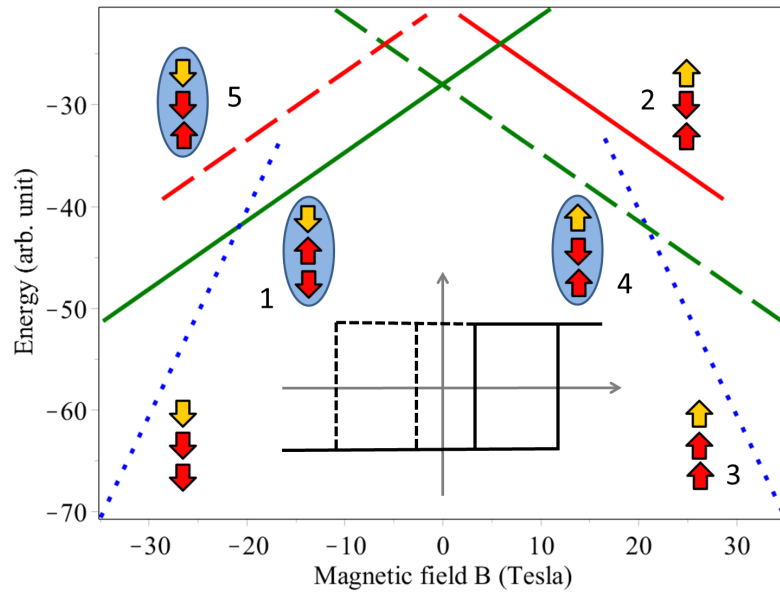


**Figure 4.10:** Energy curves of a switchable exchange bias model.

Such a splitting into intervals is also applicable at more complicated systems and multilayer stacks with shifted hysteresis loops. One example is the switchable exchange bias stack Pt/Co/Cr<sub>2</sub>O<sub>3</sub>/Pt described in detail in chapter 7. A three spin model, which is explained and further investigated in section 5.3.2, is used here to explain the parallel calculation of hysteresis loops at switchable exchange bias systems. At Pt/Co/Cr<sub>2</sub>O<sub>3</sub>/Pt it is supposed, that the spins of the antiferromagnetic layer are reversed by a high magnetic field. The complete field cycle consists of three branches to determine a magnetization curve showing a switchable loop shift (figure 4.9b). At the first branch the field is increased to switch the system. The second and third field branch describes a down and up field ramp to determine the hysteresis loop on the opposite side of the coordinate system. From the energy curves in figure 4.10 it can be seen that all three branches require different initial conditions.

At approximately  $-6\text{ T}$  three different energy minimizing states exists. To distinguish which state can be reached within each cycle, the order of the spin states has to be known. This order is reflected by the initial conditions of each branch.

- At the first branch the field is increased to switch the antiferromagnetic layer. The related initial state is the first state in figure 4.10.

- At the second branch the field is decreased. In a serial calculation, the spin reversal of the antiferromagnetic state has been passed before. Thus the fourth state is the related initial configuration of the second branch.
- At the third branch the field is increased again. The initial condition equates the fifth state.

In the following, the calculations are based on the cylindrical CoFe layer described in the former section 4.2.3. Such a single domain ferromagnetic structure equates the two local energy minima example from above (cf. figure 4.9a). The calculation of quasi-static hysteresis loops of other systems follow the same scheme as explained by the cylindrical CoFe layer in the next sections.

### 4.3.2 Calculation of the magnetization within the intervals

The quasi-static magnetization within each interval can be determined by the MC scheme (section 4.2.2) or by the SRK approach (section 4.2.1). Within the implementation of the SRK approach a hybrid parallelization is used to accelerate the calculations. The calculation of the magnetization of the independent intervals are parallelized by the message passing interface (MPI) [12]. The time consuming parts of the SRK scheme are accelerated by a multi-threading algorithm based on OpenMP [11].

Depending on the material parameters and the interactions, either solving the SRK scheme or the MC method leads to a faster relaxation. At both methods, the number of steps has to be chosen properly. The number of time or MC steps has to be at least equal to the number of steps which are necessary to rotate the magnetization at the coercive field strength completely. To obtain the limiting number of steps a spin reversal is computed at a field value that is slightly larger than the coercive field for both methods. The magnetization during the spin reversal at  $B = 4.8$  T is represented in figure 4.11.

At the MC scheme a cone of size  $R_c = 0.5$  is assumed. The damping factor in the Landau-Lifshitz equation is  $\lambda = 0.1$ . A small temperature of only 0.1 K is applied at both methods. It is used to cause a small torque at a ferromagnetic state within the Landau-Lifshitz equation and used to avoid a division by zero

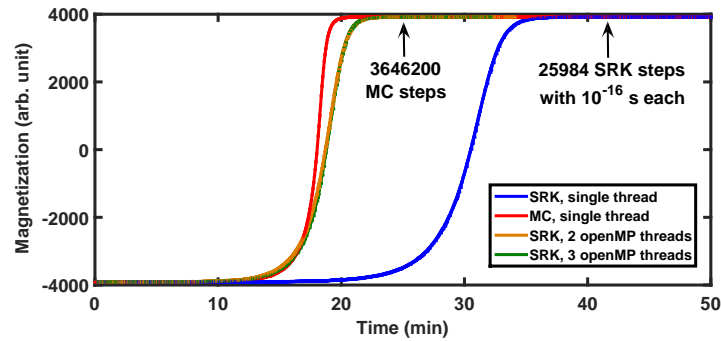


**Figure 4.11:** Determination of the necessary computational time for the CoFe layer by the evolution of the magnetization at the critical field  $B = 4.8$  T.

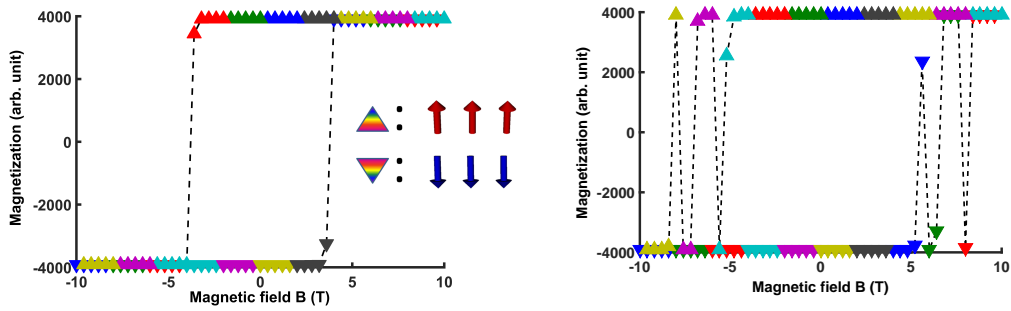
within the Monte Carlo scheme. With these parameters the MC scheme needs less than 3646200 MC steps and approximately 25 min, which is faster than the numerical calculation of the Landau-Lifshitz equation even with multi-threading.

The two branches in figure 4.9a are divided into small intervals of five field values. At the beginning of each interval a relaxation run of  $3 \cdot 10^6$  MC steps is performed starting from the related initial state. After that the magnetization of the five field values within the interval are sampled with further  $3 \cdot 10^6$  MC steps, which is sufficient to get a quasi-static behavior. Figure 4.12a illustrates these intervals and the resulting hysteresis loop. An insufficient number of steps leads to artifacts, recognizable close to the coercive fields in figure 4.12b. Here, the pre-relaxation run is performed with only  $1 \cdot 10^5$  and the sampling consists of  $5 \cdot 10^5$  MC steps.

Depending on the available number of processors, the intervals can be further divided and the speed-up increased, so that at least one processor calculates the magnetization at one field value.

### 4.3.3 Hybrid scheme for the long-range dipole-dipole interactions

The long range dipole-dipole interactions cause a dramatic increase of the computational time. To reduce the computational time the hybrid implementation of MPI and openMP is extended. Multi-threading is used to accelerate the cal-



(a) Quasi-static calculation with a sufficient number of MC steps. Adapted from I. Stockem and C. Schröder, IEEE Trans. Mag., 51, 11, 2015. ©2016 IEEE.

(b) Quasi-static calculation with an insufficient number of Monte Carlo steps.

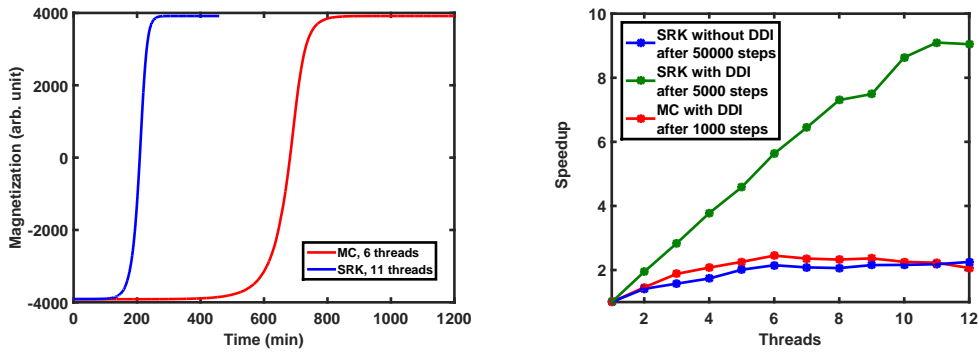
**Figure 4.12:** Quasi-static hysteresis loop of CoFe. The different initial conditions applied at each branch are represented by up- and downwards orientated triangles. The color of the triangles indicates the intervals for each processor.

ulation of the dipole-dipole interactions (DDI) in both, the MC and the SRK approach. In opposite to the calculations without DDI, the SRK scheme is much faster than the modified MC method in case that the DDI are included (figure 4.13a). The speedup with and without DDI are represented in figure 4.13b.

### 4.3.4 Temperature

A noise term is added to the Landau-Lifshitz equation (section 3.2.1) to obtain the magnetization at finite temperatures. In the MC approach, temperature is implicitly considered (section 3.2.2).

In the parallel approach a quasi-static hysteresis curve under finite temperatures is determined by calculating many loops and a subsequent averaging over the magnetization values at each field point. Figure 4.14a represents the averaged loops at 1 K, 100 K and 300 K. Additionally a single trajectory of the calculation at 300 K is shown. The number of necessary trajectories depends on the temperature. A higher temperature has a higher variance leading to a



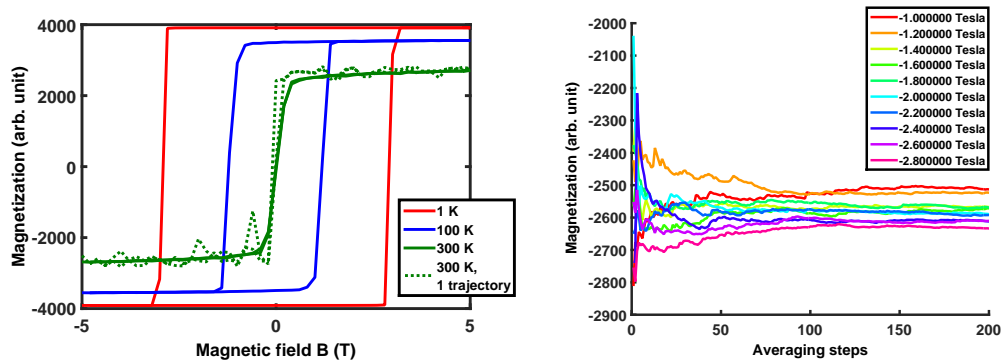
(a) Evolution of necessary computational time for the MC method and the SRK scheme with dipole-dipole interactions at the CoFe layer. (b) Speedup of the hysteresis loop calculation at the CoFe layer with dipole-dipole interactions.

**Figure 4.13:** Parallelization of the hysteresis loop calculation including dipole-dipole interactions.

higher number of necessary trajectories to get a smooth hysteresis loop. Figure 4.14b illustrates the evolution of the average magnetization for distinct field values at 300 K. An average value is reached at approximately 200 runs, which is the number of trajectories used to calculate the hysteresis loops in figure 4.14a.

### 4.3.5 Limitations of the method

The introduced method is applicable to single domain structures with a rigid magnetization to obtain quasi-static hysteresis loops. By the application of this algorithm, the history has still to be taken into account. As it is not complied with a serial calculation of depended states, the history has to be reflected by the initial states. At more complex structures or systems, the necessary branches and the related initial conditions cannot be easily obtained. In some cases, the function of the external field plays a major role to obtain the correct chronological order of the spin states. One example is the magnetization curve determination of the NiFe/IrMn exchange bias stack in section 6.8.2. If the magnetic field is slowly increased by a field ramp, the system moves into a local minimum and is trapped. A sudden field jump, as it occurs at a rectangular



(a) Thermal averaged hysteresis curves different temperatures. The green dashed line represents one trajectory at 1 K. From I. Stockem and C. Schröder, IEEE Trans. Mag., 51, 11, 2015. ©2016 IEEE.

(b) Evolution of the thermal averaged magnetization for different field values at 300, K.

**Figure 4.14:** Temperature averaging.

field pulse, leads to a different state. This state is energetically favored, but not accessible by slowly increasing fields. Thus, the parallel approach would fail to calculate hysteresis loops.

## 4.4 Concluding words on hysteresis modeling

In this section the fundamental terms regarding hysteresis are explained. Different methods have been introduced to determine hysteresis loops. The influence of the sweep rate and the cone size have been shown exemplarily at a CoFe cylindrical layer. As the serial calculation of quasi-static hysteresis loops might be very time consuming, an approach has been developed, that accelerates the calculation by parallelization. This approach has been introduced on the basis of the CoFe example as well.

A comparison with the measured results in [43, 44] and [46] implies a much lower anisotropy value of the CoFe layer. The deviation is too high to be reasoned by a wrong assumption of the CoFe layer thickness. But two other rea-

sons seem to be valid. The first one is that the dipole-dipole interactions have been neglected. From [47] it can be seen, that the energy of the dipole-dipole interactions is of the same magnitude as the magnetocrystalline anisotropy. The second one concerns the assumed structure of the layers. The assumed magnetocrystalline anisotropy is related to an ordered bcc lattice. In [44] a  $\text{Co}_{20}\text{Fe}_{60}\text{B}_{20}$  layer is prepared, at which the B atoms are transported to the CoFe(B)-Ta interface. As the fraction of the Fe atoms is higher than those of Co, the remaining Fe and Co atoms are disordered on the bcc lattice. The magnetic properties of the Ta/CoFe(B)/MgO/CoFe(B)/Ta system could be either calculated with an effective uniaxial anisotropy, that includes the dipole-dipole interactions or by considering the dipole-dipole interactions separately within the method proposed in the former section. The Ta/CoFe(B)/MgO/CoFe(B)/Ta system has not been further investigated within this thesis.





## Chapter 5

# Exchange Bias: Theory and Modeling

The term exchange bias describes a unidirectional anisotropy related to the interfacial interaction between a ferromagnetic and an antiferromagnetic material. It leads to a displacement of the hysteresis loop along the field axis. The effect was found at oxidized cobalt particles by W. H. Meiklejohn and C. P. Bean in 1956 [49]. Today the exchange bias effect is used in the memory technology to pin the magnetization of a reference layer, while the magnetization of a free layer is reversed by applying an external magnetic field (figure 5.1) [50].

In this specific application, the spins of the antiferromagnetic pinning layer are assumed to be rigid and fixed. The hysteresis loop of the pinned layer is shifted in one predefined direction along the field axis via an interfacial coupling between both layers. In other applications, the pinning layer is not totally fixed and the spins might be reversed by a high magnetic external field.

During the last decades after the discovery of the exchange bias effect several models have been proposed to explain the observed phenomena related to exchange bias [51, 52, 53, 54, 55]. Until now, no model exists that scopes all the observed phenomena at different kinds of materials, structures and their related interfaces. Each model is based on assumptions suitable for a particular group of materials or applications. The first model developed by Meiklejohn and Bean comes along with a very intuitive picture explaining some of the exchange bias phenomena qualitatively on the basis of a two layer

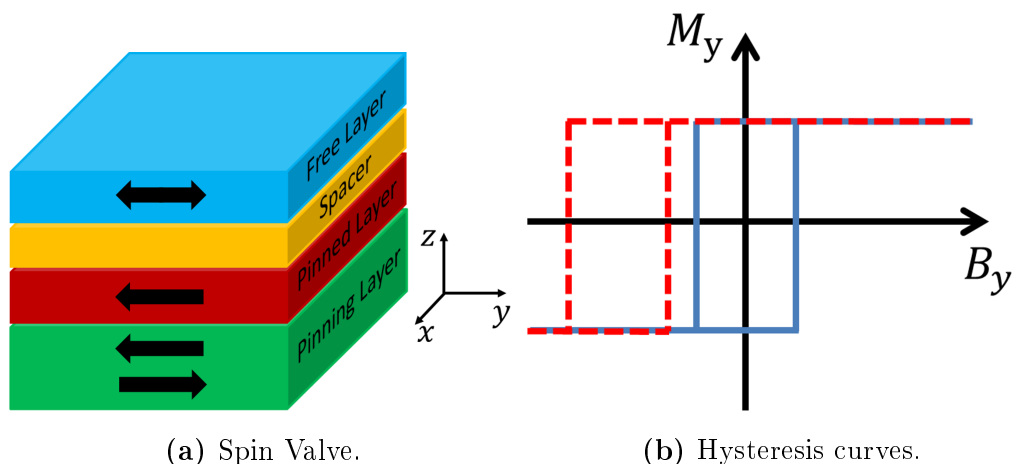


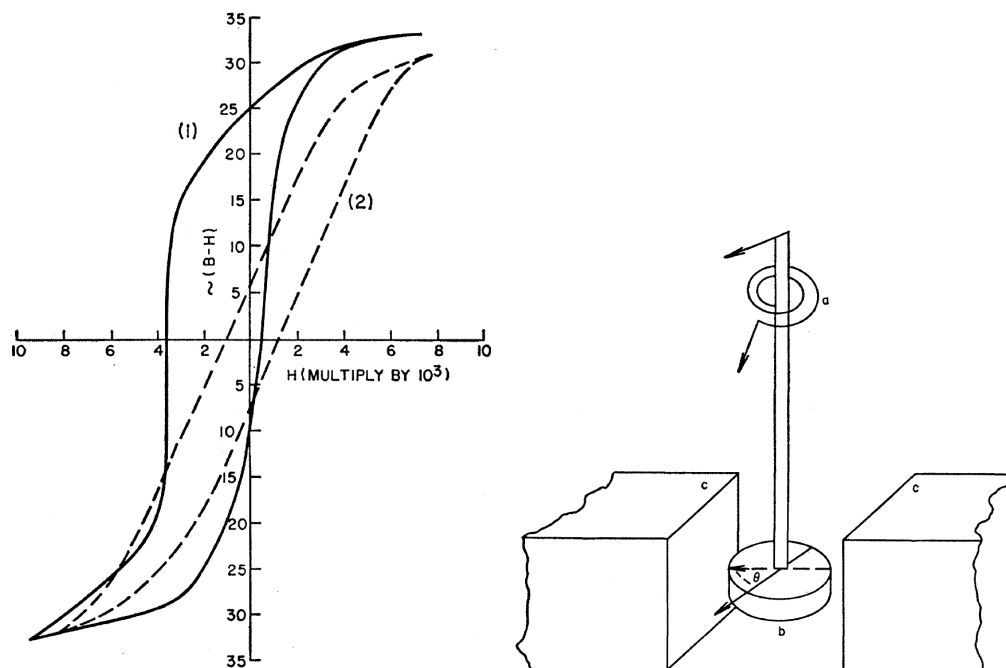
**Figure 5.1:** Representations of a spin valve and the related hysteresis curves of the free layer (blue curve) and the pinned layer (red, dashed curve).

ferromagnetic-antiferromagnetic stack [56]. But this model is based on assumptions like a coherent magnetization, which are not applicable to many systems. One example are systems that show a spring-like magnetic behavior (cf. section 5.3.3). A one dimensional chain model is introduced in section 5.2.2, which expands the degrees of freedom for the magnetization compared to the Meiklejohn-Bean model. In section 5.2.2 it is used to illustrate a spin reversal of the antiferromagnetic layer like it is observed at the Pt/Co/Cr<sub>2</sub>O<sub>3</sub>/Pt exchange bias system (cf. chapter 7). Additionally, some of the most relevant models, supporting the nowadays theoretical understanding of the exchange bias, are shortly introduced in section 5.2.3. At the end of this chapter four application related categories of exchange bias stacks are introduced.

## 5.1 Discovery of the exchange bias effect

In 1956 Meiklejohn and Bean reported the phenomena of exchange bias for the first time [49, 56]. After cooling oxidized Co particles in an applied magnetic field, they observed a shift of the hysteresis loop along the field axis. The magnetization curves of the Co particles with and without an applied field during the cooling process are shown in figure 5.2a from [56]. The displacement of the loop did not occur at particles in mercury, which prevents oxidation. Thus, the

shift have been considered as an interfacial effect between the ferromagnetic Co core and the antiferromagnetic oxide coating.



(a) Magnetization curves of the oxidized Co particles with (solid line) and without (dashed line) an external field during the cooling process.

(b) The torque magnetometer consists of a spring (a) which is mounted on the sample (b). The sample is surrounded by an electromagnet (c) inducing a magnetic field.

**Figure 5.2:** Magnetization loop and schematic representation of the torque magnetometer. Reprinted figures with permission from W. H. Meiklejohn and C. P. Bean, *Phys. Rev.*, 105, 904, 1957. Copyright 2016 by the American Physical Society.

Furthermore, Meiklejohn and Bean compared the torque curves of non-oxidized and oxidized Co particles. They used a self-made torque magnetometer illustrated in figure 5.2b. A spherical sample of non-oxidized Co particles, whose magnetization is aligned by an applied field during the cooling process, exhibits a uniaxial anisotropy with two stable energy minima. Such a spherical sample is placed in a magnetic field generated by the surrounding electromagnet. The

field and the easy axis of the uniaxial anisotropy are in an angle  $\theta$  to each other. Thus, a torque is acting on the rotatable sample trying to align the anisotropy axis of the particles with the external field. This torque is balanced by a spring mounted on the Co sample. The torque of the field acting on the Co particles can now be determined by the deflection of the spring. The torque curve, i.e. the torque as a function of  $\theta$ , of the non-oxidized Co particles is a sinusoidal curve with a period of  $\pi$  as illustrated in figure 5.3a.

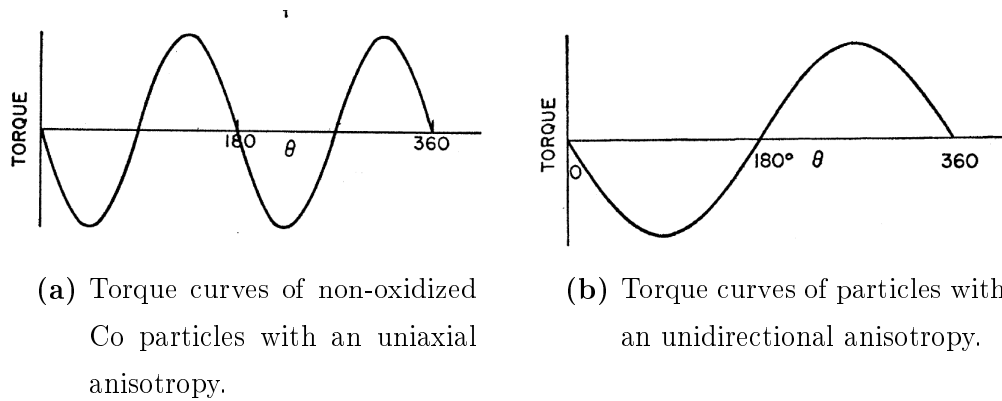


**Figure 5.3:** Schematic torque curves. Reprinted figures with permission from W. H. Meiklejohn and C. P. Bean, *Phys. Rev.*, 105, 904, 1957. Copyright 2016 by the American Physical Society.

The torque is given by equation 5.1.  $K_a$  denotes the magnetocrystalline anisotropy of the Co particles.

$$T = -K_a \sin(2\theta) \quad (5.1)$$

Due to the relation  $E = -\int T d\theta$  the energy term of the anisotropy is described by equation 5.2.  $K_0$  is a constant of integration.

$$E = K_a \sin^2(\theta) + K_0 \quad (5.2)$$

The torque curve of the oxide coated particles is also a sinusoidal function, but it exhibits a period of  $2\pi$  (figure 5.3b, 5.4). Taking the integral over the angle leads to an energy term describing the unknown anisotropy (equations 5.3 and 5.4).

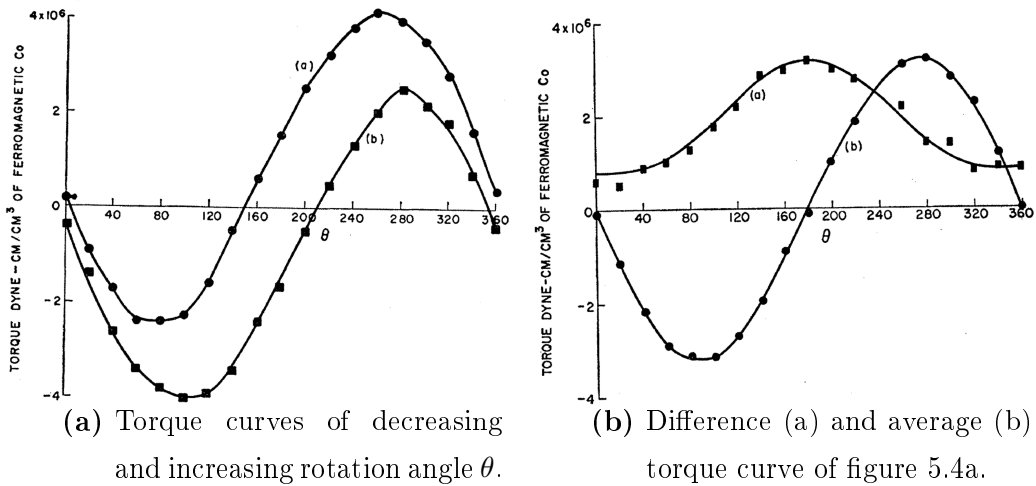


**Figure 5.4:** Measured torque curves. Reprinted figures with permission from W. H. Meiklejohn and C. P. Bean, *Phys. Rev.*, 105, 904, 1957. Copyright 2016 by the American Physical Society.

$$T = -K_u \sin(\theta) \quad (5.3)$$

$$E = \int K_u \sin(\theta) = -K_u \cos(\theta) + K_0 \quad (5.4)$$

The conditions for local minima,  $\frac{\partial E}{\partial \theta} = 0$  and  $\frac{\partial^2 E}{\partial \theta^2} > 0$ , acquire only one stable minimum at  $\theta = 0$  for the energy of the oxidized cobalt particles. Due to the fact that the magnetization tends to align with the field in only one direction, this kind of anisotropy is described as unidirectional anisotropy.

Meiklejohn and Bean showed that such a unidirectional anisotropy leads to a shift of the hysteresis loop by comparing the coercive fields of the non-oxidized and the oxidized Co–CoO system. The coercive field of the non-oxidized particles can be derived from the energy term per unit volume of the ferromagnetic layer, i.e. the sum of the anisotropy term (5.2) and the Zeeman term, which reflects the influence of the magnetic field. The spherical Co particles can be assumed as a single Stoner-Wohlfarth particle (cf. section 3.1.1). In case that the external field is applied along the related easy axis, the total energy per unit volume can be determined by equation 5.5. The angle

between the magnetization direction and the easy axes is denoted by  $\alpha$ . The saturation magnetization of the ferromagnetic material per volume is indicated by  $M_s$ .

$$\mathcal{H} = K_a \sin^2(\alpha) - \mu_0 H M_s \cos(\alpha) \quad (5.5)$$

This equates the Hamiltonian of the Stoner-Wohlfarth model. Thus, the solutions  $\alpha = \pm n\pi$  with  $n = 0, 1$  describe the two local energy minima of the Co atoms. The magnetic state of the material depends on the magnitude of the external field  $\mu_0 H$  and its history. If the magnetization and the field are initially in an antiparallel alignment, an external field that equals the coercivity of  $\mu_0 H_c = \frac{2K_a}{M_s}$  will reverse the magnetization.

The oxidized Co particles show a torque curve, which is proportional to  $\sin(\theta)$ . An integration over  $\theta$  leads to a function of the energy that is proportional to  $\cos(\theta)$  (equation 5.3). This function is added to the energy term given in equation 5.5 to deduce the Hamiltonian of the Co/CoO sample (equation 5.6).

$$\mathcal{H} = K_a - K_a \cos^2(\alpha) - \mu_0 H M_s \cos(\alpha) - K_u \cos(\alpha) + K_0 \quad (5.6)$$

To identify the coercive fields and the loop shift of the Co/CoO sample, the energy minimizing values of  $\theta$  and related fields are calculated analogously to equation 3.6 and equation 3.8 in section 3.1.1.

$$\begin{aligned} \frac{d\mathcal{H}}{d\alpha} &= 2K_a \cos(\alpha) \sin(\alpha) + \mu_0 H M_s \sin(\alpha) + K_u \sin(\alpha) \stackrel{!}{=} 0 \quad (5.7) \\ \Rightarrow \alpha_0 &= \begin{cases} \arccos\left(-\frac{\mu_0 H M_s + K_u}{2K_a}\right) \\ \pm n\pi \end{cases} \end{aligned}$$

These solutions are the extrema of the Hamiltonian. The energy minimizing spin states and the corresponding field ranges are determined by equation 5.8. The anisotropy constants and the magnetization are assumed to be greater than zero.

$$\frac{d^2\mathcal{H}}{d\alpha^2}\Big|_{\alpha_0} = 2K_a \cos^2(\alpha) - 2K_a \sin^2(\alpha) + \mu_0 H M_s \cos(\alpha) + K_u \cos(\alpha)\Big|_{\alpha_0} \stackrel{!}{>} 0 \quad (5.8)$$

$$\Rightarrow \alpha_0 = \begin{cases} \pi + 2\pi n & \text{if } \mu_0 H < \frac{2K_a - K_u}{M_s} \\ 2\pi n & \text{if } \mu_0 H > -\frac{2K_a + K_u}{M_s} \\ \arccos\left(-\frac{\mu_0 H M_s + K_u}{2K_a}\right) & \text{if } \mu_0 H < -\frac{2K_a + K_u}{M_s} \\ & \vee \mu_0 H > \frac{2K_a - K_u}{M_s} \end{cases}$$

with  $n = 0, 1, 2, \dots$

The third solution leads to complex values and is neglected.

A comparison of the energy minimizing field ranges for the Co particles and the Co/CoO sample (equation 5.8 and equation 3.8) shows the shift of the hysteresis loop by a biasing field  $\mu_0 H_{EB} = -\frac{K_u}{M_s}$ .

Meiklejohn and Bean discovered the exchange bias effect, studied the torque curve and explained the shift by a unidirectional anisotropy. In a next step they proposed a model in which the unidirectional anisotropy arises from an exchange interaction of the interfacial spins of two layer system. Among others, this model is described within the following section.

## 5.2 Exchange bias models

A proper exchange bias model should explain the effects measured in the experiments. Kiwi has specified the most important requirements of a theoretical description of the exchange bias effect in [54]. A selection of these requirements, which are relevant for the model development within this thesis, is given here: The proper model should describe the shift of the hysteresis loop qualitatively and quantitatively. It should include geometrical aspects like interface roughness, defects or different thickness of the layers. It should explain the training effect, i.e. the decrease of the exchange bias field at repeating the field cycles. Furthermore the model should be able to forecast the exchange bias at different temperatures. With a view to section 5.3 the model should reflect all categories depending on the geometry and material of the layers or composites.

Until now no model exist, which explains all effects measured at different materials and structures. Instead of one proper model, many different models have been proposed during the last sixty years. Each model explains a part of the measured data for a particular material group or application. The first model that explains the shift of the hysteresis loop at a layered system qualitatively has been developed by Meiklejohn and Bean.

### 5.2.1 Meiklejohn-Bean model

The Meiklejohn-Bean (MB) model [49, 56] is based on the torque measurements of the oxidized Co particles described in the previous section 5.1. As the displacement of the hysteresis loop does only occur, if an antiferromagnetic oxide surrounds the Co sample, the exchange bias is thought to be an interfacial effect. Therefore the MB model consists of two interfacially coupled layers. These layers and the corresponding parameters of the MB model are schematically drawn in figure 5.5. One layer represents the ferromagnetic Co core and the other layer represents the antiferromagnetic CoO shell. Furthermore the layers are assumed to be rigid, meaning that an external magnetic field rotates the spins coherently. The ferromagnetic layer shows a uniaxial anisotropy with an anisotropy constant  $K_{\text{FM}}$  as indicated by the torque curves of non-oxidized Co particles. The saturation magnetization of the ferromag-



netic layer is denoted by  $M_S$ . The spins of the antiferromagnetic layer exhibit a uniaxial anisotropy with the anisotropy constant  $K_{\text{AFM}}$  as well. Both layers share a common easy axis, which is indicated by the double-headed arrows in figure 5.5. In this section the anisotropy constant and the magnetization are given per unit length, while the constants within the former section are effective quantities of the Co and the Co–CoO samples.

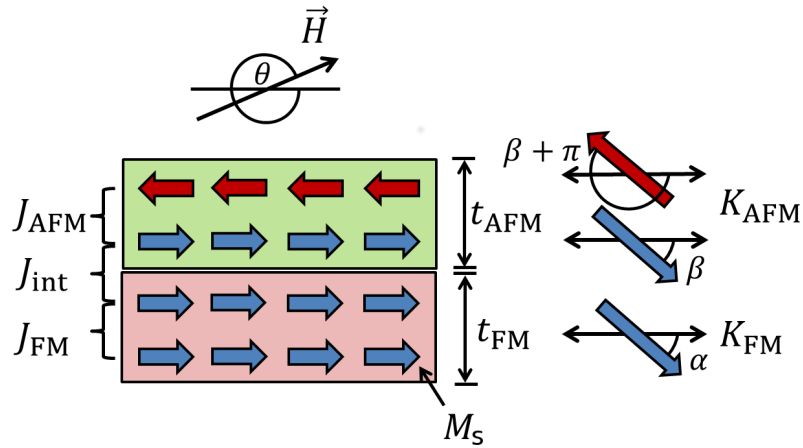


**Figure 5.5:** Schematic drawing of the ferromagnetic (reddish highlighted) and the antiferromagnetic layer (greenish highlighted) of the Meiklejohn-Bean model with the parameters described in the text.

The interfacial interaction, whose exchange constant is denoted by  $J_{\text{eb}}$ , is the key parameter of the MB model. The unidirectional anisotropy of the Co–CoO sample can be measured as soon as the sample is cooled below the Néel temperature of the antiferromagnetic oxide. The ferromagnetic spins align with a constant magnetic field applied during the temperature decrease. Due to the interfacial exchange interaction, the spins of the oxide are coherently aligned into a collinear order with respect to the magnetic structure of the ferromagnetic layer during the cooling process. The interfacial interaction is the origin of the hysteresis loop shift. If the antiferromagnetic layer exhibits a large anisotropy, the torque caused by the ferromagnetic layer cannot reverse the magnetic moments of the antiferromagnetic layer. The magnetization of the ferromagnetic layer is pinned to the spins of the antiferromagnetic surface by the interfacial interaction, which results into a shift of the hysteresis loop.

If the sample is cooled without applying an external field, the exchange interaction does still exist, but a shift of the hysteresis loop cannot be measured (cf. figure 5.2a). Without the cooling field the Co particles are randomly orientated in the sample and thus, there is no common alignment of the spins at the interface. This case is not covered within the MB model, as the layers are assumed to be in a single-domain state.

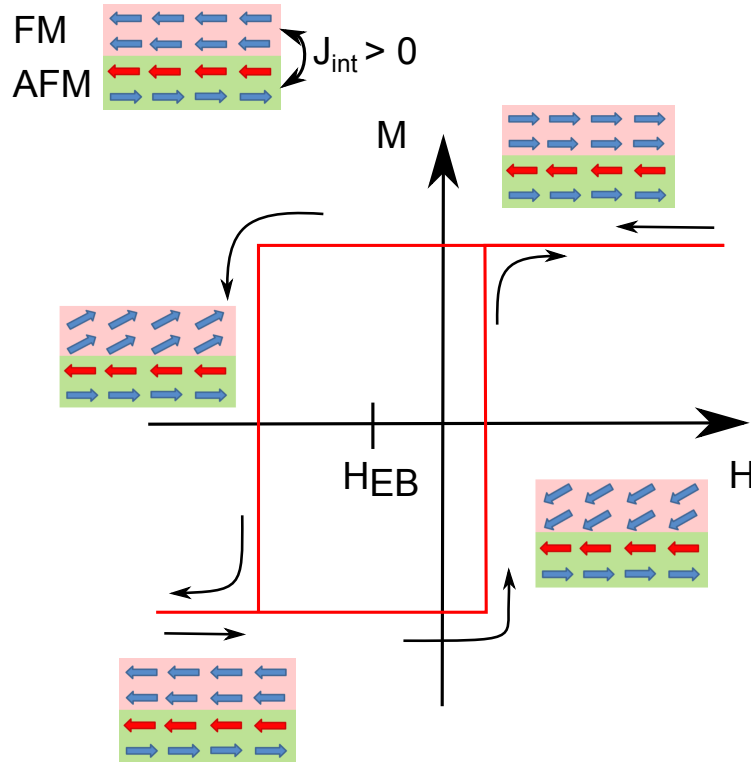


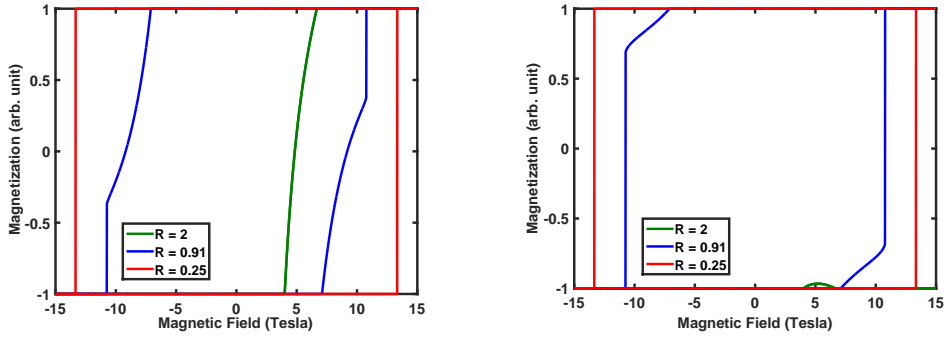
**Figure 5.6:** Schematic representation of the hysteresis loop of a bilayer system related to the Meiklejohn-Bean model.

The MB model explains the shift of the hysteresis loop phenomenologically. Figure 5.6 depicts the magnetization curve and the spin orientations during the field cycle. Within the cooling process the interfacial spins of antiferromagnetic material are aligned with the spins of the ferromagnetic material and the external field. According to figure 5.6 and figure 5.5, the easy axis is assumed to be in-plane. Initially, the ferromagnetic coupled spins are orientated against the positive field axis. If the field is increased towards positive values the ferromagnetic layer reverses its magnetization. Decreasing the field again leads to a delayed spin reversal due to the interfacial coupling.

According to the MB model, the energy per unit area of the ferromagnetic-antiferromagnetic layered system is given by equation 5.9 [51]. The angles  $\alpha$ ,  $\beta$  and  $\theta$  are defined in accordance to figure 5.5.

$$\begin{aligned} \mathcal{H} = & -J_{eb} \cos(\alpha - \beta) + K_{FM} t_{FM} \sin^2(\alpha) \\ & + K_{AFM} t_{AFM} \sin^2(\beta) - \mu_0 H M_s t_{FM} \cos(\theta - \alpha) \end{aligned} \quad (5.9)$$

Radu [55] determined the angles, which minimize the energy in dependence of the ratio  $R = \frac{K_{AFM} t_{AFM}}{J_{eb}}$  numerically. He found three regions of the ratio  $R$  showing different shapes of the magnetization curves. Figure 5.7a shows the shapes for  $R = 2$ ,  $R = 0.91$  and  $R = 0.25$  at  $\theta = 0$  and  $K_{FM} = 0$ .



(a) Magnetization curve of the ferromagnetic layer.

(b) Magnetization curve of the sublayers within the antiferromagnetic layer.

**Figure 5.7:** Magnetization curves reflecting three shapes related to the ratio  $R$  of the MB model, cf. [55].

If  $R$  exceeds one, the shift of the hysteresis loop appears. The curve approaches a step function, in case that  $R$  approaches to infinity. For smaller ratios ( $R < 1$ ), a field induced spin reversal of the ferromagnetic layer leads to a spin reversal of the antiferromagnetic layer. If  $R < 0.5$  the angles of the magnetization jump from 0 to  $\pi$  and vice versa.

The coercive field  $\mu_0 H_c = \mu_0 \left( \frac{H_c^2 - H_c^1}{2} \right)$  and the exchange bias field  $\mu_0 H_{EB} = \mu_0 \left( \frac{H_c^1 + H_c^2}{2} \right)$  at  $R = 0.25$  to  $R = 10$  are represented in figure 5.8. These curves are similar to those in [55].

The coercive fields and the exchange bias fields are normalized to the exchange bias field  $H_{eb}^\infty$  of a stack with fixed antiferromagnetic spins.

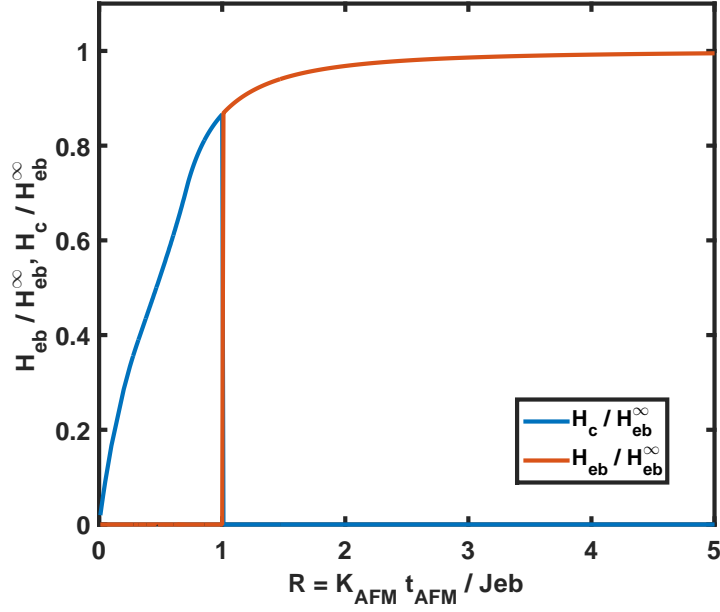


**Figure 5.8:** Exchange bias fields and coercive fields as a function of the ratio  $R$  similar to [55].

The MB model can be further simplified if we assume, that the spins of the antiferromagnetic layer are fixed. This kind of model is called the idealized Meiklejohn-Bean model. At the idealized MB model  $\beta$  becomes a constant and the coercive fields can be easily calculated by determining the first derivatives with respect to  $\alpha$ . The equations 5.11 and 5.12 are reflecting the case with  $\beta = \theta = 0$ .

$$\begin{aligned} \mathcal{H} = & -J_{eb} \cos(\alpha) + K_{FM} t_{FM} \sin^2(\alpha) \\ & - \mu_0 H M_s t_{FM} \cos(\alpha) \end{aligned} \quad (5.10)$$

$$\begin{aligned}
\frac{d\mathcal{H}}{d\alpha} &= +J_{\text{eb}} \sin(\alpha) + 2K_{\text{FM}}t_{\text{FM}} \cos(\alpha) \sin(\alpha) \\
&+ \mu_0 H M_s t_{\text{FM}} \sin(\alpha) \stackrel{!}{=} 0 \\
\Rightarrow \alpha_0 &= \begin{cases} \arccos\left(-\frac{\mu_0 H M_s t_{\text{FM}} - J_{\text{eb}}}{2K_{\text{FM}}t_{\text{FM}}}\right) \\ \pm n\pi \end{cases}
\end{aligned} \tag{5.11}$$

$$\begin{aligned}
\frac{d^2\mathcal{H}}{d\alpha^2}\Big|_{\alpha_0} &= J_{\text{eb}} \cos(\alpha) + 2K_{\text{FM}}t_{\text{FM}} \cos^2(\alpha) \\
&- 2K_{\text{FM}}t_{\text{FM}} \sin^2(\alpha) + \mu_0 H M_s t_{\text{FM}} \cos(\alpha)\Big|_{\alpha_0} \stackrel{!}{>} 0 \\
\Rightarrow \alpha_0 &= \begin{cases} \pi + 2\pi n & \text{if } \mu_0 H < \frac{2K_{\text{FM}}t_{\text{FM}} - J_{\text{eb}}}{M_s t_{\text{FM}}} = \mu_0 H_c^1 \\ 2\pi n & \text{if } \mu_0 H > -\frac{2K_{\text{FM}}t_{\text{FM}} + J_{\text{eb}}}{M_s t_{\text{FM}}} = \mu_0 H_c^2 \\ \arccos\left(-\frac{\mu_0 H M_s t_{\text{FM}} - J_{\text{eb}}}{2K_{\text{FM}}t_{\text{FM}}}\right) & \text{if } \mu_0 H < -\frac{2K_{\text{FM}}t_{\text{FM}} + J_{\text{eb}}}{M_s t_{\text{FM}}} \\ & \vee \mu_0 H > \frac{2K_{\text{FM}}t_{\text{FM}} - J_{\text{eb}}}{M_s t_{\text{FM}}} \end{cases}
\end{aligned} \tag{5.12}$$

with  $n = 0, 1, 2, \dots$

The last solution is not further taken into account, as  $\alpha_0$  is complex within the corresponding field ranges. The calculation is analog to the calculation of the exchange bias field in the former section. Here, the exchange bias field is inverse proportional to the thickness of the ferromagnetic layer (equation 5.13), while the width of the hysteresis loop is independent of this thickness (equation 5.14).

$$\mu_0 H_{\text{eb}} = \mu_0 \left( \frac{H_c^1 + H_c^2}{2} \right) = -\frac{J_{\text{eb}}}{M_s t_{\text{FM}}} \tag{5.13}$$

$$\mu_0 H_c = \mu_0 \left( \frac{H_c^1 - H_c^2}{2} \right) = \frac{2K_{\text{FM}}}{M_s} \tag{5.14}$$

In comparison with experimental values of the loop shift, the exchange bias field  $\mu_0 H_{\text{eb}}$  is much overestimated for an interfacially exchange constant  $J_{\text{eb}}$  having approximately the same value as the exchange coupling constant of the ferromagnetic material  $J_{\text{FM}}$  [51]. In section 5.2.3 other exchange bias models are shortly introduced, which reduce the shift of the hysteresis loop by considering different aspects like interfacial roughness, defects inside the

antiferromagnetic material or domain wall formation. But before, the influence of the antiferromagnetic layer thickness is further studied by a one dimensional chain model within the next section.

## 5.2.2 One dimensional chain model

The one dimensional chain model represents the layers of an exchange bias stack by  $M + N$  spins, which are arranged in a chain-like order. The exchange interactions between the spins are restricted to their next neighbors. The ferromagnetic layer is modeled by  $M$  spins favoring a parallel orientation, while the monolayers of the antiferromagnetic material are modeled by  $N$  spins favoring an antiparallel alignment. The two types of spins are interfacially exchange coupled. The rotation of the spins is assumed to be restricted to a plane. The spin orientations minimize the energy described by the exchange interactions, a uniaxial anisotropy of each spin and the interactions with an external field. Such a chain model is represented in figure 5.9.

In a simple case, all spins prefer the same magnetization direction and the same uniaxial anisotropy constant within each layer. The easy axes are assumed to be aligned with the external field along the chain. Furthermore, only three different exchange constants describe the interactions between the next neighboring atoms. The exchange constants  $J_{\text{FM}}$ ,  $J_{\text{AFM}}$  and  $J_{\text{int}}$  are related to the ferromagnetic layer, the antiferromagnetic layer and to the interfacial interaction, respectively. Furthermore, the effective magnetic moments of each spin within one layer are denoted by  $\mu_{\text{FM}}$  and  $\mu_{\text{AFM}}$ . In this case the Hamiltonian of the one dimensional chain model is given by equation 5.15.

$$\begin{aligned}
\mathcal{H} = & - J_{\text{FM}} \sum_{m=1}^{M-1} \cos(\theta_{m+1}^{\text{FM}} - \theta_m^{\text{FM}}) - J_{\text{int}} \cos(\theta_1^{\text{AFM}} - \theta_M^{\text{FM}}) \\
& - J_{\text{AFM}} \sum_{n=1}^{N-1} \cos(\theta_{n+1}^{\text{AFM}} - \theta_n^{\text{AFM}}) \\
& - D_z^{\text{FM}} \sum_{m=1}^M \cos^2(\theta_m^{\text{FM}}) - D_z^{\text{AFM}} \sum_{n=1}^N \cos^2(\theta_n^{\text{AFM}}) \\
& - \mu_{\text{FM}} B_z \sum_{m=1}^M \cos(\theta_m^{\text{FM}}) - \mu_{\text{AFM}} B_z \sum_{n=1}^N \cos(\theta_n^{\text{AFM}})
\end{aligned} \tag{5.15}$$

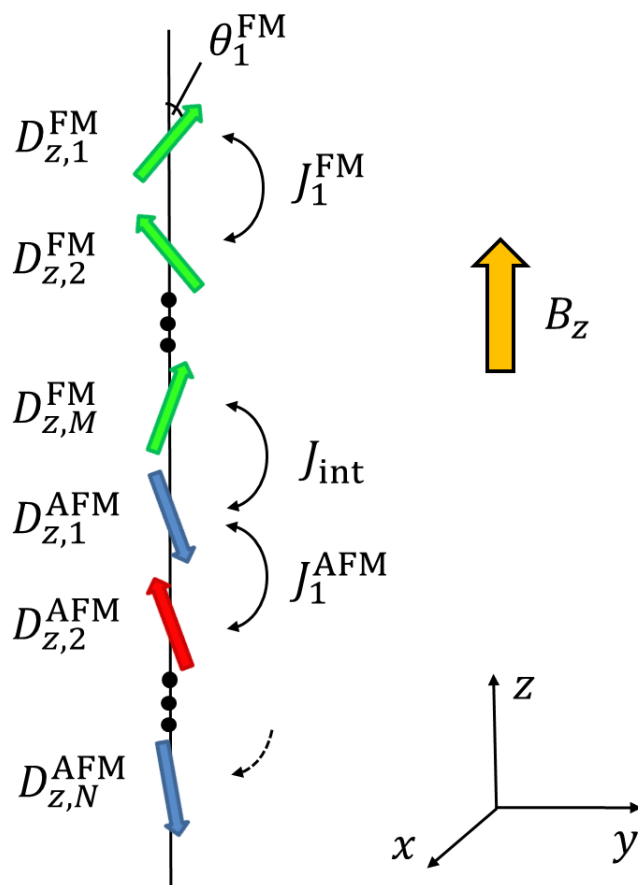


**Figure 5.9:** Schematic representation of the one dimensional chain model.

The one dimensional chain model might be a proper model to represent the exchange bias effect of multilayer systems, as it can be seen as a vertical cross section of a multilayer stack. It does not reflect the lateral dimensions of the layers, as each plane is reflected by no more than a single spin. In the following the one dimensional chain model is used to examine the spin reversal of the antiferromagnetic layer of an exchange bias system exemplarily. In this example the ferromagnetic layer is represented by only one spin, while the antiferromagnetic layer is modeled by  $N$  spins. Thus, equation 5.15 reduced to

$$\begin{aligned} \mathcal{H} = & -J_{\text{int}} \cos(\theta_1^{\text{AFM}} - \theta_1^{\text{FM}}) - J_{\text{AFM}} \sum_{n=1}^{N-1} \cos(\theta_{n+1}^{\text{AFM}} - \theta_n^{\text{AFM}}) \quad (5.16) \\ & - D_z^{\text{FM}} \cos^2(\theta_1^{\text{FM}}) - D_z^{\text{AFM}} \sum_{n=1}^N \cos^2(\theta_n^{\text{AFM}}) \\ & - \mu_{\text{FM}} B_z \cos(\theta_1^{\text{FM}}) - \mu_{\text{AFM}} B_z \sum_{n=1}^N \cos(\theta_n^{\text{AFM}}). \end{aligned}$$

In the subsequent investigation, only these spin states are taken into account, at which the spins are aligned with the anisotropy axis. Furthermore, the next neighboring spins of the antiferromagnetic layer within the considered states point into opposite directions ( $\theta = 0 \vee \theta = \pi$ ). A minimization of equation 5.16 leads to the energy curves represented in figure 5.10. Depending on the number of antiferromagnetic spins  $N$ , two or four different states are determined and shown in figure 5.10. This representation illustrates the thickness dependent spin reversal of an exchange bias stack. At a stack with a very thin antiferromagnetic layer, a magnetization reversal of the ferromagnetic layer forces a spin reversal of the antiferromagnetic coupled spins. The exchange bias field equals zero, although the width of the hysteresis loop is enhanced. As the thickness of the layer is increased, two additional spin states occur. If the system can reach these additional states directly from one of the other states, the antiferromagnetic coupled spins are not completely reversed. This is the case at  $N \geq 6$  at the example illustrated in figure 5.10.

Such a thickness dependence has been observed at the investigation of both exchange bias systems NiFe/IrMn/MgO/Pt and Pt/Co/Cr<sub>2</sub>O<sub>3</sub>/Pt.



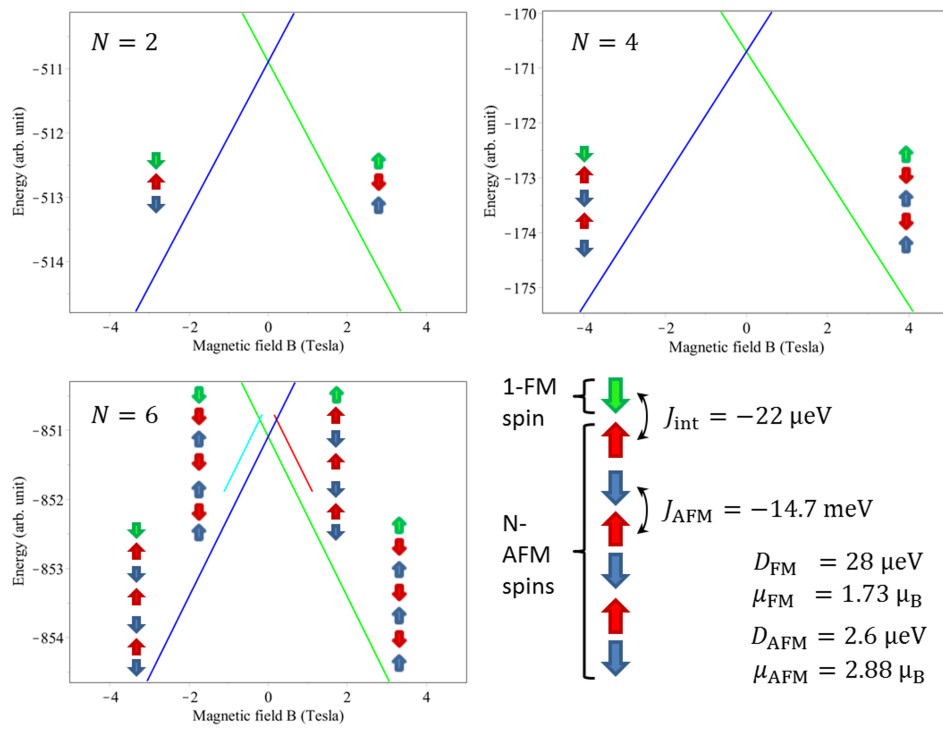


**Figure 5.10:** Energy curves of a chain model with one spin representing the ferromagnetic layer and  $N$  spins representing the antiferromagnetic layer. The energy curves of four different states are drawn.

### 5.2.3 Short Descriptions of other important exchange bias models

A larger amount of models has been proposed during the last decades to reveal most of the exchange bias related effects referring to specific structures [52, 51, 54]. In this thesis only a part of the existing models are introduced, which seem to be milestones within the research of exchange bias systems and which might be relevant for the two closer studied exchange bias stacks Pt/Co/Cr<sub>2</sub>O<sub>3</sub>/Pt and NiFe/IrMn within the next chapters.

#### Mauri model

The model by Mauri and Siegmann has been proposed in 1987 [57], approximately 30 years after the discovery of the exchange bias effect and the development of first theoretical model by Meiklejohn and Bean. Experimental results indicate a much smaller exchange bias constant as it is predicted by the MB model. This contradiction is solved by the Mauri model. The Mauri model is based on the assumption, that a partial domain wall is created inside the antiferromagnetic layer. This domain wall leads to a reduction of the exchange bias field. Even for large exchange coupling constants, the shift of the loop reaches a limiting value given in equation 5.18 at  $\lambda \gg 1$ .

The geometric parameters of the model and the domain wall are illustrated in figure 5.11.

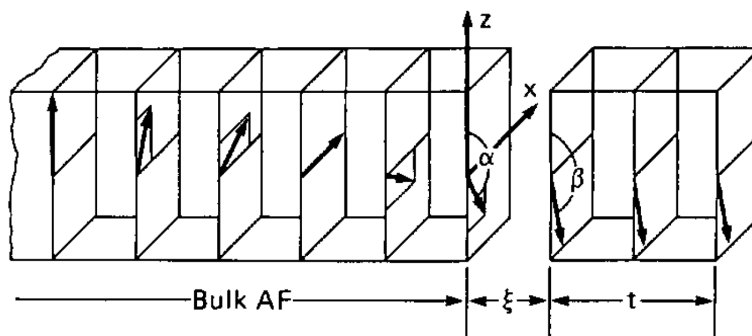


**Figure 5.11:** Schematic representation of the layers within the Mauri model. Reprinted from D. Mauri *et al.*, *J. Appl. Phys.*, 62, 3047, 1987. With the permission of AIP Publishing.

To prohibit a complete spin reversal of the antiferromagnetic layer, this layer

has to be thicker than the width of a  $180^\circ$  domain wall. Thus, the antiferromagnetic layer can be assumed to be infinite. The ferromagnetic layer is rather thin, so that the angle  $\beta$  does not change within the layer. The magnetic moments of both layers exhibit a uniaxial anisotropy along the  $z$ -axis, which is likewise the direction of the applied magnetic field. The bulk antiferromagnetic material and the ferromagnetic layer are both in a single domain state. The Hamiltonian describing the total energy  $E$  of interface within the Mauri model is given by

$$\mathcal{H} = 2\sqrt{AK}(1 - \cos \alpha) + \frac{A_{12}}{\xi}(\alpha - \beta) + K_{\text{Ft}}t \cos \beta + \mu_0 H M_s t (1 - \cos \beta). \quad (5.17)$$

The first term of equation (5.17) is the energy of the partial domain wall which occurs due to the rotation of the spins belonging to the first sublayer by an angle  $\alpha$ .  $A$  and  $K$  are the exchange stiffness and the anisotropy constant of the antiferromagnetic layer, respectively. The second term involves the energy of the interfacial coupling with an interfacial exchange stiffness  $A_{12}$ . The third term contains the energy corresponding to the uniaxial anisotropy of the ferromagnetic layer with the anisotropy constant  $K_{\text{FM}}$ . The influence of the magnetic field  $H$  on the magnetic moments within the ferromagnetic layer is described in the last term, at which  $M_s$  denotes the saturation magnetization. Minimizing this equation with respect to the angles  $\alpha$  and  $\beta$  leads to the magnetization curves represented in figure 5.12.  $\lambda = \frac{A_{12}}{\xi 2\sqrt{AK}}$ ,  $\mu = \frac{K_{\text{Ft}}t}{2\sqrt{AK}}$  and  $\kappa = \frac{\mu_0 H M_s t}{2\sqrt{AK}}$  denote the prefactors of the different energy terms normalized to the energy per area of a  $90^\circ$  domain wall.

In the case that the exchange coupling is low ( $\lambda \ll 1$ ) the hysteresis loop shift equals the calculated value of the idealized MB model. The angle  $\beta$  remains small during a spin reversal and a domain wall is not extended into the antiferromagnetic material. In the opposite case ( $\lambda \gg 1$ ) a  $180^\circ$  domain wall is created inside the antiferromagnetic layer. The exchange bias field does no longer depend on the interfacial exchange stiffness and reaches its limiting value.

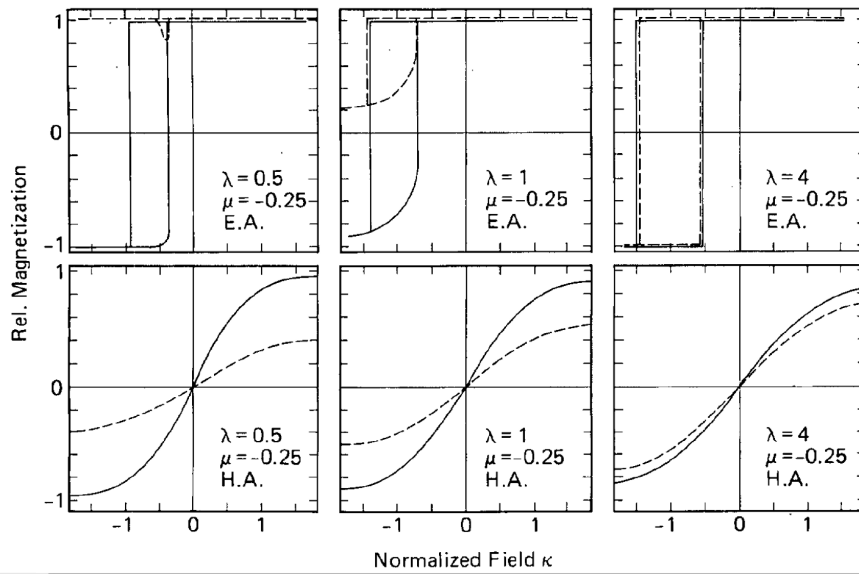


**Figure 5.12:** Characteristic magnetization curves of the Mauri model.

The upper row figures represent the magnetization with an external field applied parallel to the easy axis. In the lower row figures, the field is applied along the hard axis of the anisotropy. The solid lines are related to the magnetization of the ferromagnetic layer and the dashed lines illustrate the magnetization of the uppermost interfacial antiferromagnetic plane. Reprinted from D. Mauri *et al.*, *J. Appl. Phys.*, 62, 3047, 1987. With the permission of AIP Publishing.

The exchange bias fields of both cases are mathematically described in equation 5.18.

$$\mu_0 t H_{\text{eb}} = \begin{cases} -\frac{A_{12}}{\xi M_s} & \text{if } \lambda \ll 1 \\ -2 \left( \frac{\sqrt{AK}}{M_s} \right) & \text{if } \lambda \gg 1. \end{cases} \quad (5.18)$$

If a domain wall is created, the magnetization curves will exhibit rounded edges as it is shown in the first and the second graphic of figure 5.12. In the region of the edges, the magnetization is reversible, while the magnetization after jump, as represented in the third graphic, is irreversible. Furthermore, it can be seen from figure 5.12, that the creation of a domain wall leads to a decrease of the coercivity, i.e. the width of the hysteresis loop.

In anticipation of chapter 7, a creation of a domain wall inside the antiferromagnetic layer of the Co/Cr<sub>2</sub>O<sub>3</sub> is also observed by atomistic spin dynamics simulations and the related magnetization loops exhibit round shapes and a reduced loop width.

### Random field model

Within the Mauri model, the influence of rough interfaces or defects has not been taken into account. This structural disorder affects the exchange bias shift and leads to the formation of domain walls within the random field model proposed by Malozemoff 1987 [58].

As a starting point, Malozemoff supposed the movement of a domain wall within the ferromagnetic layer by an in-plane magnetic field as illustrated in figure 5.13.

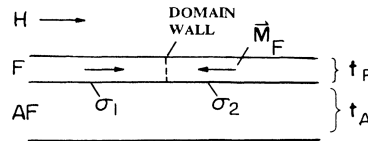


**Figure 5.13:** Movement of a domain wall by an applied magnetic field. Reprinted figure with permission from A. P. Malozemoff, Phys. Rev. B, 35, 3679, 1987. Copyright 2016 by the American Physical Society.

Depending on the surface structure of the antiferromagnetic layer, the interfacial energies  $\sigma_1$  and  $\sigma_2$  might differ at both sides of the domain wall. The difference  $\Delta = \sigma_2 - \sigma_1$  causes the exchange bias field

$$\mu_0 H_{\text{EB}} = \frac{\Delta}{2M_{\text{F}}t_{\text{F}}}, \quad (5.19)$$

at which  $M_{\text{F}}$  and  $t_{\text{F}}$  are the magnetization and the thickness of the ferromagnetic layer. Figure 5.14 presents the energies of different interfaces. A ferromagnetic spin reversal at a stack with a fully uncompensated interface might cause a domain wall inside the antiferromagnetic layer to reduce the energy (figure 5.14(b)-(d)).

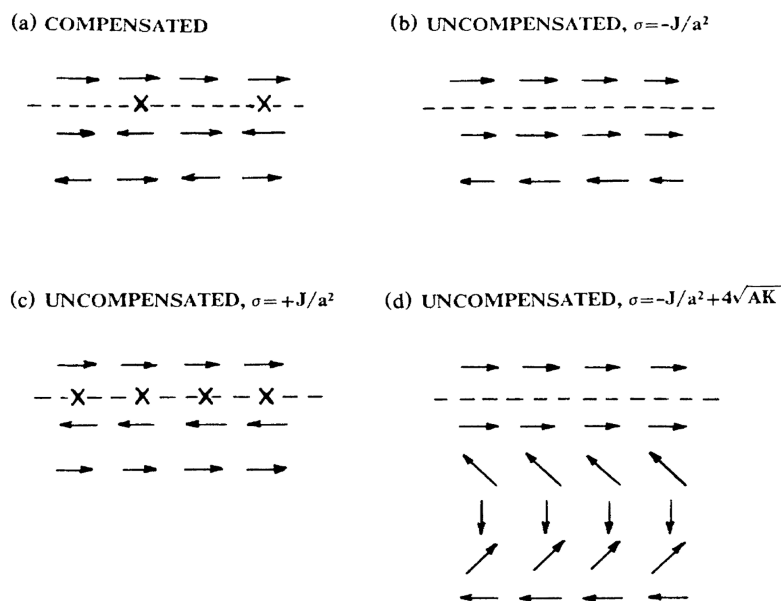


**Figure 5.14:** Side view of possible spin states. The interfacial spins of the antiferromagnetic layer (lower arrows) are coupled with the spins of the ferromagnetic (upper arrows) layer. The unfavorable spin state (c) might be avoided by the creation of a domain wall (d). Reprinted figure with permission from A. P. Malozemoff, Phys. Rev. B, 35, 3679, 1987. Copyright 2016 by the American Physical Society.

The model by Malozemoff is based on random fields that are caused, for example, by interfacial roughness. The roughness induces steps of the material surfaces as represented in figure 5.15, which change the net magnetization and the interfacial energy.

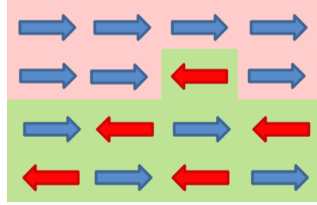


**Figure 5.15:** Schematic representation of interface roughness.

Each interface irregularity causes a local energy difference of  $\pm 2zJ$ , at which  $z$  is a number of order unity and  $J$  is the exchange constant between atoms near the interface. The total energy difference of the interface might be reduced by the formation of domain walls within the antiferromagnetic layer during the cooling process [59]. At this process the temperature is decreased from above Néel temperature to a temperature at which at least the bulk antiferromagnetic spins remain fixed despite the spin reversal of the ferromagnetic spins. As the appearance of interfacial irregularities, which might result from interfacial roughness, is random, the interfacial energy can be described by statistical methods. By minimizing the total interfacial energy, Malozemoff determined the exchange bias field

$$\mu_0 H_{\text{EB}} = \frac{2z\sqrt{AK}}{\pi^2 M_{\text{F}} t_{\text{F}}}. \quad (5.20)$$

The exchange bias field has the same structure as it is found within the Mauri model. Both models assume the creation of domain walls, whereas the origin of the walls is different. Compared to the Mauri model, the domain walls are created at imperfect or rough interfaces, while the interface within the Mauri model is assumed to be fully uncompensated. The random field model fails to explain the exchange bias at fully compensated interfaces.

### **Koon's model of compensated antiferromagnetic surfaces**

Koon introduces in 1997 a model concerning the exchange bias effect at ferromagnetic/antiferromagnetic stacks with fully compensated interfaces [60]. The

model is also called *spin flop* model, as the spins of the ferromagnetic and the antiferromagnetic layer prefer a perpendicular orientation to each other. This is comparable to the spin flop state of an antiferromagnetic material in a high magnetic field (cf. 7.3.2).

Koon exchange bias description is based on a micromagnetic model, at which each layer is represented by 15 monolayers with a simple body centered tetragonal magnetic structure as represented in figure 5.16. The antiferromagnetic layer exhibits a uniaxial anisotropy axis.

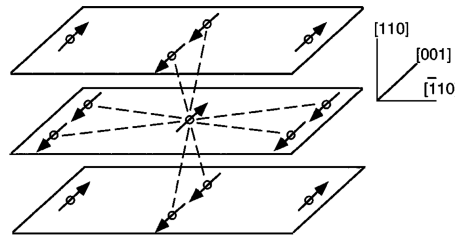


**Figure 5.16:** Representation of the tetragonal structure within Koon's model. Only the antiferromagnetic monolayers with the related spins are illustrated. Reprinted figure with permission from N. C. Koon, Phys. Rev. Lett., 78, 4865, 1996. Copyright 2016 by the American Physical Society.

He applies a relaxation method to identify the preferred spin orientation at which the spins of the outer monolayers are initially aligned along the easy axis of the antiferromagnetic layer. The inner spins are randomly orientated before the relaxation. In case of a frustrated interface, the lowest energy is obtained at  $90^\circ$  between the orientation of the spins at the interfacial ferromagnetic and antiferromagnetic layer. Furthermore, a spin canting is observed within the inner antiferromagnetic monolayers as illustrated in figure 5.17. An antiferromagnetic coupling across the interface induces a spin canting away from the magnetization direction of the ferromagnetic layer, whereas an interfacial ferromagnetic coupling forces a spin canting towards the direction of the ferromagnetic spins.

Koon supposed, that the unidirectional anisotropy of the exchange bias stack is related to the creation of an antiferromagnetic domain wall during the ferromagnetic spin reversal. He obtained this suggestion from the calculation of



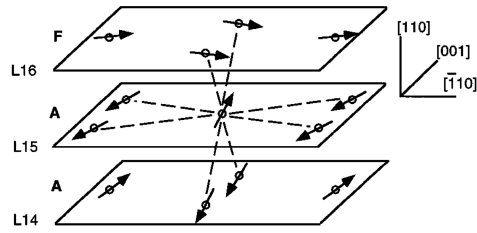


**Figure 5.17:** Spin orientation near the interface. At the lowest energy state, the spins of the lowermost ferromagnetic monolayer and the spins of the uppermost antiferromagnetic monolayer are perpendicular aligned. Reprinted figure with permission from N. C. Koon, Phys. Rev. Lett., 78, 4865, 1996. Copyright 2016 by the American Physical Society.

the energy at fixed angles between ferromagnetic magnetization direction and the antiferromagnetic easy axis. The spin structure of a former angle has been used as initial configuration of the subsequent energy calculation at a slightly increased or decreased angle. At the starting angle of  $90^\circ$  the minimum occurs as evaluated by the relaxation before. The resulting energy curves at different thicknesses of the antiferromagnetic layer are represented in figure 5.18 from [60]. If the spins states at high positive and high negative in-plane magnetic fields are equal, a second energy minimum should occur at  $270^\circ$ . This is true for thin antiferromagnetic layers, which are thinner than the theoretical domain wall width of  $w \propto \sqrt{4J/K_u}$ , which is approximately 9 monolayers in Koon's exemplary calculation.  $K_u$  and  $J$  are the uniaxial anisotropy constant and the exchange constant of the antiferromagnetic layer, respectively. At thicker layers, the spins reach a high energy meta-stable state. A transition to the low energy state appears after reaching a critical angle depending on the antiferromagnetic layer thickness. As this angle is more dependent on the interfacial interaction than on the external field, the unidirectional anisotropy might appear due to these two energy states. Thus, the perpendicular orientation of the spins and the unidirectional shift of the hysteresis loop at exchange bias systems with a compensated interface seem to be explainable by Koon's model.

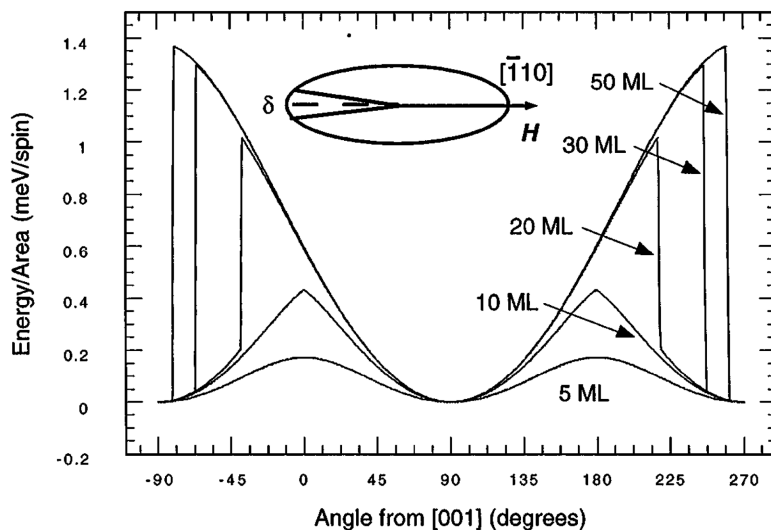


**Figure 5.18:** Energy per unit area as a function of the angle between the spins at the interface within Koon's model. Different layer thicknesses have been considered. Reprinted figure with permission from N. C. Koon, *Phys. Rev. Lett.*, 78, 4865, 1996. Copyright 2016 by the American Physical Society.

Later Schulthess and Butler [61] proved that this is not true for the hysteresis loop shift as Koon's considerations are based on the restriction, that the magnetization could only rotate in-plane. The details are described within the next section.

### Generalized random interface models

Schulthess and Butler investigate also the exchange bias at stacks with compensated interfaces [61, 62]. They used an extended classical Heisenberg model to study the spin structure during a magnetic field cycle. The model involves the Zeeman term, the exchange interactions within and between the antiferromagnetic and the ferromagnetic layer, the uniaxial anisotropies of both layers and the dipole-dipole interaction. In comparison to the model of Koon in section 5.2.3, the motion of spins is not restricted to be in-plane. The dipole-dipole interaction assures a preferred in-plane orientation of the ferromagnetic spins and thus the restriction within Koon's model becomes obsolete in this generalized random interface model.

By solving the Landau-Lifshitz equation of motion (cf. 3.2), the authors of [61] have shown that no domain wall is created inside the antiferromagnetic layer by a spin reversal as assumed by Koon. By allowing an out-of-plane magnetic component, the spins are flipped between the two degenerated spin states as shown in figure 5.19. The resulting hysteresis curve has an irreversible magnetization, but is symmetric to the vertical axis. Thus, a uniaxial anisotropy is induced which leads to an enhancement of the coercivity, but a horizontal shift of the hysteresis loop does not occur.

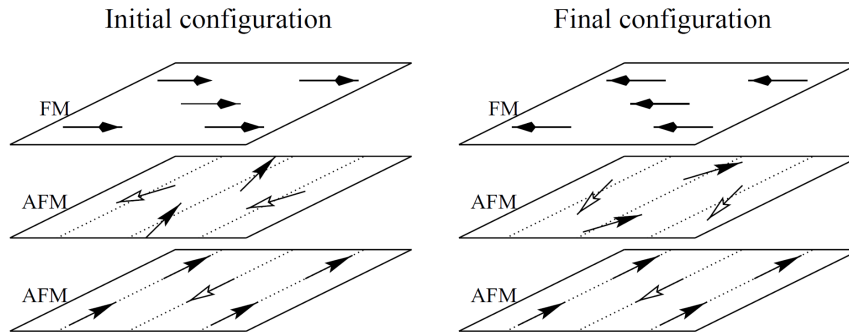


**Figure 5.19:** Schematic illustration of initial spin flop state and the final spin-flop states. Reprinted figure with permission from T. C. Schulthess and W. H. Butler, *Phys. Rev. Lett.*, 81, 4516, 1998. Copyright 2016 by the American Physical Society.

To generate a unidirectional anisotropy Schulthess and Butler combine Koons model and the model of Malozemoff described in section 5.2.3. To be more specific: They introduced defects at the interface in the sense of Malozemoff's model. This interface roughness leads to an asymmetry between the initial and the final configurations, which is a prerequisite for Koon's model. Hence the shift of the hysteresis loop is derived from Koon's model.

In conclusion, Koon's spin flop model and Malozemoff's random field model are not in contradiction to each other, but rather the combination of both models is necessary to explain important effects related to exchange bias at stacks with compensated interfaces.

### Frozen interface model

Koon's model of exchange bias at stacks with fully compensated interfaces [60] does not lead to a shift of the hysteresis loop as shown by Schulthess and Butler [61]. The frozen interface model by Kiwi [63, 64] is based on Koon's model, but the symmetry of the lowest energy states is broken by freezing the canted spins at the interface. The freezing occurs during the cooling process. A high magnetic field forces the spins at the antiferromagnetic part of the interface to rearrange into a meta-stable state. This meta-stable state exhibits a perpendicular alignment between the ferromagnetic magnetization and the easy axis of the antiferromagnetic layer. A canting occurs like it is describe within Koon's model. By clamping a fraction of the canted spins, the magnetic state of the antiferromagnetic layer does not change during a field cycle. Instead of a domain wall within the antiferromagnetic layer, an interfacial domain wall is created within the ferromagnetic layer. In this model the exchange bias field depends on the number of clamped spins and the cooling field.

### Domain state model

In the Mauri model [57], the random interface model [58] and in the generalized interface model [62], domain walls are assumed to occur at the interface of the exchange bias stack. In the domain state model by Nowak *et al.* [65] magnetic domains and thus domain walls are formed within the volume of the antiferromagnetic layer. In Nowak's model the domains are caused by dilution of the antiferromagnetic layer, i.e. by replacing magnetic atoms with non-magnetic atoms inside the antiferromagnetic material. Such domains are studied previously by Imry and Ma [59] with Ising models [66]. Nowak *et al.* combined an Ising model to represent the energy terms of the antiferromagnetic layer with a classical Heisenberg model representing the energy terms of the ferromagnetic layer. The diluted antiferromagnetic layer and a single ferromagnetic layer are sketched in figure 5.20.

Nowak *et al.* obtained the formation of domains during field cooling and the hysteresis loops at low temperatures by applying a Monte Carlo method with a heat bath coupling. Without an external field during the cooling process, no exchange bias is observed. The application of an external field at decreas-

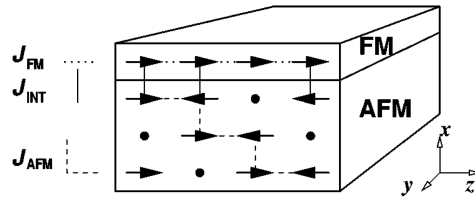


**Figure 5.20:** Domain state model. Reprinted figure with permission from U. Nowak *et al.*, Phys. Rev. B, 66, 014430, 2002. Copyright 2016 by the American Physical Society.

ing temperature supports the formation of domains reducing the total energy. The meta-stable state, which exhibits a net magnetization, is frozen by exceeding the Néel temperature of the diluted antiferromagnetic material. In this case, the spin structure of the interfacial layer is affected by the magnetic domains within the volume and a horizontal shift of the hysteresis loop appears. Furthermore a vertical shift is observed as the antiferromagnetic layer has an irreversible surplus net magnetization. The exchange bias field within this model is determined by

$$\mu_0 H_{\text{EB}} = \frac{J_{\text{INT}} m_{\text{IDS}}}{l}, \quad (5.21)$$

at which  $m_{\text{IDS}}$  refers to the irreversible domain state magnetization,  $J_{\text{INT}}$  to the interfacial coupling constant and  $l$  to the number of antiferromagnetic monolayers. This model explains experimental results like the training effect, which describes the decrease of the exchange bias at repeated measurements of the hysteresis loop. It also supports negative or positive shifts of the hysteresis loop related to the interfacial interaction and the cooling field.

### Concluding remarks on the exchange bias models

As stated before, the introduced models are relevant for today's understanding of the exchange bias effects. Some important models, as the one from Stiles and McMichael [67] or the spin wave model [68, 51] are not further explained here, as they depend on structures like polycrystalline layers, which are not considered within this thesis or they are based on physical descriptions, which could not be covered within the applied atomistic calculation methods of chapter 3.

## 5.3 Classification of exchange bias applications

As there are plenty of models describing the different effects at various multilayer exchange bias stacks, an overview is helpful to understand and categorize new experimental results of the actual research. Furthermore, such a categorization provides guidance for the development of new models. With a view on the multilayer exchange bias stacks treated within this thesis, an overview is created, which consist of four main categories:

- Conventional exchange bias systems
- Switchable exchange bias systems
- Exchange spring magnets
- Systems showing mixed magnetic characteristics

The classification into these categories depends on the physical properties of each magnetic layer or phase. The answer to the question, if the sign of the loop shift is switchable or if a domain wall appears within the exchange bias system relies on the degrees of freedom of the magnetization within each layer or phase. The relation of each category to the degrees of freedom is illustrated in table 5.1. *Fixed* means that the spins of the layer or phase point into a predefined direction and do not change their orientation during the magnetic field sweep. It has no degree of freedom. If a layer has a *rigid* magnetization, its spins rotate coherently under the influence of an external magnetic field. In case of a ferromagnetic material the angles between the spins and a defined axis are equal within the whole layer. The highest degree of freedom arises in systems where no predefined assumptions are limiting the rotation of the spins. Thus, each spin can rotate *freely* with respect to its local physical interactions.

### 5.3.1 Conventional exchange bias systems

In a conventional exchange bias system the ferromagnetic hysteresis is shifted to one side of the coordinate system. The sign of the exchange bias is not changed within the magnetic field range of the distinct application. Furthermore, the spins of the ferromagnetic layer or phase are assumed to rotate coherently under an applied magnetic field. The rotation of the antiferromagnetic moments is restricted in the way that they cannot be reversed by the

AFM \ FM	Rigid	Free
Fixed	Conventional exchange bias systems	Fully reversible exchange spring magnets
Rigid	Switchable exchange bias systems	Partially reversible exchange spring Magnets
Free		Systems showing mixed magnetic characteristics

**Table 5.1:** Exchange bias categories sorted by the degrees of freedom of each layers

torque resulting from the rotation of the ferromagnetic moments at the interface.

Meiklejohn and Bean proposed a two layer model at which both, the ferromagnetic and the antiferromagnetic layer, rotate coherently [56], cf. section 5.2.1. At least the antiferromagnetic material is assumed to have a uniaxial anisotropy. In the limiting case of an infinitely high anisotropy along the field axis, the antiferromagnetic spins are fixed independently of the magnetic field strength. In this case, the idealized MB model described at the end of section 5.2.1 is applicable. The equations 5.13 and 5.14 can be used to describe the coercive fields and the displacement of the shifted hysteresis loop schematically drawn in figure 5.1b for the typical application of an exchange bias stack within a spin valve. Here, the exchange bias stack is used to fix the magnetization of the reference layer during the complete field cycle.

### 5.3.2 Switchable exchange bias systems

In a conventional exchange bias stack the spins of the antiferromagnetic layer are assumed to be fixed. In contrast, the spins within a switchable exchange bias stack can be fully reversed. An example is the Pt/Co/Cr<sub>2</sub>O<sub>3</sub>/Pt exchange bias system (cf. chapter 7). The Cr spins within this system are reversed by a high magnetic field [14] or by the application of a magnetic and an electric field simultaneously [15]. The spin reversal of the antiferromagnetic layer leads to a switchable shift of the hysteresis curve, either to the right or to the left

hand side.

Before the magnetic behavior of the Pt/Co/Cr<sub>2</sub>O<sub>3</sub>/Pt system has been investigated by atomistic methods, a one dimensional chain model has been studied in order to gain a deeper understanding of the switchable behavior. Although the one dimensional chain model is based on the Pt/Co/Cr<sub>2</sub>O<sub>3</sub>/Pt stack, the results are generally valid and may be used to explain the magnetic behavior of other switchable exchange bias stacks.

The one dimensional chain model consists of three spins only. One spin is used to model the ferromagnetic Co layer while the other two spins represent the antiferromagnetic layer. To understand the magnetic behavior the Hamiltonian in equation 5.22 is exploited by numerical methods.

$$\begin{aligned} \mathcal{H} = & - J_{\text{int}} \vec{S}_1^{\text{AFM}} \cdot \vec{S}_1^{\text{FM}} - J_{\text{AFM}} \vec{S}_2^{\text{AFM}} \cdot \vec{S}_1^{\text{AFM}} & (5.22) \\ & - D_z^{\text{FM}} (\vec{S}_1^{\text{FM}} \cdot \vec{e}_z)^2 - D_z^{\text{AFM}} ((\vec{S}_1^{\text{AFM}} \cdot \vec{e}_z)^2 + (\vec{S}_2^{\text{AFM}} \cdot \vec{e}_z)^2) \\ & - \mu_{\text{eff}} B_z (S_{z,1}^{\text{FM}} + S_{z,1}^{\text{AFM}} + S_{z,2}^{\text{AFM}}) \end{aligned}$$

For simplification, all three spins in the chain model have the same effective magnetic moment  $\mu_{\text{eff}}$ . The interfacial coupling constant  $J_{\text{int}}$  is assumed to be positive and much smaller than the coupling constant between the two antiferromagnetically coupled spins. The magnetic layers of the Pt/Co/Cr<sub>2</sub>O<sub>3</sub>/Pt favor a perpendicular magnetization. Therefore a perpendicular uniaxial anisotropy is assumed for all three spins. In an atomistic model the anisotropy of the Cr spins is rather small compared to the anisotropy of the Co spins. But as the Cr<sub>2</sub>O<sub>3</sub> layer is much thicker than the Co layer, the effective anisotropy constant  $D_z^{\text{AFM}}$  of the antiferromagnetically coupled spins is chosen to be larger than the anisotropy constant  $D_z^{\text{AFM}}$  of the spin modeling the ferromagnetic layer. The exact values are arbitrarily chosen with respect to these restrictions. The Landau-Lifshitz equation has been solved to determine the hysteresis curves of the one dimensional chain model. It has been found that the system shows mainly six different stable magnetic states. Their occurrence depends on the maximum value of the applied magnetic field. This behavior has been interpreted with the help of the energy curves related to each of the six states.



To simplify the calculation of these curves, the rotation of the three spins is restricted to a plane. The Hamiltonian in equation 5.23 becomes

$$\begin{aligned} \mathcal{H} = & -J_{\text{int}} \cos(\theta_1^{\text{AFM}} - \theta_1^{\text{FM}}) - J_{\text{AFM}} \cos(\theta_2^{\text{AFM}} - \theta_1^{\text{AFM}}) \\ & - D_z^{\text{FM}} \cos^2(\theta_1^{\text{FM}}) - D_z^{\text{AFM}} (\cos^2(\theta_1^{\text{AFM}}) + \cos^2(\theta_2^{\text{AFM}})) \\ & - \mu_{\text{eff}} (\cos(\theta_1^{\text{FM}}) + \cos(\theta_1^{\text{AFM}}) + \cos(\theta_2^{\text{AFM}})). \end{aligned} \quad (5.23)$$

The hysteresis loops for three different maximum values of the applied field and the energy curves of the six relevant spin states are drawn in figure 5.21.

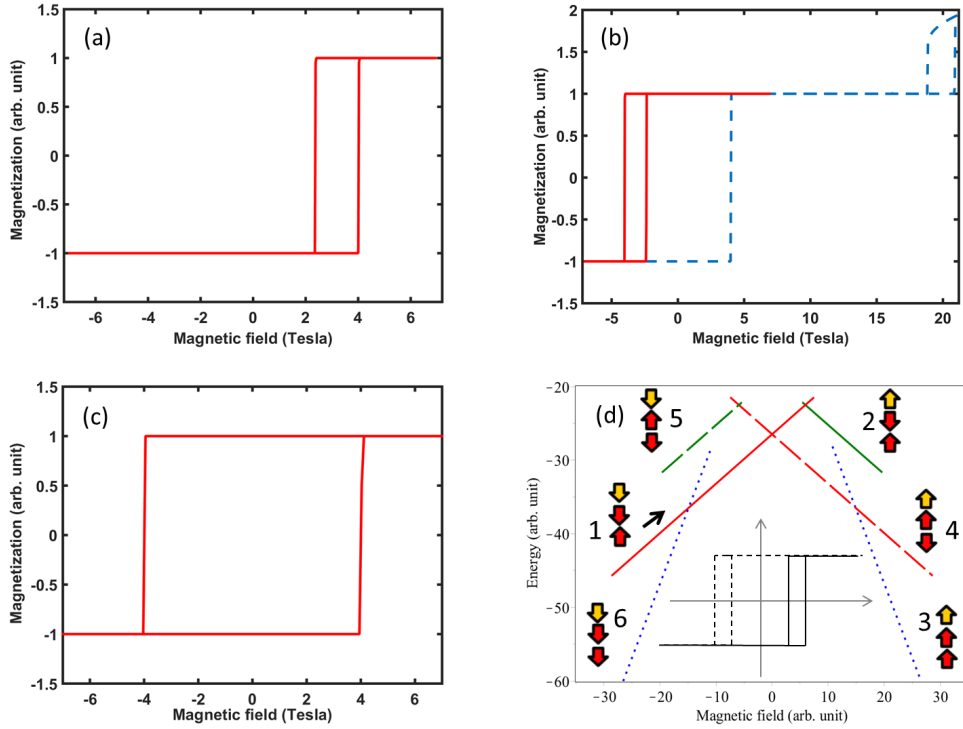


**Figure 5.21:** Magnetization curves and energy curves of a switchable exchange bias system.

The second and fifth state of figure 5.21 are no energy minimizing states, if the coupling constant  $J_{\text{int}}$  is large compared to the anisotropy of the antiferromagnetically coupled spins. In this case, a spin flip occurs, instead of a spin flop. Both states transitions are visualized in figure 5.22.

In the following, the different hysteresis curves are explained on the basis of three field ranges of the magnetic field.  $B_{\text{max}}$  is the maximum value and  $B_{\text{min}}$

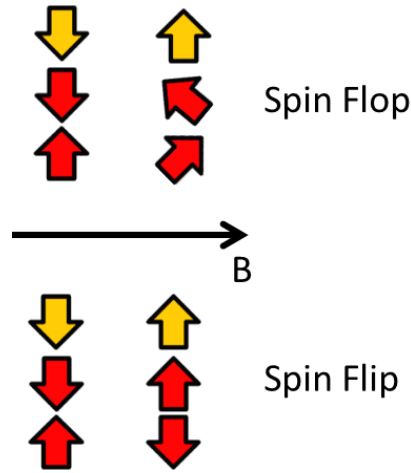


**Figure 5.22:** Schematic representation of the spin flip and spin flop states.

is the minimum value of the magnetic field.  $B_{\text{SF}}^{\text{p/n}}$  denotes the spin flop field at positive or negative fields. It is assumed, that the exchange coupling is low and that no spin flip occurs.

$B_{\text{SF}}^{\text{n}} < B_{\text{min}}$  and  $B_{\text{SF}}^{\text{p}} > B_{\text{max}}$

Initially the system is in state 1 of figure 5.21(d). At increasing fields, the energy barrier between state 1 and state 2 approaches zero and the upper spin rotates into the new spin state. While the ferromagnetic spin reverses its magnetization under the influence of an external field, the antiferromagnetically coupled spins stay fixed due to a high uniaxial anisotropy and a rather low interfacial exchange constant. The positive and negative maximum of the field strength is too small to change the state of the antiferromagnetic spins, i.e. no spin flop occurs. The system behaves like a conventional exchange bias system described in the previous section. The resulting hysteresis curve is shown in figure 5.21(a).

$B_{\text{SF}}^{\text{n}} < B_{\text{min}}$  and  $B_{\text{SF}}^{\text{p}} < B_{\text{max}}$

The same initial state is used as before. The ferromagnetic layer reverses its magnetization as soon as the external magnetic field exceeds the energy barrier resulting from the uniaxial anisotropy and the interfacial exchange coupling. If the external field is further increased, the antiferromagnetic spins are flopped.

A subsequent decrease of the field strength causes a complete reversal of the antiferromagnetically coupled spins. If the spin flop field is not reached at negative fields, the hysteresis loop is shifted to the opposite side of the field axis. The blue dotted line of figure 5.21b represents the magnetization of all three spins. The spin flop can be clearly determined from the increasing magnetization at high field values.

$$\underline{B_{\text{SF}}^n > B_{\text{min}} \text{ and } B_{\text{SF}}^p < B_{\text{max}}}$$

If the spin flop field is reached at positive and negative values, the width of the hysteresis loop is enhanced, but it is not shifted anymore. The hysteresis loop is drawn in figure 5.21(c). The symmetry occurs as all six states are reached during the field cycle.

Depending on the different parameters of the model, other states than the six states in figure 5.21(d) might occur at a given field strength. However, some of the basic properties like the switchable exchange bias can already be explained with such a simple model.

### 5.3.3 Exchange spring magnets

The term exchange spring magnet is originally used for two coupled ferromagnetic materials. It describes a composite or a multilayer system of hard magnetic material with a high uniaxial anisotropy and a soft magnetic material with a high saturation field [69]. The layers or phases are interfacially exchange coupled. In contrast to a conventional ferromagnetic material or a structure of two independent ferromagnetic materials, the hysteresis curve of an exchange spring magnet has a reversible part far beyond the zero crossing of the applied field. This can be seen from the demagnetization curves in figure 5.23.

The reversible behavior of an exchange spring magnet can be explained by the one dimensional model as sketched in figure 5.24. The hard magnetic phase is assumed to have a high uniaxial anisotropy with an easy axis parallel to the external field. The soft magnetic material has a uniaxial anisotropy with an easy axis in the same direction, but a much lower anisotropy constant. The

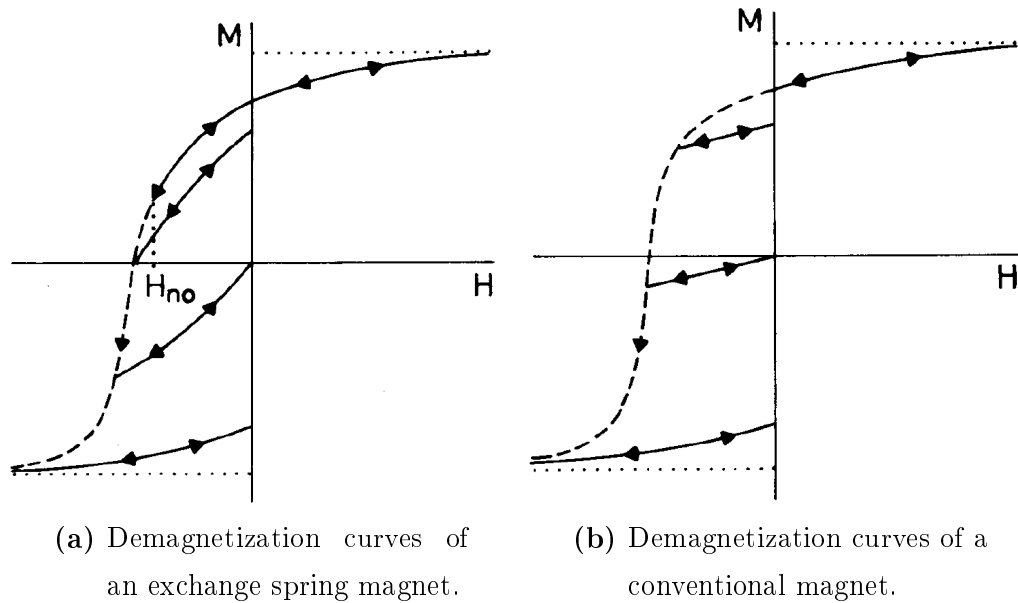


**Figure 5.23:** Reversible and irreversible demagnetization curves of a conventional magnetic material and an exchange spring magnet. From E. F. Kneller and R. Hartwig, IEEE Trans. Mag., 27, 3588. ©2016 IEEE.

magnetic moments at the interface of the hard and the soft phases are ferromagnetically exchange coupled. Under the influence of an external field, which is illustrated by a blue arrow, the spins of the upper soft magnetic layer try to rotate into the direction of the external field. Because of the interfacial coupling, a spring like rotation occurs. As long as this rotation does not proceed into the hard magnetic layer, the curve of the chain is fully reversible. A rotation of the hard magnetic moments overcoming the uniaxial anisotropy is irreversible. The corresponding field strength is denoted by  $H_{no}$  in figure 5.23a.

In exchange bias systems an antiferromagnetic material is exchange coupled to a ferromagnetic material. Scholl describes in [70] the observation of spring-like magnetic behavior within the antiferromagnetic layer at the Co/NiO exchange bias stack. With the x-ray magnetic linear dichroism (XMLD) spectroscopy Scholl has proven the existence of a partial domain wall like it is predicted by many exchange bias models. Two examples are the Mauri model [57] and the random field model [58] introduced shortly in section 5.2.3. By rotating the

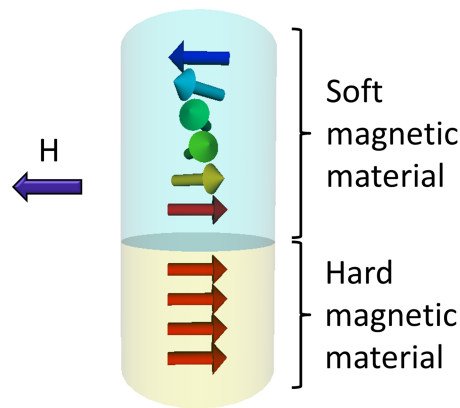


**Figure 5.24:** Illustration of the spring-like rotation of spins within the soft magnetic layer.

ferromagnetic layer with an external field, the spins of the antiferromagnetic layer are wound up and down. This behavior is similar to that of conventional exchange bias springs.

### 5.3.4 Systems showing mixed magnetic characteristics

In general, a mixture of the characteristics of the three main application categories may occur. One example is an exchange spring system with a thin hard magnetic layer. If the thickness of the hard magnetic layer is less than the width of a  $180^\circ$  domain wall, a complete spin reversal would be possible by applying a high magnetic field. Thus, a system that exhibits a spring-like rotation acts like an switchable exchange bias system.

Another example places emphasis on major and minor effects. A closer examination of the interfacial region of a conventional exchange bias stack might show a canting or a very short partial domain wall. In this case the system is qualitatively understandable within a picture of a conventional exchange bias system, although the quantitative results might differ due to the slight rotation of the interfacial antiferromagnetic spins.

In the following chapter 6 the exchange bias system NiFe/IrMn/MgO/Pt is investigated by atomistic spin dynamics simulations, at which a spring-like magnetic behavior of the IrMn layer has been supposed by the authors of [13]. Within the investigation the idea arises, that the magnetic behavior is caused by an abrupt switching of the antiferromagnetic state. Hence a spring-like

rotation is likely not the key property.

In short, the most exchange bias systems show properties of different categories. If a system exhibits several important properties of different categories within a specific application, the system might belong to this category of mixed characteristics.

# Chapter 6

## Exchange Bias: NiFe/IrMn

### 6.1 NiFe/IrMn: AFM TAMR at an exchange spring system

NiFe/IrMn is an exchange bias stack, at which a rotation of the ferromagnetic NiFe spins is thought to cause a spring-like rotation of the spins within the antiferromagnetic IrMn layer [13]. In correspondence to ferromagnetic exchange spring stacks, such a system with a spring-like rotation of the antiferromagnetic material is called an antiferromagnetic exchange spring [70] (cf. section 5.3.3).

The antiferromagnetic exchange spring is part of a NiFe/IrMn/MgO/Pt multilayer system, which is described by Park *et al.* as an antiferromagnetic tunnel junction with a spin valve like behavior [13]. Depending on an applied magnetic field, a spin valve exhibits a high or a low resistive state. The authors of [13] studied the magnetic behavior of the system experimentally. Figure 6.1a and figure 6.1b represent the resistance of the stack containing NiFe(10 nm)/IrMn(1.5 nm) against an applied magnetic field. The resistance depends clearly on the applied field. The measured signal shows a high resistive state at negative fields and a low resistive state at positive fields. Thus, the change of the resistive signal is caused by a spin rotation within either the ferromagnetic or the antiferromagnetic material. Because tunneling is sensitive to the atomic layers directly at the barrier (MgO), in this case the spin

configuration of the IrMn obviously influences the tunneling resistance.

At ferromagnetic materials a dependence of the resistance on the angle between the applied field and the current is known as the anisotropic magnetoresistive effect (AMR). The influence of the magnetization on the resistance was observed by W. Thomson in 1856 at Fe and Ni [71]. If a magnetic field is applied along the direction of a current through the sample, a high resistance will be measured. An applied magnetic field, which aligns the magnetization perpendicular to the current, is related to a low resistance. The effect arises from the spin dependent scattering of the electrons due to spin-orbit coupling [72]. The magnetoresistive effect is also measurable in tunnel devices, in which the tunnel barrier is created by an insulating material. The effect, which describes the dependence of the resistance on the magnetization of the barrier material, is called tunneling magnetoresistive effect (TMR). Conventionally, a ferromagnetic material is placed next to the tunnel barrier. In the case of the NiFe/IrMn/MgO/Pt system the antiferromagnetic IrMn is placed next to the electrical insulating layer. Hence the difference in the so called tunneling anisotropic magnetoresistance (TAMR) is caused by a change of the magnetic state of the antiferromagnetic material.

An applied magnetic field, which is much lower than the spin flop field, could not lead to a state transition of the antiferromagnetic IrMn. Figure 6.1(c) and figure 6.1(e) depict the magnetization curves of the NiFe/IrMn/MgO/Pt system with and without the IrMn layer. Without the IrMn layer the magnetization curves show only very small coercive fields. As NiFe is a soft magnetic material with small anisotropies the hysteresis loop has a non-visible loop width in this field range. Samples that contain IrMn show shifted hysteresis loops. This indicates that the NiFe layer is exchange coupled to the IrMn layer. The authors of [13] assume, that the external applied field leads to a rotation of the ferromagnetic NiFe spins, which is accompanied by a spring-like rotation of the spins within the antiferromagnetic layer. Thus, they suppose that a spin reversal of the ferromagnetic NiFe layer might cause a tilt of the antiferromagnetic coupled Mn spins [13]. Within their theory, the measured TAMR signal would arise from this tilt.

The microscopic behavior of the NiFe/IrMn stack and especially the role of



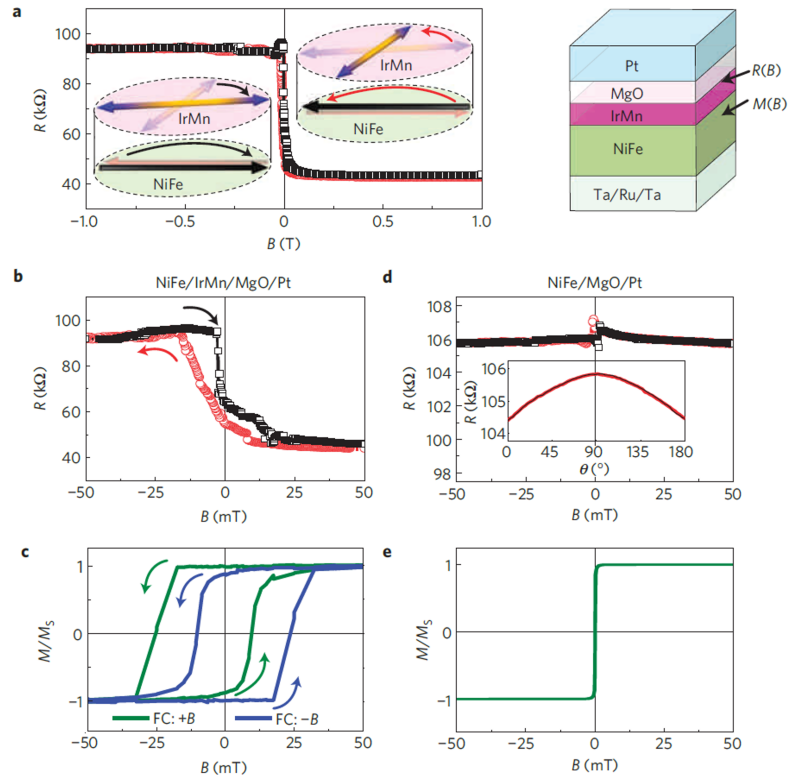


**Figure 6.1:** Experimental results from [13]. (a) Magnetoresistive signal of the NiFe/IrMn/MgO/Pt multilayer system, which is depicted on the right. The insets visualize the exchange spring effect of NiFe on IrMn. (b) Hysteric magnetoresistance of NiFe/IrMn/MgO/Pt. (c) Magnetization curve of NiFe/IrMn/MgO/Pt. The film is grown and annealed in an magnetic field. The green curve is related to a film growth at negative field and the blue curve to a growth at positive field (d) Magnetoresistive signal of the system without the IrMn layer. The inset shows the magnetoresistive signal of the sample, which is rotated in a 50 mT field. (e) Magnetization curve of the system without the IrMn layer. Reprinted by permission from Macmillan Publishers Ltd. [Nat. Mater.] Park *et al.*, 10, 5, copyright 2016.

IrMn and NiFe have been investigated by atomistic spin dynamics simulations. Starting from ground states of each individual layer, the low energy states of the interfacial coupled layers are determined (section 6.3). Based on the gained knowledge different effective models have been developed to explain the shifted hysteresis loop of figure 6.1d and the magnetic behavior described in [13]. The developed models are of finite lateral dimensions. The boundary atoms have a reduced number of neighbors, which may lead to a different magnetic behavior in comparison to structures with a low boundary-to-bulk ratio. To avoid the influence of the dangling boundary atoms, two dimensional periodic boundary conditions have been introduced in section 6.7.3. As the atomistic calculation of magnetization curves comes along with huge computational efforts, the performance has been improved by a macrospin approach (cf. section 3.4). The NiFe layer within the experimental stack has a height of 10 nm. This layer is replaced by a single macrospin leading to a similar magnetic behavior. In general, hysteresis loops depend on the sweep rate of the external field. In an experiment the sweep rate is rather low and the system is able to reach its quasi-static magnetization at each field value. Depending on the system size, a calculation of quasi-static magnetization curves is too time consuming (cf. section 4.2.3). In that case a direct comparison of the experimental and computational results is not possible. But if the effect of the sweep rate is low, predictions regarding the quasi-static magnetization at different field values might be possible. Therefore the influence of the sweep rate is discussed in section 6.7.4. Furthermore, the temperature dependence is studied and compared to experimental results (section 6.9). The different steps towards a suitable effective model are represented by the flow chart in figure 6.2.

## 6.2 Crystal structures and material parameters of NiFe/IrMn

Different crystal structures are known for both NiFe and IrMn [73, 74]. The Ni and Mn fractions are stated to be 80% for NiFe and IrMn, respectively. The atoms of both materials arrange on an fcc-lattice in an ordered or a disordered manner. In case of a disordered crystal structure the arrangement of the atoms

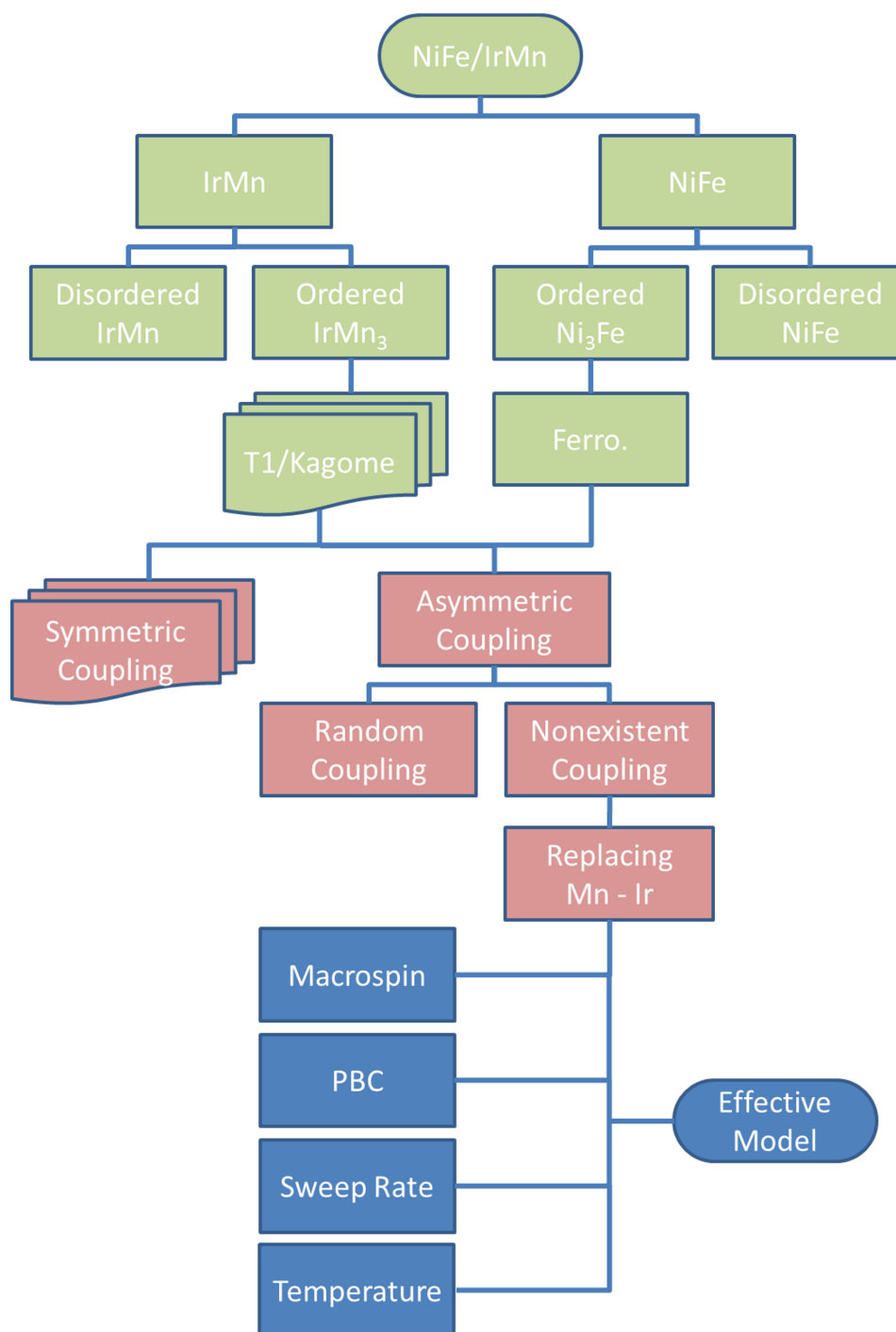


**Figure 6.2:** Workflow used for the investigation of the exchange spring system NiFe/IrMn/MgO/Pt.

on the grid changes within the sample. In atomistic spin dynamics calculations several different arrangements have to be considered to get comparable average values with respect to experimental results. Therefore the effective models have to cover larger dimensions, leading to an enormous increase of the computational effort. In the next section an effective model is introduced, which reproduce the experimental data to a huge extend. As this model is based on ordered crystal structures, the magnetic behavior of disordered structures is not further discussed.

The magnetic layers have been grown in the  $[111]$ -direction [13]. The developed effective models of the NiFe/IrMn stack consist of unit cells as depicted in figure 6.3. The  $[111]$ -direction is aligned with the  $z$ -axis. The colors indicate different atom types. The light blue sphere visualizes the non-magnetic Ir atom in the cell on the right hand side of figure 6.3. The blue, yellow and purple colored spheres represent the Mn atoms with different anisotropy easy axes. The yellow bars which define the edges of the unit cell are aligned with the three different anisotropy axes of the Mn atoms. In case of NiFe the bars do not correspond to any anisotropy. The Ni atoms are green colored and the red sphere represents the Fe atom of the considered unit cell.

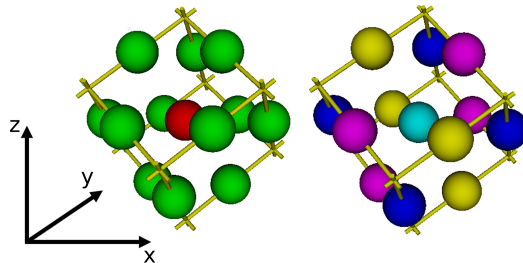


**Figure 6.3:** Schematic representation of the NiFe (left) and IrMn (right) unit cells. Explanations are given in the text above.

In the spin dynamics calculations three different energy terms are taken into account: The first term describes the isotropic exchange coupling of neighboring atoms. The second term represents the energy resulting from an uniaxial anisotropy of each spin vector and the third term is the Zeeman term, which involves the influence of the external field. All three terms are part of a Hamiltonian shown in equation 6.1.

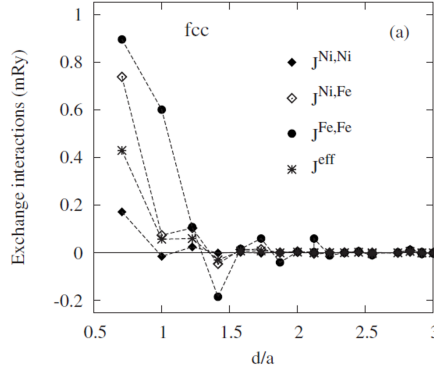


**Figure 6.4:** Exchange interaction constants of NiFe. Reprinted figure with permission from P. Yu *et al.*, Phys. Rev. B, 77, 054431, 2008. Copyright 2016 by the American Physical Society.

$$\mathcal{H} = - \sum_{i < j} J_{i,j}^{\text{NiFe}} \vec{S}_i \cdot \vec{S}_j - \sum_i D_i^{\text{NiFe}} \left( \vec{S}_i \cdot \vec{e}_i \right)^2 - \vec{B}_{\text{ext}} \sum_i \mu_{\text{eff},i} \cdot \vec{S}_i \quad (6.1)$$

$$- \sum_{k < l} J_{k,l}^{\text{IrMn}} \vec{S}_k \cdot \vec{S}_l - \sum_k D_k^{\text{IrMn}} \left( \vec{S}_k \cdot \vec{e}_k \right)^2 - \vec{B}_{\text{ext}} \sum_k \mu_{\text{eff},k} \cdot \vec{S}_k - \sum_{i < k} J_{i,k}^{\text{int}} \vec{S}_i \cdot \vec{S}_k \quad (6.2)$$

$J_{ij}$ ,  $D_i$  and  $\mu_{\text{eff},i}$  denote the exchange constant between neighboring atoms, the uniaxial on-site anisotropy constant and the effective moment of each atom, respectively. The unit vector  $\vec{e}_i$  indicates the direction of the uniaxial anisotropy axis. These parameters depend on the structure and the material of each layer as well as on the interfacial structure of the two layers.

### 6.2.1 Material data of NiFe

NiFe is a soft magnetic material with a very small anisotropy. Therefore, the uniaxial anisotropy constant  $D^{\text{NiFe}_i}$  of equation 6.1 is assumed to be zero. The material data for fcc – Ni<sub>3</sub>Fe are calculated in [75] and [76] using *ab initio* methods. The effective moments of Ni and Fe are  $0.628 \mu_B$  and  $2.637 \mu_B$  [76]. The exchange interaction constants are taken from figure 6.4 [75]. The lattice constant  $a$  of fcc-Ni<sub>3</sub>Fe is assumed to be  $a = 0.355 \text{ nm}$ .

## 6.2.2 Material data of IrMn<sub>3</sub>

The magnetic parameters of IrMn and ordered IrMn<sub>3</sub> have been determined by Szunyogh *et al.* [77]. With a lattice constant of 0.3785 nm the effective moment of Mn is specified as  $2.66 \mu_B$ . The isotropic exchange constants are depicted in figure 6.5b. Figure 6.5a [77] represents a unit cell with three Mn atoms. Each of the Mn atoms has a different easy axis with the same anisotropy constant. As the anisotropy calculated in [77] is based on a Hamiltonian related to the energy of a unit cell, the local uniaxial anisotropy constant  $D = 0.52 \text{ meV}$  of each Mn atom is taken from [78].

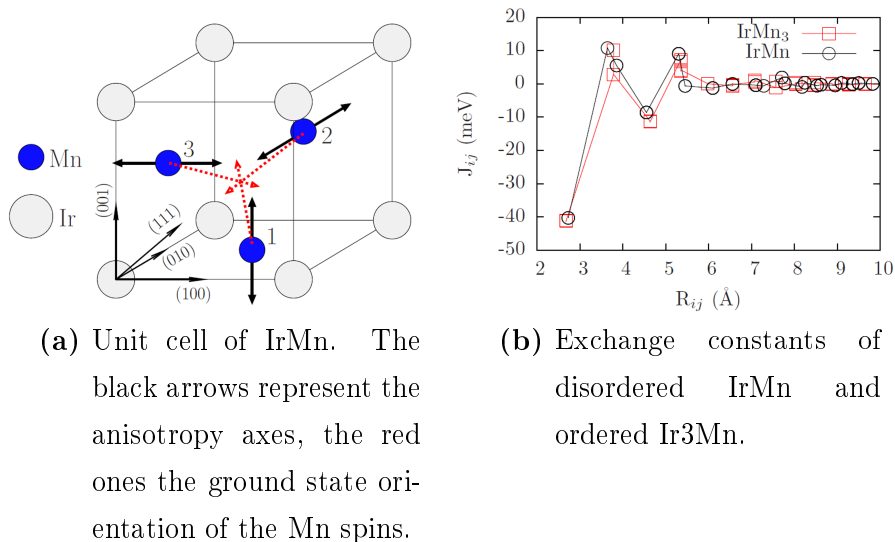


**Figure 6.5:** Material parameters of IrMn. Reprinted figures a and b with permission from L. Szunyogh *et al.*, Phys. Rev. B, 79, 020403, 2009. Copyright 2016 by the American Physical Society.

## 6.3 Ground state configurations of NiFe, IrMn and NiFe/IrMn

In a first step the ground states of IrMn and NiFe are determined independently by a Monte Carlo approach (cf. 3.2.2). Afterwards the layers are combined and the resulting ground states are compared to expectations revealed from

previous calculations regarding the individual layers.

To determine the ground states of the individual structures and the two layer stack the Hamiltonian, given in equation 6.1 is minimized at  $B = 0$  T by a Monte Carlo approach. Each calculation starts from a random orientation of the spin vectors with a finite temperature to overcome energy barriers. During  $1 \cdot 10^8$  Monte Carlo steps the temperature is decreased from 1 K to 0 K and the system rearranges towards its ground state configurations. Further information regarding the Monte Carlo procedure and the resulting states of the individual layers and the stack are discussed in the following three sections.

### 6.3.1 Ground states of NiFe

The dominating positive exchange constants indicate a ferromagnetic coupling between the Ni and Fe atoms. As there is no anisotropy considered, the spin vectors of NiFe are aligned in an arbitrary direction. Figure 6.6 depicts one of the possible orientations of the permalloy spin vectors determined by a Monte Carlo approach with an initial random orientation of the Ni and Fe spin vectors and a temperature of  $T = 1$  mK.

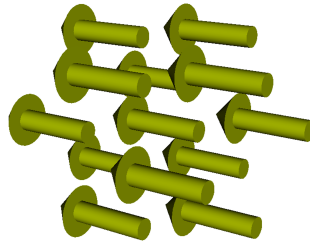


**Figure 6.6:** Ground state of NiFe

### 6.3.2 Ground states of IrMn<sub>3</sub>

IrMn<sub>3</sub> is an ideal antiferromagnetic material, meaning that the magnetization of the ground states equates zero. The spin orientations inside a unit cell depend on the anisotropy of each Mn atom and the exchange coupling between neighboring atoms. Both energy terms influence the ground state spin orientations and hence a more complicated configuration is expected. To find all degenerated ground states 300 Monte Carlo cycles of  $1 \cdot 10^8$  steps have been

performed. Initially the system has a random orientation of the spins and is heated up to 1 K. During the subsequent Monte Carlo cycles the temperature is decreased to zero. A typical evolution of the total energy during the Monte Carlo calculation is shown in figure 6.7.

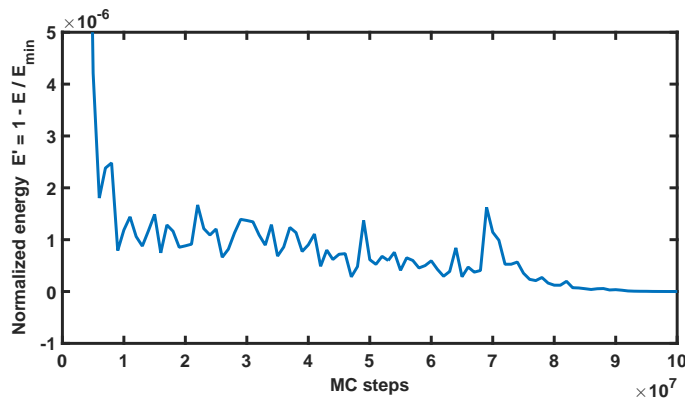
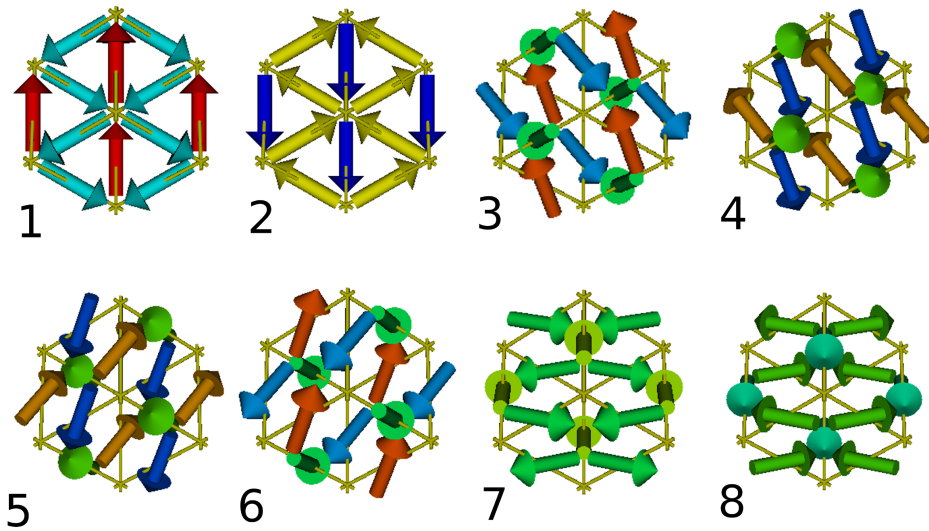


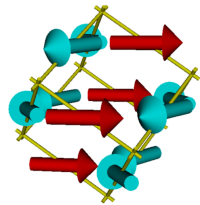
**Figure 6.7:** The figure represents a typical evolution of the energy during a Monte Carlo simulation to determine the ground states of  $\text{IrMn}_3$

In case that a constant energy is not reached during the simulation, the system is heated up again and relaxed for further  $1 \cdot 10^7$  Monte Carlo steps. In this run the initial orientation of the spins equals the resulting configuration of the previous run. Figure 6.8a represents the eight resulting ground states of  $\text{IrMn}_3$ . The high effective anisotropy of each Mn atom and the antiferromagnetic exchange between the magnetic atoms lead to a  $T1$  or kagome ground state [79]. The kagome planes can be seen in figure 6.8b. Two Mn spins of a common kagome plane are in an angle of  $120^\circ$  to each other. The MC calculations with  $1 \cdot 10^7$  MC steps result into further seven degenerated ground states. All degenerated states are depicted in a  $[111]$ -projection in figure 6.8b. The yellow bars of figure 6.8a and 6.8b represent the easy axes of the Mn atoms. The bars form a cube at which the surface normal vector of the kagome planes points into one of the corners. As a cube has eight corners, eight degenerated ground states could be identified. The results of the 300 MC runs are visualized as circles and crosses on the unit sphere in figure 6.8c. The green, blue and yellow crosses indicate the orientation of the Mn spin vectors. The different colors are related to the three types of Mn atoms with different easy axes. The red circles represent the surface normal vectors of the resulting kagome planes.

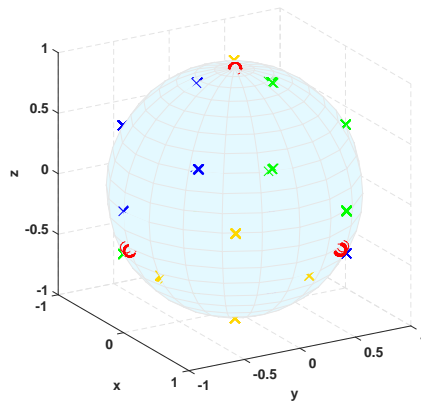




(a) Representation of the eight degenerated ground states of  $\text{IrMn}_3$ .



(b) Front view of the first ground state. The yellow bars represent the anisotropy axes.



(c) Representation of the classical spin vectors and the kagome surface normals on the surface of a unit sphere. Each accumulation of crosses is related to a spin of a  $\text{IrMn}_3$  ground state. Different colors are chosen for spins with different anisotropy axes. The red circles represent the kagome surface normals.

**Figure 6.8:** Different representations of the  $\text{IrMn}_3$  ground states.

As there are eight degenerate ground states eight similar patterns are equally distributed over the surface of the unit sphere. Since two states have common planes only four red circles appear on the sphere.

### 6.3.3 Ground states of the NiFe/IrMn stack

In regard to the development of effective models representing the magnetic behavior of a NiFe(10 nm)/IrMn(1.5 nm) bilayer stack the thickness of IrMn is increased to 1.5 nm. To decrease the computing time, NiFe layer thickness is reduced to 1 nm. The lattice constants of fcc-IrMn and fcc-NiFe are almost equal, so that a lattice constant of 0.3785 nm is assumed for both layers.

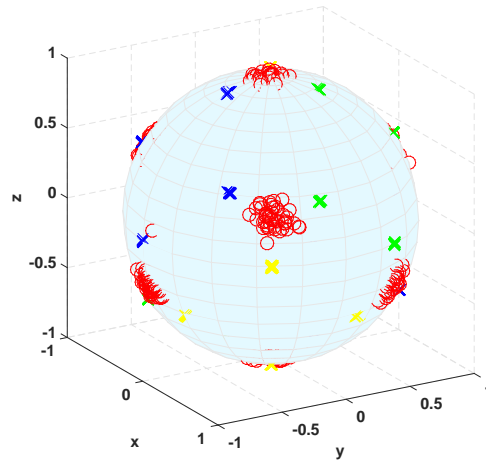


**Figure 6.9:** Representation of the ground states of NiFe/IrMn on the surface of a unit sphere. The Mn spins are illustrated by crosses at which each color indicates a different anisotropy axis of the atoms. The orientation of the central lowermost Fe spin is represented by red circles.

In this case each interfacial Fe atom has three next neighboring Mn atoms at the same distance. Thus, it seems likely to suppose that each Mn atom at the interface is equally coupled to the neighboring Fe atom. In the following this effective model is referred to  $3Mn3C$  because all three Mn atoms of the interface are assumed to be exchange coupled with the overlying Fe atom. The exchange coupling constant is supposed to be  $J_{\text{int}} = 4.3 \text{ meV}$  for all three couplings. As NiFe has no magneto-crystalline anisotropy the interfacial exchange

coupling determines the orientation of the permalloy spin vectors. In case of equal coupled Mn spins the red circles on the unit sphere in figure 6.8c are the expected orientations of the NiFe spin vectors. Monte Carlo calculations of 300 cycles confirm this expectation. Figure 6.9 represents the ground state orientations on the unit sphere. The crosses highlight the Mn spin vectors as before in figure 6.8c, while the red circles visualize the orientations of the interfacial coupled Fe spin. The eight patterns from figure 6.8c are also recognizable in figure 6.9. The eight degenerated ground states of the NiFe/IrMn stack are represented in figure 6.10.

In section 6.3.2 four surface normal vectors are related to eight IrMn degenerated ground states. The orientation of the NiFe spins is either parallel or antiparallel to the surface normal vectors calculated previously. The parallel orientation or antiparallel orientation is not random and depends on the ground state of IrMn. The interfacial exchange coupled Mn spin vectors change their orientation slightly in the way that the anisotropy energy is reduced.

## 6.4 Applied simulation methods

The ground states of NiFe, IrMn and the complete NiFe/IrMn stack have been determined by a Monte Carlo scheme (cf. section 3.2.2). As the relaxation into one of the global minima needs only a few Monte Carlo steps, no optimization of the cone size is necessary to speed up the calculations. The cone size of  $R_c$  has been arbitrarily chosen to be  $R_c = 0.5$ .

In the following the hysteresis curves of different NiFe/IrMn models are determined. The hysteresis curves are calculated by solving the Landau-Lifshitz equation (section 3.2.1, equation 3.15), as this approach ensures a correct chronological order of the obtained spins states during the field cycles. As there are several degenerated ground states of IrMn existing, the application of the parallel hysteresis loop calculation (section 4.3) is in question. A look-ahead to section 6.8 reveals that the evolution of the spins depends on the shape of the external applied field. The resulting state obtained by a field pulse differs from the resulting state after a slow increase of the external field. Such a dependence prohibits the application of the parallel algorithm.

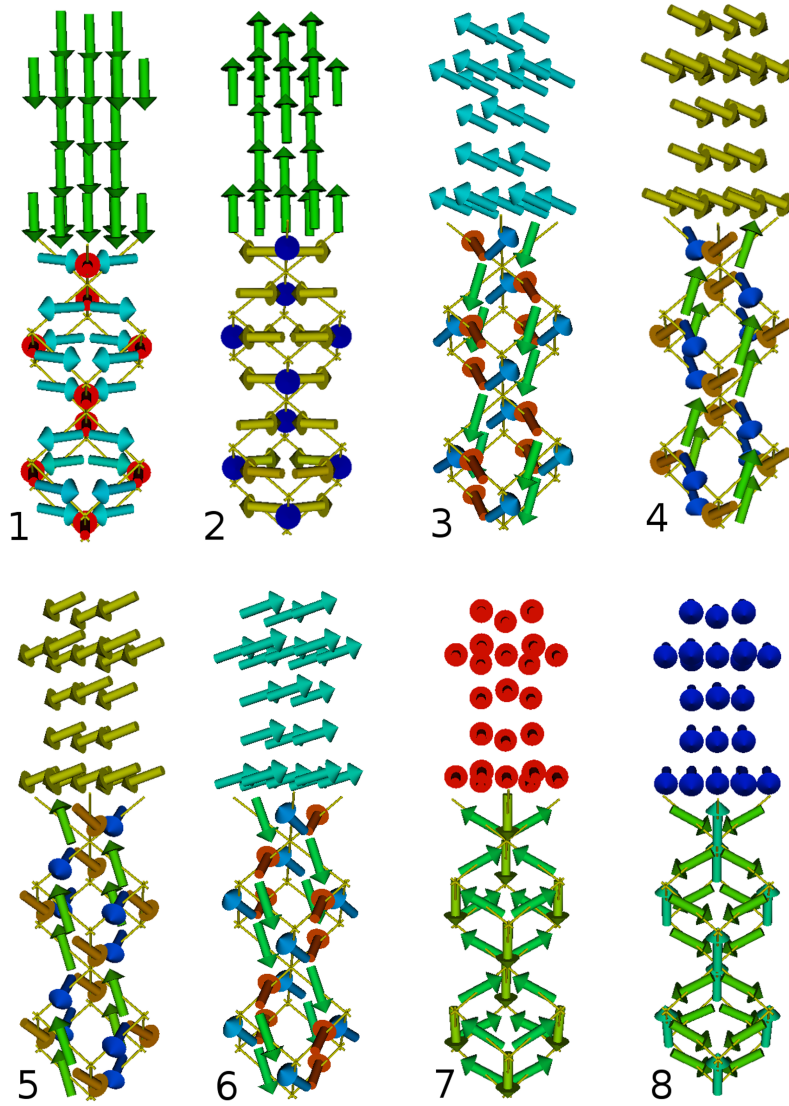


**Figure 6.10:** Eight degenerated ground states of the NiFe/IrMn stack.

## 6.5 Magnetization curves of the $3Mn3C$ model with an ideal interface structure

In the previous section a two layer stack of NiFe(1 nm)/IrMn(1 nm) is used to determine the ground states of the exchange coupled layers. In this section the magnetization curves of the effective two layer model are studied and compared to experimental magnetization curves described in [13]. During growth and annealing of the NiFe/IrMn/MgO/Pt stack, an in-plane magnetic field has been applied [13]. The magnetization curves, which are represented in figure 6.1, have been measured by an external field applied in the same direction as during growth and annealing. It is supposed that the NiFe spins align with the external field at least during annealing. Therefore, the magnetic field in the simulation is aligned with an in-plane projection of the NiFe spins at each NiFe/IrMn ground states. A schematic representation of the configuration based on the fifth ground state is represented in figure 6.11. The magnetization of the upper layer is perpendicular to the kagome plane of the first and second ground states in figure 6.10. In these cases the external field is aligned with the  $y$ -axis of figure 6.11.

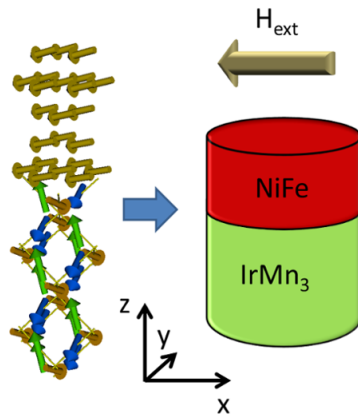


**Figure 6.11:** Schematic representation of the calculation setup.

The applied fields in the calculation are increased and decreased by a sweep rate of 8 Tms. The resulting magnetization curves are represented in figure 6.12.

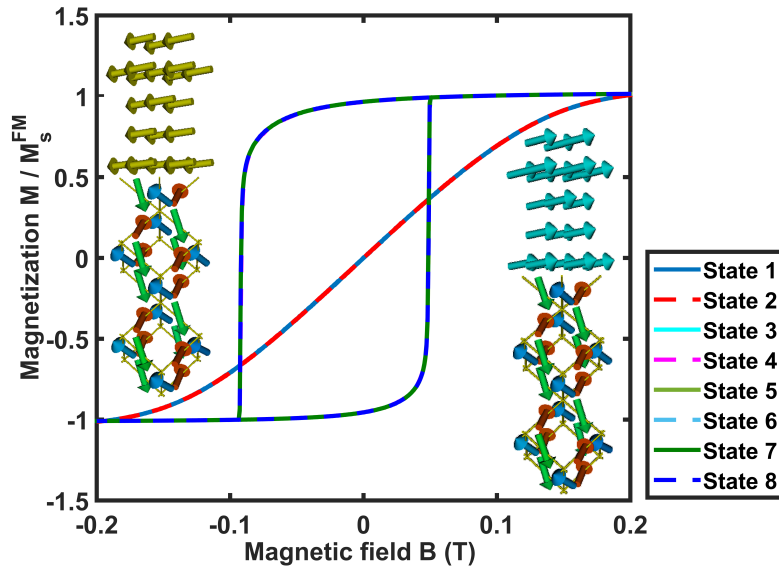


**Figure 6.12:** Magnetization curves of the  $3Mn3C$  model.

The symmetric exchange couplings at the interface induce an almost uniaxial anisotropy. The corresponding magnetization curves are comparable to those of a Stoner-Wohlfarth particle described in chapter 3.1.1. The width of the hysteresis loop depends on the angle between the easy axis and the magnetic field. Applying a field along the easy axis, leads to a rectangular hysteresis loop. The hysteresis loop disappears at fields aligned with the hard axis. The latter can be seen at the magnetization curves of the first and second state in figure 6.12. The hysteresis curves of the other states are not perfectly rectangular due to the small deviation from the easy axis.

Although most of the hysteresis curves show a horizontal loop shift, the shapes of the magnetization curves differ from the experimental magnetization curves given in figure 6.1 [13]. The blue line of figure 6.1c indicates that the magnetization suddenly changes at increasing fields and drops slowly down in an s-shaped curve at decreasing fields. To reproduce this magnetization curve, the  $3Mn3C$  model has to be modified.

## 6.6 Including interfacial defects

As the  $3Mn3C$  effective models do not lead to the expected magnetization curves, different approaches are investigated to break the symmetric coupling between the three Mn atoms and the single Fe atom. The following considerations refer to the first and second ground states of IrMn, which are represented in figure 6.8a.

### 6.6.1 Asymmetric coupling

If all three Mn atoms at the interface are equally exchange coupled to the upper Fe atom, a nearly uniaxial anisotropy with an out-of-plane axis is induced within the NiFe layer (cf. 6.5). A shifted hysteresis loop requires that the unidirectional anisotropy with an easy axis is predominantly aligned with the external field. In [13] the magnetization curve is measured by an in-plane field with the same direction as during growth and annealing. Assuming a random coupling between the three interfacial Mn atoms and the Fe atom, the symmetry would be broken, but the resulting anisotropy axis would still exhibit a perpendicular component. An in-plane anisotropy axis without any out-of-plane component occurs by equaling at least one of the couplings between Mn and Fe to zero. The unidirectional anisotropy is aligned with the external field direction by zeroing the interfacial coupling of the Mn atom, whose spin vector is parallel to the field. Furthermore the exchange constants of the remaining interfacial couplings have to be equal. In the following, this effective model is identified as  $3Mn2C$  model. The interface of the effective  $3Mn2C$  model is schematically drawn in figure 6.13. The coupling constant between Fe and the transparent pictured Mn spin vector is assumed to be zero.

Applying an external field aligned with the transparent drawn spin vector of figure 6.13 leads to comparable magnetization curves with the experimental results. The blue and green curve of figure 6.14 are related to different initial states. The green curve is determined by using the first ground state of figure 6.8a as initial condition for the Mn spin vectors. The blue curve describes the evolution of the magnetization starting from second ground state of figure 6.8a for IrMn. The blue and green curves are a mirror image of each other. Their shapes reproduce the shapes of the experimental curves given in figure 6.1c [13]:

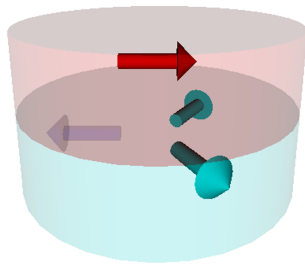


**Figure 6.13:** Schematic representation of the  $3Mn2C$  model. The coupling between the upper red colored Fe spin and the transparent blue colored Mn spin equals zero.

The green curves of the experiment and the simulation show a steep increase of the magnetization at increasing fields and an s-shaped decrease at decreasing fields. Both hysteresis loops are shifted indicating an induced unidirectional anisotropy. The shape depends on the interfacial exchange constant between Mn and Fe. The constant used here is  $J_{\text{int}} = 1.7$  meV. The influence of the exchange constant on the shape of the magnetization curve is further described in section 6.7.1.

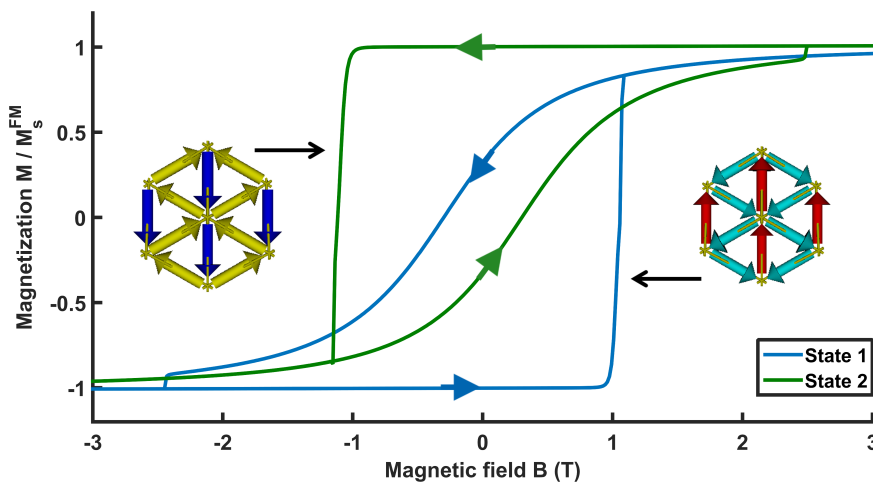


**Figure 6.14:** Magnetization curves of the  $3Mn2C$  model with different initial states. The initial states are illustrated as insets of the figure.

The authors of [13] assume that the antiferromagnetic TAMR is based on a rotation of all spins inside the antiferromagnetic layer [80]. Such a magnetic phase transition of the whole IrMn layer is observed in the simulation. During



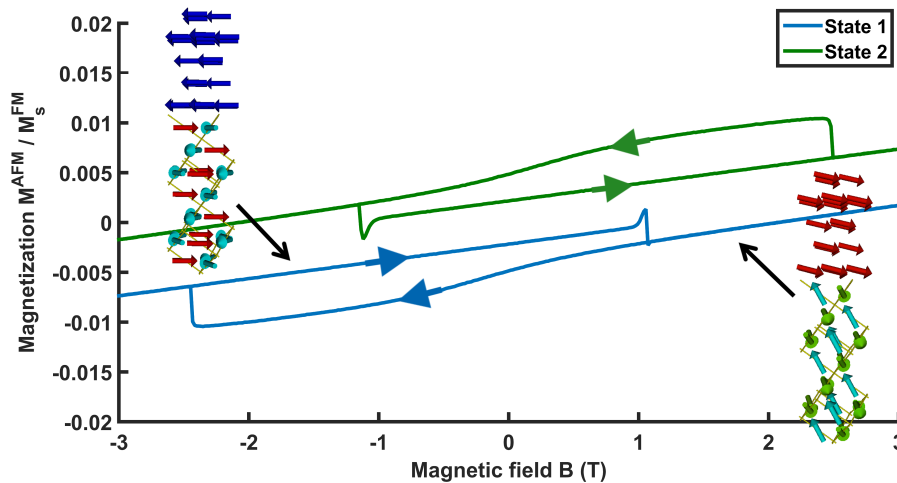


**Figure 6.15:** Magnetization curves of the Mn atoms within the  $3Mn2C$  model at different initial states. The insets illustrate the different states of the stack during the field cycle related to the blue colored magnetization curve.

the field cycle the Mn spin vectors rotate from the initial IrMn state to another ground state configuration at approximately  $B = 1$  T. The magnetization curve of the antiferromagnetically coupled Mn spins is represented in figure 6.15. The initial state and the final state of IrMn<sub>3</sub>, referring to the green curve, are given as insets of this figure. The initial state of the IrMn layer equals the first ground state of figure 6.8a and the final IrMn<sub>3</sub> state can be identified as the eights state of the same figure. As the easy axis of the induced anisotropy of the eights ground state with two exchange coupled Mn spins is not aligned in plane, the curve shape at decreasing fields differs from the shape at increasing fields. At very low fields the Mn spin vectors flip back into the first ground state.

### 6.6.2 Replacement of one Mn spin

Instead of zeroing one of the exchange couplings between Mn and Fe, a replacement of the non-coupled Mn atom by an Ir atom leads to magnetization curves with almost the same characteristic shapes. The related model is denoted by  $2Mn2C$ . Figure 6.16 depicts the ideal IrMn<sub>3</sub> interface and the interface with rearranged Mn spin vectors of the  $2Mn2C$  model.

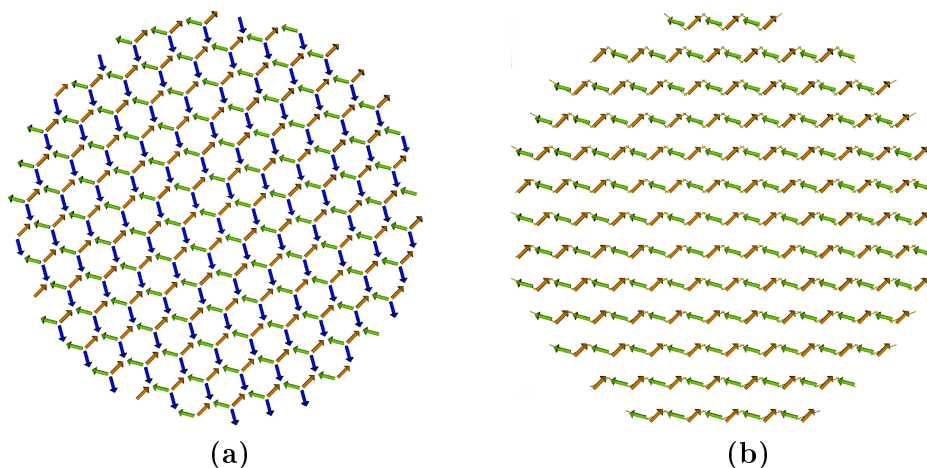


**Figure 6.16:** Interfacial Mn spins of the  $3Mn2C$  model (a) and the  $2Mn2C$  model (b).

At the modified interface the third Mn is replaced by a non-magnetic Ir atom. Therefore the Fe atom at the interface interacts only with two Mn atoms. Without an external field, the Mn spins of the IrMn layer remain nearly in one of the ground states described in section 6.3.3. At the first and second state of IrMn, the Ni and Fe spins are aligned in-plane. These states are again suggested to be the initial states for the calculation of the magnetization loops. Increasing the interfacial exchange constant to  $J_{\text{int}} = 2.2 \text{ meV}$  leads to almost the same magnetization curves as of the  $3Mn2C$  model and thus the experimentally determined curves in [13]. Due to a missing magnetic moment the remaining interfacial spins can follow the field to a larger extent before the state transition occurs. Furthermore the interfacial spins are not fully compensated, which leads to a net magnetization. This net magnetization is much lower than the magnetization of the NiFe layer. The magnetization curves of the two layers and the IrMn layer are depicted in figure 6.17 and figure 6.18 as blue solid lines. The dashed blue lines are the magnetization curves of the effective model with an asymmetrical coupling providing a direct comparison of both effective models. As a rearrangement of the interfacial layer is a probable effect of the application of an magnetic field during growth and annealing of the structure, the effective  $2Mn2C$  model with the explained structural modification is used for further investigations.

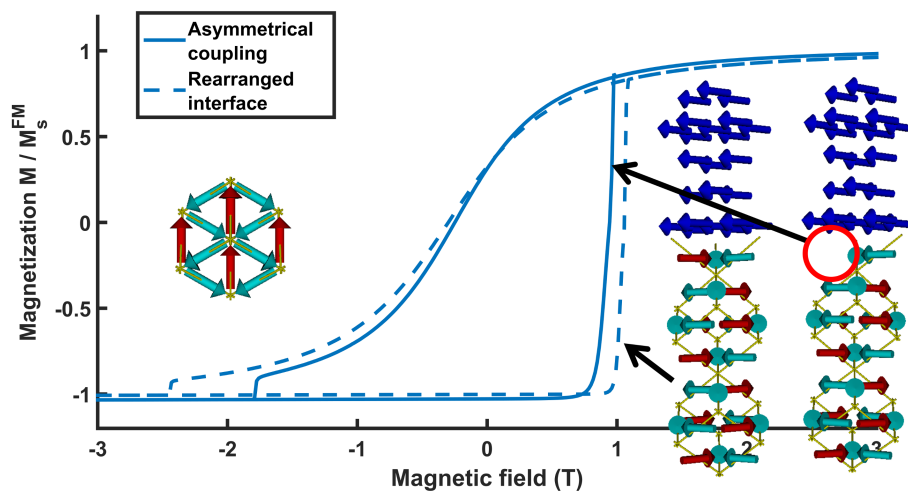


Figure 6.17: Magnetization curves of both layers of the  $3Mn2C$  and the  $2Mn2C$  model.

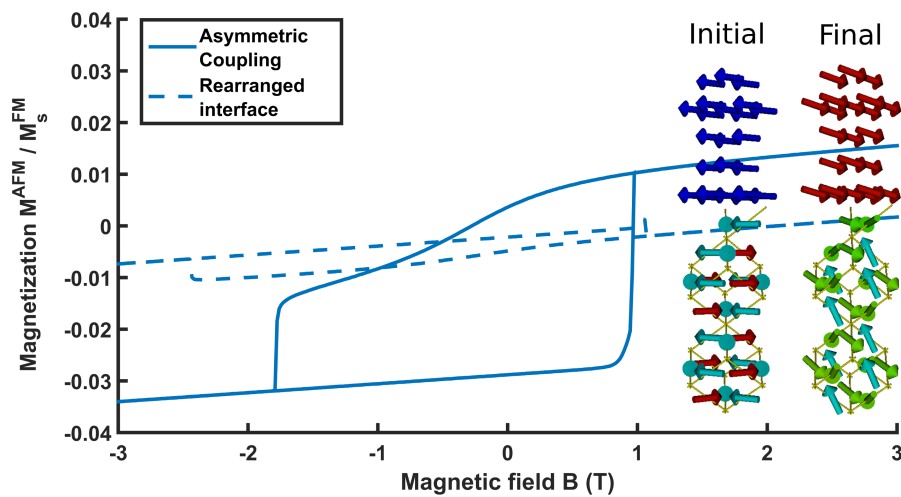


Figure 6.18: Magnetization curves of the antiferromagnetic layers within the  $3Mn2C$  and  $2Mn2C$  model.

## 6.7 Towards qualitative and quantitative comparable magnetization curves

The coercive fields of figure 6.17 are much higher than the measured fields in [13]. Furthermore, a detailed comparison of the experimental curves and the simulation based curves reveals minor differences in the shape. In the following different parameters of the  $2Mn2C$  model are studied to identify the significant criterion leading to qualitative and quantitative comparable magnetization curves.

### 6.7.1 Influence of the exchange coupling constant

The shape of the experimental curves and the shape of the calculated magnetization curves in figure 6.17 differ at decreasing fields. In the simulation a jump of the magnetization is observed. The field value, at which the jumps occurs, can be adjusted by decreasing or increasing the interfacial exchange constants between Fe and Mn. In figure 6.19 six magnetization curves with different exchange constants are depicted.

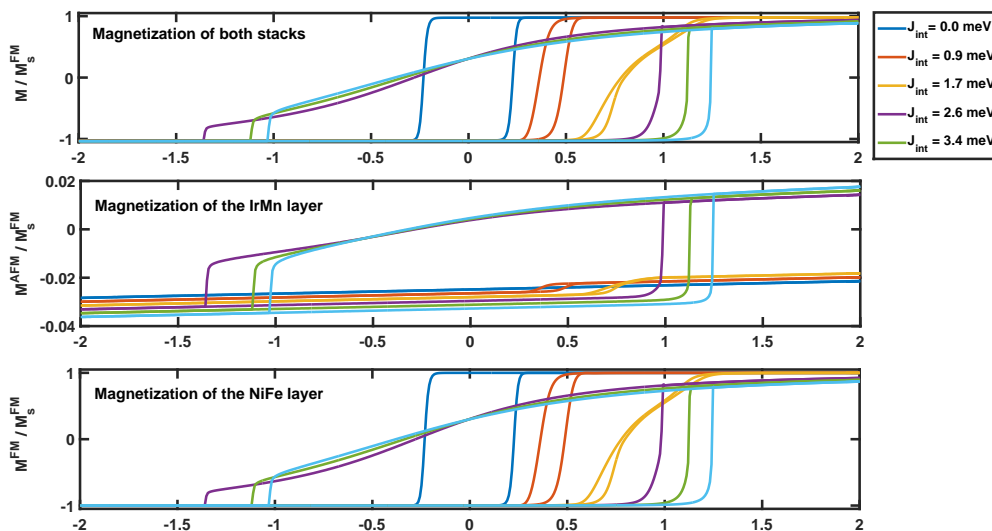


**Figure 6.19:** Magnetization curves of the  $2Mn2C$  model with different interfacial interaction constants  $J_{\text{int}}$ .

Although NiFe is assumed to be isotropic a hysteresis loop is observed at an interfacial exchange constant of  $J_{\text{int}} = 0\text{ eV}$ . The hysteresis loop has a finite

width due to the high sweep rate. The magnetization cannot reach its quasi-static magnetization states during the field cycle. This effect is further studied in section 6.7.4. A weak coupling leads to a shifted magnetization curve with a narrow hysteresis loop width. This behavior is the common exchange bias effect at which the magnetization of the NiFe layer is pinned by nearly fixed spins of the underlying IrMn layer (section 5.2.1). A stronger interfacial exchange coupling constant around  $J_{\text{int}} = 2.6 \text{ eV}$  forces a state transition of the IrMn layer, which leads to a broadening of the hysteresis loop. A further increase of the exchange coupling leads to a considerable jump of the magnetization related to a reordering of the Mn spin vectors into the initial state at the returning cycle of the external field. The stronger the exchange coupling the earlier the second phase transition occurs at decreasing fields. In the following section the exchange constant is adjusted with respect to the experimental results: On one hand the exchange constant has to be high to force a state transition. On the other hand the exchange constant has to be low to prohibit a significant jump of the magnetization at the returning cycle of the field.

### 6.7.2 Influence of the NiFe layer thickness

The coercivity of the effective  $2Mn2C$  model depends strongly on the thickness of the NiFe layer. This dependence is shown in figure 6.20 for  $h = 1 \text{ nm} - 10 \text{ nm}$ . The previously used initial configuration based on the first IrMn ground state is applied here.

Increasing the thickness leads to a decrease of the hysteresis loop width. The shape of the curves is retained: At increasing fields the magnetization rises suddenly and at decreasing fields the magnetization falls slowly in an s-shaped curve. If a rigid magnetization of the NiFe layer is assumed, i.e. the spin vectors of Ni and Fe rotate coherently under the influence of an external field, the upper layer can be modeled by a macrospin approach. The macrospin representing the upper NiFe layer has an effective magnetic moment of  $184.62 \mu_B$ . This approach leads to an appropriate curve depicted in figure 6.21.

At the macrospin model and the model with  $h_{\text{FM}} = 10 \text{ nm}$  the spin reversal of the NiFe layer occurs around  $100 \text{ mT}$ . The shapes of the magnetization at increasing and decreasing field are equal for both effective models. The most striking difference is the field strength at which the IrMn layer flips back into

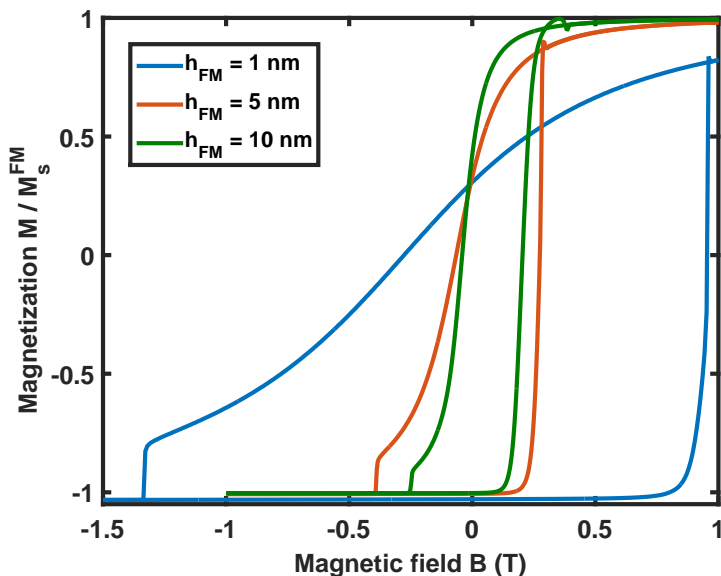


**Figure 6.20:** Magnetization curves of the  $2Mn2C$  model with different layer heights of the ferromagnetic NiFe layer.

its initial state.

### 6.7.3 Influence of the lateral dimensioning

The cylindrical models, which are used in the previous sections, have a radius of  $r = 0.27$  nm. They consist of four stacked cells as depicted in figure 6.3. Two unit cells represent the IrMn layer, followed by one cell which is composed of IrMn and NiFe modeling the interface. The fourth cell represents the NiFe layer with a thickness of 1 nm. Several NiFe unit cells are added to represent a 10 nm thick NiFe layer. Most of the atoms are located at the boundary of the model, so that these atoms have less next neighboring atoms. In comparison, structures of large lateral dimensions have an almost neglecting number of boundary atoms in contrast to the number of bulk atoms. Hence at large structures, the magnetic behavior is mainly affected by the bulk. The impact of the dangling spins at the models of restricted dimensions is determined by two different approaches. In a first approach, the radius of the effective  $2Mn2C$  model described in section 6.6.2 is increased to  $r = 0.56$  nm. Hence all atoms of the inner unit cell are surrounded by next neighboring atoms. The interfacial layers of the model with  $r = 0.56$  nm is depicted in figure 6.22.

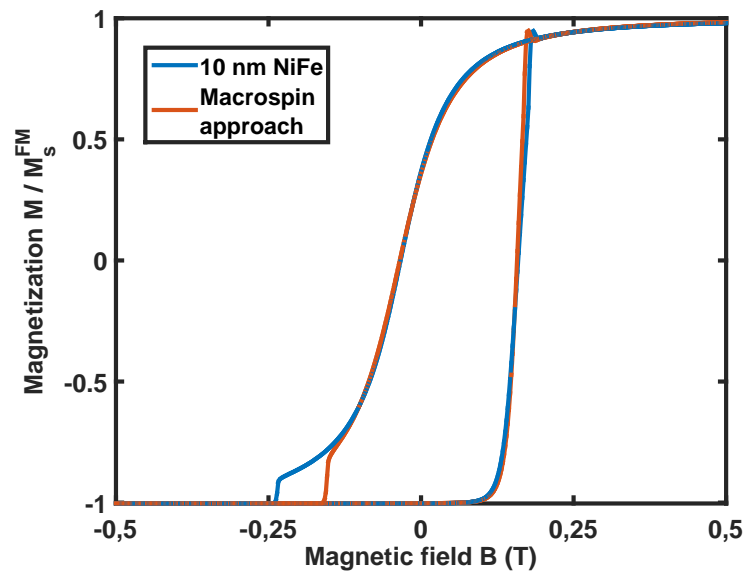


**Figure 6.21:** Magnetization curves of the  $2Mn2C$  model with an NiFe layer height of  $h_{FM} = 10$  nm and the  $2Mn2C$  model with a macrospin representation of the NiFe layer.

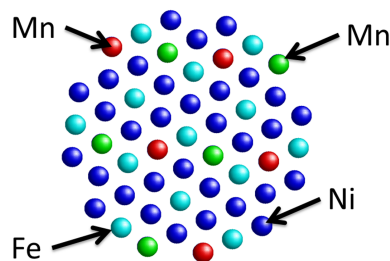


**Figure 6.22:** Representation of the interfacial Ni (blue colored), Fe (light blue colored) and Mn (green and red colored) atoms of the cylindrical  $2Mn2C$  model with a radius of  $r = 0.56$  nm.

A second approach is an implementation of periodic boundary conditions (PBC) based on the effective  $2Mn2C$  model with  $r = 0.27$  nm. The two-dimensional periodic boundary conditions are implemented by using a hexagonal unit cell as indicated by a green line in figure 6.23.

The model has been extended by shifted unit cells, which are illustrated by crosses of different colors. Atoms of these images represent the neighboring

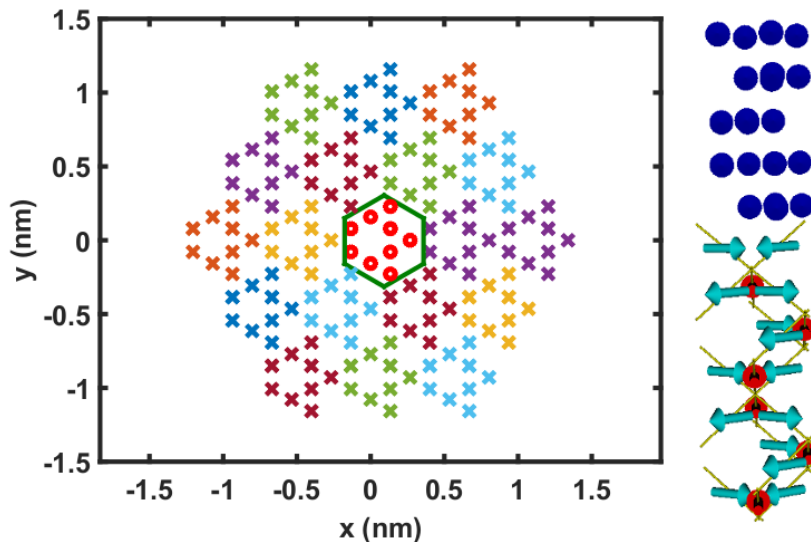


**Figure 6.23:** Illustration of the periodic boundary conditions applied to the  $2Mn2C$  model. Left: Representation of the computational cell and the image cells. Only the Mn atoms are shown. Right: Spins of computational cell.

atoms of those within the unit cell. During the calculation only atoms of the inner unit cell are taken into account. Therefore an infinite structure is modeled by a single unit cell given on the right hand side of figure 6.23.

Figure 6.24 shows the related hysteresis curves of both approaches with an interfacial exchange constant of  $J = 2.15$  meV. A third curve represents the magnetization of the  $2Mn2C$  model with a radius of  $r = 0.27$  nm.

Both approaches lead to similar results: In comparison to the  $2Mn2C$  model with many dangling atoms, the coercive field is decreased. Apart from the coercivity the shape of the curves remains asymmetric with an abrupt increase and a slow decrease of the magnetization. At the model with periodic boundaries an earlier reversal at the decreasing field branch is observed. This difference may occur due to the boundary atoms of the 0.56 nm model. In the approach with periodic boundaries, the sample is assumed to be infinite without any boundary atoms in the lateral dimension. By contrast, at a model with an increased radius, the ratio of boundary to bulk atoms is only decreased to a smaller, but finite, value.



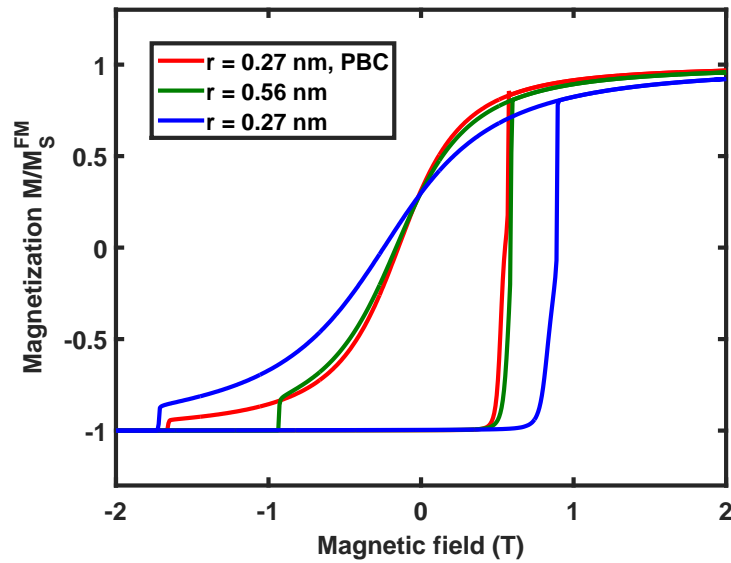


**Figure 6.24:** Magnetization curves of the  $2Mn2C$  model with two different cylindrical radii or with the application of periodic boundaries.

#### 6.7.4 Influence of the sweep rate

Because of the huge computational effort the field sweep is restricted to high frequencies in the GHz-range. Therefore the spin vectors cannot reach their quasi-static magnetic states at each field value during a calculation of a hysteresis loop in short computational time. One resulting effect can be seen in figure 6.19. A finite loop width is observed in all cases. This includes the case, at which IrMn and NiFe layers are not exchange coupled. It should be noted, that no anisotropy of the ferromagnetic layer is taken into account. The finite loop width of the blue line in figure 6.19 is just caused by the high sweep rate. The magnetization curves of the exchanged coupled two layered stack are depicted for different sweep rates in figure 6.25.

The curves above are based on a cylindrical  $2Mn2C$  model without periodic boundaries. The radius is  $r = 0.27$  nm. The thickness of the layers are 1.5 nm (IrMn) and 1 nm (NiFe). The first seven nearest neighbor shells within the IrMn and NiFe layers are taken into account. The atoms of the interfacial layers are exchange coupled with a coupling constant of  $J = 2.6$  meV. The calculation of the magnetization curve with a sweep rate of  $8$  T/ $\mu$ s takes around

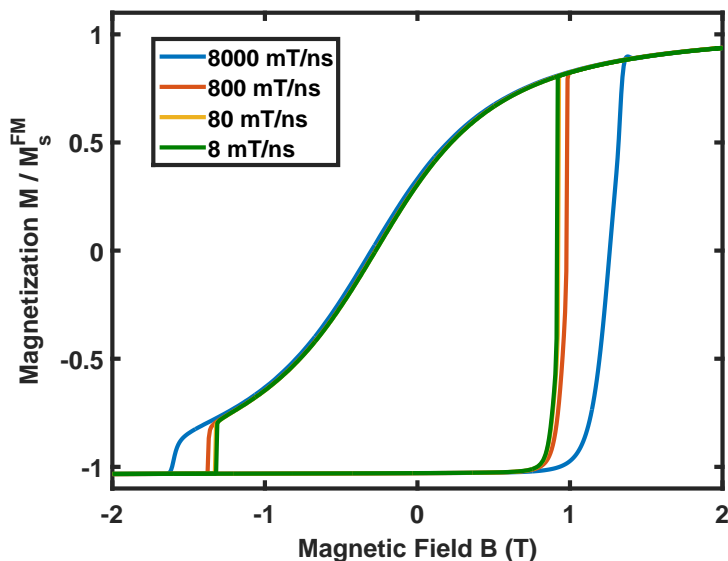


**Figure 6.25:** Magnetization curves of the  $2Mn2C$  model resulting from different sweep rates of the applied magnetic field.

25 h computational time on a single processor. A parallel computation of the magnetization curve as described in chapter 4.3 is not applicable for the NiFe/IrMn stack (cf. section 6.4). By comparing the yellow and green curve in figure 6.25 one finds that a sweep rate of 80 mT/ns is sufficient to get a quasi-static magnetization curve for the described model.

## 6.8 Switching by high magnetic fields at finite temperatures

In the supplementary information of [13] it is stated that the sign of the TAMR signal can be reversed by applying a high magnetic field of 10 T which is visualized in figure 6.26.

A negative magnetic field during growth and annealing leads to the blue magnetization curve shown in figure 6.1c. Applying a field of 10 T before the magnetization measurement results into the green curve shown in figure 6.1c at the measurement.

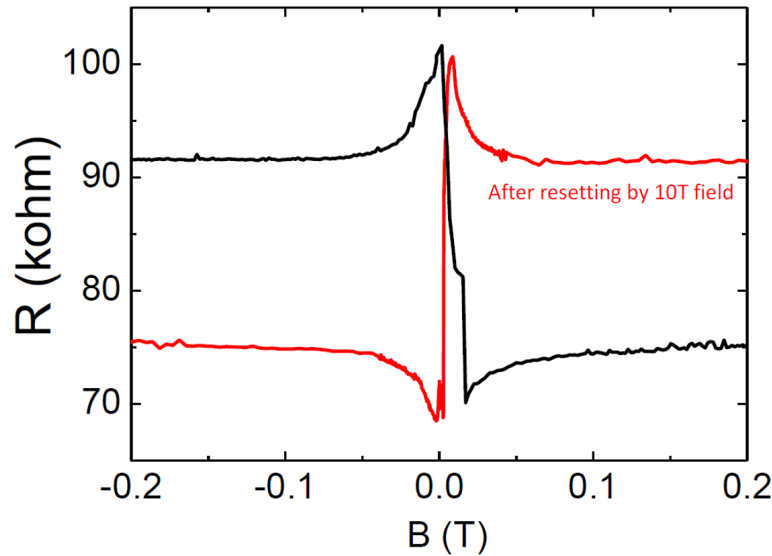


**Figure 6.26:** The magnetic field dependent resistance measured before and after applying a high magnetic field pulse. Reprinted by permission from Macmillan Publishers Ltd. [Nat. Mater.] Park *et al.*, 10, 5, copyright 2016.

### 6.8.1 Applying a high magnetic field pulse

In the following the effective model described in section 6.6.2 is used to study the impact of a high magnetic field pulse. A macrospin approach, as explained in section 6.7.2, cannot be used with finite temperatures without further improvements of the effective magnetic moments of each macrospin (cf. section 3.4). Therefore the number of atoms representing the NiFe layer has not been reduced. Figure 6.27 shows the final states of the effective model after applying a rectangular field pulse of 10 T for 0.5 ns at different temperatures.

Without a finite temperature or at almost 0 K, the high field has no influence on the hysteresis loop. The first state of figure 6.27 represents the final state at almost 0 K. In this case only the Ni and Mn spins are rotated due to the external field. The Mn spins remain at their initial orientation. Thus, no switching is expected by applying a high field pulse at  $T = 0$  K. Increasing the temperature to 1 K, the Mn spins rotate from their initial state into the second state of figure 6.8a after 1 ns. The final state is recognized as the initial state of the green curve of figure 6.14. Thus, the curve is switched by a high field pulse at finite temperatures. The same behavior could be observed at 2 K

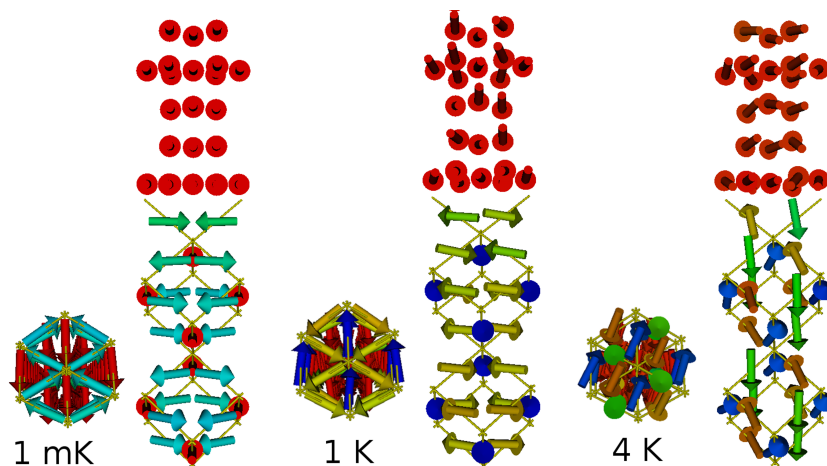


**Figure 6.27:** Final states of the  $2Mn2C$  model after applying a rectangular field pulse of 10 T with duration of 0.5 ns at different temperatures.

and 3 K, but with stronger fluctuations of the spin vectors. At 4 K the states of IrMn seem to vary randomly between different states of figure 6.8a. Such a random state transition of the spins within the antiferromagnetic layer is discussed in section 6.9.1 as well.

## 6.8.2 Applying a magnetic field ramp

Instead of applying a high magnetic field pulse, the field is increased from  $B = 0$  T to  $B = 10$  T in 1 ns at a temperature of 1 mK. In this case a IrMn state transition from the first state to eighth state is observed at 1 T.

The evolution of the states depends on the time dependent function of the external field. In case of a high field pulse, the Zeeman term of the Hamilton in equation 6.1 dominates the magnetic behavior. In opposite, the field strength and the related energies are low during the first time steps in the case of a field ramp. Hence, solving the time dependent Landau-Lifshitz equation (section 3.2.1) leads to a different evolution of the states, which can be seen in figure 6.28.

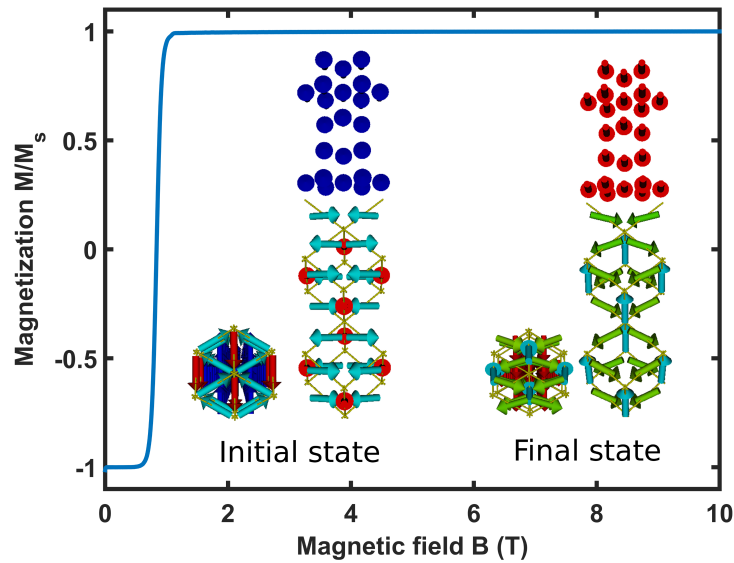


**Figure 6.28:** Magnetization curve due to an applied field ramp. The insets represent the initial (left) and the final (right) magnetic state of the  $2Mn2C$  model.

## 6.9 Atomistic spin dynamics of NiFe/IrMn at finite temperatures

In [80] the temperature dependence of the exchange bias stacks NiFe(10 nm)/IrMn(1.5 nm<sub>3</sub> nm) are studied by the superconducting quantum interference device (SQUID) and TAMR measurements. Within a SQUID measurement the hysteresis loop of the stack is obtained. Angular depended TAMR measurements are providing information about the spin states of the antiferromagnetic IrMn layer. Figure 6.29 depicts the SQUID results at 5 K, 50 K and 100 K from [80].

The stacks with an 3 nm and an 1.5 nm thick IrMn layer show the same characteristic at different temperatures. Thus, the effects are categorized into three temperature ranges:

- Low temperature range

The hysteresis loops are asymmetric and horizontally shifted. The width of the loops are enhanced.

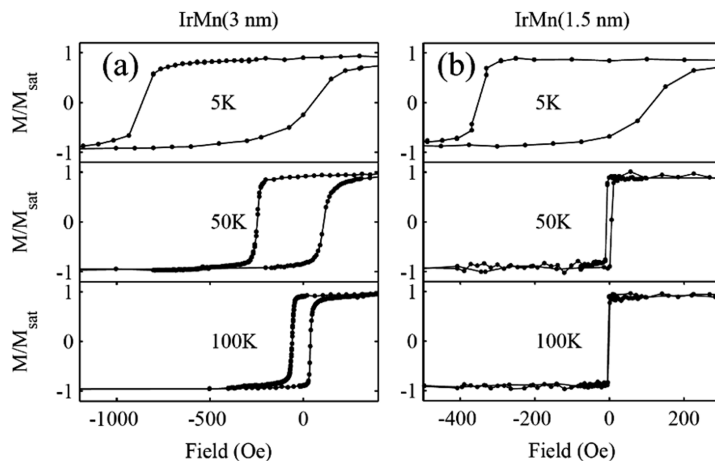


**Figure 6.29:** Magnetization curves of the NiFe/IrMn stack with a IrMn layer height of 3 nm (left) and 1.5 nm (right) at different temperatures. Reprinted figure with permission from Martí *et al.*, Phys. Rev. Lett., 108, 017201, 2012. Copyright 2016 by the American Physical Society.

- Mid temperature range  
At this temperature range the hysteresis loops are symmetric. The enhancement of the coercivity is still present. The shift of the hysteresis loops decreases with increasing temperature.
- High temperature range  
The loops are not shifted anymore and the coercivity is approximately zero.

In the following the results of the temperature dependent calculations regarding the effective  $2Mn2C$  model with a NiFe layer thickness of 10 nm are presented and compared to those of [80]. It is supposed that periodic boundaries with a rather small computational cell in conjunction with finite temperatures might lead to wrong results. This supposition is based on correlation of the fluctuations caused by the periodic boundaries. Temperature is induced by adding a fluctuation term to the Landau-Lifshitz equation. This term leads to an additional random variation in the orientation of each spin vector. As the neighboring spins of the image cells are those of the unit cell, these spins would obtain the same fluctuations. This correlation might permit a non-physical thermal agitation of the complete structure. To apply periodic boundary con-

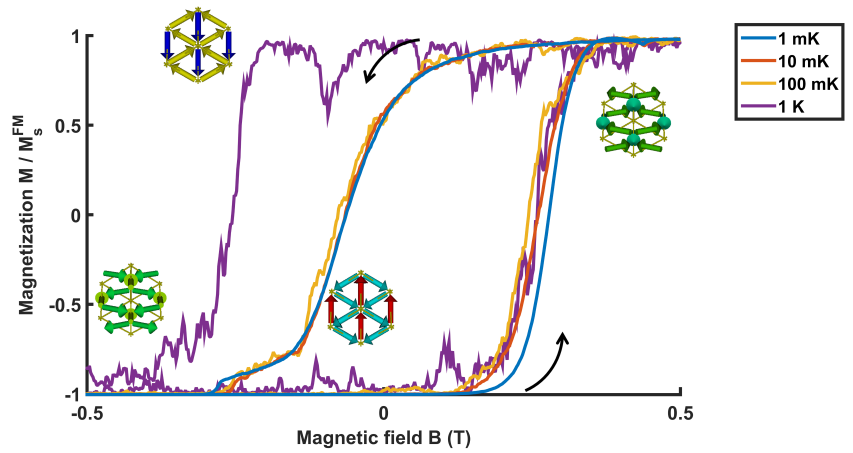
ditions with such a small unit cell as illustrated in figure 6.23, it has to be ensured that this method leads to physical results especially for simulations at finite temperatures. Thus the calculations at finite temperatures are based on the  $2Mn2C$  model without periodic boundaries. The cylindrical model is restricted to a radius of  $r = 0.27$  nm.

### 6.9.1 Temperature dependence of the 1.5 nm IrMn sample

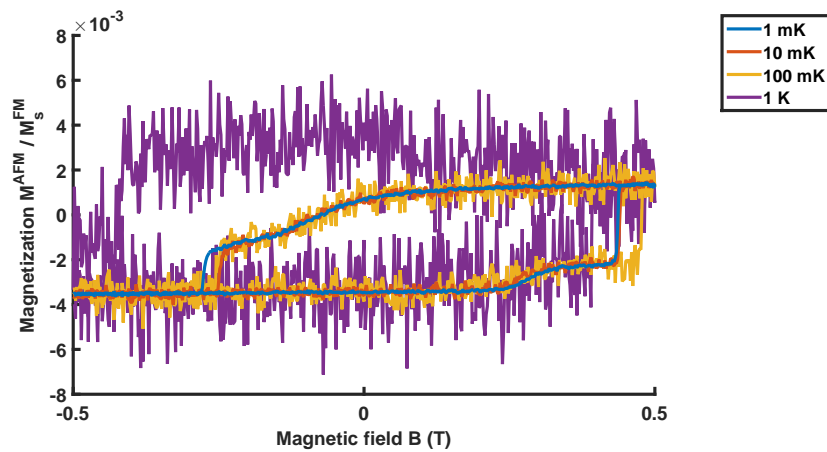
The magnetization curves of the 1.5 nm IrMn sample with an interfacial exchange coupling constant of  $J_{\text{int}} = 2.59$  meV are shown in figure 6.30. From this figure two different temperature ranges are identified. These temperature ranges correspond to the low and mid temperature range of the description above.

The single trajectories of the magnetization at a temperature up to 100 mK exhibit a loop shift and an enhancement of the coercivity. Furthermore, these curves are asymmetric. The curve shape becomes reasonable by the consideration of the occurring spin states during the field cycle. The antiferromagnetic coupled spins undergo a spin reversal from the first to the seventh state and return to their initial state at the decreasing field branch of the hysteresis loop calculation. This is the same behavior as described in the former sections without temperature fluctuations. A significant difference is observed at a higher temperature of 1 K. The magnetization loop is symmetric and the coercivity is enhanced. The loop is centered around the zero field axis. Apart from the zero loop shift, these properties correspond to the mid temperature range of the former list. The related state transitions are represented as insets of figure 6.30a. At 1 K the antiferromagnetic layer pass through a  $180^\circ$  spin reversal, which leads to a symmetric and non-shifted hysteresis loop.

If the temperature is further increased, the antiferromagnetic IrMn layer changes its magnetic state independently of the external magnetic field. The thermal fluctuations exceed the impact of the interfacial exchange coupling between the ferromagnetic and the antiferromagnetic layer. All eight states of figure 6.8a have been observed. This behavior explains the decreasing shift and the approximately zero hysteresis loop width in the high temperature range.



(a) Hysteresis loops of the ferromagnetic NiFe layer.



(b) Hysteresis loops of the antiferromagnetic IrMn layer.

**Figure 6.30:** Temperature dependence of the NiFe/IrMn with a 1.5 nm thick antiferromagnetic layer. Only single trajectories of the magnetization are illustrated.

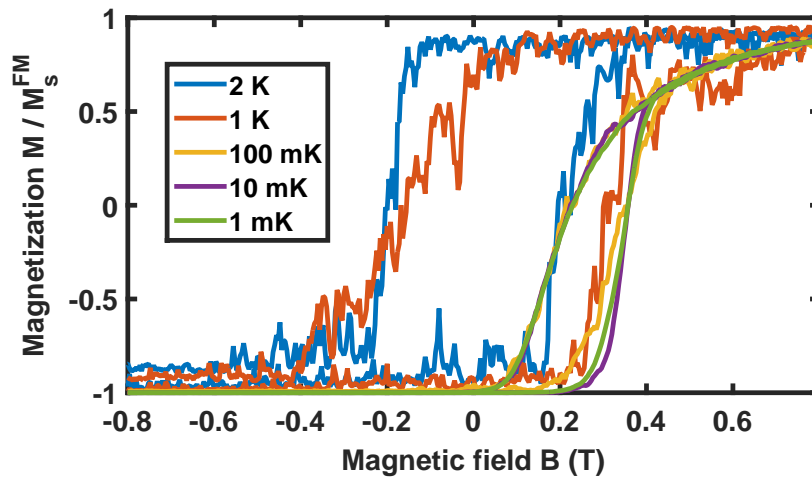


### 6.9.2 Temperature dependence of the 3 nm IrMn sample

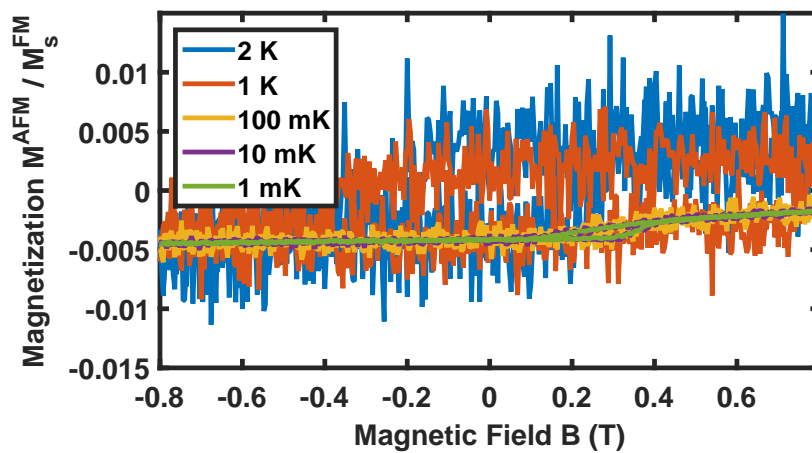
An increase of the IrMn layer thickness to 3 nm changes the magnetic behavior. With an exchange coupling constant of  $J_{\text{int}} = 2.59 \text{ meV}$ , the Mn spins keep their initial orientations during the complete hysteresis cycle in the low temperature range. The NiFe spins are exchange biased and reverse their magnetization as soon as the external field exceeds the energy barrier resulting from the interfacial coupling. This behavior is comparable to an idealized MB model (section 5.2.1). This effect occurs also from a low interfacial coupling as shown in section 6.7.1.

As the experimental curves of the 3 nm thick IrMn sample indicate a rotation of the antiferromagnetic coupled spins, the interfacial constant of the  $2Mn2C$  model should be increased. A macrospin approach has been used to speed up the determination of the interfacial constant, which causes a spin rotation of the antiferromagnetic layer (cf. section 6.7.2). It has been observed that the exchange constant has to be increased to a value of approximately 5.2 meV to force a state transition from the first to the seventh state at increasing fields. That is around twice the value of the  $2Mn2C$  model with a 1.5 nm thick IrMn layer. The macrospin approach leads to slightly lower coercivities at the field decreasing branch. To ensure a state reversal, the interfacial exchange constant is increased to 6.0 meV for the finite temperature calculations with an atomistic representation of the NiFe layer. The magnetization curves of the stack with a 3 nm IrMn layer and  $J_{\text{int}} = 6.0 \text{ meV}$  are represented in figure 6.31. The sweep rate of the field has been increased to 1 T/ns to reduce the computational times in spite of a necessarily decrease of the time step length (cf. section 3.2.1).

Although the macrospin model shows a state transition from the first to the eighth IrMn state at low temperatures, this transition is not recognized at the model with a 10 nm thick NiFe layer. Instead an exchange spring behavior (cf. section 5.3.3) is observed for temperatures up to 100 mK. The uppermost Ni and Fe spins reverse their magnetization completely with the external field. The ferromagnetic and antiferromagnetic spins near the interface obtain a slight rotation. At a temperature of 1 K the spins rotate from the first state in figure 6.8a to the third state at increasing field cycle. At the decreasing field cycle a transition from the third state to fifth state is observed. Just a



(a) Hysteresis loops of the ferromagnetic NiFe layer.



(b) Hysteresis loops of the antiferromagnetic IrMn layer.

**Figure 6.31:** Temperature dependence of the NiFe/IrMn with a 3 nm thick antiferromagnetic layer. Only single trajectories of the magnetization are illustrated.

slight increase of the temperature to 2 K leads to a  $180^\circ$  reversal of the spins as described in the previous section for the mid temperature range.

The high temperature case is not further studied. If the temperature would be increased to higher values, the time steps within the Landau-Lifshitz equation (section 3.2.1, equation 3.15) have to be reduced to prevent a change of the spin length. A reduction of the time step length leads to an enormous increase of the computational time. Furthermore, a calculation of a single trajectory becomes insufficient to determine the hysteresis loops. Thus, the magnetization has to be sampled and averaged over many cycles, which also increases the computational effort.

## 6.10 Comparison with experimental properties and conclusion

Different effective models have been implemented to reproduce the magnetic behavior of the NiFe/IrMn stack described in [13] and [80] qualitatively. To calculate the spin dynamics of a multilayer stack is a very time consuming task, especially the calculation of quasi-static hysteresis loops. Therefore a macrospin approach and the implementation of periodic boundary conditions have been used to decrease the computational effort. With these methods, the magnetic behavior of the most promising  $2Mn2C$  model has been studied in detail. Based on the ground states of an ordered IrMn<sub>3</sub> structure, the  $2Mn2C$  model is used to explain nearly all experimentally observed properties:

- At low temperatures the hysteresis loop is shifted in the experiment and in the calculation results. A shift of the hysteresis loop occurs due to the common exchange bias effect. Spins of the NiFe layer are interfacially coupled to spins of the antiferromagnetic layer.
- The asymmetric shape of the hysteresis loop at low temperatures described in [13] and [80] can be explained by the state transition of the antiferromagnetic layer. The Mn spins reverse from the first (second) to the eighth (seventh) state of figure 6.8a during the field cycle of a slowly changing magnetic field. Each state induces a unidirectional anisotropy

with a different easy axis leading to a different evolution of the magnetization at the increasing and decreasing field branch.

- In the experiment the TAMR signal of high positive and high negative fields differs at low temperatures. The authors of [80] conclude that this signal is related to a spin reversal into a meta-stable state with a rotation angle of each spin less than  $180^\circ$ . This conclusion equates the observed state transitions in the calculation. In both initial states the antiferromagnetic spins are aligned in-plane. After the transition into the seventh or eighth state each spin has an out-of-plane component. This may lead to a different TAMR signal at high positive and negative fields.
- At low and medium temperatures the coercivity is enhanced compared to a sample without IrMn [80]. The enhancement results from the interfacial exchange coupling between the antiferromagnetic and the ferromagnetic layer. With the used interfacial exchange constant, a rotation of the NiFe spins leads to a spin reversal of the IrMn layer. Such a broadening of the hysteresis loop is also explained within the Meiklejohn and Bean model (section 5.2.1).
- At medium temperatures the exchange bias field decreases, but the loop width is still enhanced [80]. In the calculation it is observed that higher temperatures lead to a full spin reversal at high magnetic fields. In this case the hysteresis loop is enhanced but centered around the zero field axis. This is in agreement with the measured TAMR signal and the explanations in [80].
- At high temperatures the coercivity of the NiFe/IrMn/MgO/Pt becomes approximately zero, which equates the coercivity of pure NiFe. The calculations at higher temperatures of 2 K (1.5 nm stack, section 6.9.1), indicate the same result. With increasing temperature, the fluctuations overcome the exchange coupling of both layers. Thus, the magnetic behavior of the upper NiFe layer becomes independent from the lower IrMn layer.

- In [13] it is described that the TAMR signal is switchable by applying a high magnetic field pulse of 10 T. This effect is related to a full spin reversal of the antiferromagnetic layer. The reversal occurring from a high field pulse is fully reproduced by the simulation and described in section 6.8.1.

In contrast to the assumption by Park *et al.* [13], no decisive spring like rotation of the spins within the antiferromagnetic material is observed. Instead most of the experimentally findings are explainable by an abrupt state transition of these spins.

The major differences between the  $2Mn2C$  model and the experimental results are the quantitative values regarding the coercive fields and the temperature ranges. Assuming that all material parameters are properly chosen, the interfacial exchange constant of the  $2Mn2C$  model remains unknown. The strength of the exchange coupling has a direct impact on the shape of the hysteresis curve and the state transitions at finite temperatures. As the  $2Mn2C$  model is just an effective model, it is probable, that the true interfacial structure differs from the assumption of a symmetric interface with a regular replacement of each third Mn atom by an Ir atom. However, the observed state transitions at the  $2Mn2C$  model may occur at experimental structures as well. The minor differences in the curve shape, the more important differences at the temperature values and the coercive fields might disappear by an irregular interfacial structure and a thermal averaging.



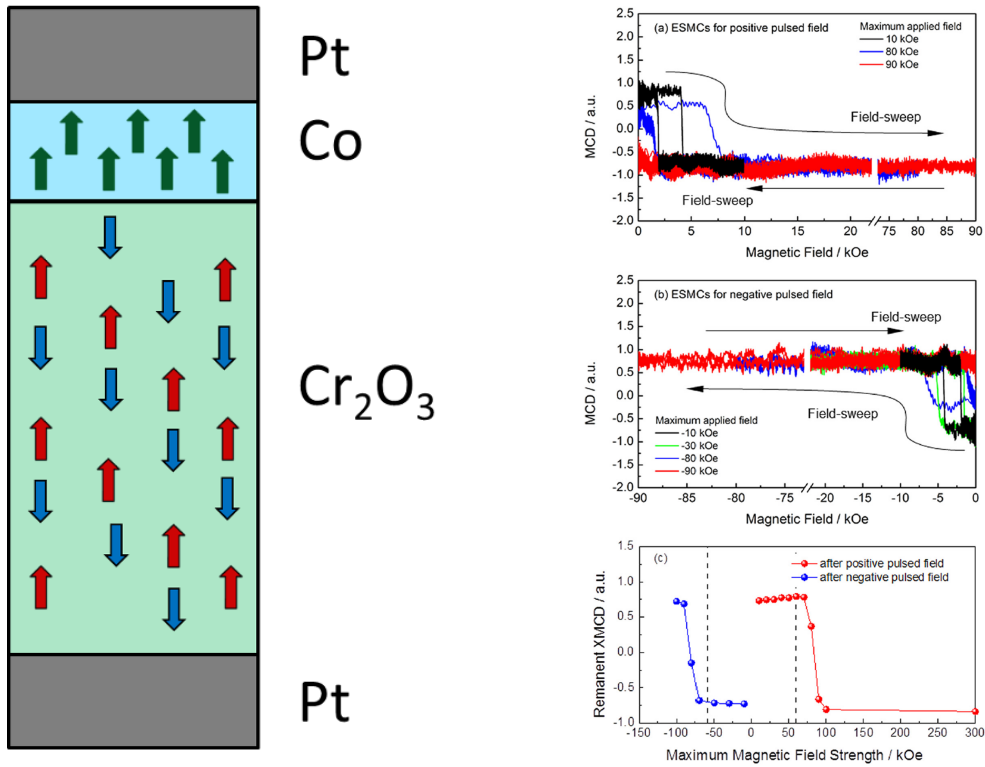
# Chapter 7

## Exchange Bias: Pt/Co/Cr<sub>2</sub>O<sub>3</sub>/Pt

The second exchange bias system in this thesis is the Pt/Co/Cr<sub>2</sub>O<sub>3</sub>/Pt multilayer. The stack is schematically represented in figure 7.1a. The Pt layer induces a perpendicular anisotropy at the thin Co layer. The Cr atoms of the Cr<sub>2</sub>O<sub>3</sub> layer exhibit a perpendicular anisotropy as well. The induced uniaxial anisotropy of Co is superimposed by a unidirectional anisotropy caused by the interfacial exchange coupling between the Cr and Co atoms. Hence the system under investigation is a perpendicular exchange bias (PEB) stack. PEB stacks are of high interest for spintronics as these stacks are highly integrable and less power consuming compared to in-plane magnetic multilayer systems [81, 82]. Furthermore, the direction of the unidirectional anisotropy of Pt/Co/Cr<sub>2</sub>O<sub>3</sub>/Pt can be switched by either a high magnetic field [14] (figure 7.1b) or by applying a magnetic and an electric field simultaneously (figure 7.5). Therefore, this effect offers an additional functionality of spin valves.

### 7.1 Significant characteristics of the multilayer Pt/Co/Cr<sub>2</sub>O<sub>3</sub>/Pt stack

The exchange bias effect is commonly explained by the existence of uncompensated spins of the antiferromagnetic layer, which stay fixed during a spin reversal of the ferromagnetic spins [51]. To understand the role of the uncompensated spins at the Co/Cr<sub>2</sub>O<sub>3</sub> interface, the Pt(1.0 nm)/Co(0.5 nm)/Cr<sub>2</sub>O<sub>3</sub>(120 nm)/Pt(20 nm) stack has been grown and experimentally studied

(a) Pt/Co/Cr<sub>2</sub>O<sub>3</sub>/Pt stack.(b) Pt/Co/Cr<sub>2</sub>O<sub>3</sub>/Pt magnetization curves.

**Figure 7.1:** (a) Schematic representation of the Pt/Co/Cr<sub>2</sub>O<sub>3</sub>/Pt stack. (b) Element specific magnetization curves for positive and negative applied field pulses (upper figures). Illustration of the switching in dependence on the remanence of the maximum applied magnetic field strength. Reprinted from Y. Shiratsuchi *et al.*, Appl. Phys. Lett., 100, 262413, 2012. With the permission of AIP Publishing.



by Shiratsuchi *et al.* [16]. The sample has been heated up to  $T = 315$  K, which is above the Néel temperature of  $\text{Cr}_2\text{O}_3$ . Afterwards the stack is cooled down to  $T = 235$  K and to  $T = 180$  K in an applied external field of  $B = \pm 0.4$  T. The experimental results show that the exchange bias effect appears suddenly at temperatures lower than  $T = 235$  K (figure 7.3). At  $T = 180$  K vertical shifts of the Cr hysteresis loops could be observed. The related element-specific magnetization curves determined from x-ray magnetic circular dichroism (XMCD) are shown in figure 7.3 and 7.4. The vertical shifts of the Cr hysteresis loops and the XMCD signals indicate the existence of uncompensated unreserved Cr spins. The coercivity of the system decreases to 25% at  $T = 180$  K compared to the the coercivity at  $T = 235$  K.

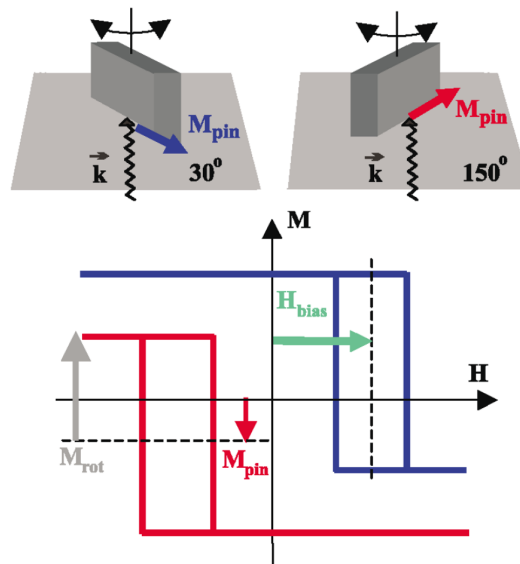


**Figure 7.2:** Vertical and horizontal shift of the hysteresis loops of an exchange bias stack. The vertical shift is caused by unreserved uncompensated spins. Reprinted figure with permission from H. Ohldag *et al.*, Phys. Rev. Lett., 91, 017203,2003. Copyright 2016 by the American Physical Society.

The ratio of unreserved and reversed uncompensated spins can be obtained by the vertical shift of the Cr XMCD signal in figure 7.4. Figure 7.2 illustrates the magnetization of the pinned spins, which do not change their orientation in an external field and the rotatable spin, which reverse their orientation during the

field cycle. In the case of Pt/Co/Cr<sub>2</sub>O<sub>3</sub>/Pt, around 33 % of the uncompensated AFM spins would be pinned and do not reverse their magnetization.

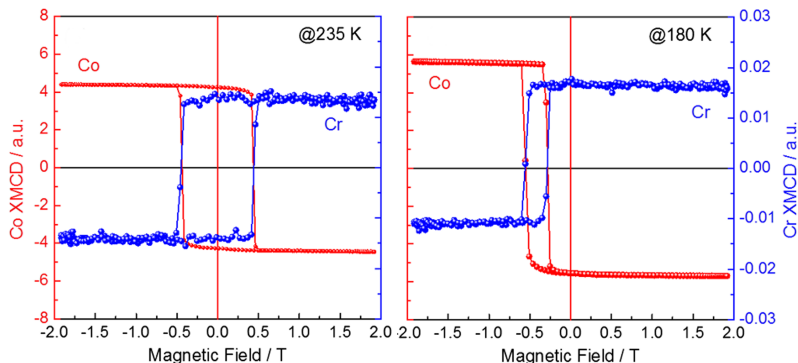


**Figure 7.3:** Element specific hysteresis loops of Co and Cr at  $T = 235$  K and  $T = 280$  K. At lower temperatures, a shift of the hysteresis loops appears. Reprinted figure with permission from Y. Shiratsuchi *et al.*, Phys. Rev. Lett., 109, 077202, 2012. Copyright 2016 by the American Physical Society.

In many exchange bias systems, the existence of pinned spins could not be proofed. The authors of [17] believe, that this may be related to the fact, that the fraction of pinned spins is very tiny. A high ratio, like 33 %, would lead to a greater shift of the Cr hysteresis loops. Therefore, the authors of [16] suppose, that the uncompensated Cr spins do not fully reverse its magnetization. Instead of a full reversal, the interfacial Cr spins are canted.

Another significant property of the Pt/Co/Cr<sub>2</sub>O<sub>3</sub>/Pt system is the shape of the hysteresis curves in figure 7.5, which has been captured to highlight the magnetoelectric (ME) effect in [15]. Here, the experimentally studied Pt(5 nm)/Co(0.8 nm)/Cr<sub>2</sub>O<sub>3</sub>(200 nm)/Pt(20 nm) stack differs only in the thickness of the layers compared to the stack described in [16]. Before the measurements the system is heated up above the Néel temperature of Cr<sub>2</sub>O<sub>3</sub> and cooled down to  $T = 253$  K in an external field of  $B = \pm 0.6$  T, which is slightly higher than in [16]. The curves of figure 7.5 represent the signal of an anomalous hall measurement (AHE), which is proportional to the magnetization of the stack. At the system under consideration, the sign of the exchange field can be reversed by applying a magnetic and electric field simultaneously. Both hysteresis loops

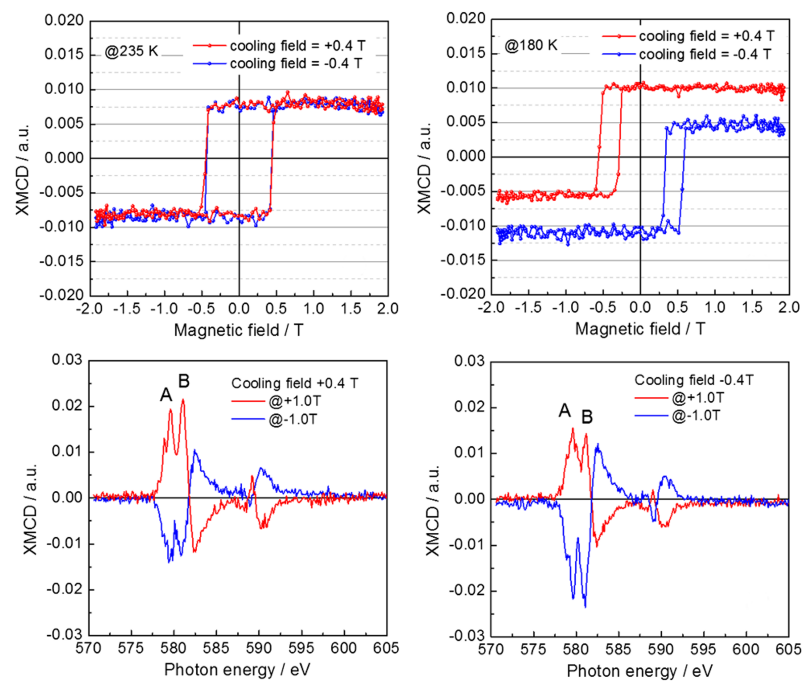


**Figure 7.4:** Element specific hysteresis loop signals of Cr at  $T = 235$  K and  $T = 280$  K after field cooling at negative and positive fields (upper figure). XMCD signal at  $\pm 1$  T at both temperatures (lower figure). Reprinted figure with permission from Y. Shiratsuchi *et al.*, Phys. Rev. Lett., 109, 077202, 2012. Copyright 2016 by the American Physical Society.

are mirror images of each other and both are not symmetric regarding the horizontal axis. The curved shape of the red (blue) line near positive (negative) saturation indicates a complex energy landscape.

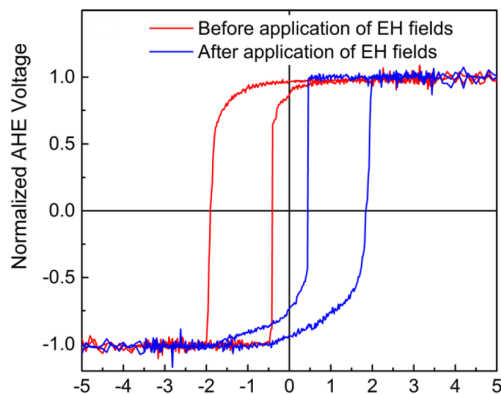


**Figure 7.5:** Different magnetization curves resulting from AHE measurements before and after magnetoelectric switching. Reprinted from K. Toyoki *et al.*, Appl. Phys. Lett., 106, 162404, 2015. With the permission of AIP Publishing.

Simple models, like the Meiklejohn-Bean model described in section 5.2.1, lead to shifted, but symmetric hysteresis loops. In the case of Pt/Co/Cr<sub>2</sub>O<sub>3</sub>/Pt the magnetization before (after) switching exhibits an abrupt change at the coercive fields near negative (positive) saturation.

In a simplified picture, the exchange bias field  $H_{\text{EB}}$  decreases with increasing temperature, as the thermal fluctuations overcome the energy barrier of the unidirectional anisotropy at lower fields. For the same reason, the width of the hysteresis loop narrows [53]. The temperature dependence of the exchange bias field at Co/Cr<sub>2</sub>O<sub>3</sub> differs from the temperature dependence of this picture, as it exhibits an increasing and a decreasing branch [82]. The exchange bias field is proportional to the unidirectional anisotropy energy  $J_K = M_s H_{\text{ext}} t_F$ , which is shown in figure 7.6a.  $t_F$  denotes the thickness of the ferromagnetic Co layer and  $M_s$  denotes its saturation magnetization.

The blocking temperature, i.e. the temperature at which the exchange bias field becomes zero, depends on the thickness of the layers. Figure 7.6a shows the exchange bias field from 80 K to 320 K for different Cr<sub>2</sub>O<sub>3</sub> layer thicknesses  $t_{\text{Cr}_2\text{O}_3}$ . The blocking temperature at thinner layers decreases, while the shape

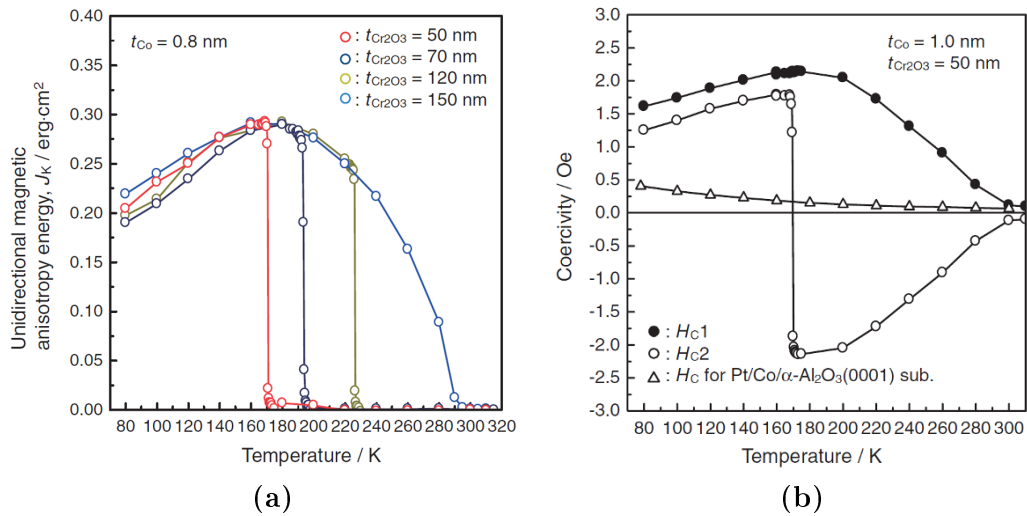


**Figure 7.6:** Temperature dependence of (a) exchange bias fields and (b) coercive fields at different layer thicknesses. (a), (b) from [82]. Copyright 2016, The Japan Society of Applied Physics.

of the curves, up to the blocking temperature, does not change. For very thick layers, the blocking temperature correlates to the Néel temperature of  $\text{Cr}_2\text{O}_3$ . The thickness of the Co layer  $t_{\text{Co}}$  influences the blocking temperature as well. A multilayer stack with  $t_{\text{Co}} = 0.5 \text{ nm}$  and  $t_{\text{Cr}_2\text{O}_3} = 50 \text{ nm}$  exhibits a larger blocking temperature as the same stack with  $t_{\text{Co}} = 1 \text{ nm}$  [82].

The coercive fields of a stack with  $t_{\text{Co}} = 1 \text{ nm}$  and  $t_{\text{Cr}_2\text{O}_3} = 50 \text{ nm}$  are shown in figure 7.6b at different temperatures. From this, one can see that the coercive fields at the positive and negative magnetization branch are increasing before the exchange bias field drops to zero.

The significant temperature dependence, especially the increasing exchange bias field with increasing temperature, is assumed to be related to a temperature dependent tilt of the interfacial magnetization of the antiferromagnetic layer [82, 83].

The interfacial magnetism of Pt/Co/ $\text{Cr}_2\text{O}_3$ /Pt is investigated by atomistic spin dynamics simulations and described in the following sections. First, the magnetic properties of the ferromagnetic Co layer and the antiferromagnetic  $\text{Cr}_2\text{O}_3$  layer are introduced separately. The subsequent sections cover the re-

sults of the calculation regarding the Pt/Co/Cr<sub>2</sub>O<sub>3</sub> stack. The lower Pt layer is not further considered in the following models as no influence on the magnetic properties resulting from this layer has been observed in the calculations. The different models based on the Pt/Co/Cr<sub>2</sub>O<sub>3</sub> stack reveal some of the major effects, which lead to the experimentally observed magnetic behavior. The microscopic origin of most of these properties could not be identified and it is supposed that an unknown energy term exist. The impact of this energy term is described to high extend and may support the future research on this topic.

## 7.2 Simulation method and periodic boundary conditions

Before discussing the results of the atomistic spin dynamics calculations, the simulation methods are briefly mentioned and the used energy terms are introduced. Subject of the simulations are magnetic ground states without an applied field and the magnetic response of the system to an external magnetic field, i.e. the magnetization curve. Both are determined by solving the stochastic Landau-Lifshitz equation described in section 3.2.1. Equation 7.1 involves the relevant energy terms of this chapter. These terms are the symmetric exchange coupling between neighboring spins, an energy term modeling a uniaxial anisotropy of each spin and the Zeeman term, which takes the influence of the external field into account. Long range dipole-dipole interactions are neglected, because these interactions would strongly increase the computational effort, while their influence on the magnetic behavior is expected to be small compared to the influence of the uniaxial anisotropies.

$$\mathcal{H} = - \sum_{i < j} J_{i,j} \vec{S}_i \cdot \vec{S}_j - \sum_i D_i \left( \vec{S}_i \cdot \vec{e}_i \right)^2 - \mu_{\text{eff},i} \sum_i \vec{B}_{\text{ext}} \cdot \vec{S}_i \quad (7.1)$$

The computational effort is minimized by applying two and three dimensional periodic boundary conditions (PBC) as in the previous chapter. The computational cell has a hexagonal base as shown in figure 7.14. The hexagonal shape is suitable for both kind of lattices, namely the fcc-(111) lattice of the Pt and Co layers and the corundum structure of Cr<sub>2</sub>O<sub>3</sub>. The impact of the periodic boundary conditions related to the spin flop field of Cr<sub>2</sub>O<sub>3</sub> are discussed in

section 7.3.2.

The calculation of magnetic hysteresis loops is accelerated by the parallel algorithm introduced in chapter 4.3. A heat bath coupling with finite temperatures is essential in conjunction with collinear initial states (cf. section 3.2.1). Only very low temperatures have been taken into account, so that a sampling over many magnetic field cycles is not required. Furthermore, the impact of temperature in combination with PBC has been not yet determined and the combined use might lead to unphysical results.

## 7.3 Material properties and material parameters of Pt/Co/Cr<sub>2</sub>O<sub>3</sub>

The magnetic behavior of the exchange bias stack Pt/Co/Cr<sub>2</sub>O<sub>3</sub> depends on the properties of each layer and the exchange coupling between the layers. The significant property of the free Co layer is its perpendicular anisotropy, which is induced by the interfacial Pt and Cr spins. Therefore, the magnetization curve of Co with an induced anisotropy is determined. Cr<sub>2</sub>O<sub>3</sub> is an antiferromagnetic material with a collinear orientation of the spins as ground state. The stability of the collinear state plays a major role in the ability of generating interfacial domain walls or permitting spin reversal processes. When switching the sign of the exchange bias direction, the antiferromagnetic coupled spins have to reverse their orientation. This is the case by applying a high field or by a combination of electric and magnetic fields. If only Cr<sub>2</sub>O<sub>3</sub> is considered, the significant property to describe the stability against a magnetic field is the spin flop field. The spin flop field denotes the field strength at which the spins rotate suddenly into the so called spin flop state. Thus, the spin flop field of Cr<sub>2</sub>O<sub>3</sub> is calculated and compared to values known from literature [84].

### 7.3.1 Perpendicular magnetized Co

The investigation of the perpendicular magnetic anisotropy (PMA) of the Co layer is reported in [85]. The PMA is an interfacial effect, which results most likely from hybridization of the orbitals at a magnetic and non-magnetic material interface [86, 87]. The hybridization leads to a high orbital magnetic

moment, which couples to the spin moment. The spin-orbit coupling of the Co atoms generate the perpendicular uniaxial anisotropy. By changing the Co thickness and the stacking number  $n$  of  $[\text{Pt}/\text{Co}]_n/\text{Cr}_2\text{O}_3$  superlattices, Shiratsuchi observed, that at both, the Pt/Co and the Co/ $\text{Cr}_2\text{O}_3$  interfaces, a perpendicular anisotropy [85] is induced. The effective anisotropy, which has been measured for different thickness of the Co layer, is shown in figure 7.7.

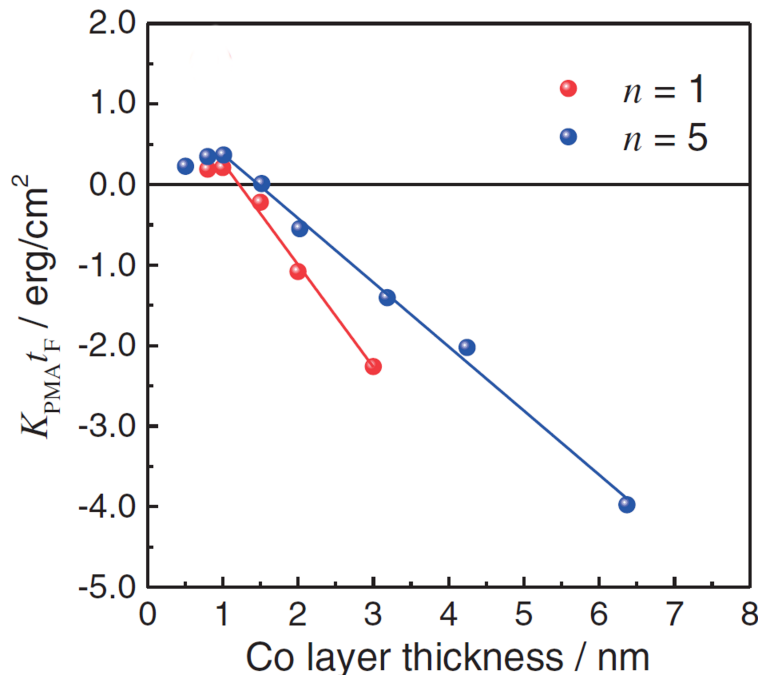


**Figure 7.7:** Dependence of the perpendicular magnetic anisotropy on the Co layer thickness for different stacking numbers  $n$ . From Y. Shiratsuchi, Appl. Phys. Express, 5, 043004, 2012. Copyright 2016, The Japan Society of Applied Physics.

The red dots represent the anisotropy of a stack with  $n = 1$ . As the temperature at the experiments has been higher than the Néel temperature of  $\text{Cr}_2\text{O}_3$ , the authors of [85] ascribe the measured anisotropies to the PMA and not to the exchange bias effect, which occurs only at lower temperatures.

In the following atomistic spin dynamics calculations are compared to experimental results of Pt(1.0 nm)/Co(0.5 nm)/ $\text{Cr}_2\text{O}_3$ (120 nm)/Pt(20 nm), which are described in [16]. Therefore the effective anisotropy of a 0.5 nm thick Co layer is required for the spin dynamics calculations. Based on the red dots



of figure 7.7 the effective anisotropy per cubic centimeter is assumed to be  $0.4 \text{ erg cm}^3$ . The lattice structure of the ultrathin Co layer is supposed to be face-centered-cubic (fcc) with a lattice constant of  $a = 0.3548 \text{ nm}$  [88]. Therefore the effective anisotropy per Co atom is around  $30 \mu\text{eV}$ . The effective magnetic moment and the exchange interaction constants of fcc-Co are calculated and described in [89]. The effective magnetic moment of each Co atom is  $0.17321 \mu_B$ . The exchange constants of atoms within the first neighbor shell are much higher than exchange constants between more distant atoms. Thus, only the first neighbor interactions with a constant of  $J_{\text{CoCo}} = 14.8 \text{ meV}$  are taken into account.

The  $0.5 \text{ nm}$  thick Co layer is grown in [111]-direction and is therefore modeled by two monolayers. Figure 7.8 shows the calculated magnetization curve of the Co layer.

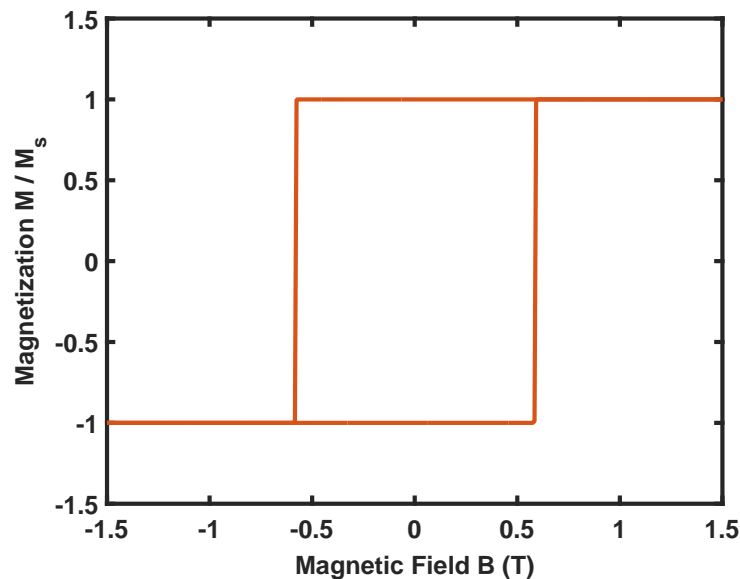


**Figure 7.8:** Magnetization curve of a  $0.5 \text{ nm}$  thick Co layer with a perpendicular magnetic anisotropy with an effective anisotropy derived from [85].

In this kind of model, the Pt layer itself is not involved in the calculations and only its influence on the Co atoms, i.e. the PMA is considered. An alternative approach is to induce the anisotropy by interfacial couplings. Besides the exchange coupling between the Co and Cr atoms, an exchange interaction be-

tween the Co atoms and the magnetic Pt atoms is supposed. The Pt atoms at the Pt/Co interface exhibit a spontaneous magnetic orbital and spin moment, which has been determined from XMCD measurements by Suzuki *et al.* [90]. The spin-orbit coupling is modeled by a perpendicular uniaxial anisotropy. If the interfacial Pt atoms are exchange coupled to the underlying interfacial Co atoms, the magnetization of Co exhibits a non-vanishing coercive field, i.e. a perpendicular anisotropy is induced by the magnetic Pt atoms. The orbital and spin moment of the Pt atoms are represented in figure 7.9 [90].

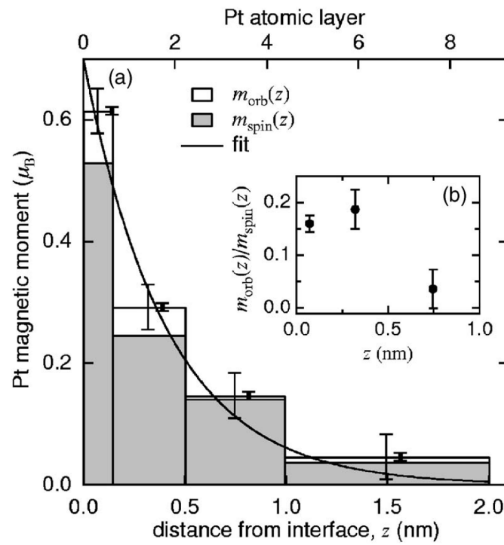


**Figure 7.9:** (a) Pt spin magnetic moment  $m_{spin}(z)$  and orbit magnetic moment  $m_{orb}(z)$  as function of distance  $z$  from the interface. (b) Ratio of orbital to spin magnetic moment. Reprinted figure with permission from M. Suzuki *et al.*, Phys. Rev. B, 72, 054430, 2005. Copyright 2016 by the American Physical Society.

To decrease the number of variables in the model, an effective magnetic moment of  $\mu_{eff,Pt} = 0.2 \mu_B$  is assumed for each Pt atom of the 1 nm thick Pt layer. The exchange coupling constant and the anisotropy constant are chosen properly, so that the coercivity equates 0.5 T again. In [85] it is stated that the PMA at the Co/Cr<sub>2</sub>O<sub>3</sub> interface is comparable to the the PMA value induced at the Pt/Co interface. Based on the opposite magnetization of the uncompensated Cr the Co spins in figure 7.3, an antiferromagnetic coupling between the neighboring Cr and Co spins is expected. Even if the temperature is higher

than the Néel temperature of the antiferromagnetic layer, a high exchange coupling constant would force an ordered magnetic state at the interface and support a PMA. In the following the exchange coupling constant between the uppermost Cr spins and the Co spins is assumed to be  $J_{\text{CoCr}} = -14.6 \text{ meV}$ . This value equals the exchange constant between the next neighboring Cr spins of the  $\text{Cr}_2\text{O}_3$  bulk [91]. The Cr effective moment and the perpendicular uniaxial anisotropy are also related to the bulk values and given by  $\mu_{\text{eff,Cr}} = 2.86 \mu_B$  and  $D_{\text{Cr}} = 2.98 \mu\text{eV}$  [91, 92]. A more detailed description of the structure and the material parameters of bulk  $\text{Cr}_2\text{O}_3$  is given in section 7.3.2. The coercivity of the Co layer induced by Cr atoms at the interface is around 0.25 T. The values of the exchange constant related to Pt and Co and the uniaxial anisotropy constant of Pt have to be chosen with respect to the expected coercivity of 0.5 T. An antiferromagnetic coupling of Co and the next neighboring Pt atoms of  $J_{\text{PtCo}} = -8.62 \text{ meV}$  and a Pt anisotropy of  $D_{\text{Pt}} = 2.59 \mu\text{eV}$  leads to the expected coercivity. Figure 7.10 shows all three hysteresis loops.

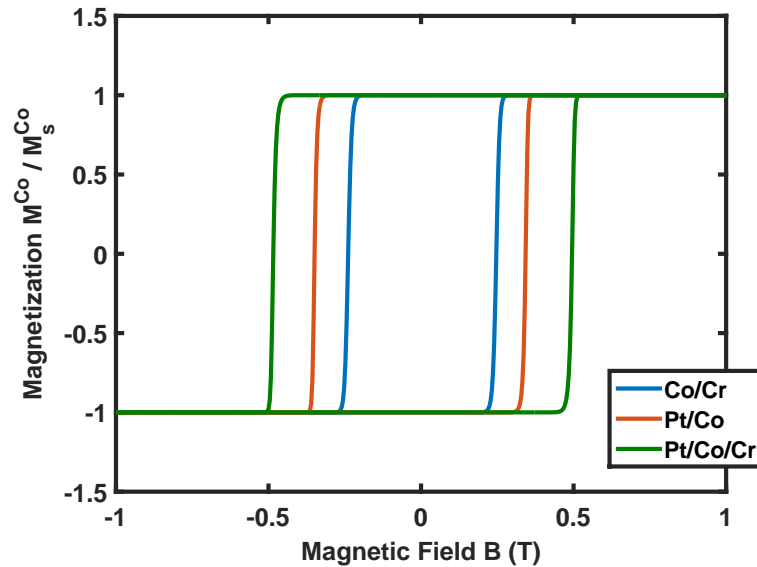


**Figure 7.10:** Hysteresis loops of Pt/Co/Cr. The perpendicular magnetic anisotropy is modeled by interfacial interactions between magnetic Pt atoms and Co and between Co and Cr.

To reduce the computational effort as much as possible, the Pt layer is neglected in the following calculation of the Pt/Co/ $\text{Cr}_2\text{O}_3$  stack. The induced

anisotropy has been taken into account by an effective uniaxial anisotropy of  $D_{\text{Co}} = 10.34 \mu\text{eV}$  per Co atom. Together with the exchange coupled Cr atoms of the interface, the expected coercivity is also reached.

Thin Co/Pt multilayer films with a broken inversion symmetry and a high spin-orbit coupling permit chiral spin structures, the so called Skyrmions, which are related to the Dzyaloshinskii-Moriya interaction [93]. The Dzyaloshinskii-Moriya interaction forces the neighboring spins  $S_i$  and  $S_j$  to be orthogonal to each other and to a Dzyaloshinskii-Moriya axis  $\vec{D}_{ij}$  (cf. equation 7.2).

$$\mathcal{H}_{\text{DM}} = \sum_{i < j} \vec{D}_{i,j} \cdot (\vec{S}_i \times \vec{S}_j) \quad (7.2)$$

The orientation of this axis depends on the symmetry of the interface. The appearance and the role of such an exchange interaction related to the magnetic behavior of the Pt/Co/Cr<sub>2</sub>O<sub>3</sub> stack is discussed in section 7.5.4.

### 7.3.2 Antiferromagnetic Cr<sub>2</sub>O<sub>3</sub>

Cr<sub>2</sub>O<sub>3</sub> has a corundum structure with 12 Cr and 18 O sites. The Cr atoms of the hexagonal unit cell are shown in figure 7.11. The lattice constant  $a = 0.495 \text{ nm}$  denotes the edge length of the hexagon. The height of the unit cell is given by  $c = 1.3566 \text{ nm}$ . The cell has a periodicity of six planes. Each plane has three buckled Cr spins, which are slightly shifted away from the plane.

As compared with cobalt, the chromium atoms exhibit a rather small uniaxial anisotropy of  $2.98 \mu\text{eV}$  along the  $c$ -axis of the hexagonal unit cell [92]. At the ground state the next neighboring spins are antiparallely aligned along the easy axis of the hexagonal corundum structure. The exchange interactions within the first five next neighbor shells are taken into account. The related exchange constants are listed in table 7.1 [91] and the next neighboring atoms are schematically represented by oval shapes on a projection of the primitive unit cell in figure 7.12.

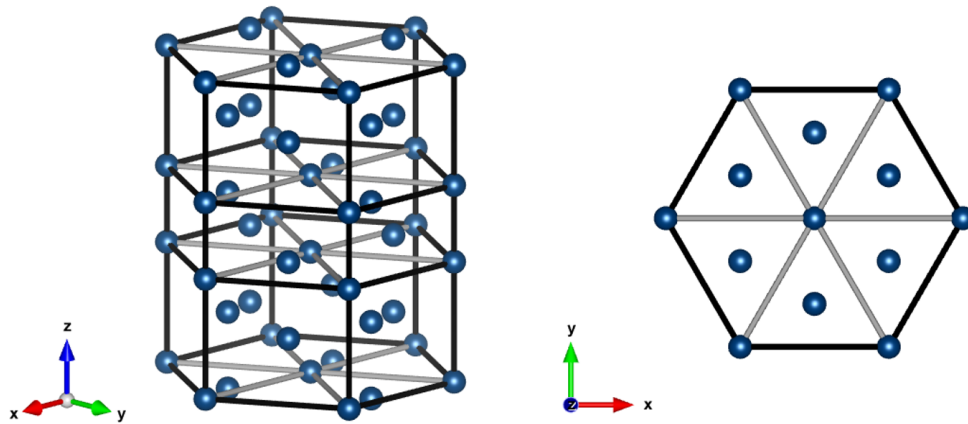


**Figure 7.11:** Front view (left) and top view (right) of the  $\text{Cr}_2\text{O}_3$  hexagonal unit cell. Only the Cr atoms are shown.

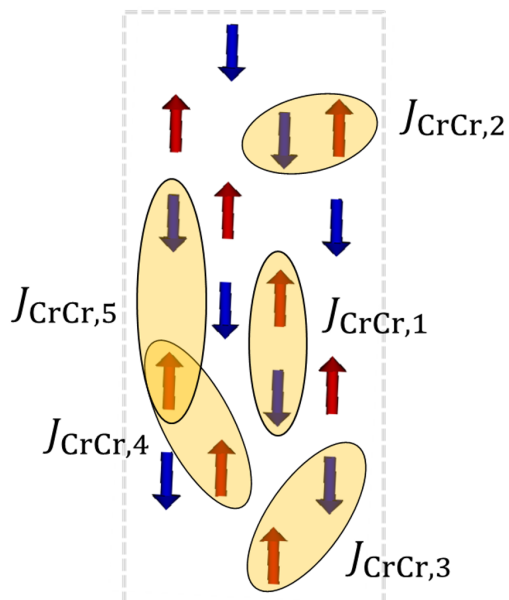


**Figure 7.12:** Projection of the unit cell. The oval shapes represent the next neighboring atoms.

Identifier	$J_{\text{CrCr}}$ (meV)
$J_{\text{CrCr},1}$	-14.6
$J_{\text{CrCr},2}$	-11.1
$J_{\text{CrCr},3}$	2.11
$J_{\text{CrCr},4}$	2.96
$J_{\text{CrCr},5}$	-2.16

**Table 7.1:** Exchange interaction constants of  $\text{Cr}_2\text{O}_3$ .

A magnetic field is applied parallel to the easy  $c$ -axis. If the field overcomes a critical field strength, a sudden state transition of the Cr spins occurs. The new state is the spin flop state, which has been shortly introduced in section 3.1.2. At the spin flop state, the next neighboring Cr spins make the same angle with the easy axis and rotate into the direction of the external field. The critical field strength is denoted as spin flop field  $B_{\text{SF}}$ . The antiferromagnetic state and the spin flop state of  $\text{Cr}_2\text{O}_3$  are shown in figure 7.13.

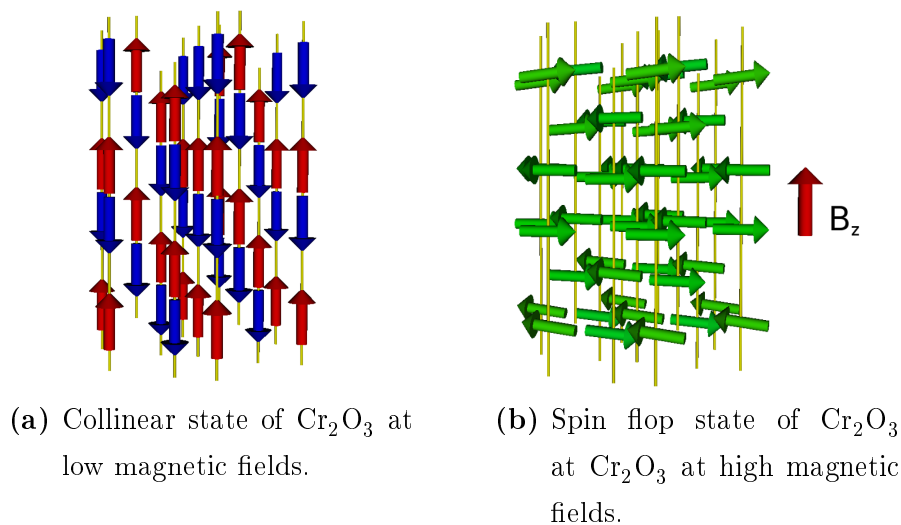


**Figure 7.13:** Spin state of  $\text{Cr}_2\text{O}_3$  at different magnetic field strengths.

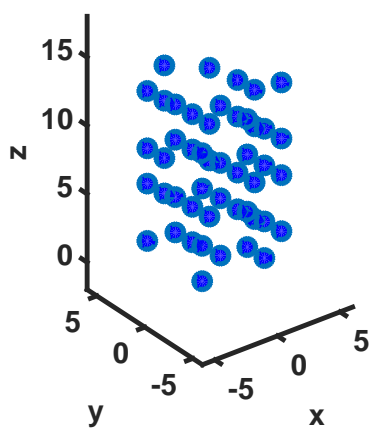
The first order transition from an antiferromagnetic state to the spin flop state occurs at 5.8 T [84]. A comparison of the computational determined spin flop field illustrates the necessity of periodic boundaries. In the following, the spin flop field is calculated for a  $\text{Cr}_2\text{O}_3$  sample with and without periodic boundaries and a layer height varied between  $1c$  and  $4c$ . The geometry of the sample is selected in such a way, that it could be easily extended in all three spatial directions. Therefore, the sample is based on the dimensions of the corundum unit cell described above. This cell has been shifted to support the application of periodic boundaries. Three different boundary conditions are considered. In the first case, no periodic boundary condition is applied to the sample, whose Cr atoms are shown in figure 7.14a. In this figure the height of the sample equals  $1c$ . The atoms at the surface have less next neighbors compared to the inner atoms, which may affect the magnetic behavior and thus the spin flop field. In the second and third case the bulk to boundary ratio is

increased by introducing two and three dimensional periodic boundaries. In the second case the sample equates the computational cell, which is extended in the lateral dimension by image cells. Figure 7.14b represents the atoms of the computational and the image cells. The hexagonal computational cell is highlighted in figure 7.14b by a green line. In the third case the periodic boundaries are applied to all three dimensions. The image atoms and the atoms of the computational cell are shown in figure 7.14c.

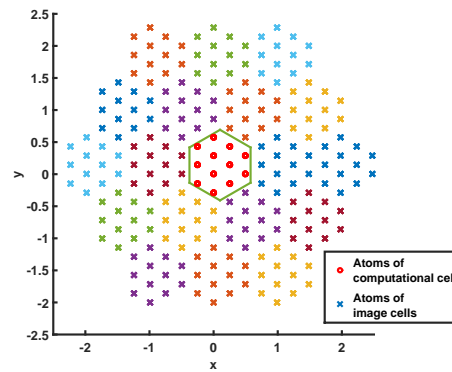
The magnetization at increasing magnetic fields are represented in figure 7.15 for all cases. With the extension of the sample by periodic boundaries, the spin flop field increases. An increasing height of the sample or the computational cell leads also to an increase of the spin flop field. The highest spin flop field with a computational cell height of  $4c$  and three dimensional periodic boundaries is approximately 5.4 T, which is less than 5.8 T, referring to the value described in [84].

Four different reasons may lead to an underestimated spin flop field in the calculation:

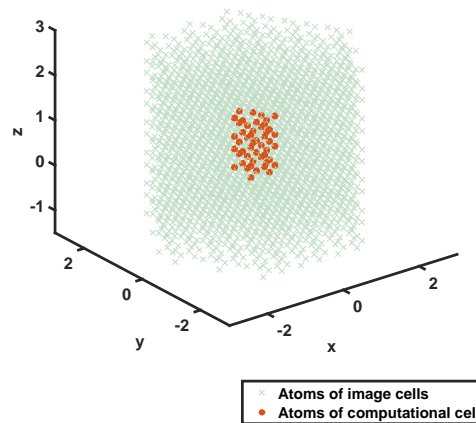
1. The computational cell contains only a small number of atoms. A trend towards rising spin flop fields with increasing number of spins in the computational cell is visible in figure 7.15. This trend leads to the conclusion, that a too small computational cell is responsible for the underestimated spin flop field.
2. A very low temperature of 1 K is used to prohibit a stagnation of the spins in a state, which represents no local energy minimizing configuration (cf. chapter 3.2.1). As the external field is increased in a rather short time interval of 50 fs, a quasi-static spin state could not be reached at each field value. In this dynamic simulation temperature cannot be processed as an average over many samples as for each simulation step only one specific sample is taken. This leads to a non-physical spin evolution.
3. The third reason is a combination of the ones described above. The application of periodic boundaries at a small unit cell combined with a finite temperature may lead to an early state transition. If a single spin of the computational cell is agitated by temperature, it rotates into



(a) Single unit cell without periodic boundaries



(b) Top view of the computational cell and the surrounding image cells in case of two dimensional boundary conditions.



(c) Side view of the computational cell and the surrounding image cells in case of three dimensional boundary conditions.

**Figure 7.14:** Illustration of periodic boundary conditions.



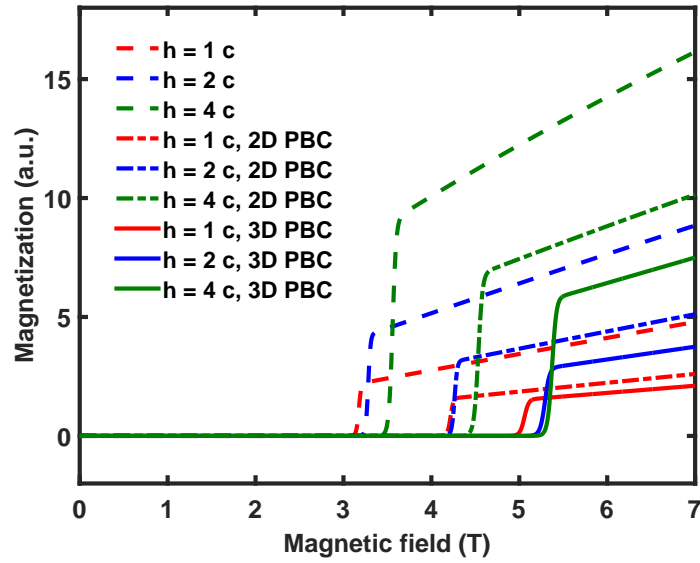


**Figure 7.15:** Magnetization curve at increasing external fields of Cr<sub>2</sub>O<sub>3</sub> with different layer heights  $h$  and boundary conditions.

another state. Its image atoms imitate this rotation, which might initiate a state transition of the complete system.

4. A fourth possible reason of an underestimated spin flop field is simply a wrong assumption of the material parameters. The effect of parameter deviations is examined and described next.

To verify the influence and the sensitivity of the different material parameters, the spin flop field of a one dimensional chain model has been studied. The model is comparable to the one dimensional chain model for exchange bias systems introduced in section 5.2.2. Here, the chain consists of  $N$  atoms with equal material parameters. Each atom of the model has an effective spin moment and a uniaxial anisotropy. Only next neighboring atoms are antiferromagnetically coupled with an exchange constant  $J_{\text{AFM}}$ . Assuming that every second spin exhibits the same angle with the anisotropy axis, the Hamiltonian can be reduced to a summation of three energy terms given in equation 7.3. The applied magnetic field  $\vec{B}$  is aligned with the anisotropy axis of uniaxial anisotropy.

$$\begin{aligned}
\mathcal{H} = & - (N - 1)J_{\text{AFM}} \cos(\alpha - \beta) \\
& - \frac{1}{2}ND_{\text{AFM}}^z \cos^2(\alpha) - \frac{1}{2}ND_{\text{AFM}}^z \cos^2(\beta) \\
& - \frac{1}{2}N\mu B^z \cos(\alpha) - \frac{1}{2}N\mu B^z \cos(\beta)
\end{aligned}$$

The antiferromagnetic orientation of the spins will be retained under an increasing magnetic field as long as  $\alpha - \beta = 180^\circ$  minimizes equation 7.3. Otherwise the spins have to rotate into another state. At a spin flop transition the spins tend to rotate perpendicular to the magnetic field. Both spins make the same angle with the field axis  $\alpha = -\beta$ . As the field is further increased, the spins point more and more along the external field direction until they are fully aligned with the external field. The spin flop field  $B_{\text{SF}}^z$ , at which the spins tend to be perpendicular to the field axis, can be determined by calculating the principal minors of the Hessian of equation 7.3. As soon as one of the principal minors with  $\alpha = 0^\circ$  and  $\beta = 180^\circ$  becomes greater or equal to zero the critical field is reached and the spin flop occurs. With the assumptions above, the spin flop transition is given by

$$B_{\text{crit}} = 2 \frac{\sqrt{-ND_{\text{AFM}}^z (2NJ_{\text{AFM}} - ND_{\text{AFM}}^z - 2J_{\text{AFM}})}}{N\mu}. \quad (7.3)$$

It should be noted, that equation 7.3 is only valid if every second spin makes the same angle with the easy axis. As the exchange constants of  $\text{Cr}_2\text{O}_3$  are high, it is assumed that equation 7.3 reflects the influence of the material parameters properly. Thus, an increase of the anisotropy constant, an increase of the exchange constant and a decrease of the effective magnetic moment lead to an enhancement of the spin flop field. The variation of the spin flop field due to a change of the exchange constant and the effective magnetic moment per spin by 5% of the original values (black line) are visualized in figure 7.16. The spin flop field converges against a maximum very soon as the number of spins is increased. The material values of the black line are chosen in such a way, that the spin flop field converges approximately against 5.8 T. The anisotropy constant and the effective magnetic moment are equaling the Cr values of  $\text{Cr}_2\text{O}_3$ . As remaining variable parameter, the exchange constant between next neighboring spins has been adjusted to match  $B_{\text{SF}}^z = 5.8 \text{ T}$  at  $N = 100$ . The lines that connect the spin flops fields in figure 7.16 are just to guide the eye.

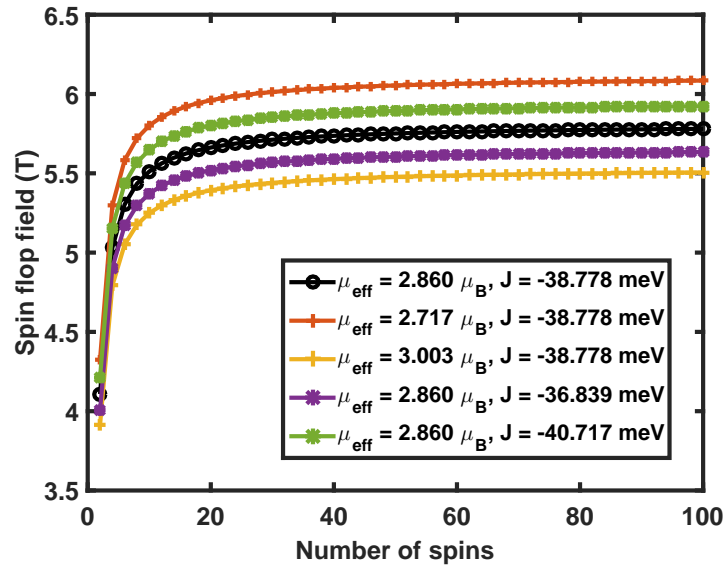


**Figure 7.16:** Spin flop fields against the number of spins of the  $N$ -spin chain model for different parameter sets. The deviation of the exchange constant and the magnetic moment are  $\pm 5\%$  from the parameters used to calculate the black line.

Although the calculated spin flop field of the  $\text{Cr}_2\text{O}_3$  sample does not reach the denoted field strength with the described material parameters and by applying periodic boundary conditions, the models of the two layer  $\text{Co}/\text{Cr}_2\text{O}_3$  stack in the next sections are based on these parameters. An adjustment of the parameters is not further considered as too many parameters influence the spin flop field and the reasons for a deviation are manifold. It is important to bear in mind, that the mentioned reasons, which lead to a deviation of the spin flop field, may influence the quantitative magnetic behavior of the full stack and do not only effect the spin flop field of  $\text{Cr}_2\text{O}_3$ .

### 7.3.3 Structure of the interface

The Pt atoms play a minor role, as their magnetic behavior is modeled by an effective magnetic anisotropy of the Co spins. For this reason only the Co and the  $\text{Cr}_2\text{O}_3$  layer are taken into account. The lattice constant of the ultrathin fcc-Co is assumed to be increased by 14.15% to fit the surface structure of

$\text{Cr}_2\text{O}_3$ . Thus, the pattern of the Cr atoms is continued by Co atoms. A projection of the interfacial layers along the c-axis is shown in figure 7.17.

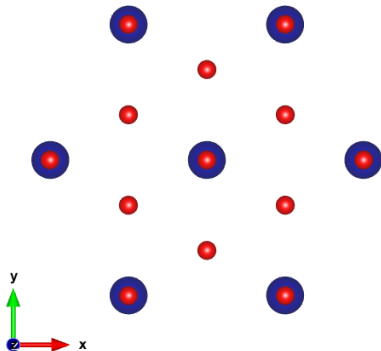


**Figure 7.17:** Top view of interfacial layers of the  $\text{Co}/\text{Cr}_2\text{O}_3$  stack. Cr atoms are blue colored and Co are red colored.

Depending on the interface position relative to the lattice, the Cr spins of the  $\text{Cr}_2\text{O}_3$  uppermost layer are either compensated or uncompensated. In case of a compensated surface the net magnetization becomes zero. This is the case, if all spins of a single plane in figure 7.11 are spins of the surface. Otherwise the surface consists of only non-buckled spins and the net magnetization does not average to zero. Hence, the  $\text{Cr}_2\text{O}_3$  surface is said to be uncompensated. Most exchange bias models are based on the assumption of interfacial uncompensated spins, but also compensated spins could be the origin of the exchange bias effect [51] (cf. section 5.2.3).

The XMCD measurements at  $\text{Co}/\text{Cr}_2\text{O}_3$  prove a net magnetization of the Cr spins as described in section 7.1. This net magnetization results from the ferromagnetic surface of non-buckled spins as shown in figure 7.18 from the supplementary material of [83]. The spins at the surface are pointing all up- or downwards, depending on the ground state of the underlying Cr atoms of the bulk. As every step of a stepped surface shows the same spin configuration, roughness is not expected to affect the magnetic behavior.

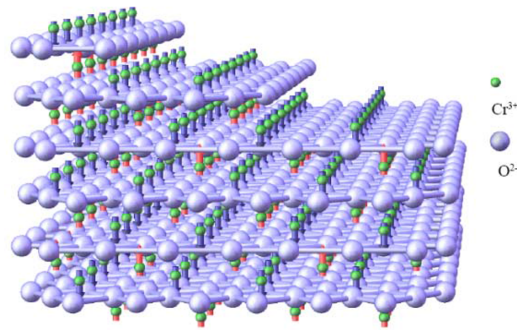


**Figure 7.18:** Spin structure of  $\text{Cr}_2\text{O}_3$  with a stepped (0001) surface. This kind of stepped interface shows no roughness. Reprinted by permission from Macmillan Publishers Ltd. [Nat. Mater.] He, X. *et al.*, 10, 5, 2010. Copyright 2016.

### Introduction of different coupling scenarios

At the coherent interface different options exist to couple the ferromagnetic and the antiferromagnetic layer. The XMCD measurements of the system [16], from which the resulting hysteresis loops are illustrated in figure 7.3, indicate an opposite magnetization of the Co and the uncompensated Cr spins. Based on the atomic structure of  $\text{Cr}_2\text{O}_3$  shown in figure 7.18, the uncompensated spins are located at the uppermost plane of the antiferromagnetic layer. Figure 7.12 is extended to illustrate possible interfacial interactions between different neighboring atoms of both materials in figure 7.19.

In a first step, the interfacial interactions are assumed to be restricted to an exchange interaction between the uncompensated Cr spins and the lowermost Co spins. Two cases of weak and strong coupling are discussed. The weak coupling is more simple to handle, e.g., by the MB model, whereas the strong coupling requires much more considerations.

## 7.4 Weak coupling between interfacial Co and Cr spins

A very weak exchange constant  $J_{\text{CoCr},1}$  does not explain most of the observed effects described in section 7.1. Due to the induced anisotropy by the interfacial Pt atoms, the reversal of the Co spins leads to a hysteresis loop with a finite

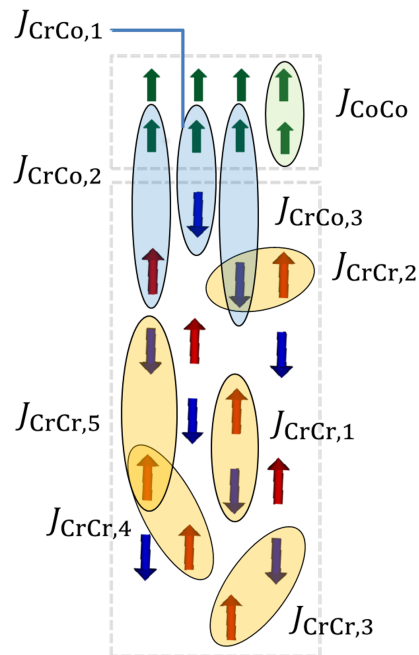


**Figure 7.19:** Schematic projection of Co/Cr<sub>2</sub>O<sub>3</sub> stack as an extension of figure 7.12. Different pairs of neighboring atoms are highlighted with blue oval shapes.

width. The exchange coupling causes a shift of the hysteresis loop. Thus, the magnetization of the Co atoms during a field cycle corresponds to the measured data. In contrast, the out-of-plane magnetization of the uncompensated Cr spins does not change during the increasing or decreasing field branch. Figure 7.20 represents the normalized magnetization curves of the ferromagnetic and the antiferromagnetic layer, which are coupled by an exchange constant of  $J_{\text{CrCo},1} = 172.35 \mu\text{eV}$  between the interfacial atoms.

Such a magnetic behavior is comparable to the idealized Meiklejohn and Bean model (cf. section 5.2.1), at which the antiferromagnetic spins are fixed.

## 7.5 Strong coupling between interfacial Co and Cr spins

A strong coupling between the interfacial spins will create an interfacial domain wall inside the antiferromagnetic layer (section 7.5.1). The calculated magnetization curves match already the experimental results quite well. Next, the

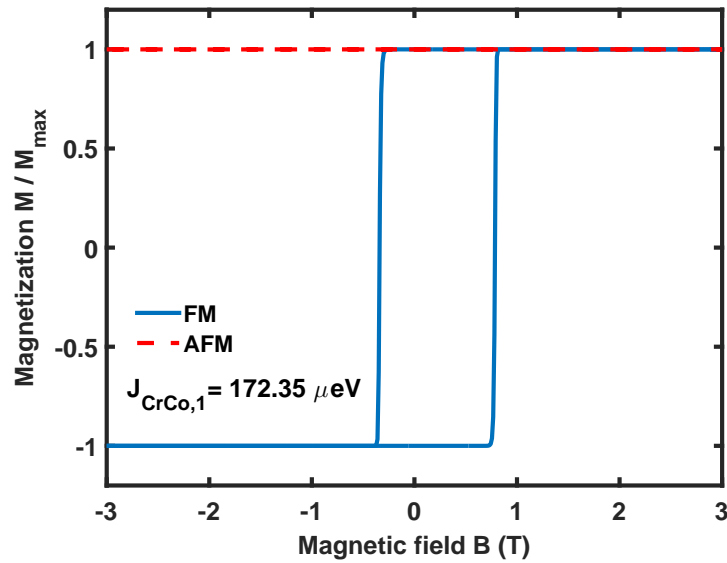


**Figure 7.20:** Magnetization curves of Co/Cr<sub>2</sub>O<sub>3</sub> with a weak exchange interaction between the interfacial Cr and Cr atoms.

properties of such a domain wall are described. As the magnetization loop is shifted in contrast to the experiment, countermeasures are required. Different scenarios to archive the expected magnetic behavior are discussed in section 7.5.2.

### 7.5.1 Creation of an interfacial domain wall

The creation of an interfacial domain wall is described within the Mauri model (cf. section 5.2.3). The wall seems to be related to a magnetization curve, which is comparable to those of the experiments.

A part of the interfacial domain wall of a 80 nm thick Cr<sub>2</sub>O<sub>3</sub> layer deposited on a 0.5 nm thick Co layer is shown in figure 7.21a. The related magnetization curve is given in figure 7.21b.

The hysteresis loop is shifted to the right hand side due to an interfacial exchange coupling of  $J_{\text{CrCo},1} = -14.6 \text{ meV}$  per Cr-Co pair. The strength of the coupling equals the interaction between the next neighbouring Cr spins of the Cr<sub>2</sub>O<sub>3</sub> bulk. This value is also used to determine the effective anisotropy of Co in section 7.3.1 to achieve the required coercivity of 0.5 T.

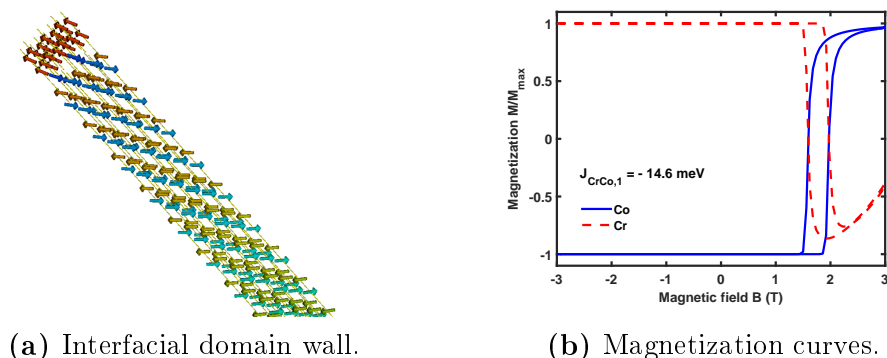


**Figure 7.21:** The case of a strong interfacial coupling. (a) By applying a magnetic field an interfacial domain wall is created at the interface between Co and  $\text{Cr}_2\text{O}_3$ . (b) The related hysteresis curves of the Co and the  $\text{Cr}_2\text{O}_3$  layer.

The shape of the Co magnetization curve caused by a strong interfacial exchange constant matches the curve shape of the experiments described by Toyoki [15] very well. The asymmetric shape of the blue line regarding the horizontal axis can be recognized from figure 7.5 of section 7.1. The magnetization curve of the antiferromagnetic layer becomes negative as the ferromagnetic spins reverse their magnetization. After reaching a negative peak, the net magnetic moment rises again against zero. This increase is caused by the spins of the domain wall. The magnetization of the surface spins and the spins of the lower layers are shown in figure 7.22.

Aside from the increase of the net magnetization of the lower antiferromagnetic spins, it is assumed that the creation of an interfacial domain wall plays a major role for the magnetic behavior of the Pt/Co/ $\text{Cr}_2\text{O}_3$  multilayer stack. The creation and the properties of an antiferromagnetic domain wall will be considered in more detail in the following section.

## 7.5.2 Properties of an interfacial domain wall

At a domain wall the spins reverse their orientation along the material between two domains. In case of Co/ $\text{Cr}_2\text{O}_3$  the Co layer represents one domain, while the bulk Cr spins represent the other domain. Without an external field and a single antiferromagnetic coupling between the uppermost Cr and the lowermost



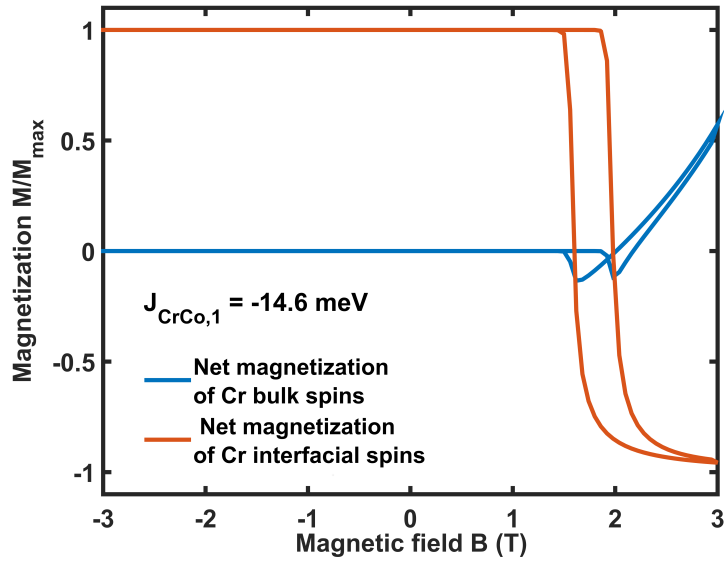


**Figure 7.22:** Magnetization curves of the uppermost Cr spins (red line) and the lower Cr spins (blue line).

Co spins, the Cr spins are pointing along the  $c$ -axis and the Cr spins are collinear like it is sketched in figure 7.19. Without any further energy term, the collinear state is the ground state. Thus, the ground state possesses no domain wall at zero fields. With a negative external field along the  $c$ -axis, which overcomes an energy barrier related to the anisotropies of both layers, the Co spins start to reverse their magnetization and force an interfacial domain wall in the antiferromagnetic material as shown in figure 7.21a.

The domain wall width increases by a stronger alignment of the Co spins with the external field. To prohibit a complete reversal of the antiferromagnetic layer, the layer thickness has to be larger than the width of a  $180^\circ$  domain wall. In figure 7.23 the  $z$ -component of the Cr spins are represented for different domain walls. The uppermost Cr spins are fixed to a certain angle with the  $c$ -axis, while the underlying spins are relaxed without an external field.

From figure 7.23 it can be seen, that a  $180^\circ$  domain wall has a width of approximately 45 nm. This value matches the domain wall width of 38 nm given in [94] very well. In opposite to a ferromagnetic domain wall, an antiferromagnetic domain wall could not propagate due a constant magnetic field. As  $\text{Cr}_2\text{O}_3$  is a magnetoelectric material, a domain wall can be propelled by applying an electric and magnetic fields simultaneously. The driving force of the

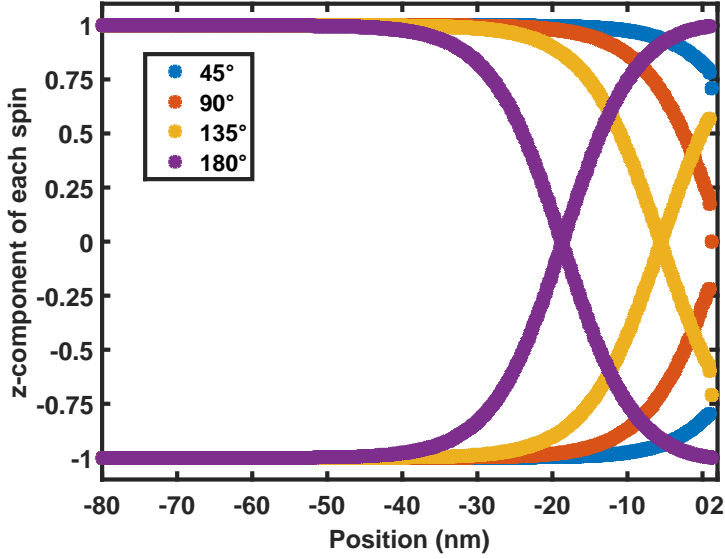


**Figure 7.23:**  $z$ -component of the magnetization for a  $45^\circ$ ,  $90^\circ$ ,  $135^\circ$  and  $180^\circ$  domain wall. The Cr spins of the uppermost layer are fixed to the related angles.

wall is given by  $\vec{F} = 2\vec{E}\hat{a}\vec{H}$  [94], at which  $\hat{a}$  is the magnetoelectric tensor and  $\vec{E}$  and  $\vec{H}$  are the electric and magnetic field. The electric field is thought to cause a shift of the Cr atoms inside  $\text{Cr}_2\text{O}_3$  as illustrated in figure 7.24 [95].

This shift has an impact on the  $g$ -tensor and thus, on the effective magnetic moment of each Cr atom as well. By increasing or decreasing the effective magnetic moments of each second sublayer, the structure exhibits a net moment and becomes ferrimagnetic. Assuming that the  $\text{Cr}_2\text{O}_3$  layer becomes ferrimagnetic, the wall can be moved by a magnetic field. The direction of the movement along the layer depends on the effective magnetic of each sublayer of the ferrimagnetic material. The direction of the wall movement is illustrated in figure 7.25a. If the magnetic moments of the uppermost sublayer are larger than those of the second sublayer, a positive magnetic field moves the wall upwards.

At the Pt/Co/ $\text{Cr}_2\text{O}_3$  stack the wall is created by the rotation of the Co spins and pinned at the interface. In case that the interfacial sublayer consist of Cr atoms with a larger magnetic moment than the next lower sublayer, the domain wall is pressed against the Co layer at positive magnetic fields. This configuration would lead to a greater exchange bias as shown in figure 7.25b.

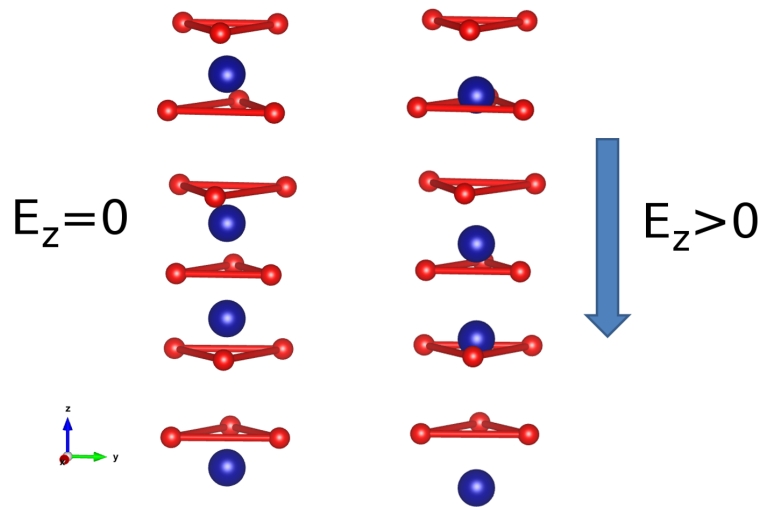
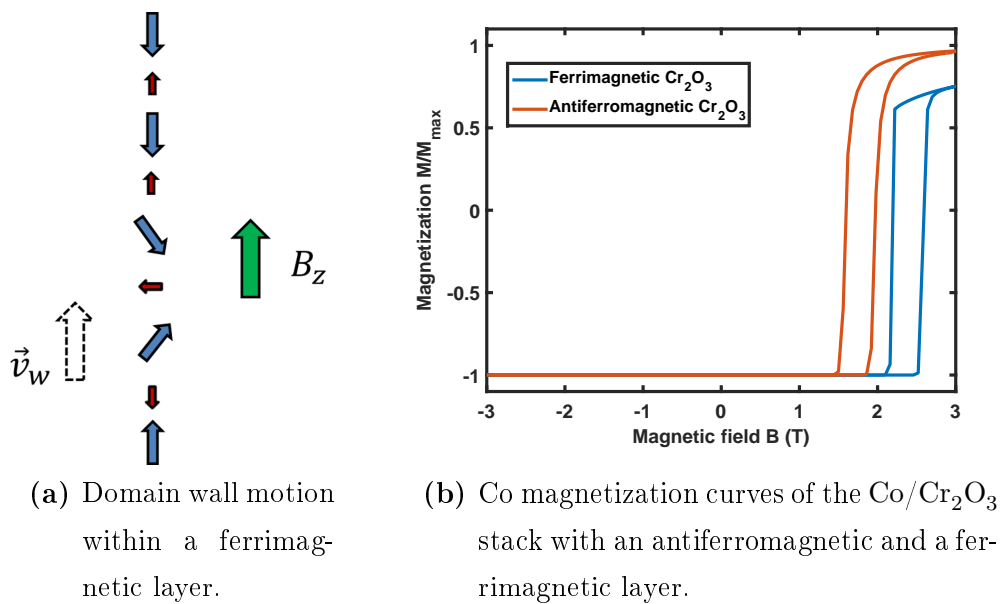


**Figure 7.24:** Shift of the Cr atoms due to the magnetolectric effect. Redrawn from [95].



(a) Domain wall motion within a ferrimagnetic layer.

(b) Co magnetization curves of the Co/Cr<sub>2</sub>O<sub>3</sub> stack with an antiferromagnetic and a ferrimagnetic layer.

**Figure 7.25:** (a) Schematic representation of domain wall motion within a ferrimagnetic layer. The wall moves upwards with the velocity  $\vec{v}_w$  driven by a positive magnetic field  $B_z$ . The larger drawn arrows represent spins with a higher magnetic moment. (b) Magnetization loops of the Co spins upon the antiferromagnetic Cr<sub>2</sub>O<sub>3</sub> with Cr spins of equal effective magnetic moments (red line) and upon the ferrimagnetic Cr<sub>2</sub>O<sub>3</sub> (blue line).

Based on the opposite scenario with smaller Cr magnetic moments at the interface, a reversal of the Co spins at a positive magnetic field would lead to a movement of the wall downwards until all Cr spins are reversed.

### 7.5.3 Shift of the hysteresis loop

The hysteresis loops of the stack with equal Cr effective moments are shifted to the right hand side of the coordinate system. A comparison of the shape and the position of the calculated curve in figure 7.21b with the experimental determined curves in figure 7.5 indicate a mirror-inversion. Either the hysteresis should be shifted to the opposite side of the coordinate system or the creation of the wall should occur at magnetic fields of opposite sign. Three different strategies are investigated to get closer to the experimental results.

#### Rotated anisotropy axes

In figure 7.5 the magnetization at the increasing field cycle has neither reached positive saturation, nor remains at negative saturation at  $B = 0$  T. Such a magnetic behavior can also be seen in the Stoner-Wohlfarth model (cf. section 3.1.1) of a single spin with a uniaxial anisotropy and an easy axis, which has a non-zero angle with the external applied field. In opposite to the hysteresis loops of the Pt/Co/Cr<sub>2</sub>O<sub>3</sub>/Pt stack, the hysteresis loop related to Stoner-Wohlfarth model is not shifted and exhibits a point reflection in the origin of the coordinate system as seen in figure 3.2b.

A rotation of the uniaxial axes of the ferromagnetic layer, the antiferromagnetic layer or both layers, does not lead to comparable results with the experiments. Figure 7.26 illustrates the Co magnetization curves of the stack at which the particular easy axes make an angle of 45° with the field axis. At these cases the hysteresis loop width approaches zero. Furthermore the typical curve shape with a steep (slow) increase at the lower (upper) half of the coordinate plane disappears. Thus, it is concluded, that a modification of the uniaxial anisotropy does not lead to the expected effects.

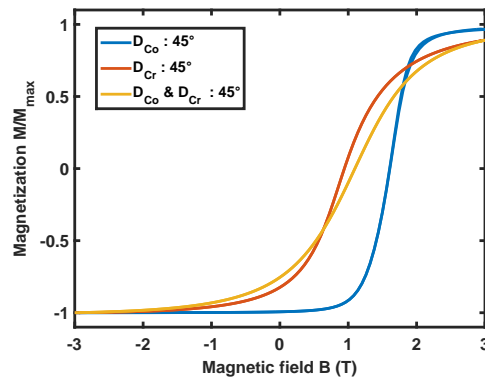


**Figure 7.26:** Magnetization curves of the Co/Cr<sub>2</sub>O<sub>3</sub> layer with different anisotropy axes. The angles of the Co layer, the Cr<sub>2</sub>O<sub>3</sub> layer or both layers is rotated by 45°. The remaining axes are perpendicular.

### Additional interfacial exchange coupling

Another approach to meet the experimental results is to shift the hysteresis loop by an additional exchange bias coupling. This can be done by introducing a second exchange bias coupling between the lowermost Co spins and the Cr spins of the second sublayer. The exchange bias constant  $J_{\text{CrCo},2}$  should have the same sign as the first coupling to force a shift of the loop to the left hand side. Both interactions are competing and the loop is shifted back to the origin. However, by increasing the coupling constant  $J_{\text{CrCo},2}$  a domain wall is also created at negative field values. Thus, the hysteresis loop has a curved shape at the upper and the lower half of the coordinate system. Furthermore, the loop is narrowed as the influence of interactions approaches to equal values. The related hysteresis curves of the antiferromagnetic and the ferromagnetic layer are represented in figure 7.27.

### Second unidirectional exchange bias by an additional spin

Instead of a second coupling between Cr and Co, the Co layer can be exchanged biased to an additional spin with a fixed orientation. The second exchange bias leads to a shift of the magnetization loop without a change of its shape as shown in figure 7.28. The inset of figure 7.28a sketches the unreserved, uncompensated spin which is exchange coupled to one of the Co atoms. A

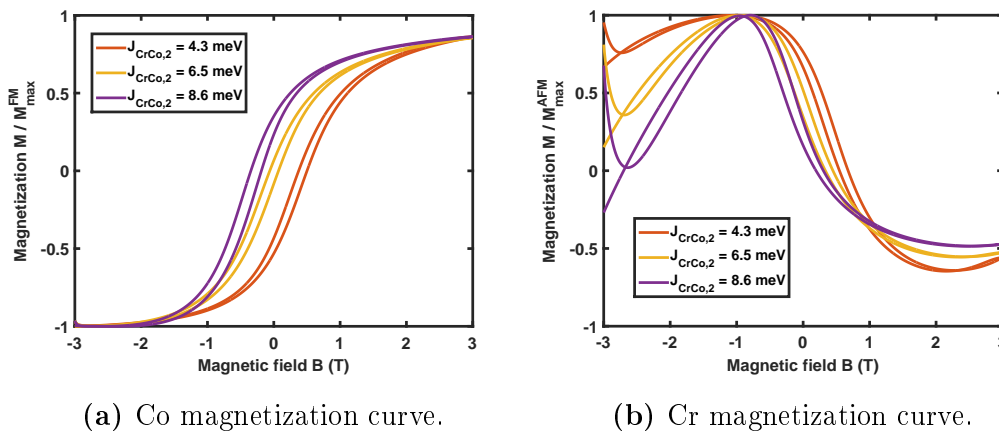


**Figure 7.27:** Magnetization curves of the Co/Cr<sub>2</sub>O<sub>3</sub> stack with a second interfacial exchange interaction.

coupling constant of  $J_{\text{Co,Add}} = 1.29$  meV is sufficient to shift the loop to the left hand side of the coordinate system.

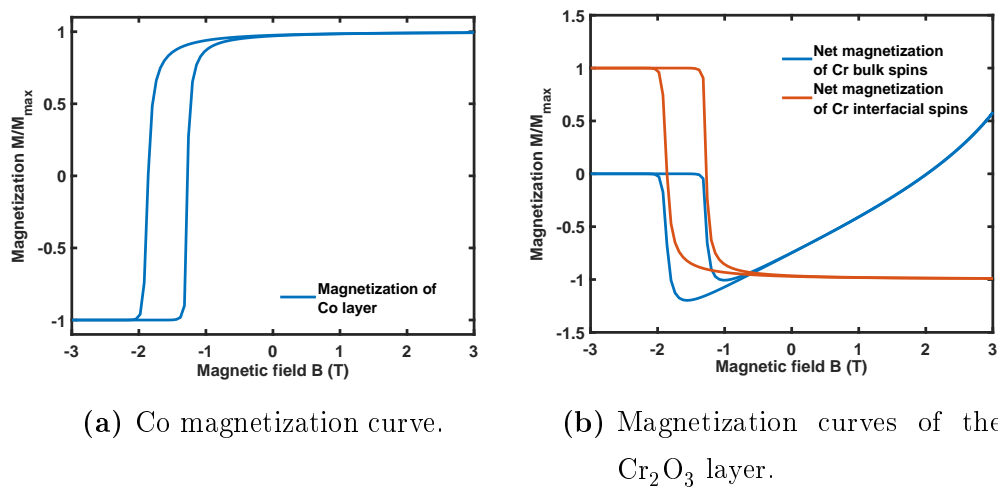


**Figure 7.28:** Magnetization curves of the Co/Cr<sub>2</sub>O<sub>3</sub> stack with an fixed additional spin, which interacts with the Co layer.

The additional spin leads to a unidirectional anisotropy, which models the experimental results to a high extend. The additional unreserved spin itself is thought to be non-physical. The origin of such a unidirectional anisotropy is discussed in the next section.

### 7.5.4 Origin of the second unidirectional anisotropy

The origin of the second unidirectional anisotropy is related either to the ferro- or the antiferromagnetic layer. An energy term, which has not been considered yet, includes the Dzyaloshinskii-Moriya interaction and is given in equation 7.2. This interaction is based on the symmetry of the structure [96]. If a center of inversion is located between the two magnetic ions, the Dzyaloshinskii-Moriya interaction vanishes. The symmetry is broken at the interface between different materials. At the Pt/Co interface the Dzyaloshinskii-Moriya interactions supports Skyrmions, which are chiral magnetic states at the surface of the structure [93, 97]. These states exhibit domain walls in-plane as shown in figure 7.29 [98].

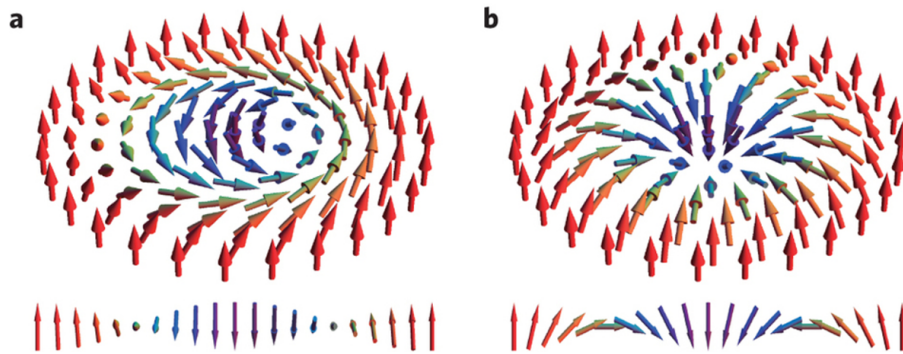


**Figure 7.29:** Magnetic Skyrmion states. Reprinted by permission from Macmillan Publishers Ltd: Nat. Mater., [98], copyright 2016.

The structure of the wall and thus the creation of chiral Skyrmions depends on the size and the shape of the sample [99]. In [99] a stable chiral Skyrmion is observed at a Pt/Co/MgO square sample with a side length of 420 nm. Figure 7.30 illustrates magnetic domains, which are caused by the Dzyaloshinskii-Moriya interaction between the Co atoms of the same monolayer at a much smaller cylindrical sample.

Such domain walls are not observed experimentally at Pt/Co/Cr<sub>2</sub>O<sub>3</sub>/Pt. In [100] the spatial distribution of the Co and the Cr magnetization is determined via XMCD measurements. Without applying a high magnetic field pulse, two different domains are observed. These domains are related to the two ground states of Cr<sub>2</sub>O<sub>3</sub>. The Co spins are orientated either up- or downwards, depend-

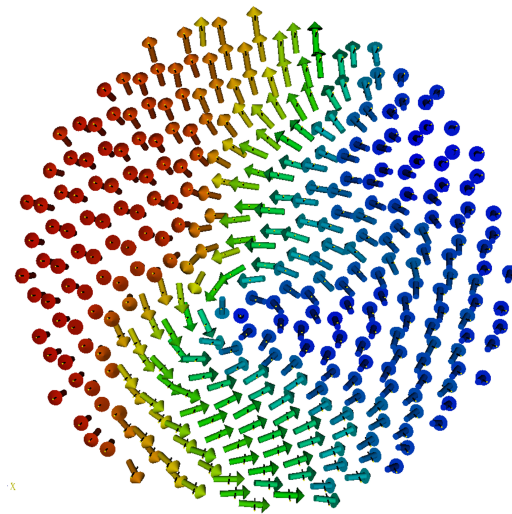


**Figure 7.30:** Co layer Dzyaloshinskii-Moriya interaction.

ing on the ground state of the underlying Cr spins. The magnetization curve of the Co spins shows a negative and positive exchange bias, which is related to the two different domains. After applying a high field pulse during cooling, the loop is shifted either to the right or the left side, which means, that one of these domains vanishes. In other words, the exchange bias and the related effects occurring at the Pt/Co/Cr<sub>2</sub>O<sub>3</sub> stack can be considered separately for each domain. A Dzyaloshinskii-Moriya interaction, which may occur at the Co/Pt interface, seems to play a minor role in the investigation of the second unidirectional anisotropy. Furthermore, the effect of the Dzyaloshinskii-Moriya interaction at Co may be reduced by a concurring DM term generated by a broken symmetry at the Co/Cr<sub>2</sub>O<sub>3</sub> interface.

In opposite to the Co/Pt interface, the Dzyaloshinskii-Moriya interactions might play a larger role between the interfacial Cr spins. An origin of the unidirectional anisotropy based on the antiferromagnetic layer would also explain part of the temperature dependence. The exchange bias field reaches zero around the Néel temperature. This requires both kinds of interactions, which generate the exchange bias to vanish around zero. If the second unidirectional anisotropy is also caused by the Cr<sub>2</sub>O<sub>3</sub> layer, it should be vanish at Néel temperature as well.

Cr<sub>2</sub>O<sub>3</sub> itself exhibits no broken symmetry, so that Dzyaloshinskii-Moriya inter-



action does not appear between the magnetic Cr ions without further changes. As  $\text{Cr}_2\text{O}_3$  is a magnetoelectric material, the magnetization can be influenced by an electric field. The electric field may have an effect on all energy terms in equation 7.1 as explained in [101]. In addition to a change of the g-factor (cf. section 7.5.2), it supports the existence of the Dzyaloshinskii-Moriya interaction within  $\text{Cr}_2\text{O}_3$  [102, 103]. By applying an electric field perpendicular to the  $c$ -axis, the spins might be inclined in-plane and generate a net magnetization. Although no external electric field applied during the measurements in [14], similar effects might arise due to the field cooling under a high external magnetic field and cause the expected shift of the hysteresis loop. Targeting models with proper material values are difficult to identify, as the interactions between the magnetic field, electric polarization and the electric field and magnetic polarization affects many parameters. Hence, further computations to reveal the origin of the second unidirectional anisotropy are not pursued within this thesis.

## 7.6 Explained and non-explained effects

An effective model has been introduced, which explains many of the measured effects, but failed to give a microscopic understanding of the magnetic behavior at the Co/ $\text{Cr}_2\text{O}_3$  interface. First the perpendicular magnetic anisotropy appearing at the Pt/Co interface has been modeled by an effective uniaxial anisotropy of the Co spins. After that, the  $\text{Cr}_2\text{O}_3$  layer has been introduced and coupled the ferromagnetic layer by the uppermost Cr and the lowermost Co spin. The Co magnetization curve of this model already exhibits the expected shape of the experimental results. Furthermore, the decrease of the coercivity matches the experimental findings quite well. The shape of the magnetization curve and the decrease of the coercivity are based on the formation of a domain wall and thus, it is assumed, that the formation of a domain wall is one of the key properties of the system. By implementing a second unidirectional anisotropy with an additional uncompensated and fixed spin, the hysteresis loop is shifted to the correct field range. Although the origin of the unidirectional anisotropy is yet unclear, the switching of the exchange bias and a part

of the temperature dependence observed in the experiments can be recognized by the effective model.

### 7.6.1 Magnetic and magnetoelectric switching of the exchange bias

The sign of the exchange bias is switchable either by a high magnetic field or by applying an lower magnetic field and an electric field simultaneously [14, 15]. Both observations are explainable by the computational results and physical backgrounds described in previous sections. Before any measurement the Pt/Co/Cr<sub>2</sub>O<sub>3</sub>/Pt stack has been heated over Néel temperature of Cr<sub>2</sub>O<sub>3</sub> and cooled down under an external magnetic field between  $B = 0.4$  T and  $B = 0.6$  T [14, 16, 15, 100], respectively. The lower bulk Cr<sub>2</sub>O<sub>3</sub> spins are suspected to be in one of the two collinear states during the measurements. The upper spins are thought to form an interfacial domain wall due to the unknown effect introduced in section 7.5.3 and 7.5.4. This state is the energetically most favorable state at high positive fields. At negative fields, the Cr spins are forced to build a complete collinear state. Increasing the field again, after reaching spin flop, all Cr spins reverse their magnetization. This also includes the spins, which might be involved in the unknown effect. Thus the antiferromagnetic Cr spins could relax into a state with an interfacial domain wall at the top and collinear spins at the bottom again. A reversal of all spins within the stack would lead to mirrored magnetization curves as illustrated in figure 7.31. A simulation including the reversal of the spins by a high negative field pulse could not be performed, as the initial state of the system depends on the unknown interaction.

The required field strength to switch the exchange bias is determined experimentally in [14] and is given by approximately  $B_{\text{SF}} = 9$  T. Applying an electric field of  $-2500$  kVcm simultaneously, the sign of the shift is switched at only  $-1$  T [15]. This can be explained by the magnetoelectric effect. As mentioned in section 7.5.2, the electric field induces a shift of the Cr atoms, which affects the magnetic moments of each Cr<sub>2</sub>O<sub>3</sub> sublayer. Due to the arising net magnetization, the antiferromagnetic material becomes ferrimagnetic. In case of ferrimagnetic structure, a domain wall can be propelled by a magnetic field

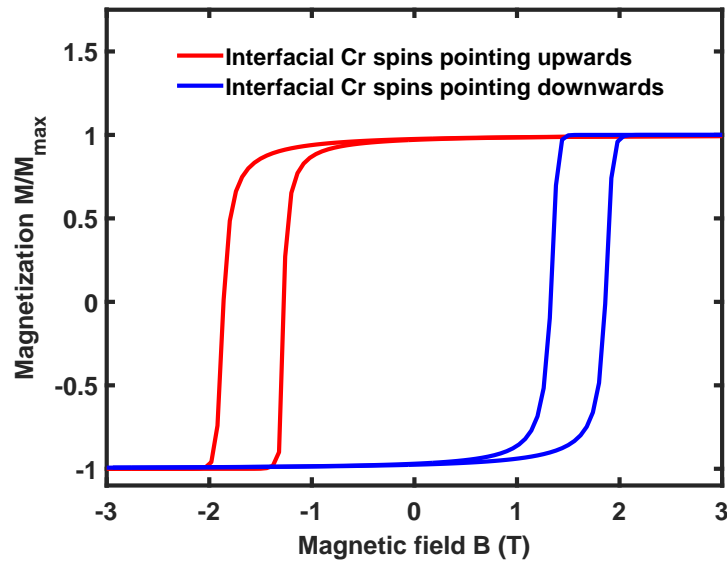


**Figure 7.31:** Switchable behavior of exchange bias stack is modeled by different initial conditions.

and move along the layer. The interfacial wall, which is formed by the positive magnetic field applied during cooling, is moved downwards until it leaves the  $\text{Cr}_2\text{O}_3$  layer. Thus a reversal of all spins is initialized by an electric field and a rather small magnetic field.

### 7.6.2 Temperature dependence

The experimentally observed temperature dependence of the exchange bias field represented in figure 7.6 [82] can be partly recognized from the effective model of two different exchange coupling phenomena. The exchange bias field increases at rising temperature, before it drops to zero around the Néel temperature. Within the effective model, the interfacial interaction between the Co and the Cr layer shifts the loop to positive values of the magnetic field, while the additional spin supports a shift to the negative values. By increasing the temperature, the impact of the exchange coupling between Cr and Co is reduced and the loop is further shifted to the left side. A further increase of the temperature would influence both couplings and the coercivity of each layer. If the second unidirectional anisotropy is caused by an effect of the antiferromagnetic material, it would also vanish at Néel temperature and the

exchange bias field would drop to zero.

This model does not explain the abrupt collapse of the exchange bias field at stacks of lower thickness as shown in figure 7.6a. It might be that the unknown effect, which caused the second unidirectional anisotropy, is also related to this temperature behavior. Assuming that the effect comes along with the generation of a ferrimagnet the temperature might depin the interfacial wall, which would support a wall movement and lead finally to a complete spin reversal of the antiferromagnetic layer.

## 7.7 Open-ended questions and outlook

Although many of the observed magnetic properties of the Pt/Co/Cr<sub>2</sub>O<sub>3</sub>/Pt stack are revealed by the introduced effective model, some properties remain unexplained. This concerns for example the correspondence between the experimental hysteresis loops and the calculated ones. The shifted hysteresis loop of the Co atoms matches the measured magnetization curve quite well, but the hysteresis loop of the antiferromagnetic layer shows some minor differences. The uppermost spins change their directions simultaneously with the Co spins. But the generated domain wall leads to an increase of the magnetization against zero. Furthermore, the hysteresis loops of the experiments show a vertical shift, which has not been observed in the curves determined by simulation.

As mentioned above, the temperature dependence could only be partly explained by the effective model. The idea that the abrupt disappearance of the exchange bias field at stacks with thin antiferromagnetic layer depends on the unknown effect has not been proven yet. To prove that, the origin of the second unidirectional anisotropy has to be found and the related properties have to be studied. In case of a mutual interaction between the magnetic field and the dielectric polarization, effects which are based on the magnetoelectric properties might play a major role for the physical origin of the second unidirectional anisotropy. As the investigation of the physical origin is a difficult and surely time consuming task with many parameters, it has not been treated within this thesis and is left for future research.

# Chapter 8

## Summary and Outlook

Within this thesis the magnetic properties of multilayer systems have been investigated. The main focus has been on exchange bias stacks, which are an elementary part of today's magnetic memory devices [104]. As it is a challenge to save a huge number of data on a very limited cell size with a very low power consumption, the interfacial effects based on the atomic structure and the interactions with external magnetic or electric fields have to be understood. An appropriate method to study these effects are atomistic spin dynamics simulations is shown in this thesis.

The investigations of the multilayer structures related to this thesis are based on the development of effective models. This includes the exchange bias systems NiFe/IrMn/MgO/Pt and Pt/Co/Cr<sub>2</sub>O<sub>3</sub>/Pt, which have been discussed in detail within chapter 6 and 7. The development and improvement of effective models involves the calculation of magnetic quantities and a subsequent comparison with experimental results. Therefore, different methods have been introduced and adapted to fulfill the requirements of multilayer stacks (section 3 and section 4).

The time independent magnetic behavior has been determined by minimizing the related extend classical Heisenberg Hamiltonian. The energy curves, introduced in section 3.1, illustrate the local minima against the magnetic field. This is a proper representation to obtain characteristic values like coercive fields of simple models. This representation has been applied to a simple chain

model, which has been studied to understand the typical thickness dependent behavior of exchange bias systems like it is observed at both mainly studied structures in this thesis. The energy curves of the one dimensional chain model in section 5.2.2 show that a  $180^\circ$  spin reversal cannot occur at an exchange bias stacks with a quite thick antiferromagnetic layer.

The time dependent magnetic properties have been studied by two different methods. The first one is a Landau-Lifshitz approach, at which a time dependent stochastic equation is solved. This method naturally leads to the correct chronological order of the spin states. The second one is a Monte Carlo scheme, at which a new spin state is determined by a random rotation of spins and a subsequent evaluation of the energy difference between the actual and the former magnetic state. However, this method is modified to determine some kind of pseudo dynamics [65].

One significant property of exchange bias stacks is the occurrence of hysteresis seen as a hysteresis loop within a magnetization curve. The calculation of quasi-static hysteresis loops is a very time consuming task. To reduce the computational time, a method has been developed to parallelize the calculation. A hysteresis loop arises due dependence between the actual magnetic state and the former magnetic states. If parts of the history are known, this information can be used to create independent parts of the complete hysteresis cycle. Each part is correspondence to a certain initial condition, which prevents the chronological order. The independent parts could be further divided into intervals, so that the magnetization of each field value can be calculated on different processors in parallel. The calculation of each magnetic state can either be done by solving the stochastic Landau-Lifshitz equation or by applying a Monte Carlo scheme. For speeding up calculations including long term dipole-dipole interactions, a hybrid implementation is developed. Within the implementation, the parallelization of the intervals is based on the message passing interface (MPI), while the calculation of the dipole-dipole interactions is accelerated by multiple threads using openMP. Within this parallel scheme, finite temperature are considered by averaging over several trajectories.

This method has been explained in section 4.3 based on a single CoFe layer.

This layer is part of a magnetic tunnel junction, which can be switched by a thermally excited, spin polarized current [43].

A parallelization of the hysteresis loop calculation is not always possible. Another method to reduce the computational time is to combine neighboring spins to a single macrospin. Such a macrospin approach is applicable, if a homogenous magnetization of the neighboring spins can be assumed.

The different approaches have been applied to determine the static and dynamic properties of the exchange bias stacks NiFe/IrMn/MgO/Pt and Pt/Co/Cr<sub>2</sub>O<sub>3</sub>/Pt. Both exchange bias stacks show a special characteristic. NiFe/IrMn/MgO/Pt is described by Park *et al.* as a tunnel junction with a spin valve like magnetoresistance. The change of the magnetoresistance of this system due to an applied field seems to be based on a rotation of the antiferromagnetic coupled Mn spins. With the calculation of the ground states and the spin dynamics, an effective model has been established, at which the antiferromagnetic IrMn layer undergoes a state transition during the field cycle. Each of the states during a complete field cycle are one of the eight degenerated ground states of IrMn. Besides the agreement regarding the rotation of the Mn spins, the shape of the hysteresis curves determined experimentally and by atomistic spin dynamics simulations are nearly equivalent. Furthermore the temperature dependent magnetization curves have been explained on the basis of the effective model. As the calculation of thermal averaged hysteresis loop means a huge computational effort, only single trajectories at rather low temperatures have been calculated. The determination of the thermal averaged hysteresis loops at the same temperatures as applied during the experiments [80] might strengthen the established model.

The special characteristic of the Pt/Co/Cr<sub>2</sub>O<sub>3</sub>/Pt system is the switchable sign of the exchange bias. By applying a high magnetic field or a rather low magnetic field in conjunction with an electric field simultaneously, the hysteresis loop is shifted to the opposite side of the field axis at a subsequent hysteresis loop measurement. Although no perfect effective model has been found, which explains all experimentally determined effects, the occurrence of an interfacial wall is very probable. By introducing an additional fixed spin, which is interfacially coupled to the ferromagnetic layer, the shapes of the magnetization

curves have been qualitatively obtained. The origin of effects, that act like an additional exchange bias field, might be related to the magnetoelectric properties of the  $\text{Cr}_2\text{O}_3$  structure. The combination of spin dynamics with a change of the atomic structure due to magnetoelectric effects is left for future research.

In section 5 some of the most important exchange bias models have been introduced. None of them might directly explain the behavior of the two studied exchange bias stacks. The Mauri model is based on the creation of an interfacial domain wall within the antiferromagnetic layer, like it has been observed at the NiFe/IrMn/MgO/Pt stack. But it does not account for a complete spin reversal, which is a property of both studied systems. Although a complete spin reversal is permitted within the Meiklejohn-Bean model, this model fails to explain other properties, e.g., the vertical shift of the hysteresis loop at Pt/Co/Cr<sub>2</sub>O<sub>3</sub>/Pt.

Within this thesis it becomes evident, that the magnetic properties of exchange bias stacks depend on the individual structures and material parameters of each layer. This implies, that no general exchange bias model can exist, which covers all properties of different exchange bias systems.

Rather than searching for a general exchange bias model, several models have to be developed to describe and explain the properties of the individual systems. The further development of the simulation methods shown within this thesis might support the future investigations of other multilayer structures.



# Bibliography

- [1] P. Tipler and G. Mosca, *Physics for Scientists and Engineers*. No. 1-33 in *Physics for Scientists and Engineers*, W. H. Freeman, 2004.
- [2] P. Mohn, *Magnetism in the Solid State: An Introduction*, ch. A Historical Introduction, pp. 1–11. Berlin, Heidelberg: Springer Berlin Heidelberg, 2003.
- [3] W. Gilbert, *De magnete*. Courier Corporation, 1958.
- [4] J. C. Maxwell, “A dynamical theory of the electromagnetic field,” *Proceedings of the Royal Society of London*, vol. 13, pp. 531–536, 1863.
- [5] Weiss, Pierre, “L’hypothèse du champ moléculaire et la propriété ferromagnétique,” *J. Phys. Theor. Appl.*, vol. 6, no. 1, pp. 661–690, 1907.
- [6] W. Heisenberg, “Zur Theorie des Ferromagnetismus,” *Zeitschrift für Physik*, vol. 49, no. 9, pp. 619–636, 1928.
- [7] A. Fert, “Nobel lecture: Origin, development, and future of spintronics,” *Rev. Mod. Phys.*, vol. 80, pp. 1517–1530, Dec 2008.
- [8] M. Julliere, “Tunneling between ferromagnetic films,” *Physics Letters A*, vol. 54, no. 3, pp. 225 – 226, 1975.
- [9] W. F. Brown, “Thermal fluctuations of a single-domain particle,” *Journal of Applied Physics*, vol. 34, no. 4, pp. 1319–1320, 1963.
- [10] L. Engelhardt and C. Schröder, “Simulating computationally complex magnetic molecules,” *Molecular Cluster Magnets*, pp. 241–291, 2011.

- [11] L. Dagum and R. Menon, “OpenMP: an industry standard API for shared-memory programming,” *Computational Science & Engineering, IEEE*, vol. 5, no. 1, pp. 46–55, 1998.
- [12] D. W. Walker and J. J. Dongarra, “MPI: a standard message passing interface,” *Supercomputer*, vol. 12, pp. 56–68, 1996.
- [13] B. G. Park, J. Wunderlich, X. Marti, V. Holy, Y. Kurosaki, M. Yamada, H. Yamamoto, A. Nishide, J. Hayakawa, A. B. S. J. Hayakawa, and T. Jungwirth, “A spin-valve-like magnetoresistance of an antiferromagnet-based tunnel junction,” *Nature Materials*, vol. 10, no. 5, pp. 347 – 351, 2011.
- [14] Y. Shiratsuchi, K. Wakatsu, T. Nakamura, H. Oikawa, S. Maenou, Y. Narumi, K. Tazoe, C. Mitsumata, T. Kinoshita, H. Nojiri, and R. Nakatani, “Isothermal switching of perpendicular exchange bias by pulsed high magnetic field,” *Applied Physics Letters*, vol. 100, no. 26, 2012.
- [15] K. Toyoki, Y. Shiratsuchi, A. Kobane, C. Mitsumata, Y. Kotani, T. Nakamura, and R. Nakatani, “Magnetoelectric switching of perpendicular exchange bias in Pt/Co/ $\alpha$ -Cr<sub>2</sub>O<sub>3</sub>/Pt stacked films,” *Applied Physics Letters*, vol. 106, no. 16, 2015.
- [16] Y. Shiratsuchi, H. Noutomi, H. Oikawa, T. Nakamura, M. Suzuki, T. Fujita, K. Arakawa, Y. Takechi, H. Mori, T. Kinoshita, M. Yamamoto, and R. Nakatani, “Detection and *In Situ* Switching of Unreversed Interfacial Antiferromagnetic Spins in a Perpendicular-Exchange-Biased System,” *Phys. Rev. Lett.*, vol. 109, p. 077202, Aug 2012.
- [17] H. Ohldag, A. Scholl, F. Nolting, E. Arenholz, S. Maat, A. T. Young, M. Carey, and J. Stöhr, “Correlation between exchange bias and pinned interfacial spins,” *Phys. Rev. Lett.*, vol. 91, p. 017203, Jul 2003.
- [18] A. Aharoni, *Introduction to the Theory of Ferromagnetism*. International series of monographs on physics, Oxford University Press, 2000.

- [19] W. Heitler and F. London, “Wechselwirkung neutraler Atome und homöopolare Bindung nach der Quantenmechanik,” *Zeitschrift für Physik*, vol. 44, no. 6, pp. 455–472, 1927.
- [20] J. Lindner and M. Farle, “Magnetic Anisotropy of Heterostructures,” in *Magnetic Heterostructures: Advances and Perspectives in Spinstructures and Spintransport* (H. Zabel and S. D. Bader, eds.), pp. 45–96, Berlin, Heidelberg: Springer Berlin Heidelberg, 2008.
- [21] E. C. Stoner and E. P. Wohlfarth, “A Mechanism of Magnetic Hysteresis in Heterogeneous Alloys,” *Philosophical Transactions of the Royal Society of London. Series A, Mathematical and Physical Sciences*, vol. 240, no. 826, pp. pp. 599–642, 1948.
- [22] S. Rohart, V. Repain, A. Thiaville, and S. Rousset, “Limits of the macrospin model in cobalt nanodots with enhanced edge magnetic anisotropy,” *Phys. Rev. B*, vol. 76, p. 104401, Sep 2007.
- [23] D. Hinzke, *Computersimulationen zur Dynamik magnetischer Nanostrukturen*. PhD thesis, Universität Duisburg-Essen, Fakultät für Physik, 2002.
- [24] L. D. Landau and E. Lifshitz, “On the theory of the dispersion of magnetic permeability in ferromagnetic bodies,” *Phys. Z. Sowjetunion*, vol. 8, no. 153, pp. 101–114, 1935.
- [25] D. S. Lemons and A. Gythiel, “Paul Langevin’s 1908 paper “On the Theory of Brownian Motion” [“Sur la théorie du mouvement brownien,” *C. R. Acad. Sci. (Paris)* 146, 530–533 (1908)],” *American Journal of Physics*, vol. 65, no. 11, pp. 1079–1081, 1997.
- [26] W. Coffey, Y. Kalmykov, and J. Waldron, *The Langevin Equation: With Applications in Physics, Chemistry and Electrical Engineering*. World Scientific Series in Contemporary Chemical Physics, World Scientific, 1996.
- [27] V. Antropov, S. Tretyakov, and B. Harmon, “Spin dynamics in magnets: Quantum effects and numerical simulations,” *Journal of applied physics*, vol. 81, no. 8, pp. 3961–3965, 1997.

- [28] N. Metropolis, A. W. Rosenbluth, M. N. Rosenbluth, A. H. Teller, and E. Teller, “Equation of State Calculations by Fast Computing Machines,” *The Journal of Chemical Physics*, vol. 21, no. 6, pp. 1087–1092, 1953.
- [29] T. L. Gilbert, “A phenomenological theory of damping in ferromagnetic materials,” *IEEE Transactions on Magnetism*, vol. 40, pp. 3443–3449, Nov 2004.
- [30] D. Suess, T. Schrefl, W. Scholz, J. V. Kim, R. L. Stamps, and J. Fidler, “Micromagnetic simulation of antiferromagnetic/ferromagnetic structures,” *IEEE Transactions on Magnetism*, vol. 38, pp. 2397–2399, Sep 2002.
- [31] G. A. Maugin, “A note on micromagnetics at high temperature,” *Applied physics*, vol. 11, no. 2, pp. 185–186, 1976.
- [32] M. Pohlit, I. Stockem, F. Porrati, M. Huth, C. Schröder, J. Müller, “Experimental and theoretical investigation of the magnetization dynamics of an artificial square spin ice cluster.” Submitted, 2016.
- [33] W. Rave, K. Fabian, and A. Hubert, “Magnetic states of small cubic particles with uniaxial anisotropy,” *Journal of Magnetism and Magnetic Materials*, vol. 190, no. 3, pp. 332 – 348, 1998.
- [34] G. Bertotti, *Hysteresis in Magnetism: For Physicists, Materials Scientists, and Engineers*. Electromagnetism, Elsevier Science, 1998.
- [35] W. Wernsdorfer, R. Clérac, C. Coulon, L. Lecren, and H. Miyasaka, “Quantum nucleation in a single-chain magnet,” *Phys. Rev. Lett.*, vol. 95, p. 237203, Nov 2005.
- [36] P. Bruno, G. Bayreuther, P. Beauvillain, C. Chappert, G. Lugert, D. Renard, J. P. Renard, and J. Seiden, “Hysteresis properties of ultrathin ferromagnetic films,” *Journal of Applied Physics*, vol. 68, no. 11, pp. 5759–5766, 1990.
- [37] G. Zhang, W. Hübner, E. Beaurepaire, and J.-Y. Bigot, “Laser-Induced Ultrafast Demagnetization: Femtomagnetism, a New Frontier?” in *Spin Dynamics in Confined Magnetic Structures I* (B. Hillebrands and

- K. Ounadjela, eds.), pp. 245–289, Berlin, Heidelberg: Springer Berlin Heidelberg, 2002.
- [38] M. C. Hickey and J. S. Moodera, “Origin of intrinsic gilbert damping,” *Phys. Rev. Lett.*, vol. 102, p. 137601, Mar 2009.
- [39] B. Heinrich, “Spin relaxation in magnetic metallic layers and multilayers,” in *Ultrathin Magnetic Structures III: Fundamentals of Nanomagnetism* (J. A. C. Bland and B. Heinrich, eds.), pp. 143–210, Berlin, Heidelberg: Springer Berlin Heidelberg, 2005.
- [40] J. García-Otero, M. Porto, J. Rivas, and A. Bunde, “Monte carlo simulation of hysteresis loops of single-domain particles with cubic anisotropy and their temperature dependence,” *Journal of Magnetism and Magnetic Materials*, vol. 203, no. 1–3, pp. 268 – 270, 1999.
- [41] U. Nowak, R. W. Chantrell, and E. C. Kennedy, “Monte carlo simulation with time step quantification in terms of langevin dynamics,” *Phys. Rev. Lett.*, vol. 84, pp. 163–166, Jan 2000.
- [42] D. Hinzke and U. Nowak, “Magnetic relaxation in a classical spin chain,” *Phys. Rev. B*, vol. 61, pp. 6734–6740, Mar 2000.
- [43] J. C. Leutenantsmeyer, M. Walter, V. Zbarsky, M. Münzenberg, R. Gureev, K. Rott, A. Thomas, G. Reiss, P. Peretzki, H. Schuhmann, M. Seibt, M. Czerner, and C. Heiliger, “Parameter space for thermal spin-transfer torque,” *Spin*, vol. 03, no. 01, p. 1350002, 2013.
- [44] J. C. Leutenantsmeyer, V. Zbarsky, M. von der Ehe, S. Wittrock, P. Peretzki, H. Schuhmann, A. Thomas, K. Rott, G. Reiss, T. H. Kim, M. Seibt, and M. Muenzenberg, “Spin-Transfer Torque Switching at Ultra Low Current Densities,” *Materials Transactions*, vol. 56, no. 9, 2015.
- [45] T. Liu, Y. Zhang, J. Cai, and H. Pan, “Thermally robust Mo/CoFeB/MgO trilayers with strong perpendicular magnetic anisotropy,” *Scientific reports*, vol. 4, 2014.

- [46] S. Ikeda, K. Miura, H. Yamamoto, K. Mizunuma, H. Gan, M. Endo, S. Kanai, J. Hayakawa, F. Matsukura, and H. Ohno, “A perpendicular-anisotropy CoFeB-MgO magnetic tunnel junction,” *Nature materials*, vol. 9, no. 9, pp. 721–724, 2010.
- [47] D. Kim and J. Hong, “Origin of thickness dependent spin reorientation transition of B2 type FeCo alloy films,” *Journal of Applied Physics*, vol. 114, no. 21, 2013.
- [48] I. Stockem and C. Schröder, “A Fast Method for Calculating Magnetic Hysteresis Loops,” *IEEE Transactions on Magnetics*, vol. 51, Nov 2015.
- [49] W. H. Meiklejohn and C. P. Bean, “New Magnetic Anisotropy,” *Phys. Rev.*, vol. 102, pp. 1413–1414, Jun 1956.
- [50] E. Tsymbal and I. Žutić, *Handbook of Spin Transport and Magnetism*. Boca Raton: CRC Press, 2012.
- [51] J. Nogués and I. K. Schuller, “Exchange bias,” *Journal of Magnetism and Magnetic Materials*, vol. 192, no. 2, pp. 203–232, 1999.
- [52] A. Berkowitz and K. Takano, “Exchange anisotropy - a review,” *Journal of Magnetism and Magnetic Materials*, vol. 200, no. 1-3, pp. 552–570, 1999.
- [53] R. L. Stamps, “Mechanisms for exchange bias,” *Journal of Physics D: Applied Physics*, vol. 33, no. 23, p. R247, 2000.
- [54] M. Kiwi, “Exchange bias theory,” *Journal of Magnetism and Magnetic Materials*, vol. 234, no. 3, pp. 584 – 595, 2001.
- [55] F. Radu and H. Zabel, “Exchange bias effect of ferro-/antiferromagnetic heterostructures,” in *Magnetic Heterostructures* (H. Zabel and S. Bader, eds.), vol. 227 of *Springer Tracts in Modern Physics*, pp. 97–184, Springer Berlin Heidelberg, 2008.
- [56] W. H. Meiklejohn and C. P. Bean, “New Magnetic Anisotropy,” *Phys. Rev.*, vol. 105, pp. 904–913, 1957.

- [57] D. Mauri, H. C. Siegmann, P. S. Bagus, and E. Kay, “Simple model for thin ferromagnetic films exchange coupled to an antiferromagnetic substrate,” *Journal of Applied Physics*, vol. 62, no. 7, pp. 3047–3049, 1987.
- [58] A. P. Malozemoff, “Random-field model of exchange anisotropy at rough ferromagnetic-antiferromagnetic interfaces,” *Phys. Rev. B*, vol. 35, pp. 3679–3682, Mar 1987.
- [59] Y. Imry and S.-k. Ma, “Random-field instability of the ordered state of continuous symmetry,” *Phys. Rev. Lett.*, vol. 35, pp. 1399–1401, Nov 1975.
- [60] N. C. Koon, “Calculations of exchange bias in thin films with ferromagnetic/antiferromagnetic interfaces,” *Phys. Rev. Lett.*, vol. 78, pp. 4865–4868, Jun 1997.
- [61] T. C. Schulthess and W. H. Butler, “Consequences of spin-flop coupling in exchange biased films,” *Phys. Rev. Lett.*, vol. 81, pp. 4516–4519, Nov 1998.
- [62] T. C. Schulthess and W. H. Butler, “Coupling mechanisms in exchange biased films (invited),” *Journal of Applied Physics*, vol. 85, no. 8, pp. 5510–5515, 1999.
- [63] M. Kiwi, J. Mejía-López, R. D. Portugal, and R. Ramírez, “Exchange bias model for Fe/FeF<sub>2</sub> : Role of domains in the ferromagnet,” *EPL (Europhysics Letters)*, vol. 48, no. 5, p. 573, 1999.
- [64] M. Kiwi, J. Mejía-López, R. Portugal, and R. Ramírez, “Positive exchange bias model: Fe/FeF<sub>2</sub> and Fe/MnF<sub>2</sub> bilayers,” *Solid State Communications*, vol. 116, no. 6, pp. 315 – 319, 2000.
- [65] U. Nowak, K. D. Usadel, J. Keller, P. Miltényi, B. Beschoten, and G. Güntherodt, “Domain state model for exchange bias. I. Theory,” *Phys. Rev. B*, vol. 66, p. 014430, Jul 2002.
- [66] E. Ising, “Beitrag zur theorie des ferromagnetismus,” *Zeitschrift für Physik*, vol. 31, no. 1, pp. 253–258, 1925.

- [67] M. D. Stiles and R. D. McMichael, “Model for exchange bias in polycrystalline ferromagnet-antiferromagnet bilayers,” *Phys. Rev. B*, vol. 59, pp. 3722–3733, Feb 1999.
- [68] H. Suhl and I. K. Schuller, “Spin-wave theory of exchange-induced anisotropy,” *Phys. Rev. B*, vol. 58, pp. 258–264, Jul 1998.
- [69] E. F. Kneller and R. Hawig, “The exchange-spring magnet: a new material principle for permanent magnets,” *IEEE Transactions on Magnetics*, vol. 27, pp. 3588–3560, Jul 1991.
- [70] A. Scholl, M. Liberati, E. Arenholz, H. Ohldag, and J. Stöhr, “Creation of an antiferromagnetic exchange spring,” *Phys. Rev. Lett.*, vol. 92, p. 247201, Jun 2004.
- [71] W. Thomson, “On the electro-dynamic qualities of metals:—effects of magnetization on the electric conductivity of nickel and of iron,” *Proceedings of the Royal Society of London*, vol. 8, pp. 546–550, 1856.
- [72] J. Inoue, “GMR, TMR and BMR and Related Phenomena,” in *Nanomagnetism and Spintronics* (T. Shinjo, ed.), pp. 15 – 92, Amsterdam: Elsevier, 2009.
- [73] L. Swartzendruber, V. Itkin, and C. Alcock, “The Fe-Ni (iron-nickel) system,” *Journal of Phase Equilibria*, vol. 12, no. 3, pp. 288–312, 1991.
- [74] H. Okamoto, “The Ir-Mn (Iridium-Manganese) system,” *Journal of Phase Equilibria*, vol. 17, no. 1, pp. 60–62, 1996.
- [75] P. Yu, X. F. Jin, J. Kudrnovský, D. S. Wang, and P. Bruno, “Curie temperatures of fcc and bcc nickel and permalloy: Supercell and Green’s function methods,” *Phys. Rev. B*, vol. 77, p. 054431, Feb 2008.
- [76] D. Hinzke, U. Atxitia, K. Carva, P. Nieves, O. Chubykalo-Fesenko, P. M. Oppeneer, and U. Nowak, “Multiscale modeling of ultrafast element-specific magnetization dynamics of ferromagnetic alloys,” *Phys. Rev. B*, vol. 92, p. 054412, Aug 2015.



- [77] L. Szunyogh, B. Lazarovits, L. Udvardi, J. Jackson, and U. Nowak, “Giant magnetic anisotropy of the bulk antiferromagnets IrMn and IrMn<sub>3</sub> from first principles,” *Phys. Rev. B*, vol. 79, p. 020403, Jan 2009.
- [78] R. Yanes, J. Jackson, L. Udvardi, L. Szunyogh, and U. Nowak, “Exchange bias driven by Dzyaloshinskii-Moriya interactions,” *Phys. Rev. Lett.*, vol. 111, p. 217202, Nov 2013.
- [79] V. Hemmati, M. L. Plumer, J. P. Whitehead, and B. W. Southern, “Monte Carlo simulations of magnetic ordering in the fcc kagome lattice,” *Phys. Rev. B*, vol. 86, p. 104419, Sep 2012.
- [80] X. Martí, B. G. Park, J. Wunderlich, H. Reichlová, Y. Kurosaki, M. Yamada, H. Yamamoto, A. Nishide, J. Hayakawa, H. Takahashi, and T. Jungwirth, “Electrical measurement of antiferromagnetic moments in exchange-coupled IrMn/NiFe stacks,” *Phys. Rev. Lett.*, vol. 108, p. 017201, Jan 2012.
- [81] A. Moser, K. Takano, D. T. Margulies, M. Albrecht, Y. Sonobe, Y. Ikeda, S. Sun, and E. E. Fullerton, “Magnetic recording: advancing into the future,” *Journal of Physics D: Applied Physics*, vol. 35, no. 19, p. R157, 2002.
- [82] Y. Shiratsuchi, T. Fujita, H. Oikawa, H. Noutomi, and R. Nakatani, “High Perpendicular Exchange Bias with a Unique Temperature Dependence in Pt/Co/ $\alpha$ -Cr<sub>2</sub>O<sub>3</sub> (0001) Thin Films,” *Applied Physics Express*, vol. 3, no. 11, p. 113001, 2010.
- [83] X. He, Y. Wang, N. Wu, A. N. Caruso, E. Vescovo, K. D. Belashchenko, P. A. Dowben, and C. Binck, “Robust isothermal electric control of exchange bias at room temperature,” *Nat Mater*, vol. 9, pp. 579–585, Jul 2010.
- [84] M. Fiebig, D. Fröhlich, and H. J. Thiele, “Determination of spin direction in the spin-flop phase of Cr<sub>2</sub>O<sub>3</sub>,” *Phys. Rev. B*, vol. 54, pp. R12681–R12684, Nov 1996.

- [85] Y. Shiratsuchi, H. Oikawa, S. ichi Kawahara, Y. Takechi, T. Fujita, and R. Nakatani, “Strong Perpendicular Magnetic Anisotropy at Co(111)/ $\alpha$ -Cr<sub>2</sub>O<sub>3</sub> (0001) Interface,” *Applied Physics Express*, vol. 5, no. 4, p. 043004, 2012.
- [86] M. T. Johnson, P. J. H. Bloemen, F. J. A. den Broeder, and J. J. de Vries, “Magnetic anisotropy in metallic multilayers,” *Reports on Progress in Physics*, vol. 59, no. 11, p. 1409, 1996.
- [87] N. Nakajima, T. Koide, T. Shidara, H. Miyauchi, H. Fukutani, A. Fujimori, K. Iio, T. Katayama, M. Nývlt, and Y. Suzuki, “Perpendicular Magnetic Anisotropy Caused by Interfacial Hybridization via Enhanced Orbital Moment in Co/Pt Multilayers: Magnetic Circular X-Ray Dichroism Study,” *Phys. Rev. Lett.*, vol. 81, pp. 5229–5232, Dec 1998.
- [88] J. de Miguel, A. Cebollada, J. Gallego, R. Miranda, C. Schneider, P. Schuster, and J. Kirschner, “Influence of the growth conditions on the magnetic properties of fcc cobalt films: from monolayers to superlattices,” *Journal of Magnetism and Magnetic Materials*, vol. 93, pp. 1 – 9, 1991.
- [89] M. Pajda, J. Kudrnovský, I. Turek, V. Drchal, and P. Bruno, “*Ab initio* calculations of exchange interactions, spin-wave stiffness constants, and Curie temperatures of Fe, Co, and Ni,” *Phys. Rev. B*, vol. 64, p. 174402, Oct 2001.
- [90] M. Suzuki, H. Muraoka, Y. Inaba, H. Miyagawa, N. Kawamura, T. Shimatsu, H. Maruyama, N. Ishimatsu, Y. Isohama, and Y. Sonobe, “Depth profile of spin and orbital magnetic moments in a subnanometer Pt film on Co,” *Phys. Rev. B*, vol. 72, p. 054430, Aug 2005.
- [91] S. Shi, A. L. Wysocki, and K. D. Belashchenko, “Magnetism of chromia from first-principles calculations,” *Phys. Rev. B*, vol. 79, p. 104404, Mar 2009.
- [92] R. A. Alikhanov, v. Dimitrijević, A. Kowalska, S. Kraśnicki, H. Rżany, J. Todorović, and A. Wanic, “Neutron investigation of the Spin System

- Dynamics in  $\alpha$ -Cr<sub>2</sub>O<sub>3</sub>,” *Physica Status Solidi (b)*, vol. 32, no. 1, pp. 41–48, 1969.
- [93] H. Yang, A. Thiaville, S. Rohart, A. Fert, and M. Chshiev, “Anatomy of Dzyaloshinskii-Moriya Interaction at Co/Pt Interfaces,” *Phys. Rev. Lett.*, vol. 115, p. 267210, Dec 2015.
- [94] K. D. Belashchenko, O. Tchernyshyov, A. A. Kovalev, and O. A. Tretiakov, “Magnetoelectric domain wall dynamics and its implications for magnetoelectric memory,” *ArXiv e-prints*, Jan. 2016.
- [95] M. Fiebig, “Revival of the magnetoelectric effect,” *Journal of Physics D: Applied Physics*, vol. 38, no. 8, p. R123, 2005.
- [96] T. Moriya, “Anisotropic superexchange interaction and weak ferromagnetism,” *Phys. Rev.*, vol. 120, pp. 91–98, Oct 1960.
- [97] F. Freimuth, S. Blügel, and Y. Mokrousov, “Berry phase theory of Dzyaloshinskii–Moriya interaction and spin–orbit torques,” *Journal of Physics: Condensed Matter*, vol. 26, no. 10, p. 104202, 2014.
- [98] I. Kezsmarki, S. Bordacs, P. Milde, E. Neuber, L. M. Eng, J. S. White, H. M. Ronnow, C. D. Dewhurst, M. Mochizuki, K. Yanai, H. Nakamura, D. Ehlers, V. Tsurkan, and A. Loidl, “Neel-type skyrmion lattice with confined orientation in the polar magnetic semiconductor GaV4S8,” *Nat Mater*, vol. 14, pp. 1116–1122, Nov 2015. Article.
- [99] O. Boulle, J. Vogel, H. Yang, S. Pizzini, D. de Souza Chaves, A. Locatelli, T. O. Mentès, A. Sala, L. D. Buda-Prejbeanu, O. Klein, M. Belmeguenai, Y. Roussigné, A. Stashkevich, S. M. Chérif, L. Aballe, M. Foerster, M. Chshiev, S. Auffret, I. M. Miron, and G. Gaudin, “Room-temperature chiral magnetic skyrmions in ultrathin magnetic nanostructures,” *Nat Nano*, vol. advance online publication, Jan 2016. Article.
- [100] Y. Shiratsuchi, Y. Kotani, S. Yoshida, Y. Yoshikawa, K. Toyoki, A. Kobane, R. Nakatani, and T. Nakamura, “Direct observations of ferromagnetic and antiferromagnetic domains in Pt/Co/Cr<sub>2</sub>O<sub>3</sub>/Pt perpendicular exchange biased film,” *AIMS Materials Science*, vol. 2, no. 201504484, pp. 484–496, 2015.

- [101] G. A. Gehring, “On the microscopic theory of the magnetoelectric effect,” *Ferroelectrics*, vol. 161, no. 1, pp. 275–285, 1994.
- [102] R. Hornreich and S. Shtrikman, “Statistical Mechanics and Origin of the Magnetoelectric Effect in  $\text{Cr}_2\text{O}_3$ ,” *Phys. Rev.*, vol. 161, pp. 506–512, Sep 1967.
- [103] M. Date, J. Kanamori, and M. Tachiki, “Origin of Magnetoelectric Effect in  $\text{Cr}_2\text{O}_3$ ,” *Journal of the Physical Society of Japan*, vol. 16, no. 12, pp. 2589–2589, 1961.
- [104] S. Parkin, X. Jiang, C. Kaiser, A. Panchula, K. Roche, and M. Samant, “Magnetically engineered spintronic sensors and memory,” *Proceedings of the IEEE*, vol. 91, pp. 661–680, May 2003.

# Danksagung

Zuallererst möchte ich mich bei Prof. Dr. Günter Reiss und Prof. Dr. Christian Schröder für die gute Unterstützung während der letzten Jahre bedanken.

Prof. Dr. Günter Reiss unbürokratisches Vorgehen half mir von Beginn an bei der Einschreibung an der Universität Bielefeld, bis zum Ende bei der erfolgreichen Beantragung des Abschlussstipendiums und den letzten organisatorischen Schritten. Sein fachlicher Rat aus experimenteller Sicht ergänzte die mit Schwerpunkt auf der Theorie liegenden Diskussionen mit Prof. Dr. Christian Schröder sehr gut.

Ich möchte Prof. Dr. Christian Schröder dafür danken, dass er mir gerade am Anfang meiner Doktorandenzeit durch die Beantwortung vieler Fragen den Einstieg ins Thema sehr erleichtert hat. Die darauffolgenden lebhaften Diskussionen, trugen sowohl zu meinem Erkenntnisgewinn, als auch zu meiner persönlichen Entwicklung bei. Ferner unterstützte er mich mit motivierenden Worten und teils aktiver Mithilfe bei der Fehlersuche während der Weiterentwicklung der Software.

In diesem Zusammenhang möchte ich auch Thomas Hilbig, Prof. Dr. Jürgen Schnack und dem Team vom PC<sup>2</sup> der Universität Paderborn für den Support und für Zugang zu verschiedenen Rechenclustern danken. Auf einem einfachen Laptop wären Berechnungen der Spindynamik mit mehreren hundert Atomen kaum möglich gewesen.

Aber auch kleine Spinmodelle bergen Schwierigkeiten. So danke ich Prof. Dr. Heinz-Jürgen Schmidt und Arne Kolkman für ihre Hilfe zum mathematischen

Verständnis der Herleitung von kleinen Modellen.

Die guten Erklärungen von JProf. Dr. Markus Meinert erweiterten mein Verständnis für die Physik kleiner Strukturen. Außerdem trugen die von ihm berechneten Austauschkonstanten bei der Untersuchung des CoFe bei.

Ganz besonders möchte ich Dr. Lisa Teich danken, mit der ich lange ein Büro teilte. Sie unterstützte mich vor allem zu Beginn mit verwaltungstechnischen Angelegenheiten, aber auch bei fachlichen Fragen. Sogar nach dem Umzug der Fachhochschule in Bielefeld, stand ihre Tür für mich immer offen. So wurde ihr Büro im neuen Fachhochschulgebäude zu meiner ersten Anlaufstelle zu Wochenbeginn.

Des Weiteren bedanke ich mich bei allen an der Fachhochschule Bielefeld, mit denen ich meine Zeit dort verbracht habe. Dies schließt sowohl die Arbeitsgruppe CMSE, als auch Sabine Wolf-Homeyer und Vanessa Homburg mit ein.

In guter Erinnerung bleiben mir die Konferenzbesuche mit Prof. Dr. Christian Schröder, Lisa Teich, Simon Bekemeier und vielen Mitarbeitern, sowie Doktoranden der Arbeitsgruppe Dünne Schichten & Physik der Nanostrukturen an der Universität Bielefeld. Nebst dem wissenschaftlichen Austausch habe ich das nette Miteinander sehr genossen.

Im Laufe der Promotionszeit nahm ich an einem Mentoring Programm der Universität Bielefeld teil. Neben den Workshops, motivierten die Gespräche mit meiner wirklich netten Peergruppe sehr. Dabei wurde mir bewusst, dass die Herausforderungen bei den Doktorandinnen anderer Fachbereich sehr ähnlich sind. Ich danke dieser Gruppe und auch den Programmorganisatoren Yulika Ogawa-Müller und Pia Brocke für die sehr angenehmen Treffen.

Im diesem Rahmen bedanke ich mich auch beim Land NRW und der Bielefelder Universität für die Finanzierung meines Promotionsvorhabens.

Ganz zum Schluss, aber nicht weniger, möchte ich meiner Familie danken.

Dabei denke ich an meinen Vater, der von meiner Kindheit an versucht meine Fragen zu beantworten und mich stets bei meinen Vorhaben unterstützt. Nicht zuletzt, beim Korrekturlesen dieser Dissertationsschrift. Ich danke meiner Mutter, ohne sie wäre ich vermutlich in den letzten Wochen während des Schreibprozesses im Chaos versunken. Großer Dank gilt meinem Mann Patrick, der mich durch alle Hochs und Tiefs, die ein Promotionsvorhaben mit sich bringt, begleitet hat. Nicht selbstverständlich ist die Rücksicht meines noch sechsjährigen Sohnes Gregor. Er hat sich sicherlich häufiger Zeit zum Spielen mit mir gewünscht. Stattdessen hat sich mein Bruder öfters um ihn gekümmert, was mir den Rücken frei hielt. Auch Pia, der Freundin meines Bruders, und vielen weiteren möchte ich für das Korrekturlesen danken.

Ohne die Unterstützung im beruflichen wie auch im privaten Umfeld wäre diese Arbeit sicherlich nicht zustande gekommen.